

THE THEORY, MEASUREMENT, AND APPLICATIONS OF MODE SPECIFIC
SCATTERING PARAMETERS WITH MULTIPLE MODES OF PROPAGATION

By

DAVID E. BOCKELMAN

A DISSERTATION PRESENTED TO THE GRADUATE SCHOOL OF THE
UNIVERSITY OF FLORIDA IN PARTIAL FULFILLMENT OF THE
REQUIREMENTS FOR THE DEGREE OF DOCTOR OF PHILOSOPHY

UNIVERSITY OF FLORIDA

1997

Copyright 1997

By

DAVID E. BOCKELMAN

ACKNOWLEDGMENTS

The author would like to acknowledge the significant support of Motorola Radio Products Group Applied Research, without which this work would not have been possible. Many members of the staff of Applied Research gave support, advice and assistance which has been received with gratitude. The author would especially like to thank Charles Backof, Vice-President and Director of Research, Radio Products Group, who urged the pursuit of this work, and Dr. Wei-Yean Hwong, Principal Member of the Technical Staff, who gave his time and direction. The author is indebted to Robert Stengel, Member of the Technical Staff, who provided motivation for this work and guidance through its completion.

Furthermore, the author would like to thank Professor William R. Eisenstadt, who demonstrated his generosity by giving essential support in technical and personal matters. The author would also like to thank the members of his advisory committee for their support and direction, who were critical elements in the partnership between the University, Motorola, and the student. Also appreciated by the author is the help of the staff of the University of Florida Microelectronics Lab, and the help of many others who can not be listed here.

Of all who gave their support and assistance, none was as critical as the author's wife, Erika. Her unquestioning commitment was the light which has led the way to this conclusion.

TABLE OF CONTENTS

ACKNOWLEDGMENTS	ii
TABLE OF CONTENTS.....	iii
ABSTRACT.....	vii
CHAPTERS	
1 INTRODUCTION	1
2 PRIOR THEORIES AND TECHNIQUES	6
2.1. Fundamental Theories of Analysis	7
2.1.1. Coupled Transmission Line Pairs	7
2.1.2. Analog Methods.....	9
2.1.3. Linear Network Representations	11
2.1.3.1. Analog Network Parameters	12
2.1.3.2. RF Network Parameters.....	15
2.2. Measurement Techniques	20
2.2.1. Single Mode Analog Measurements.....	21
2.2.2. Single Mode RF and Microwave Measurements.....	22
2.2.2.1. Scalar Power Measurements Including Baluns	22
2.2.2.2. Scattering Parameters with Baluns	24
2.3. Summary of Past Theory and Techniques	26
3 FUNDAMENTAL THEORY OF MODE SPECIFIC S-PARAMETERS.....	27
3.1. Mode Specific Scattering Parameters in Differential Circuits.....	27
3.1.1. Fundamental Definitions for Differential Circuits.....	28
3.1.1.1. Modal Voltage and Currents	30
3.1.1.2. Coupled Mixed-Mode Signals	32
3.1.1.3. Mixed-Mode Scattering Parameters	37
3.1.2. Choice of Reference Impedances for Multiple Modes	39
3.1.3. Relationship of Mixed-Mode and Standard S-Parameters	42
3.1.4. Interpretations of Multi-Mode Scattering Parameters	46
3.2. Generalizations of Mode Specific Scattering Parameters.....	53
3.2.1. Other modes.....	53
3.2.2. Eigen modes.....	57

4	CONSTRUCTION OF THE PURE-MODE VECTOR NETWORK ANALYZER.....	61
4.1.	Basic Operation of the PMVNA.....	62
4.1.1.	Fundamental Concepts.....	62
4.1.2.	General PMVNA Test-Set Architecture.....	63
4.2.	Implementation of a Practical PMVNA.....	65
4.2.1.	System Level Description.....	66
4.2.2.	Test-Set Construction.....	69
4.2.3.	Detailed Operation.....	72
4.2.4.	Control Software.....	77
4.3.	On-Wafer Measurements.....	79
5	ACCURACY OF THE PURE-MODE VECTOR NETWORK ANALYZER.....	82
5.1.	Probe-to-Probe Crosstalk.....	83
5.1.1.	Simulated Probe Crosstalk.....	84
5.1.2.	Measured Probe Crosstalk.....	88
5.2.	Uncertainty Calculations.....	90
5.2.1.	Discussion of Accuracies.....	99
5.2.2.	Uncertainty Model Derivation.....	101
5.2.3.	Order of Uncertainty Calculations.....	106
5.3.	Conclusions on Accuracy.....	107
6	CALIBRATION OF THE PURE-MODE VECTOR NETWORK ANALYZER.....	108
6.1.	Types of VNA Measurement Errors.....	108
6.2.	Primary PMVNA Calibration.....	110
6.2.1.	Raw Performance.....	110
6.2.2.	PMVNA Error Model.....	115
6.2.3.	Development of Calibration Equation.....	121
6.2.4.	Switching Errors and Non-Pure Mode Generation.....	124
6.2.5.	Solution of the Calibration Problem.....	128
6.2.6.	Coaxial Calibration Standards.....	132
6.2.7.	On-Wafer Calibration Standards.....	134
6.3.	Phase Offset Pre-Calibration.....	139
6.3.1.	Phase Offset Standards.....	140
6.3.1.1.	First Principles.....	141
6.3.1.2.	Offset Model.....	142
6.3.1.3.	Modified T-Matrix Solution.....	144
6.3.2.	Phase Offset Of An Unknown DUT.....	150
6.3.2.1.	Variable Offset Model.....	150
6.3.2.2.	Using Multiple Offset Standards.....	151
6.3.2.3.	Calculating the Offset of an Arbitrary DUT.....	152
6.3.2.4.	Diagonalized Form.....	153
6.4.	Calibration Procedure.....	154

7	VERIFICATION OF THE PMVNA	156
8	POWER SPLITTER AND COMBINER ANALYSIS	167
8.1.	Splitters	169
8.2.	Combiners	178
8.3.	Extensions to Arbitrary Phase	180
9	THIN-FILM METAL-ON-CERAMIC STRUCTURES	183
9.1.	Differential Transmission Lines	184
9.1.1.	Uniform Differential Transmission Line	184
9.1.2.	Balanced Step Differential Transmission Line	189
9.1.3.	Unbalanced Step-Up Differential Transmission Line	194
9.2.	Comparison Between Measurements and Simulations	199
9.2.1.	Unbalanced Step Differential Transmission Line	200
9.2.2.	Balanced Step Differential Transmission Line	206
9.3.	Crosstalk Between Differential Transmission Lines	212
9.3.1.	Balanced Differential Transmission Lines	214
9.3.2.	Unbalanced Differential Transmission Lines	230
10	PASSIVE INTEGRATED CIRCUIT STRUCTURES	239
10.1.	Transmission Lines without Metal Ground Planes	243
10.1.1.	Single-Ended Transmission Lines	243
10.1.2.	Simple Uniform Differential Transmission Line	248
10.2.	Transmission Lines with Ground Metal Ground Planes	252
10.2.1.	Single-Ended Transmission Lines	253
10.2.2.	Uniform Differential Transmission Lines	254
10.3.	Unbalanced Differential Transmission Lines	259
10.4.	Vertical Differential Transmission Lines	265
10.5.	Pad-to-Pad Crosstalk	275
11	PROPERTIES OF MIXED-MODE S-PARAMETERS	291
11.1.	Symmetry of Reciprocal Devices	291
11.1.1.	General	291
11.1.2.	Port-Symmetric Reciprocal Devices	293
11.2.	Balanced Devices	294
11.3.	Indefinite Mixed-Mode S-Parameters	297
11.4.	Device Mode Specific Gains of Ideally Balanced Differential Circuit	304
11.4.1.	Transducer Power Gains	305
11.4.2.	Maximum Power Gains	308
11.4.3.	Power Gain Circles	313
12	CONCLUSIONS	318

APPENDICES

A	ANALOG HALF-CIRCUIT TECHNIQUES.....	323
B	ANALOG MEASUREMENT TECHNIQUES	327
C	TRANSMISSION OF MODES FROM COUPLED TO UNCOUPLED LINES	330
D	SIMULATED S-PARAMETERS OF DIFFERENTIAL AMPLIFIER.....	334
E	DESCRIPTION OF HP8510 VNA SUB-SYSTEMS	339
F	DETAILS OF HP8517 TEST-SET MODIFICATIONS.....	348
G	PMVNA CONTROL SOFTWARE	357
H	MULTI-PORT T-MATRIX DEFINITION	383
I	ERROR TERMS OF PMVNA AND FOUR-PORT VNA.....	387
J	DEMONSTRATION OF COEFFICIENT MATRIX RANK	390
	LIST OF REFERENCES	403
	BIOGRAPHICAL SKETCH	412

Abstract of Dissertation Presented to the Graduate School of the University of Florida in
Partial Fulfillment of the Requirements for the Degree of Doctor of Philosophy

THE THEORY, MEASUREMENT, AND APPLICATIONS OF MODE SPECIFIC
SCATTERING PARAMETERS WITH MULTIPLE MODES OF PROPAGATION

by

David E. Bockelman

May 1997

Chairman: William R. Eisenstadt

Major Department: Electrical and Computer Engineering

Mode-specific scattering parameters (s-parameters) are defined from fundamental concepts. Such s-parameters directly express the response of a device in its intended modes of operation. The development is specifically applied to high frequency differential circuits. Differential circuits are shown to be characterized by four sets of s-parameters: (1) pure differential mode s-parameters with a differential-mode input and output, (2) pure common-mode s-parameters with a common-mode input and output, (3) mode-conversion s-parameters with a differential-mode input and a common-mode output, and (4) mode-conversion s-parameters with a common-mode input and a differential-mode output. All of these sets of mode-specific s-parameters are shown to be useful in analysis of a differential circuit.

A specialized system, called the pure-mode vector network analyzer (PMVNA), is developed for the measurement of the mode-specific s-parameters of a high frequency differential circuit. The calibration of this analyzer is developed and implemented. Verifica-

tion establishes error correction accuracy. The PMVNA is shown to have accuracy advantages for the measurement of differential circuits when compared to a traditional four-port analyzer.

The mode-specific s -parameter concepts are applied to several practical high frequency differential circuits. Power splitters and combiners are analyzed with these concepts. Traditional specifications of phase and magnitude imbalance are shown to correspond to spurious mode responses. Differential transmission line structures, implemented on ceramic substrates, are examined. The effects of imbalance and symmetry are analyzed with mode-specific s -parameters. Several structures on a silicon integrated circuit (IC) are measured. The effects of differential topology on circuit-to-circuit coupling are quantified. Basic design methods are advanced for the design of high frequency differential circuits.

CHAPTER 1 INTRODUCTION

In many applications, devices and circuits have been designed for only a single mode of operation. In the most general sense, a mode is a particular electromagnetic field configuration for a given device or circuit. In the case of one or two conductors, the modes are usually frequency dependent, so the existence of simultaneous modes can be avoided by proper selection of operating frequencies (or by proper physical design for a given frequency). However, with three or more conductors, there will usually exist multiple modes even in static cases. In such situations, the simultaneous existence of two or more modes can be difficult to avoid.

Differential circuits are a particular class of circuits of historic importance with three conductors. Sometimes called balanced circuits, the primary operation of differential circuits is to respond to the difference between two signals, such as $\Delta v_1 = v_1 - v_2$ as

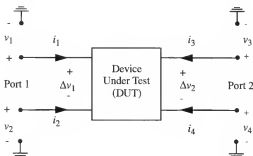


Figure 1-1. Schematic of two-port differential circuit.

shown in Figure 1-1. The two conductors can also have a common voltage (or a current flow) with respect to a third conductor, namely ground. As a result, two modes of operation are generally possible with differential circuits: the differential-mode and the common-mode. Furthermore, both modes can exist simultaneously in general.

There are many applications of differential circuits. Twisted pair transmission lines, operational amplifiers, baluns, coupled transmission lines, power splitters and combiners are all examples of differential circuits [1 - 3]. More recent applications include radio frequency (RF) low noise amplifiers (LNA) with differential inputs and outputs, as well as double-balanced mixers such as Gilbert cell mixers [4].

RF differential circuit applications have become common as the commercial demand for radio systems has grown. Two characteristics of differential circuits make them particularly attractive for RF applications. The first advantage of the differential circuit is circuit-to-circuit isolation. This characteristic has been exploited for many years, most notably in telephone systems in the form of twisted-pair wire transmission lines [5]. The higher isolation of differential circuits (with respect to single-ended circuits) is due to the nullification of any noise common to both constituent signals in the differential signal, i.e. $(v+n) - (-v+n) = 2v$ where n represents an interfering signal. This isolation increase is important to integrated circuit (IC) implementations. As integration density increases, and operation frequencies increase, improving circuit-to-circuit isolation is critical. As a result, differential circuits are being applied where only single-ended circuits have traditionally been used.

Second, the differential circuit has increased dynamic range when compared to a ground referenced, or single-ended, circuit. With a given voltage swing v , a pure differen-

tial signal will be doubled, i.e. $v - (-v) = 2v$. This increased dynamic range is particularly important as the supply voltages decrease in modern radio systems. This decreasing supply voltage has made single-ended implementations of receiver functions difficult, since maximum signal swing in a circuit is typically less than the supply voltage. By implementing radio functions with differential circuits, the available signal swing, and hence the dynamic range, can be increased while retaining a low supply voltage.

The emphasis of traditional RF and microwave techniques has been to avoid the simultaneous existence of multiple modes. As a result, there is a lack of self-consistent, rigorous theory that is applicable to the measurement, analysis and design of RF and microwave differential circuits. Typically, differential circuits are designed and analyzed with traditional analog techniques, which employ lumped element assumptions. RF and microwave differential circuits contain distributed circuit elements, and require distributed circuit analysis and testing. Furthermore, traditional methods of testing differential circuits have required the application and measurement of voltages and currents, which is difficult at RF and microwave frequencies. Scattering parameters (s-parameters) have been developed for characterization and analysis at these frequencies, but have been applied primarily to single-ended circuits. A modification of existing s-parameter techniques is needed for accurate measurement, analysis and design of differential circuits at microwave frequencies. This work extends the definitions of s-parameters to mode-specific representations, where the s-parameters are defined in terms of the natural modes of operation of a circuit.

This dissertation presents original work in the following areas. The traditionally accepted definitions of differential and common-mode voltages and currents are shown

for the first time to be non-orthogonal, and therefore unacceptable for direct application of these definitions for power calculations. New orthogonal definitions for these voltages and currents are presented, and shown to be appropriate for power calculations. Multiple mode s -parameters are developed which for the first time completely describes the linear behavior of an RF differential circuit. These concepts are verified through simulations of RF differential circuitry. The first network analyzer for the measurement of multi-mode s -parameters is constructed, and the inherent accuracy advantages of the system are established. Fundamental work in multi-port network analyzer calibration proceeds beyond any previously published work, and a verification procedure establishes the accuracy of the calibration. Measurements with the multi-mode network analyzer includes the first of integrated differential circuits. Extensions of s -parameter design techniques to multi-mode circuits are presented that will formalize the design and analysis of RF differential circuits.

This dissertation is organized in the following manner. In Chapter 2, techniques for analysis and measurement of differential circuits, prior to this work, are discussed. Chapter 3 presents original work of extending scattering parameter theory to differential circuits. A new measurement system for the measurement of mode-specific s -parameters is introduced in Chapter 4. Chapter 5 examines the accuracy, and establishes the intrinsic accuracy advantages, of this system for the measurement of differential circuits. The calibration theory and implementation for the new measurement system is developed in Chapter 6. In Chapter 7, the results of accuracy verification of this new system are presented. The remaining chapters of the dissertation focus on applications of the mode-specific s -parameter concepts. Chapter 8 applies the new mode-specific concepts to power

splitters and combiners. Several thin-film metal differential structures, fabricated on aluminum oxide, are studied in Chapter 9. Circuit-to-circuit crosstalk for IC structures on silicon is studied in Chapter 10, and conclusions are made about practical implementation of ICs. Chapter 11 discusses properties of the new s -parameters and provides basic analysis and design tools for use with RF differential circuits. Chapter 12 concludes this dissertation with a summary, some discussions, and remarks on future research.

CHAPTER 2

PRIOR THEORIES AND TECHNIQUES

This chapter serves as a summary of past theoretical and experimental techniques that are applied to differential circuits. The focus of the chapter is RF and microwave differential circuits. However, lower frequency work has had a profound effect on the subject, so the examination will include relevant analog techniques.

In the area of theoretical analysis, the subjects presented include multi-mode transverse electromagnetic (TEM) structures such as coupled transmission lines. The analog methods that have provided the basic concepts of differential circuit analysis are summarized. Network representation of a differential circuit is reviewed, and its application to an RF differential circuit is explored. The traditionally accepted definitions of differential and common-mode voltages and currents are shown to be non-orthogonal, i. e., as a system, the definitions do not conserve energy.

The measurement techniques of RF differential circuits are then summarized. Analog differential circuit measurement techniques are briefly examined as background. All widely practiced measurement approaches for RF and microwave differential circuits are presented in general, and are shown to provide inadequate characterization of the device under test.

2.1. Fundamental Theories of Analysis

The topics presented in the following sections represent some of the most prominent concepts in differential circuit analysis. The subjects are coupled transmission lines, analog methods, and network representations, and each topic holds a unique concept which shapes later theoretical developments.

2.1.1. Coupled Transmission Line Pairs

In a survey of prior work in the RF and microwave fields, one early area of work is found to share many concepts with differential circuits in general. The work done in coupled transmission lines, and their applications, describe multiple mode behavior that is analogous to differential circuit modes. The importance of this transmission line work in this context is the treatment of the simultaneous existence of two modes of propagation.

The coupled transmission line pair theories have their foundations in electromagnetic field descriptions [6, 7]. Systematic treatment of the coupled pair transmission line begins with the examination of the two fundamental TEM modes. Planar coupled transmission lines such as stripline are of particular importance due to fabrication advantages. As a result, much early work considers planar structures. With such structures, the two fundamental TEM modes are called odd and even for their respective field symmetry, with

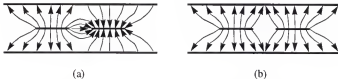


Figure 2-1. Electric field distributions in planar coupled transmission lines.
a) Odd-mode electric field; b) Even-mode electric field.

the terminology apparently first introduced by Cohn [6]. Representations of the electric field distributions for the two fundamental TEM modes are shown in Figure 2-1. In Figure 2-1(a) the signal conductors are at equal but opposite potentials and carry equal but opposite currents, and hence this is called the odd mode. In Figure 2-1(b) the signal conductors are the same potential and carry equal currents; this is called the even mode.

Early work was limited to only physically symmetric structures [6], and the terms even and odd apply only with such limitations. Tripathi later extended the theory to include any coupled pair transmission line structure [8]. With this extension, the two modes became c and π -modes, respectively, and the symmetry in the field distribution was lost. With the loss of the even and odd-modes, the direct analogy to differential and common-modes becomes less clear.

Although important for the treatment of simultaneous modes, the coupled transmission line work is limited to transmission line applications. The theory is cast in terms of characteristic impedances, propagation constants, etc., and is not directly applicable to a general differential circuit. Previous work has been specific to descriptions of coupled transmission lines [6, 8 - 15] and shielded balanced transmission lines. In the literature, the coupled transmission work has been most commonly applied to directional couplers [2, 16 - 18] rather than to differential circuits in general. All of the referenced work deals with specific TEM structures, and is not suitable for characterization of a generic differential circuit.

Despite the narrow application of prior work, the theory of coupled transmission lines provides the foundation on which general multi-mode network analysis is built. Scattering parameters are a relative measure of a network's response, so any mode-spe-

cific s -parameters must be defined with respect to some reference impedance. In Chapter 3, the theory of coupled transmission lines will be used to rigorously define the reference impedance for the different modes.

2.1.2. Analog Methods

Traditional analog methods play a central role in the prior work with differential circuits. The work, which employs lumped element assumptions, is used primarily for audio or near-audio frequencies. Of course, most any general analog circuit techniques can be applied to an analog differential circuit, but some specialized concepts are of particular importance.

Analog theories have provided the fundamental definitions of differential and common-mode voltages. Referring to Figure 1-1, the differential-mode voltage at port one is defined as

$$v_{d1} \equiv v_1 - v_2 \quad (2-1)$$

and the common-mode voltage at port one is defined as

$$v_{c1} \equiv \frac{v_1 + v_2}{2} \quad (2-2)$$

The differential current into port one is

$$i_{d1} \equiv \frac{i_1 - i_2}{2} \quad (2-3)$$

and the common-mode current into port one is

$$i_{c1} \equiv \frac{i_1 + i_2}{2} \quad (2-4)$$

with similar definitions at port two. These definitions have lead to voltage gain concepts

$$A_d = \frac{v_{d2}}{v_{d1}} \quad A_c = \frac{v_{c2}}{v_{c1}} \quad (2-5)$$

These definitions are widely accepted as evidenced by examples found in the texts by Gray and Meyer [4], Middlebrook [19] and Giacoletto [20], as well as other recent works [12, 21].

Of particular interest in analog techniques is the method of differential and common-mode half-circuits. This technique allows circuit analysis simplification by considering separately the response of the circuit to a pure differential signal and a pure common-mode signal [4]. For an instructive example of the application of half-circuit methods, see Appendix A. These analog techniques are useful in gaining insight into differential amplifier operation. However, these techniques have some limitations. First, these equivalent circuit approaches can become intractable as high frequency effects are included. Also, they are inherently lumped element approaches, and are not easily adapted to include distributed circuit elements that become important at RF and higher frequencies.

The most fundamental limitation is that the half-circuit techniques are applied only to symmetric differential circuits. It has been shown [19], that perfectly symmetric (or balanced) differential circuits exhibit no mode conversion. By limiting the analysis to symmetric circuits, or by neglecting any asymmetry, the phenomenon of mode conversion is completely ignored. Mode conversion occurs when a stimulus of a pure mode creates an output of more than one mode. For example, if a pure differential signal drives an amplifier, and both a differential-mode and a common-mode output signal are produced, then some conversion from differential to common-mode has occurred.

Mode conversion is an important phenomenon for RF and microwave differential circuits, and in amplifiers in particular. It has also been shown [19] that mode conversion will affect the maximum achievable common-mode rejection ration (CMRR). A critical parameter of differential amplifier design, CMRR quantifies the ability of an amplifier to amplify differential signals and reject common-mode signals. Understanding, predicting, and measuring the phenomenon of mode conversion can be important to the performance of RF differential circuits.

2.1.3. Linear Network Representations

Linear time-invariant (LTI) network representation is a basic and useful circuit analysis technique which is widely applied to two-port and three-terminal circuits of both analog and RF applications [22]. Network representations are distinctly suitable for

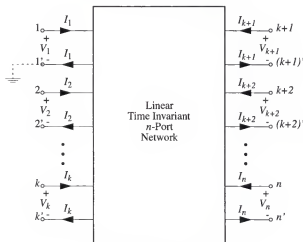


Figure 2-2. Notation of an n -port linear time-invariant network.

descriptions of distributed element circuits as encountered in RF and microwave applications. It is of use then to examine the application of LTI network theory to differential circuits.

A circuit, or network, with n pairs of terminals which are used as input/output connections is known as an n -port network. The notation conventions for an n -port network are shown in Figure 2-2. The dashed line connecting the 1' terminal to ground indicates that some or all of the return terminals can be grounded. The behavior of the network is described by a set of equations that are expressed in terms of the defined voltages and currents (or quantities that are related), which can be written in matrix form. The matrix description leads to a convenient set of parameters for a circuit. Some commonly used parameters are impedance Z , admittance Y , hybrid h , and chaining $ABCD$. These parameters are all based on voltage and current descriptions of the network. Other parameters, such as scattering parameters (s-parameters), are based on functions of voltage and current.

2.1.3.1. Analog Network Parameters

Network representations can be applied to differential circuits in at least two ways. One possible application of network theory is to interpret each input and output terminal of the differential circuit as a port with the return path grounded. This approach is quite common, and will be referred to as the standard approach to network representation. With this approach, all of the inputs and outputs of the differential circuit are ground referenced (single-ended). In this case, the network will always have $2n$ ports, where n is number of differential inputs and outputs. For example, a differential amplifier can be represented as

a four-port network, shown in Figure 2-3. Here the port voltages are related to the differential and common-mode voltages [12, 19, 20] by

$$\begin{aligned} v_1 &= \frac{v_{d1}}{2} + v_{c1} & v_3 &= \frac{v_{d2}}{2} + v_{c2} \\ v_2 &= -\frac{v_{d1}}{2} + v_{c1} & v_4 &= -\frac{v_{d2}}{2} + v_{c2} \end{aligned} \quad (2-6)$$

The port currents can similarly be related to differential and common-mode currents

$$\begin{aligned} i_1 &= i_{d1} + i_{c1} & i_3 &= i_{d2} + i_{c2} \\ i_2 &= -i_{d1} + i_{c1} & i_4 &= -i_{d2} + i_{c2} \end{aligned} \quad (2-7)$$

By defining the port voltages and currents as such, the network description of the differential circuit can be completed in terms of any useful parameters.

There is a critical limitation with this particular approach to network representation of differential circuits. Since all port voltages and currents are functions of both differential and common-mode quantities, all the resulting network parameters will also be combinations of both mode responses. The response of the circuit to a specific mode is not obvious from inspection of the parameters. This commingling of the modal responses

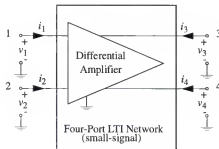


Figure 2-3. Network representation of differential amplifier.

is a distinct disadvantage, since the implicit purpose of a differential circuit is to provide a certain response to a differential stimulus. So, although the standard approach to network representation is a sufficient description of differential circuits, it is non-intuitive. Therefore, a second approach to network descriptions of differential circuits will be described.

The second type of network representation of differential circuits describes the circuit explicitly in terms of modal responses. By using modal definitions of voltage and current as given in (2-1) to (2-4), a network description can be defined. First, the inputs and outputs must be paired appropriately. For example, ports one and two can be paired to create a differential port. This pairing of signals is extremely useful in low-noise systems, as discussed in Chapter 1. For example the z-parameters of a differential amplifier can be defined [20] as

$$\begin{bmatrix} v_{d1} \\ v_{c1} \\ v_{d2} \\ v_{c2} \end{bmatrix} = \begin{bmatrix} z_{d1,d1} & z_{d1,c1} & z_{d1,d2} & z_{d1,c2} \\ z_{c1,d1} & z_{c1,c1} & z_{c1,d2} & z_{c1,c2} \\ z_{d2,d1} & z_{d2,c1} & z_{d2,d2} & z_{d2,c2} \\ z_{c2,d1} & z_{c2,c1} & z_{c2,d2} & z_{c2,c2} \end{bmatrix} \begin{bmatrix} i_{d1} \\ i_{c1} \\ i_{d2} \\ i_{c2} \end{bmatrix} \quad (2-8)$$

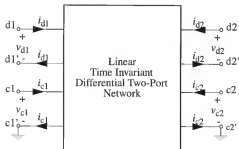


Figure 2-4. Modal notation of an two-port differential network.

This network description can be interpreted directly in terms of differential and common-mode responses. The network diagram can be modified to reflect the explicit modes, as shown in Figure 2-4. This approach will be called the modal network representation. Note that a two-port differential circuit is represented again by a four-port network; in general, an n -port differential circuit will have a $2n$ -port network. The separation of the differential and common-mode ports in the network representation is a useful conceptual tool. The modal network representation presented thus far is useful in the analysis of analog differential circuits. However, the application of this technique to RF and microwave circuits is of limited use as will be discussed in the next section.

2.1.3.2. RF Network Parameters

Power-based scattering parameters are widely used in RF and microwave fields to represent circuits and devices with distributed elements. As its name implies, scattering parameters represent a scattering or separation of a signal by a device under test. The scattered signals are the reflected and transmitted electromagnetic waves that are produced when a device is stimulated with an incident wave. Scattered wave descriptions of networks are very important when operation frequencies are high enough such that circuit elements become a significant fraction of a wavelength (approximately one tenth of a wavelength). Scattering parameters originate in transmission line concepts. As such, they are always defined with respect to a characteristic impedance, or reference impedance. The primary benefit of s -parameters is ease in measurement. In distinction to voltage-current derived parameters, s -parameters are measured with ports terminated in the characteristic impedance. This has meaningful practical implications, since short-circuits and

open-circuits are extremely difficult to realize at RF and microwave frequencies due to distributed element effects.

Scattering parameters will first be developed in terms of transmission line quantities, to provide insight into their wave aspect. Following this definition, the generalized definition will be given.

The following development is summarized from Gonzalez [23]. The voltage and current along a transmission line, such as in Figure 2-5, satisfy the set of differential equations

$$\begin{aligned}\frac{d^2}{dx^2}V(x) - \gamma^2 V(x) &= 0 \\ \frac{d^2}{dx^2}I(x) - \gamma^2 I(x) &= 0\end{aligned}\quad (2-9)$$

where γ is the propagation constant. The general solution of (2-9) is

$$\begin{aligned}V(x) &= Ae^{-\gamma x} + Be^{\gamma x} \\ I(x) &= \frac{A}{Z_0}e^{-\gamma x} - \frac{B}{Z_0}e^{\gamma x}\end{aligned}\quad (2-10)$$

where A and B are complex constants and Z_0 is the characteristic impedance. The propagation constant and the characteristic impedance can be expressed in terms of the parameters R , G , L , C which are the resistance, conductance, inductance, and capacitance per unit length of the transmission line

$$\gamma = \sqrt{(R + j\omega L)(G + j\omega C)} \quad Z_0 = \sqrt{\frac{R + j\omega L}{G + j\omega C}} \quad (2-11)$$

Given the phasor notation $V^*(x) = Ae^{-\gamma x}$ and $V(x) = Be^{\gamma x}$, and by limiting the transmission line to be lossless (i.e. $Z_0 = \text{Re}\{Z_0\}$), then the important normalized quantities are defined

as

$$\begin{aligned}
 v(x) &= \frac{V(x)}{\sqrt{Z_0}} & i(x) &= I(x) \sqrt{Z_0} \\
 a(x) &= \frac{V^+(x)}{\sqrt{Z_0}} & b(x) &= \frac{V^-(x)}{\sqrt{Z_0}}
 \end{aligned}
 \tag{2-12}$$

With these definitions, (2-10) becomes

$$\begin{aligned}
 v(x) &= a(x) + b(x) \\
 i(x) &= a(x) - b(x)
 \end{aligned}
 \tag{2-13}$$

The a and b waves are the incident and reflected/transmitted normalized power waves, and they are the primary quantities of s -parameters.



Figure 2-5. Terminated transmission line.

When applied to an n -port network, such as in Figure 2-2, the a and b waves result in a s -parameter description

$$\begin{bmatrix} b_1 \\ b_2 \\ \dots \\ b_n \end{bmatrix} = \begin{bmatrix} s_{11} & s_{12} & \dots & s_{1n} \\ s_{21} & s_{22} & \dots & s_{2n} \\ \dots & \dots & \dots & \dots \\ s_{n1} & s_{n2} & \dots & s_{nn} \end{bmatrix} \begin{bmatrix} a_1 \\ a_2 \\ \dots \\ a_n \end{bmatrix}
 \tag{2-14}$$

or simply $\bar{b} = \bar{S}\bar{a}$ where the bar over a lower-case variable represents a column vector [23].

The definition of s -parameters can be generalized to include complex characteristic impedances. This generalization also removes the dependency of the s -parameter on

transmission lines. The definition is based on a generalized power wave at the n -th port [23 - 25]

$$\begin{aligned} a_n &= \frac{1}{2\sqrt{\operatorname{Re}(Z_n)}}[v_n + i_n Z_n] \\ b_n &= \frac{1}{2\sqrt{\operatorname{Re}(Z_n)}}[v_n - i_n Z_n^*] \end{aligned} \quad (2-15)$$

The s -parameter matrix equation (2-14) remains the same.

Scattering parameters have not been widely applied to the analysis or measurement of differential circuits. S -parameters would provide the same benefits to RF differential circuits as they do for other RF and microwave circuits. Conceptually, the representation of differential circuits with s -parameters is not difficult. In fact, with the standard network representation discussed earlier, a n -port differential circuit can be described with a $2n$ -by- $2n$ s -parameter matrix, without any additional consideration. However, this approach has the same disadvantages as previously described, namely, the parameters do not provide useful indications of the differential and common-mode responses. For a illustration of the difficulties of interpreting the standard four-port s -parameters of an RF differential amplifier, see Appendix D.

The above limitations could be removed by extending s -parameter theory to a modal network representation. This extension has not been completed prior to this work, and this dissertation later presents the extension.

A straight-forward extension of s -parameter theory to a modal network representation would apply the traditional definitions of modal voltages and currents in (2-1) through (2-4) to the generalized power wave definitions of (2-15). However, the voltage and current definitions of (2-1) through (2-4) are not an acceptable basis for a power wave

network representation. Straight-forward application of these definitions results in quantities that do not conserve energy. The difficulties with power calculations using these quantities can be demonstrated with a simple example.

Suppose two sources of power have potentials \bar{V}_1 and \bar{V}_2 and source currents \bar{I}_1 and \bar{I}_2 , respectively. Assume the sources are harmonically time varying (so \bar{V}_i and \bar{I}_i are phasors, as indicated by the bar over the upper-case variable) but have no specific phase relation. The power delivered by the two sources is

$$P_1 = \text{Re}(\bar{V}_1 \bar{I}_1^*) \quad P_2 = \text{Re}(\bar{V}_2 \bar{I}_2^*) \quad (2-16)$$

and the total power in both sources is

$$P_T = P_1 + P_2 \quad (2-17)$$

By definitions (2-1) through (2-4), the differential and common-mode voltage and current can be expressed as

$$\begin{aligned} \bar{V}_d &= \bar{V}_1 - \bar{V}_2 & \bar{I}_d &= \frac{1}{2}(\bar{I}_1 - \bar{I}_2) \\ \bar{V}_c &= \frac{1}{2}(\bar{V}_1 + \bar{V}_2) & \bar{I}_c &= \frac{1}{2}(\bar{I}_1 + \bar{I}_2) \end{aligned} \quad (2-18)$$

The power in each mode is then

$$P_d = \text{Re}(\bar{V}_d \bar{I}_d^*) \quad P_c = \text{Re}(\bar{V}_c \bar{I}_c^*) \quad (2-19)$$

If the modal definitions are consistent, then the total power of the modes must be equal to the total power of the sources by the conservation of energy. Expanding (2-19)

$$\begin{aligned} P_d &= \frac{1}{2}[\text{Re}(\bar{V}_1 \bar{I}_1^*) + \text{Re}(\bar{V}_2 \bar{I}_2^*) - \text{Re}(\bar{V}_1 \bar{I}_2^*) - \text{Re}(\bar{V}_2 \bar{I}_1^*)] \\ P_c &= \frac{1}{4}[\text{Re}(\bar{V}_1 \bar{I}_1^*) + \text{Re}(\bar{V}_2 \bar{I}_2^*) + \text{Re}(\bar{V}_1 \bar{I}_2^*) + \text{Re}(\bar{V}_2 \bar{I}_1^*)] \end{aligned} \quad (2-20)$$

and the sum of mode power is

$$P_d + P_c = \frac{1}{4} [3 \operatorname{Re}(\overline{V_1} \overline{I_1}^*) + 3 \operatorname{Re}(\overline{V_2} \overline{I_2}^*) - \operatorname{Re}(\overline{V_1} \overline{I_2}^*) - \operatorname{Re}(\overline{V_2} \overline{I_1}^*)] \quad (2-21)$$

Expanding the sum of the source powers in (2-17)

$$P_T = P_1 + P_2 = \operatorname{Re}(\overline{V_1} \overline{I_1}^*) + \operatorname{Re}(\overline{V_2} \overline{I_2}^*) \neq P_d + P_c \quad (2-22)$$

which clearly shows that the voltage and current definitions of (2-1) through (2-4) are not directly usable in power calculations.

The voltage and current definitions of (2-1) through (2-4) can be used for power and power-wave calculations if care is taken to account for the non-orthogonal nature of the system. However, it is much more convenient to define new mode voltages and currents that are orthogonal. These new definitions are given in Chapter 3, Section 3.1.1

Despite the advantages of scattering parameters, there is no acceptable theoretical treatment of s-parameter network representations for differential circuits prior to this work. The attempts at applying s-parameters to RF differential circuits have relied upon intuitive notions of differential s-parameters [26, 21]. As such, the prior incomplete theories have not treated several fundamental principles that a rigorous theory requires. The principles in question are conservation of energy (orthogonality) in the modes, precise definitions of reference impedances for all modes, rigorous definitions of all pure modal responses, and self-consistent definitions of conversion responses between modes.

2.2. Measurement Techniques

When examining prior work on circuits with multiple simultaneous modes of propagation, consideration must be given to accepted measurement techniques. The state of the theoretical development, and of the organization of the field as a whole, can be

observed in the completeness and accuracy (or the lack thereof) of generally accepted measurement techniques.

Again, the scope of this survey of prior work will be limited to subjects related to differential circuits. The topics presented in the following sections represent some of the most widely practiced measurement techniques for differential circuits. The subjects are divided between the analog techniques, RF/microwave scalar approaches, and scattering parameter measurements. The treatment of the measurement techniques is not intended to be exhaustive, but it is representative of the common types of measurements presently applied to differential circuits.

2.2.1. Single Mode Analog Measurements

Analog measurements of differential circuits are typically direct measurements of voltages and currents, which are primarily limited to audio or near-audio frequencies (i.e. typical analog frequencies) [27]. The reason for this limitation is due to distributed nature of circuits as frequencies approach RF. With distributed circuits, there will be transmission line effects. With transmission line effects, the voltage and current will be functions of the position along the line. Furthermore, parasitic capacitances and inductances become significant at these frequencies, and effect the performance of the DUT. As a result, it is difficult to make unambiguous measurements of voltage and current at RF and higher frequencies.

Differential analog measurements typically employ single-ended to differential converters (called baluns) to stimulate and measure the DUT in an ideally pure differential mode. However, these converters are not ideal, and they affect the accuracy of the measurements. Most significantly, the measurements inevitably include the effects of these

converters, and little can be done to remove them. For a more detailed description of typical analog differential measurements, see Appendix B.

2.2.2. Single Mode RF and Microwave Measurements

When a differential circuit operates in the RF/microwave frequencies, voltage and current measurements are no longer practical. Instead, the appropriate measurements deal with transmission of waves and power. Some of the most common and important RF measurements of differential circuits are presented below.

The primary difficulty with RF differential measurements, like analog measurements, is the generation and reception of differential signals. Also like analog measurements, RF measurements require baluns. For RF, center-tapped transformers are available that can operate to 1 GHz [28]. For higher frequencies, power splitter/combiners, such as hybrid couplers, are generally used. The one consequential difference from the analog baluns is that the RF/microwave baluns have more non-ideal performance.

Differential-mode RF measurements can be made with the use of 180° power splitters/combiners, and common-mode RF measurements can be made with 0° power splitters/combiners. Like the analog measurements, these RF/microwave measurements assume single-mode inputs and output, and are called single mode measurements.

2.2.2.1. Scalar Power Measurements Including Baluns

One widely used type of RF measurement of differential circuits is a scalar power measurement. This measurement provides the magnitude of the power gain. The measurement may take the form of a constant amplitude input signal swept across frequency, resulting in a gain versus frequency characteristic. Alternatively, the input power level

can be swept at a fixed frequency, resulting in a output power versus input power characteristic.

Regardless of the specific measurement, scalar power measurements have the same basic instrumentation. The signal source is an RF signal generator, the measurement instrument is a power meter or a spectrum analyzer, and RF baluns must be used. A typical measurement system is shown in Figure 2-6.

Like the analog measurements, the scalar RF power measurements include the effects of the baluns. The effects of the baluns are even more difficult to remove at RF frequencies than at analog. This difficulty is due to the increased non-ideal performance of the baluns. The non-ideal performance is typically specified in terms of loss, magnitude imbalance, and phase imbalance. The effect of the baluns on the accuracy of the measurement can be examined qualitatively.

RF baluns, such as 180° 3 dB hybrid couplers, have magnitude and phase imbalance in the splitting of a signal. Ideally, a 180° 3 dB hybrid coupler would take a single input signal and split it into two equal amplitude signals with 180° phase difference. With

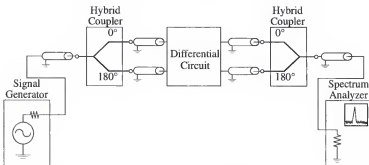


Figure 2-6. RF scalar power measurement of differential circuit.

an ideal splitter a pure differential mode signal could be constructed. However, the magnitude and phase imbalance means that the two outputs of the splitter are not exactly equal amplitude, and the phase difference is not 180° . As a result, a pure differential signal is not produced by a real power splitter, and a test circuit is only driven in an approximately single mode fashion. The magnitude and phase imbalance also affect the combination of two signals. In essence, the imbalance causes a spurious response to a common mode input. The combined effect of the imbalances in the power splitter and combiner is to measure a commingled response of the circuit to both a large differential and small common-mode input. The differential and common-mode responses cannot be distinguished by the instruments, and the overall measurement accuracy is reduced. These effects are examined in detail in Chapter 8.

2.2.2.2. Scattering Parameters with Baluns

A less prevalent, but important, technique for RF/microwave differential circuits is single mode (differential) s-parameter measurement [26]. This approach, as implied by its name, attempts to measure s-parameters of a circuit with input signals and output signals of a single (differential) mode.

Like other single mode measurements, this technique employs baluns. The most common application of this method is the measurement of the differential response of a circuit with s-parameters. The measurement system includes a standard two-port vector network analyzer (VNA) which automatically measures the s-parameters of a two-port device and a pair of 180° 3dB power splitters/combiners. This approach has also been applied to on-wafer measurements of differential circuits [26]. The schematic of the system is shown in Figure 2-7.

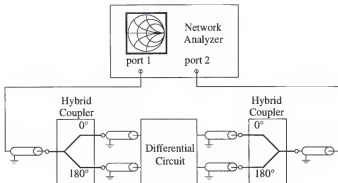


Figure 2-7. S-Parameter measurement of differential circuit.

This measurement technique suffers from the same problems as the scalar RF measurements. The magnitude and phase imbalance in the splitters/combiners and the neglect of mode conversion will all produce errors in the measured s-parameters. However, the s-parameter approach represents an important extension of measurement techniques. In contrast to scalar measurements, s-parameters are by their nature vector quantities, and hence they represent both magnitude and phase measurements.

Another limitation of this technique as reported is the lack of rigorous definition of differential and common-mode scattering parameters. Calibration of the measurement system, a necessity for all accurate VNA measurements, is also undefined. Although limited in accuracy due to the cited problems, a calibration for this system could be derived from the theory presented later in this work.

2.3. Summary of Past Theory and Techniques

Clearly, an opportunity exists to extend the accuracy of analysis, design, and measurement of differential circuits into the RF and microwave frequencies. By combining the core principles of differential circuits traditionally belonging to the analog domain with established RF techniques like scattering parameters, a strong contribution to both fields is achieved. In the next chapter, the concepts of multi-mode analog differential circuits are extended into a rigorous theory for the analysis, measurement and design of RF differential circuits.

CHAPTER 3 FUNDAMENTAL THEORY OF MODE SPECIFIC S-PARAMETERS

3.1. Mode Specific Scattering Parameters in Differential Circuits

A severe limitation in differential-mode/common-mode circuit characterization is a lack of applicable power wave and s-parameter theory in terms of these two modes. There is no previously reported way to describe s-parameters based on mixed differential-mode/common-mode propagation. Previous work most closely related to this work has been specific to descriptions of coupled transmission lines [8 - 15] and shielded balanced transmission lines. Work by the National Bureau of Standards on balanced transmission lines used s-parameters to describe differential-mode propagation, but neglected common-mode propagation and any mode conversions [21]. In the literature, the coupled transmission work has been most commonly applied to directional couplers [2, 16 - 18] with Cohn and Levy [3] providing a historical perspective on the role of coupled transmission lines in directional coupler development. Past work on coupled transmission lines has largely focused on voltage/current relationships and Z , Y , and $ABCD$ -parameter descriptions of TEM circuits. One notable exception to the $Z/Y/ABCD$ -parameter approach is work by Krage and Haddad [29] which employs traditional normalized power waves to describe coupler behavior. However, all of the referenced prior work deals with specific TEM structures, and is not suitable for characterization of a generic differential circuit.

The following sections contain original work in the definitions of multi-mode power waves and s-parameters. Portions of this work have been published in summary form [30]. The details of the development of multi-mode s-parameters, and new related material, are contained in the remainder of the chapter.

3.1.1. Fundamental Definitions for Differential Circuits

In a practical RF/ microwave implementation, a differential circuit is based on pairs of coupled transmission lines. A schematic of a typical two-port RF/ microwave differential system is shown in Figure 3-1. Essential features of the microwave differential circuit in Figure 3-1 are the coupled pair transmission line on the input and output of the DUT. As described in Chapter 2, this coupled line structure allows the propagation of two TEM modes.

It is conceptually beneficial to define a signal that propagates between the lines of the coupled-pair (as opposed to propagating between one line and ground). Such signals are known as differential signals, and can be described by a difference of voltage ($\Delta v_1 \neq 0$,

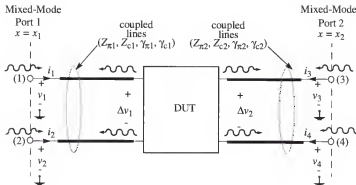


Figure 3-1. Schematic of RF differential two-port network.

$\Delta v_2 \neq 0$) and current flow between the individual lines in a pair. By such a definition, the signal is not referenced to a ground potential, but rather the signal on one line of the coupled pair is referenced to the other. Further, this differential signal should propagate in a TEM, or quasi-TEM, fashion with a well-defined characteristic impedance and propagation constant. Coupled line pairs, as in Figure 3-1, allow propagating differential signals (the quantities of interest) to exist. The differential circuit discussion in this chapter will be limited to the two-port case, but the generalized theory for n -port circuits can be readily derived from this work.

Most practical implementations of Figure 3-1 will incorporate a ground plane, or some other global reference conductor, either intentionally or unintentionally. This ground plane allows another mode of propagation to exist, namely common-mode propagation. Conceptually, the common-mode wave applies equal signals with respect to ground at each of the individual lines in a coupled pair, such that the differential voltage is zero (i.e. $\Delta v_1 = \Delta v_2 = 0$). The ability of the microwave differential circuit to propagate both common-mode and differential-mode signals requires any complete theoretical treatment to include characterization of all simultaneously propagating modes. For convenience, the simultaneous propagation of two or more modes (namely, differential-mode, and common-mode) on a coupled transmission line will be referred to in this work as mixed-mode propagation, from which mixed-mode s -parameters will be defined.

To begin the development of a rigorous theory of mixed differential and common-mode normalized power waves, the two modes must be defined in a self-consistent fashion. A differential signal propagates between the lines of the coupled-pair (as opposed to propagating between one line and ground), and a common-mode signal propagates with

equal signals with respect to ground at each of the individual lines in a coupled pair. The ability of the microwave differential circuit to propagate both common-mode and differential-mode signals requires any complete theoretical treatment to include characterization of all simultaneously propagating modes. For convenience, the simultaneous propagation of two or more modes (namely, differential-mode, and common-mode) on a coupled transmission line will be referred to as mixed-mode propagation, from which mixed-mode s-parameters will be defined.

3.1.1.1. Modal Voltage and Currents

At this point, it is important to define the differential and common-mode voltages and currents to develop a self-consistent set of mixed-mode s-parameters. Referring to Figure 3-1, define the differential-mode voltage at a point, x , to be the difference of between voltages on node one and node two

$$v_d(x) = v_1 - v_2 \quad (3-1)$$

This standard definition establishes a signal that is no longer referenced to ground. In a differential circuit, one would expect equal current magnitudes to enter the positive input terminal as leaves the negative input terminal. Therefore, the differential-mode current is defined as one-half the difference between currents entering nodes one and two

$$i_d(x) = \frac{1}{2}(i_1 - i_2) \quad (3-2)$$

These definitions differ from previously published definitions by Zysman and Johnson [12] due to change in references. The common-mode voltage in a differential circuit is typically the average voltage at a port. Hence, common-mode voltage is one half the sum of the voltages on nodes one and two

$$v_c(x) = \frac{1}{2}(v_1 + v_2) \quad (3-3)$$

The common-mode current at a port is simply the total current flowing into the port.

Therefore, define the common-mode current as the sum of the currents entering nodes one and two

$$i_c(x) = i_1 + i_2 \quad (3-4)$$

Note that the differential current includes the return current, and the return current for the common-mode signal flows through the ground plane. For this reason, the differential-mode current is halved where the common-mode current is not. This definition of common-mode current differs from the traditionally accepted definition [4, 12, 19 - 21].

Definitions in (3-1) to (3-4) are self-consistent with the differential power delivered to a differential load. This can be shown by demonstrating that these definitions conserve the total energy in the modes. The power at each terminal ($x = 0$ for example) can be expressed as

$$P_1 = \text{Re}(v_1 i_1^*) \quad P_2 = \text{Re}(v_2 i_2^*) \quad (3-5)$$

and the total power in both sources is

$$P_T = P_1 + P_2 \quad (3-6)$$

The power in each mode is

$$P_d = \text{Re}(v_d i_d^*) \quad P_c = \text{Re}(v_c i_c^*) \quad (3-7)$$

By definitions (3-1) to (3-4)

$$\begin{aligned} P_d &= \frac{1}{2}[\text{Re}(v_1 i_1^*) + \text{Re}(v_2 i_2^*) - \text{Re}(v_1 i_2^*) - \text{Re}(v_2 i_1^*)] \\ P_c &= \frac{1}{2}[\text{Re}(v_1 i_1^*) + \text{Re}(v_2 i_2^*) + \text{Re}(v_1 i_2^*) + \text{Re}(v_2 i_1^*)] \end{aligned} \quad (3-8)$$

and the sum of mode power is

$$P_d + P_c = \frac{1}{2} [2\text{Re}(v_1 i_1^*) + 2\text{Re}(v_2 i_2^*)] = \text{Re}(v_1 i_1^*) + \text{Re}(v_2 i_2^*) \quad (3-9)$$

Expanding the sum of the source powers in (3-6)

$$P_T = P_1 + P_2 = \text{Re}(v_1 i_1^*) + \text{Re}(v_2 i_2^*) \quad (3-10)$$

Therefore the sum of the modal power is equal to the total power

$$P_d + P_c = P_1 + P_2 = P_T \quad (3-11)$$

and energy is conserved by the definitions of common and differential-mode voltages and currents.

3.1.1.2. Coupled Mixed-Mode Signals

To begin the presentation of mixed-mode s -parameters, a general asymmetric coupled transmission line pair over a ground plane will be analyzed. This analysis yields multiple propagating modes all referenced to ground. These modes will be used to express the

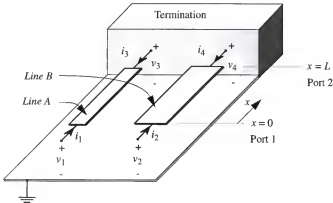


Figure 3-2. Schematic of terminated asymmetric coupled-pair transmission line.

desired differential signal between the lines of the coupled-pair, as well as the common signal referenced to ground. Figure 3-2 is a diagram of such a coupled-pair transmission line, with all pertinent voltages and currents denoted. Also shown in Figure 3-2 is a representation of a termination for the coupled-pair line. Subject to the simplifying assumptions, the mathematical results of this chapter are applicable to any pair of conductors with a nearby ground conductor.

Referring again to Figure 3-2, the behavior of the coupled-line pair can be described by [8]

$$\begin{aligned}
 \frac{dv_1}{dx} &= -(z_1 i_1 + z_m i_2) \\
 \frac{dv_2}{dx} &= -(z_2 i_2 + z_m i_1) \\
 \frac{di_1}{dx} &= -(y_1 v_1 + y_m v_2) \\
 \frac{di_2}{dx} &= -(y_2 v_2 + y_m v_1)
 \end{aligned} \tag{3-12}$$

where z_1 and z_2 are self-impedances per unit length; y_1 and y_2 are admittances per unit length; and z_m and y_m are mutual impedance and admittance per unit length, respectively. Also, a harmonic time dependence (i.e. $e^{j\omega t}$) is assumed.

The solution to the set of equations (3-12) as published by Tripathi [8] is given as

$$\begin{aligned}
 v_1 &= A_1 e^{-\gamma_c x} + A_2 e^{\gamma_c x} + A_3 e^{-\gamma_\pi x} + A_4 e^{\gamma_\pi x} \\
 v_2 &= A_1 R_c e^{-\gamma_c x} + A_2 R_c e^{\gamma_c x} + A_3 R_\pi e^{-\gamma_\pi x} + A_4 R_\pi e^{\gamma_\pi x} \\
 i_1 &= \frac{A_1}{Z_{c1}} e^{-\gamma_c x} - \frac{A_2}{Z_{c2}} e^{\gamma_c x} + \frac{A_3}{Z_{\pi1}} e^{-\gamma_\pi x} - \frac{A_4}{Z_{\pi2}} e^{\gamma_\pi x} \\
 i_2 &= \frac{A_1 R_c}{Z_{c1}} e^{-\gamma_c x} - \frac{A_2 R_c}{Z_{c2}} e^{\gamma_c x} + \frac{A_3 R_\pi}{Z_{\pi1}} e^{-\gamma_\pi x} - \frac{A_4 R_\pi}{Z_{\pi2}} e^{\gamma_\pi x}
 \end{aligned} \tag{3-13}$$

where A_1 , and A_3 represent the phasor coefficients for the forward (positive x) propagating c and π -modes, respectively, and A_2 , and A_4 represent the phasor coefficients for the reverse (negative x) propagating c and π -modes, respectively. The characteristic impedance of the c -modes are represented by Z_{c1} and Z_{c2} for lines A and B, respectively, and the characteristic impedance of the π -modes are represented by $Z_{\pi1}$ and $Z_{\pi2}$ for lines A and B, respectively. Additionally, $R_c = v_2/v_1$ for $\gamma = \pm\gamma_c$, $R_\pi = v_2/v_1$ for $\gamma = \pm\gamma_\pi$, and

$$\gamma_{c,\pi}^2 = \frac{y_1 z_1 + y_2 z_2}{2} + y_m z_m \pm \frac{1}{2} \sqrt{(y_1 z_1 - y_2 z_2)^2 + 4(z_1 y_m + y_2 z_m)(z_2 y_m + y_1 z_1)} \quad (3-14)$$

Each voltage/current pair at each node represent a single propagating signal referenced to the ground potential. These signals will be called nodal waves.

A practical simplification in the development of mixed-mode s-parameter theory is to assume symmetric coupled pairs (i.e. lines A and B have equal width) as reference transmission lines. This assumption allows simple mathematical formulations of mixed-mode s-parameters. Furthermore, this assumption is not overly limiting, since reference lines may be made arbitrarily short. For symmetrical lines, in (3-13) $R_c = 1$ and $R_\pi = -1$, and the c and the π -modes become the even and odd modes, respectively, as first used by Cohn [6]. For notational purposes, we shall use the substitutions $c \rightarrow e$ and $\pi \rightarrow o$ for even-mode and odd-mode, respectively. With these substitutions, the mode characteristic impedances and propagation constants become

$$\begin{aligned} Z_{c1} &= Z_{c2} = Z_e \\ Z_{\pi1} &= Z_{\pi2} = Z_o \\ \gamma_c &= \gamma_e \quad \gamma_\pi = \gamma_o \end{aligned} \quad (3-15)$$

Expressing (3-13) in the symmetric case

$$\begin{aligned}
v_1 &= A_1 e^{-\gamma_e x} + A_2 e^{\gamma_e x} + A_3 e^{-\gamma_o x} + A_4 e^{\gamma_o x} \\
v_2 &= A_1 e^{-\gamma_e x} + A_2 e^{\gamma_e x} - A_3 e^{-\gamma_o x} - A_4 e^{\gamma_o x} \\
i_1 &= \frac{A_1}{Z_e} e^{-\gamma_e x} - \frac{A_2}{Z_e} e^{\gamma_e x} + \frac{A_3}{Z_o} e^{-\gamma_o x} - \frac{A_4}{Z_o} e^{\gamma_o x} \\
i_2 &= \frac{A_1}{Z_e} e^{-\gamma_e x} - \frac{A_2}{Z_e} e^{\gamma_e x} - \frac{A_3}{Z_o} e^{-\gamma_o x} + \frac{A_4}{Z_o} e^{\gamma_o x}
\end{aligned} \tag{3-16}$$

As before, these voltage/current pairs are nodal waves at each terminal that are referenced to ground.

Expressing the differential and common-mode values (3-1) through (3-4) in terms of the line voltages and currents (3-16)

$$\begin{aligned}
v_d(x) &= 2 \left(A_3 e^{-\gamma_o x} + A_4 e^{\gamma_o x} \right) \\
i_d(x) &= \frac{A_3}{Z_o} e^{-\gamma_o x} - \frac{A_4}{Z_o} e^{\gamma_o x} \\
v_c(x) &= A_1 e^{-\gamma_e x} + A_2 e^{\gamma_e x} \\
i_c(x) &= 2 \left(\frac{A_1}{Z_e} e^{-\gamma_e x} - \frac{A_2}{Z_e} e^{\gamma_e x} \right)
\end{aligned} \tag{3-17}$$

Recall that A_1 and A_2 are the forward and reverse phasor coefficient for the even-mode propagation, and A_3 and A_4 are the forward and reverse phasor coefficient for the odd-mode propagation. If a short hand notation is introduced, a better understanding of these definitions can be had. Let

$$\begin{aligned}
v_o^+(x) &\equiv A_3 e^{-\gamma_o x} & v_o^-(x) &\equiv A_4 e^{\gamma_o x} & i_o^+(x) &\equiv \frac{A_3}{Z_o} e^{-\gamma_o x} & i_o^-(x) &\equiv \frac{A_4}{Z_o} e^{\gamma_o x} \\
v_e^+(x) &\equiv A_1 e^{-\gamma_e x} & v_e^-(x) &\equiv A_2 e^{\gamma_e x} & i_e^+(x) &\equiv \frac{A_1}{Z_e} e^{-\gamma_e x} & i_e^-(x) &\equiv \frac{A_2}{Z_e} e^{\gamma_e x}
\end{aligned} \tag{3-18}$$

Then (3-16) becomes

$$\begin{aligned}
 v_1 &= v_e^+(x) + v_e^-(x) + v_o^+(x) + v_o^-(x) \\
 v_2 &= v_e^+(x) + v_e^-(x) - v_o^+(x) - v_o^-(x) \\
 i_1 &= i_e^+(x) - i_e^-(x) + i_o^+(x) - i_o^-(x) \\
 i_2 &= i_e^+(x) - i_e^-(x) - i_o^+(x) + i_o^-(x)
 \end{aligned} \tag{3-19}$$

and (3-17) becomes

$$\begin{aligned}
 v_d(x) &= 2(v_o^+(x) + v_o^-(x)) \\
 i_d(x) &= i_o^+(x) - i_o^-(x) = \frac{v_o^+(x) - v_o^-(x)}{Z_o} \\
 v_c(x) &= v_e^+(x) + v_e^-(x) \\
 i_c(x) &= 2(i_e^+(x) - i_e^-(x)) = 2 \frac{v_e^+(x) - v_e^-(x)}{Z_e}
 \end{aligned} \tag{3-20}$$

Note that, in general, $Z_o \neq Z_e$.

Characteristic impedances of each mode can be defined as the ratio of the voltage to current of the appropriate modes at any point, x , along the line. These impedances can be expressed in terms of the even and odd-mode (ground referenced) characteristic impedances

$$Z_d = \frac{v_d^+(x)}{i_d^+(x)} = \frac{2v_o^+(x)}{v_o^+(x)/Z_o} = 2Z_o \tag{3-21}$$

$$Z_c = \frac{v_c^+(x)}{i_c^+(x)} = \frac{v_e^+(x)}{(2v_e^+(x))/Z_e} = \frac{Z_e}{2} \tag{3-22}$$

These relations between the even/odd mode characteristic impedances and the differential/common mode characteristic impedances are consistent with the matched load terminations discussed in the literature [9, 10].

3.1.1.3. Mixed-Mode Scattering Parameters

Now that voltages, currents, and characteristic impedances have been defined for both differential and common modes, the normalized power waves can be developed. By the definition for a generalized power wave at the n -th port [23, 24]

$$\begin{aligned} a_n &= \frac{1}{2\sqrt{\operatorname{Re}(Z_n)}} [v_n + i_n Z_n] \\ b_n &= \frac{1}{2\sqrt{\operatorname{Re}(Z_n)}} [v_n - i_n Z_n^*] \end{aligned} \quad (3-23)$$

where a_n is the normalized wave propagating in the forward (positive x) direction; b_n is the normalized wave propagating in the reverse (negative x) direction; and Z_n is the characteristic impedance of the port. With the above definitions, the differential normalized waves become, at port one

$$\begin{aligned} a_{d1} = a_d(x_1) &= \frac{1}{2\sqrt{\operatorname{Re}(Z_d)}} [v_d(x) + i_d(x)Z_d] \Big|_{x=x_1} \\ b_{d1} = b_d(x_1) &= \frac{1}{2\sqrt{\operatorname{Re}(Z_d)}} [v_d(x) - i_d(x)Z_d^*] \Big|_{x=x_1} \end{aligned} \quad (3-24)$$

Similarly, define the common-mode normalized waves, at port one, as

$$\begin{aligned} a_{c1} = a_c(x_1) &= \frac{1}{2\sqrt{\operatorname{Re}(Z_c)}} [v_c(x) + i_c(x)Z_c] \Big|_{x=x_1} \\ b_{c1} = b_c(x_1) &= \frac{1}{2\sqrt{\operatorname{Re}(Z_c)}} [v_c(x) - i_c(x)Z_c^*] \Big|_{x=x_1} \end{aligned} \quad (3-25)$$

Analogous definitions at port two can easily be found by setting $x = x_2$.

Imposing the condition of low-loss transmission lines on the coupled-pair of Figure 3-1, the characteristic impedances are approximately purely real [23]. Under this restriction, $Z_d = \text{Re}\{Z_d\} \equiv R_d$ and $Z_c = \text{Re}\{Z_c\} \equiv R_c$. With this assumption, the normalized wave equations at port one can be simplified

$$\begin{aligned} a_{d1} &= \frac{1}{2\sqrt{R_{d1}}} [v_{d1}(x) + i_{d1}(x)R_{d1}] \Big|_{x=x_1} \\ b_{d1} &= \frac{1}{2\sqrt{R_{d1}}} [v_{d1}(x) - i_{d1}(x)R_{d1}] \Big|_{x=x_1} \end{aligned} \quad (3-26)$$

$$\begin{aligned} a_{c1} &= \frac{1}{2\sqrt{R_c}} [v_c(x) + i_c(x)R_c] \Big|_{x=x_1} \\ b_{c1} &= \frac{1}{2\sqrt{R_c}} [v_c(x) - i_c(x)R_c] \Big|_{x=x_1} \end{aligned} \quad (3-27)$$

With the normalized power waves defined, the development of mixed-mode s-parameters is straight forward. The definition of generalized s-parameters [24, 23] is

$$\bar{b} = S\bar{a} \quad (3-28)$$

where the bar over the lower-case letters denote an n -dimensional column vector and the bold upper-case letter an n -by- n matrix. Given a coupled-line two-port like Figure 3-1, or any arbitrary mixed-mode two-port, the generalized mixed-mode s-parameters can be described by

$$\begin{aligned} b_{d1} &= s_{dd11}a_{d1} + s_{dd12}a_{d2} + s_{dc11}a_{c1} + s_{dc12}a_{c2} \\ b_{d2} &= s_{dd21}a_{d1} + s_{dd22}a_{d2} + s_{dc21}a_{c1} + s_{dc22}a_{c2} \\ b_{c1} &= s_{cd11}a_{d1} + s_{cd12}a_{d2} + s_{cc11}a_{c1} + s_{cc12}a_{c2} \\ b_{c2} &= s_{cd21}a_{d1} + s_{cd22}a_{d2} + s_{cc21}a_{c1} + s_{cc22}a_{c2} \end{aligned} \quad (3-29)$$

Each parameter has the notation

$$s_{m_o m_i p_o p_i} = s_{(\text{output-mode})(\text{input-mode})(\text{output-port})(\text{input-port})} \quad (3-30)$$

to indicate the modes and ports of the signal path which the parameter represents. The differential and common-modes are denoted by a subscript d and c, respectively, and the ports are denoted by their port number, in this case, one and two. The set of equations in (3-29) can be expressed as a partitioned matrix

$$\begin{bmatrix} b_{d1} \\ b_{d2} \\ b_{c1} \\ b_{c2} \end{bmatrix} = \begin{bmatrix} S_{dd} & S_{dc} \\ S_{cd} & S_{cc} \end{bmatrix} \begin{bmatrix} a_{d1} \\ a_{d2} \\ a_{c1} \\ a_{c2} \end{bmatrix} \quad (3-31)$$

The following names are used: S_{dd} are the differential s-parameters, S_{cc} the common-mode s-parameters, and S_{dc} and S_{cd} the mode-conversion or cross-mode s-parameters. In particular, S_{dc} describes the conversion of common-mode waves into differential-mode waves, and S_{cd} describes the conversion of differential-mode waves into common-mode waves. These four partitions are analogues to four transfer gains (A_{cc} , A_{dd} , A_{cd} , A_{dc}) introduced by Middlebrook [19]. These mixed-mode two-port s-parameters can be shown graphically (see Figure 3-3) as a traditional four-port. It must be remembered, however, that the ports are conceptual tools only, and not physically separate ports.

3.1.2. Choice of Reference Impedances for Multiple Modes

If one is to make a general purpose RF measurement port, the values of characteristic port impedances must be chosen. It is useful to require the even and odd-mode characteristic impedances of the measurement system to be equal, thus reducing the number of different valued matched terminations required. In contrast, it is difficult to fabricate

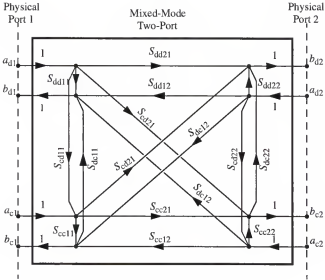


Figure 3-3. Signal flow diagram of mixed-mode two-port network.

accurate lumped termination standards for coupled lines where Z_e does not equal Z_o . If the characteristic impedances of the lines are defined to be equal (say, 50Ω), then a further simplification of the above expressions can be accomplished with the substitution $Z_e = Z_o = Z_0$ where in the low-loss case $Z_0 = \text{Re}\{Z_0\} \equiv R_0$.

By choosing equal even and odd-mode characteristic impedances, one is selecting a special case of coupled transmission line behavior, as described in (3-12). Enforcing equal even and odd-mode characteristic impedances is equivalent to the conditions of uncoupled transmission lines. As has been shown in the literature [9], the condition $Z_e = Z_o$ results in the mutual impedances and admittances being zero ($z_m=0$, $y_m=0$). Under these conditions, the describing differential equations of the transmission line system

(3-12) clearly become uncoupled, resulting in two independent transmission line solutions. Although very specific, this is a valid solution to (3-12), and all results up to this point are also valid under the special case of equal even and odd-mode characteristic impedances. Therefore, we choose the reference lines of the mixed-mode s -parameters to be uncoupled transmission lines. The key to this choice is that these uncoupled reference lines can be easily interfaced with a coupled line system, as discussed below.

To interpret the meaning of uncoupled reference transmission lines, consider a system of transmission lines: one coupled pair and one uncoupled pair connected in series. If even and odd (or e and π) modes are both propagating (forward and reverse) on the coupled pair, then it can be shown that the waves propagating on each of the uncoupled transmission lines are linear combinations of the waves propagating on the coupled system (see Appendix C). Furthermore, the differential and common-mode normalized waves of the coupled pair system can be reconstructed from the normalized waves at a point on the uncoupled line pairs (see Appendix C). This point of reconstruction is arbitrary, and one may choose the point to be the interface between the coupled system and the uncoupled reference lines.

It is interesting to note that an alternative requirement can be found through which the nodal and mixed-mode waves can be related. One could require the differential-mode and common-mode characteristic impedances to be equal (i.e. $Z_d = Z_c = Z_0$). The relationship between mixed-mode and standard s -parameters (discussed in the next section) will change, however. This alternate requirement may have value in some cases, but the original requirement ($Z_e = Z_o = Z_0$) best relates mixed-mode s -parameters to standard s -parameters.

3.1.3. Relationship of Mixed-Mode and Standard S-Parameters

The most straightforward means of implementing a mixed-mode s-parameter measurement system is to directly apply differential and common-mode waves while measuring the resulting differential and common-mode waves. Unfortunately, the generation and measurement of these modes of propagation is not easily achievable with standard vector network analyzers (VNA). However, under certain conditions, one can relate the total nodal waves (each representing two modes of propagation) to the desired differential and common-mode waves. These nodal waves are readily generated and measured with standard VNAs, and with consideration, the differential and common-mode waves, and hence the mixed-mode s-parameters, can be calculated. Therefore, the relationships between the normalized mixed-mode waves (a_{d1} , b_{d1} , a_{c1} , b_{c1} , etc.) and the nodal waves (a_1 , b_1 , a_2 , b_2 , etc.) will be derived, and the necessary conditions for these relationships to exist will be found.

To begin the development of the relationship between the nodal and mixed-mode normalized power waves, the normalized differential-mode incident wave at mixed-mode port one, a_{d1} , will be expressed in terms of the normalized single-ended (nodal) power waves at port one, a_1 , and at port two, a_2 . First, the normalized nodal waves of the coupled lines at the interface are defined, with $Z_0 \approx R_0$, as

$$\begin{aligned} a_i &= \frac{1}{2\sqrt{R_0}}[v_i + i_i R_0] \\ b_i &= \frac{1}{2\sqrt{R_0}}[v_i - i_i R_0] \end{aligned} \quad (3-32)$$

where a_i and b_i are the normalized forward and reverse propagating nodal waves at node i , respectively, and $i \in \{1, 2, 3, 4\}$. Next, the definition of the normalized differential-mode incident wave at mixed-mode port one, a_{d1} , will be repeated

$$a_{d1} = \frac{1}{2\sqrt{R_{d1}}} [v_{d1}(x) + i_{d1}(x)R_{d1}] \Big|_{x=x_1} \quad (3-33)$$

Recalling that the differential voltage and current at port one are defined through (3-1) and (3-2) as

$$\begin{aligned} v_{d1}(x) &= v_1(x) - v_2(x) \\ i_{d1}(x) &= \frac{1}{2}(i_1(x) - i_2(x)) \end{aligned} \quad (3-34)$$

and that the differential reference characteristic impedance is defined in (3-21), with the substitution $Z_e = Z_o = Z_0 \approx R_o$, as

$$R_{d1} = 2R_o \quad (3-35)$$

then (3-33) can be re-written as

$$\begin{aligned} a_{d1} &= \frac{1}{2\sqrt{R_{d1}}} [v_{d1}(x) + i_{d1}(x)R_{d1}] \Big|_{x=x_1} \\ &= \frac{1}{\sqrt{2}} \left\{ \frac{1}{\sqrt{R_o}} [v_1(x) - v_2(x) + R_o(i_1(x) - i_2(x))] \right\} \Big|_{x=x_1} \\ &= \frac{1}{\sqrt{2}} \left\{ \frac{1}{\sqrt{R_o}} [v_1(x) + R_o i_1(x)] - \frac{1}{\sqrt{R_o}} [v_2(x) + R_o i_2(x)] \right\} \Big|_{x=x_1} \end{aligned} \quad (3-36)$$

By applying the definition of normalized waves at port one and two (3-32), then (3-36) becomes simply

$$a_{d1} = \frac{1}{\sqrt{2}}(a_1 - a_2) \quad (3-37)$$

This equation has a meaningful analogy with the differential voltage and current definitions. Similarly, the differential and common-mode waves at port one are

$$\begin{aligned} a_{d1} &= \frac{1}{\sqrt{2}}(a_1 - a_2) & a_{c1} &= \frac{1}{\sqrt{2}}(a_1 + a_2) \\ b_{d1} &= \frac{1}{\sqrt{2}}(b_1 - b_2) & b_{c1} &= \frac{1}{\sqrt{2}}(b_1 + b_2) \end{aligned} \quad (3-38)$$

Similarly, for port two

$$\begin{aligned} a_{d2} &= \frac{1}{\sqrt{2}}(a_3 - a_4) & a_{c2} &= \frac{1}{\sqrt{2}}(a_3 + a_4) \\ b_{d2} &= \frac{1}{\sqrt{2}}(b_3 - b_4) & b_{c2} &= \frac{1}{\sqrt{2}}(b_3 + b_4) \end{aligned} \quad (3-39)$$

Equations (3-38) and (3-39) represent important relationships from which mixed-mode s-parameters can be determined with a practical measurement system.

By using the definition of s-parameters [23] for a four port network together with the relations in (3-38) and (3-39), a transformation between mixed-mode and standard s-parameters can be found. The transformation can be developed by considering the relationships between the standard and mixed-mode incident waves, a , which can be written

$$\begin{bmatrix} a_{d1} \\ a_{d2} \\ a_{c1} \\ a_{c2} \end{bmatrix} = \frac{1}{\sqrt{2}} \begin{bmatrix} 1 & -1 & 0 & 0 \\ 0 & 0 & 1 & -1 \\ 1 & 1 & 0 & 0 \\ 0 & 0 & 1 & 1 \end{bmatrix} \begin{bmatrix} a_1 \\ a_2 \\ a_3 \\ a_4 \end{bmatrix} \quad (3-40)$$

or, compactly

$$\vec{a}^{\text{mm}} = M \vec{a}^{\text{std}} \quad (3-41)$$

where \vec{a}^{mm} and \vec{a}^{std} are the mixed-mode a -waves vectors, respectively, and

$$M = \frac{1}{\sqrt{2}} \begin{bmatrix} 1 & -1 & 0 & 0 \\ 0 & 0 & 1 & -1 \\ 1 & 1 & 0 & 0 \\ 0 & 0 & 1 & 1 \end{bmatrix} \quad (3-42)$$

Similarly, for the response waves, b , it is found

$$\vec{b}^{\text{mm}} = M \vec{b}^{\text{std}} \quad (3-43)$$

Applying the generalized definition of s -parameters from (3-28), it can be shown

$$S^{\text{mm}} = M S^{\text{std}} M^{-1} \quad (3-44)$$

where S^{mm} are the mixed-mode s -parameters, S^{std} are the standard four-port s -parameters.

The transformation in (3-44) gives additional insight into the nature of mixed-mode s -parameters. The transformation is a similarity transformation, which indicates that a change of basis has occurred between standard and mixed-mode s -parameters. Conceptually, the nodal currents and voltages correspond to the basis of standard four-port s -parameters, and the modal currents and voltages of (3-1) to (3-4) correspond to the basis of mixed-mode s -parameters. (precisely what is meant by a basis of an s -parameter representation will be explored in Section 3.2).

The transformation (3-44) also gives information into the nature of the chosen mode-specific a - and b -waves. It is easily demonstrated that the operator M has the property $M^{-1} = M^T$ (where the superscript T indicates the matrix transpose operator). This indicates that the M operator is a unitary (also called orthonormal) operator [31]. This can be easily demonstrated by applying the definition of a unitary operator

$$M(M^*)^T = \mathbf{I} \quad (3-45)$$

where $*$ indicates the complex conjugate. A unitary transformation is one that transforms one orthonormal bases to another orthonormal bases. If it is accepted (until Section 3.2, where it can be established) that standard four-port s -parameters are operators in an orthonormal basis, then it follows from (3-45) that the definitions of the differential and common-mode normalized power waves must also represent an orthonormal basis. This is yet another indication that the mode currents and voltages in (3-1) to (3-4) provide a self-consistent framework for power calculations.

Further, it indicates clearly that the two sets of s -parameters are different representations of the same device, and that, ideally, the two representations contain the same information about the device. However, it will be shown in Section 5.2 that transformation according to (3-44) of measured data from practical measurement systems (with measurement errors) can lead to significant errors in the transformed data.

3.1.4. Interpretations of Multi-Mode Scattering Parameters

Equations (3-26) and (3-27) form the basis of an ideal mixed-mode s -parameter measurement system. These equations can be implemented into a microwave simulator, and can provide a quick and simple method of illustrating the usefulness of mixed-mode s -parameters.

The circuit in Figure 3-4 was implemented into Hewlett-Packard's Microwave Design System (MDS) [32]. The phase difference, Θ , between the two sources was set to 0° for the common-mode and common-to-differential-mode forward s -parameters. For the forward differential-mode and differential-to-common-mode s -parameters, the phase difference was set to 180° . In each case, the nodal waves were calculated from (3-26) and (3-27), and the s -parameters were calculated with the appropriate ratios. The reverse s -

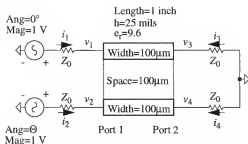


Figure 3-4. Schematic of mixed-mode simulation of symmetric coupled-pair line.

parameters were calculated by driving mixed-mode port two of the DUT, with 50Ω loads at port one.

The first example of mixed-mode s -parameters uses a DUT of a pair of coupled microstrip transmission lines, with symmetric (i.e. equal width) top conductors. This symmetric coupled-pair, and the accompanying circuitry, is shown in Figure 3-4. Each runner width is $100\mu\text{m}$ with an edge-to-edge spacing of $100\mu\text{m}$. The substrate is 25 mil thick alumina with a relative permittivity of 9.6 with a loss tangent of 0.001, and the metal conductivity is that of copper, $\sim 5.8 \times 10^7 \text{ S/m}$. A one-inch section of this line was simulated in MDS as described above, and the mixed-mode s -parameters at 5 GHz are

$$\begin{bmatrix} S_{dd} & S_{dc} \\ S_{cd} & S_{cc} \end{bmatrix} = \quad (3-46)$$

$$\begin{bmatrix} 0.001 \angle -141^\circ & 0.972 \angle 9.53^\circ & 0 & 0 \\ 0.972 \angle 9.53^\circ & 0.001 \angle -141^\circ & 0 & 0 \\ 0 & 0 & 0.341 \angle -60.4^\circ & 0.915 \angle -26.4^\circ \\ 0 & 0 & 0.915 \angle -26.4^\circ & 0.341 \angle -60.4^\circ \end{bmatrix}$$

As expected, each partitioned sub-matrix demonstrates the properties of a reciprocal, passive and (port) symmetric DUT. The differential s-parameters, S_{dd} , show the coupled pair possesses an odd-mode characteristic impedance of 50Ω (100Ω differential impedance), and has low-loss propagation in the differential mode. The common-mode s-parameters, S_{cc} , show the coupled pair possesses an even-mode characteristic impedance other than 50Ω . Actually, the even-mode impedance of the pair is 140Ω (70Ω common-mode impedance). Note the cross-mode s-parameters are zero for the symmetric coupled pair indicating no conversion between propagation modes.

The second example is similar to the first, except the coupled microstrip transmission lines are asymmetric (i.e. unequal widths). This asymmetric coupled-pair, and the accompanying circuitry, is shown in Figure 3-5. One top conductor width is $100\mu\text{m}$, and the second is $170\mu\text{m}$, with an edge-to-edge spacing of $65\mu\text{m}$. Again, the substrate is 25 mil thick alumina with a relative permittivity of 9.6 with a loss tangent of 0.001, and the metal conductivity is that of copper. A one-inch section of this line was simulated in MDS at 5 GHz, and the mixed-mode s-parameters are

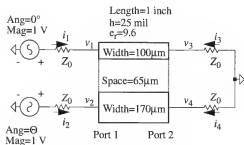


Figure 3-5. Schematic of mixed-mode simulation of asymmetric coupled-pair line.

$$\begin{bmatrix} S_{dd} & S_{dc} \\ S_{cd} & S_{cc} \end{bmatrix} = \quad (3-47)$$

$$\begin{bmatrix} 0.003 \angle -175^\circ & 0.956 \angle 1.819^\circ & | & 0.005 \angle -177^\circ & 0.031 \angle 80.7^\circ \\ 0.956 \angle 1.819^\circ & 0.003 \angle -175^\circ & | & 0.031 \angle 80.7^\circ & 0.005 \angle -177^\circ \\ 0.005 \angle -177^\circ & 0.031 \angle 80.7^\circ & | & 0.502 \angle 48.0^\circ & 0.844 \angle -40.2^\circ \\ 0.031 \angle 80.7^\circ & 0.005 \angle -177^\circ & | & 0.844 \angle -40.2^\circ & 0.502 \angle 48.0^\circ \end{bmatrix}$$

As in the first example, each partitioned sub-matrix demonstrates the properties of a reciprocal, passive and (port) symmetric DUT. Also like the first example, the differential s-parameters show the coupled pair possesses an odd-mode characteristic impedance of nearly 50Ω (actually 49Ω), and has low-loss propagation in the differential mode. The common-mode s-parameters show the coupled pair has a greater degree of mismatch than the first example (the even-mode impedance is 152Ω in this case).

The most important difference between the two examples is seen in the cross-mode s-parameters. The data in (3-47) shows significant conversion between propagation modes, particularly in transmission parameters S_{dc21} and S_{cd21} . Note these two sub-matrices are equal indicating equal conversion from differential to common-mode and from common to differential-mode. These non-zero s-parameters can be interpreted conceptually in the following way. In the case of S_{cd21} , a pure differential mode wave is impinging on port 1 of the DUT. However, at port 2, both differential and common-mode waves exist. Some of the energy of the differential wave is converted to a common-mode propagation, and the total energy is preserved (except for losses in the metal and dielectric).

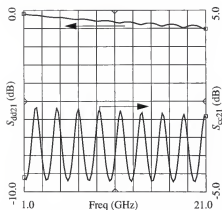


Figure 3-6. Simulated magnitude in dB of S_{dd21} and S_{cc21} versus frequency for asymmetric coupled-pair transmission line

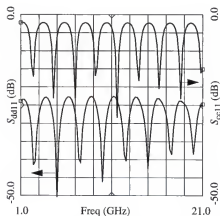


Figure 3-7. Simulated magnitude in dB of S_{dd11} and S_{cc11} versus frequency for asymmetric coupled-pair line.

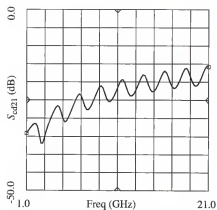


Figure 3-8. Simulated magnitude in dB of S_{cd21} versus frequency for asymmetric coupled-pair line.

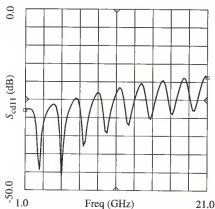


Figure 3-9. Simulated magnitude in dB of S_{cd11} versus frequency for asymmetric coupled-pair line.

This example circuit was simulated across frequency, and the magnitudes of selected mixed-mode s-parameters are plotted in Figures 3-6, 3-7, 3-8 and 3-9. Figure 3-6 shows both S_{dd21} and S_{cc21} in dB from 1 GHz to 21 GHz. The ripple pattern across frequency in the common-mode transmission (S_{cc21}) indicates an impedance mismatch at the ports for common-mode propagation. At the higher frequencies of the plot, the finite conductivity of the conductors is evident as average loss increases. The differential-mode transmission (S_{dd21}) shows smaller ripples (0.2 dB maximum), indicating smaller mismatch, and also shows lower average loss. However, the losses due to the reflections at the ports do not account for all of the ripple in the differential transmission. As can be seen in Figure 3-7, the return loss for the differential mode is greater than 20 dB, which can account for approximately 0.04 dB of worst case loss (over ohmic losses). Mode conversion accounts for the remaining reduction in the differential-mode, and hence S_{dd21} is reduced. Here, differential energy is converted to both common-mode transmission S_{cd21} and common-mode reflection S_{cd11} . Figure 3-8 shows the cross-mode transmission S_{cd21} in dB, and Figure 3-9 shows the cross-mode reflection S_{cd11} in dB. The minima in the differential-mode transmission S_{dd21} correspond to a worst case point in the relative phases of S_{dd21} , S_{cd21} , and S_{cd11} . In a low loss transmission line case, the insertion loss due to mode conversion and miss-match can be shown to be approximately

$$\text{Loss(dB)} = -10 \log \left[1 - (|S_{dd11}|^2 + |S_{cd21}|^2 + |S_{cd11}|^2) \right] \quad (3-48)$$

This is consistent with the increasing ripple in S_{dd21} with increasing frequency since the mode conversion (S_{cd21} and S_{cd11}) increases with frequency.

The use of mixed-mode s-parameters can be further illustrated with an example of a differential amplifier. Such an example is found in Appendix D.

3.2. Generalizations of Mode Specific Scattering Parameters

3.2.1. Other modes

The voltages and currents of (3-1) to (3-4) represent only one possible definition of modes. There are infinitely many such definitions with a four-port network, although the chosen set has important practical value. Furthermore, a network with more ports can support more modes of propagation. It is useful to generalize the proceeding work to include all possible mode definitions as it leads to insight into the nature of the mixed-mode definitions presented.

To begin the generalization, it is helpful to establish the concept of an s-parameter matrix as a linear operator. Traditionally, an s-parameter matrix is interpreted from a physical view, where the elements of the matrix represent the gain coefficients of a certain input-to-output path. The operator interpretation views the s-parameter matrix as an operator that maps one n -dimensional vector space into an m -dimensional space [31] (with typical devices, m and n are equal). With such an interpretation, it will be shown that the transformation to another mode definition can be regarded simply as a transformation of coordinates.

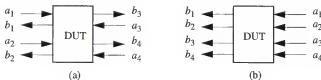


Figure 3-10. Two views of a four-port s-parameter matrix.
a) The physical view. b) The linear operator view.

To illustrate the operator view of s -parameters, consider the four-port example in Figure 3-10. Define basis vectors corresponding to each physical port

$$\hat{p}_1 = \begin{bmatrix} 1 \\ 0 \\ 0 \\ 0 \end{bmatrix} \quad \hat{p}_2 = \begin{bmatrix} 0 \\ 1 \\ 0 \\ 0 \end{bmatrix} \quad \hat{p}_3 = \begin{bmatrix} 0 \\ 0 \\ 1 \\ 0 \end{bmatrix} \quad \hat{p}_4 = \begin{bmatrix} 0 \\ 0 \\ 0 \\ 1 \end{bmatrix} \quad (3-49)$$

One can clearly see that these vectors are linearly independent, that is

$$c_1 \hat{p}_1 + c_2 \hat{p}_2 + c_3 \hat{p}_3 + c_4 \hat{p}_4 \neq 0 \quad (3-50)$$

for all possible complex scalars $\{c_1, c_2, c_3, c_4\} \in \mathbb{C}$, where \mathbb{C} is the set of all complex numbers. Furthermore, this set of basis vectors $\{\hat{p}_1, \hat{p}_2, \hat{p}_3, \hat{p}_4\}$ have a zero scalar product, that is

$$\hat{p}_i \cdot \hat{p}_j = \begin{cases} 0 & i \neq j \\ 1 & i = j \end{cases} \quad (3-51)$$

This means that the system of basis vectors is orthonormal. Continuing, an arbitrary set of input signals becomes

$$\vec{a} = a_1 \hat{p}_1 + a_2 \hat{p}_2 + a_3 \hat{p}_3 + a_4 \hat{p}_4 \quad (3-52)$$

and the output signals are

$$\vec{b} = b_1 \hat{p}_1 + b_2 \hat{p}_2 + b_3 \hat{p}_3 + b_4 \hat{p}_4 \quad (3-53)$$

With the basis definitions of (3-49), the coordinates of the input and output signals are

$$\vec{a} = \begin{bmatrix} a_1 \\ a_2 \\ a_3 \\ a_4 \end{bmatrix} \quad \vec{b} = \begin{bmatrix} b_1 \\ b_2 \\ b_3 \\ b_4 \end{bmatrix} \quad (3-54)$$

The traditional s-parameter matrix equation, $b = Sa$, can now be said to express a linear operator, S , mapping an input space to an output space. It is important to note that both the input and output spaces have the same basis vectors.

Now, considering the same example, define a new set of basis vectors, $\{\hat{p}_1', \hat{p}_2', \hat{p}_3', \hat{p}_4'\}$. These new basis vectors can describe any arbitrary mode definitions. In the case of the differential/common-mode definitions of (3-1) to (3-4) they are

$$\hat{p}_1' = \hat{p}_{d1} \quad \hat{p}_2' = \hat{p}_{e1} \quad \hat{p}_3' = \hat{p}_{d2} \quad \hat{p}_4' = \hat{p}_{e2} \quad (3-55)$$

where the new subscripts are used to clearly indicate that the new basis does not correspond to physical network ports. Assuming linear relationships between the old and new bases, they can be generally related

$$\begin{aligned} \hat{p}_1 &= x_{11}\hat{p}_1' + x_{12}\hat{p}_2' + x_{13}\hat{p}_3' + x_{14}\hat{p}_4' \\ \hat{p}_2 &= x_{21}\hat{p}_1' + x_{22}\hat{p}_2' + x_{23}\hat{p}_3' + x_{24}\hat{p}_4' \\ \hat{p}_3 &= x_{31}\hat{p}_1' + x_{32}\hat{p}_2' + x_{33}\hat{p}_3' + x_{34}\hat{p}_4' \\ \hat{p}_4 &= x_{41}\hat{p}_1' + x_{42}\hat{p}_2' + x_{43}\hat{p}_3' + x_{44}\hat{p}_4' \end{aligned} \quad (3-56)$$

An input signal vector in the new basis

$$\vec{a}' = a_1'\hat{p}_1' + a_2'\hat{p}_2' + a_3'\hat{p}_3' + a_4'\hat{p}_4' \quad (3-57)$$

has the coordinates in the new basis

$$\vec{a}' = \begin{bmatrix} a_1' \\ a_2' \\ a_3' \\ a_4' \end{bmatrix} \quad (3-58)$$

By expressing the input vector in the original basis (3-52) in terms of the new basis vectors via (3-56), and then by equating the coefficients of the basis vectors, it can be shown that

$$\begin{bmatrix} a_1' \\ a_2' \\ a_3' \\ a_4' \end{bmatrix} = \begin{bmatrix} x_{11} & x_{12} & x_{13} & x_{14} \\ x_{21} & x_{22} & x_{23} & x_{24} \\ x_{31} & x_{32} & x_{33} & x_{34} \\ x_{41} & x_{42} & x_{43} & x_{44} \end{bmatrix} \begin{bmatrix} a_1 \\ a_2 \\ a_3 \\ a_4 \end{bmatrix} \quad (3-59)$$

which can be simply expressed as

$$\bar{a}' = X\bar{a} \quad (3-60)$$

where X is a transformation of coordinates matrix. Therefore, the translation between different mode definitions is simply a transformation of coordinates. In the case of the differential/common-mode definitions, it can be shown that (3-60) becomes

$$\bar{a}^{\text{mm}} = M\bar{a}^{\text{std}} \quad (3-61)$$

As illustrated in (3-53), the input and output vector spaces share the same basis vectors, so the output in the new basis becomes

$$\bar{b}' = X\bar{b} \quad (3-62)$$

or, for differential/common-modes

$$\bar{b}^{\text{mm}} = M\bar{b}^{\text{std}} \quad (3-63)$$

The linear operator representing the DUT can be translated between bases by

$$S' = XSX^{-1} \quad (3-64)$$

In general, if both sets of bases are orthonormal, as defined in (3-51), then the transformation matrix, X , will always be unitary, that is $X(X^*)^T = I$. Conversely, if a defined transformation matrix is unitary, then both systems of basis vectors are orthonor-

mal [31]. With the concept of s-parameters as linear operators, one can define any number of new and potentially useful modes of propagation.

3.2.2. Eigen modes

One particularly interesting new mode definition arising from the operator view of networks is the concept of eigen-modes. Eigen-values arise from the diagonalization of a matrix, and the matrix of eigen-vectors become the transformation matrix. Symbolically,

$$\Lambda = T^{-1}ST \quad (3-65)$$

where

$$\Lambda = \text{diag}(\lambda_1, \dots, \lambda_n) \quad (3-66)$$

where λ_i are the eigen-values of S , and T is a matrix whose columns are composed of the eigen-vectors of S [33].

In linear system analysis, eigen-values represent the natural frequencies of a system. When described in state space notation, the state-feedback matrix, A , determines these natural frequencies. The natural frequencies, or eigen-values, are the solutions to

$$|\lambda I - A| = 0 \quad (3-67)$$

Corresponding to each eigen-value, λ_i , there is a eigen-vector, \bar{e}_i , such that

$$(\lambda_i I - A)\bar{e}_i = \bar{0} \quad (3-68)$$

Physically, the eigen-values are the complex frequencies at which the system will have (unforced) oscillations, and the eigen-vectors are the amplitude coefficients of each of the state variables under the conditions of oscillation.

In contrast, the eigen-values and vectors of an s-parameter matrix do not represent system oscillations. For an s-parameter operator, the eigen-vectors represent the coeffi-

cients of a transformation to a new basis. The new basis further represents new modes of propagation. This new basis is special, in that it transforms the operator, S , into a diagonal matrix. For this reason, the modes corresponding to the eigen-vectors of a operator, S , will be called canonical modes. The eigen-values represent the DUT response in terms of the canonical modes.

In general, an n -port device will have n canonical modes. When stimulated by one of the canonical modes, the device will generate a response proportional to only the mode by which it was stimulated. There is only one port definition possible for canonical modes. Each canonical mode is formed from a linear combination of signals at all of the physical ports. There are n possible canonical modes of propagation supported by a device with n physical ports. This removes any ambiguity that exists in the port numbering convention¹.

The canonical representation of a device allows for very simple calculations of responses. Since the canonical form of a device is a one-port (multi-mode) network, the response of the device to a canonical mode input is simply a reflection of the same canonical mode. The canonical mode reflection has a scaling, or gain, factor that is conceptually equivalent to the traditional definition of reflection coefficients. The eigen-values of a s -parameter matrix are the canonical reflection coefficients. Furthermore, a given device generates no conversion between its canonical modes. As a result, the canonical representation can be interpreted as the natural modes of a device.

It is interesting to note that eigen-values of a matrix, S , remain unchanged by a change of basis (i. e. a similarity transformation as in (3-65)). The eigen-values, therefore,

1. The definitions of mixed-mode s -parameters presented in Section 3.1.1 define (nodal) ports one and two as mixed-mode port one, and so on. However, any other combination of two ports could have also been chosen as a mixed-mode port.

are immutable properties of an s -parameter matrix, and the canonical modes of a device are properties of the device. Eigen-vectors are not unique, since they need only to be independent. As stated earlier, infinitely many modes (not independent) can be defined for a given network. However, the consistency of the eigen-values across all such bases indicates the all representations of a device are leaving the essence of the device unchanged. Mixed-mode s -parameters are indeed an equivalent representation of a standard four-port s -parameter matrix.

Not every device has a canonical representation. A matrix, S , is diagonalizable if and only if S has n linearly independent eigen-vectors. It can be shown [33] that S has n linearly independent eigen-vectors if S has n distinct eigen-values (the converse is not true, however). Therefore, if all eigen-values are different, then one can be assured the device has a canonical representation. If some values are repeated, then the existence of a canonical representation depends on S .

If an s -parameter matrix does not have n linearly independent eigen-vectors, then it is possible to find n independent generalized eigen-vectors. Under these conditions, the new operator matrix is not diagonalizable, but generally in Jordan form. A Jordan form matrix has some non-zero off-diagonal elements. Such a device requiring a Jordan form representation will exhibit mode-conversion between some of its canonical modes. Despite this limitation, the Jordan form representation of an s -parameter operator can have some utility in calculations.

Not every non-diagonalizable matrix has a Jordan form representation. In such cases, other decomposition methods are available, such as LDU-factorization [33]. These decompositions cause representations that are as close as possible to a diagonal form.

This work can be extended to include these other representations of an s-parameter operator.

With the fundamental theory of mixed-mode s-parameters developed, the application of these concepts to practical circuits can begin. The first step in this progression is to measure the mixed-mode s-parameters of an RF differential circuit. These new s-parameters require the design and construction of a specialized measurement system. The development of this new system is the subject of the next chapter.

CHAPTER 4

CONSTRUCTION OF THE PURE-MODE VECTOR NETWORK ANALYZER

As a result of the limitations of measuring RF differential circuits and devices with a single-mode system, as discussed in Chapter 2, a custom vector network analyzer (VNA) has been designed to measure mixed-mode s -parameters in the most direct and accurate fashion. The existence of a transformation between standard and mixed-mode s -parameters, discussed in Section 3.1.3, suggests two possible approaches to the measurement of differential circuits. One approach is the use of a traditional four-port VNA. A traditional VNA would measure standard s -parameters by stimulating each terminal of the differential circuit individually, and these s -parameters would then be transformed to mixed-mode s -parameters for analysis. Alternatively, the mixed-mode s -parameters of the differential circuit can be measured directly by stimulating each mode individually. A pure differential-mode stimulus could be produced, and the differential- and common-mode responses of the DUT could be measured, thus providing a direct measurement of mixed-mode s -parameters. A network analyzer that directly measures mixed-mode s -parameters will be referred to as a pure-mode vector network analyzer (PMVNA) due to its generation and measurement of pure single mode signals.

The two approaches do not yield equally accurate mixed-mode s -parameters of differential devices, however. It is shown in Chapter 5 that the PMVNA has an accuracy advantage over a traditional four-port VNA while measuring a differential circuit. Mixed-mode s -parameters generated by transforming standard s -parameters measured by a tradi-

tional four-port VNA exhibit higher levels of uncertainty in a differential device measurement than those measured by a PMVNA. This accuracy advantage of a pure-mode measurement system provides motivation for the development of a specialized measurement system for differential circuits. Portions of this chapter have been published in summary form [34].

4.1. Basic Operation of the PMVNA

4.1.1. Fundamental Concepts

As discussed above, the most straightforward means of implementing a mixed-mode s -parameter measurement system is to directly apply differential and common-mode waves while measuring the resulting differential and common-mode waves. Unfortunately, the generation and measurement of these modes of propagation is not easily achievable with standard vector network analyzers (VNA). However, as shown in (3-38) and (3-39), one can relate the total nodal waves to the desired differential and common-mode waves. These nodal waves are readily generated and measured with standard VNAs, and with consideration, the differential and common-mode waves, and hence the mixed-mode s -parameters, can be calculated.

Equations (3-38) and (3-39) represent important relationships from which a PMVNA can be constructed with components of standard single-ended VNAs. To understand the utility of the above relationships, consider Figure 4-1, which is a conceptual model for a PMVNA system. By adjusting the phase difference, Θ , between the two sources to 0° or 180° one can determine the common-mode or differential-mode forward s -parameters, respectively. Conceptually, the measured quantities are the voltages and currents. These values can be related to the normalized nodal waves, a_1, b_1, a_2, b_2 , etc.,

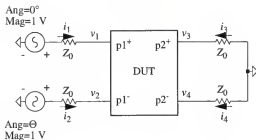


Figure 4-1. Conceptual diagram of pure-mode measurement system.

through the generalized definitions given in (3-32). From these nodal waves, the differential and common-mode normalized waves, and, hence, the mixed-mode s -parameters, can be calculated. Physically, the various ratios of nodal waves, a_1, b_1, a_2, b_2 , etc., are measured, and from these ratios the mixed-mode s -parameters are found.

4.1.2. General PMVNA Test-Set Architecture

The physical implementation of a mixed-mode s -parameter measurement system can be achieved with extensions of standard VNA techniques. The differential stimulus of a coupled two-port requires the input waves at the reference plane to be 180° apart. One possible way this can be achieved through a single signal source is with the use of a 180° 3dB hybrid splitter/combiner. The construction of the differential reflected and transmitted waves, via (3-38) and (3-39), can be also completed through a 180° splitter/combiner. The common-mode stimulus of a coupled two-port requires the input waves at the reference plane to be 0° apart. This can also be achieved through a single signal source with the use of a 0° 3dB hybrid splitter/combiner, with the construction of the common-mode reflected and transmitted waves also completed through a 0° splitter/combiner.

A VNA test-set is the portion of the test system that generates the normalized power waves, a and b . A typical test-set uses directional couplers to separate the forward and reverse waves. A test-set also samples the stimulus signal, either with a directional coupler or a power splitter. The test-set generally down-mixes all signal to an intermediate frequency (IF), so that all RF functions of the VNA (other than the RF signal source) are contained within the test-set. A test-set also provides RF switches to allow automated measurement of all s -parameters of the DUT with a single connection.

A basic pure-mode test-set is shown in part in Figure 4-2. The figure includes mechanisms by which all of the mixed-mode wave components are generated. Not shown are the down mixers and the rest of the VNA system, which are discussed in Section 4.2.1 and Appendix E. When switch one (denoted as SW1) is in position one, the 3dB hybrid coupler, H1, splits the RF signal into two signals with nominally equal amplitudes and 180° phase difference, thus generating the differential-mode RF stimulus signal. Note that all switches have their unused ports terminated in 50Ω loads in all cases. By placing SW1 in position two, the coupler, H1, again splits the RF signal into two signals, in this case with nominally equal amplitudes and 0° phase difference, thus generating the common-mode RF stimulus signal. Switches SW2 and SW3, which operate in concert, provide the means to stimulate either mixed-mode port one or two. Directional couplers D1, D2, D3, and D4 separate all forward and reverse signals at each single-ended port (i.e. nodal waves). These nodal waves are combined, in accordance to (3-38) and (3-39), in 3dB hybrid couplers H2, H3, H4, H5, each providing a (nominal) sum and difference between the corresponding nodal waves. The output of these couplers are proportional to the differential and common-mode normalized power waves (a_{d1} , a_{c1} , b_{d1} , b_{c1} , etc.).

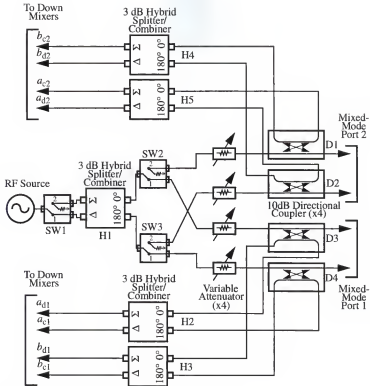


Figure 4-2. RF Section of basic test-set of PMVNA.

From the appropriate ratios of these power waves, the mixed-mode s-parameters can be calculated.

4.2. Implementation of a Practical PMVNA

Rather than build an entire PMVNA from elementary components (such as directional couplers and mixers), a more practical approach has been followed by modifying a

standard VNA. As will be discussed below, a PMVNA can be constructed in a straightforward manner by adapting a modular Hewlett-Packard 8510 VNA system. First, a system-level description of the PMVNA, as implemented for this work, will be given. Following this, a detailed description of the PMVNA test-set will be given. Next, the operation of the PMVNA will be detailed, and the control software will then be described.

4.2.1. System Level Description

The construction of the PMVNA is based the Hewlett-Packard 8510C VNA system. The complete block diagram of the implemented system is shown in Figure 4-3. The basic idea behind the implemented PMVNA is to use the sub-systems of a standard 8510 (each contained as a single piece of test equipment) in a non-standard configuration with little or no modification to the individual sub-systems. The sub-systems (85101, 85102, 8517, 85651, etc.) are shown in Figure 4-3. For a description of these sub-systems and the standard 8510 configuration, see Appendix E.

Basically, the PMVNA is an 8510 VNA with two test-sets, where both test-sets are used simultaneously. The implementation of a PMVNA with an HP8510 VNA requires the addition of a second 8517 test-set to supply all required RF hardware. Some additional control hardware, and some minor modifications to the 8517 test sets are also needed, as will be described below.

The flexibility of the 8510 VNA system greatly facilitates the implementation of a PMVNA. One important feature of the 8510 is exploited in order to reduce the complexity of the control software and hardware in the adaptation to the PMVNA. The feature, known as Option 001, allows selection between multiple test-sets. The option is actually an additional circuit board for switching IF signals which is installed in one of the two

test-sets. The board works in coordination with features of the 8510 operating system (standard firmware of the 8510). The operating system of the standard 8510 allows the selection of a test-set to be accomplished simply by changing the address of the active test-set (contained in a register in the 85101) to the address of the desired test-set. The address of the active test-set can be set through standard general purpose interface bus

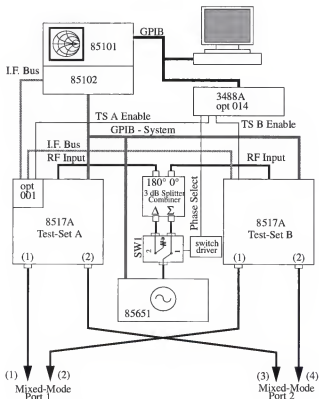


Figure 4-3. PMVNA system block diagram.

(GPIB) commands. The availability of the test-set selection function to GPIB commands enables high-level control of the sub-systems in the PMVNA.

The PMVNA system also requires some minor modifications to the control hardware of the test-sets. As developed by HP, Option 001 allows the selection of one active test-set, and the deactivation of all other test-sets. This deactivation includes the moving of the RF port selection switch (internal to the test-set) to a terminated position, so that no RF signal is present at the ports of the deselected test-sets. Also upon deactivation, the variable attenuators in a test-set (used to control the incident power on a DUT) are re-set to 0 dB. The suppressing of the RF signal from the inactive test-sets and the change of attenuation setting are unwanted side effects. The modification to both test-sets is needed to allow RF to continue at the ports of inactive test-sets and to keep the attenuator settings unchanged. The modification requires a minor change to the test-set digital control hardware to allow the masking of commands to change the position of the RF port selector switch or attenuators. The masking of system commands is achieved through a single digital control signal for each test-set. When the signal, called test-set enable, is asserted, the test set can receive system commands effecting RF switch and attenuators; otherwise, these system commands are blocked (other system commands are unaffected by the modification). With these changes, the option 001 can now be used to multiplex the two test-sets while maintaining an uninterrupted RF signal at the ports. For complete details of the test-set modifications, see Appendix F.

These hardware changes are implemented to block unwanted system commands from the 8510 operating system as the active test-set is changed. An alternative to these hardware modifications is to change the operating system. Such a change, to allow

switching between test-sets without changing the RF switch position or attenuator settings, is certainly possible, and quite attractive since it would eliminate the need for any modification of the test equipment of the 8510 system. The option of modifying the 8510 operation system is unavailable, however, as it is proprietary property of Hewlett-Packard. Due to the unavailability of the operating system software, the hardware modifications have been performed.

A single 3dB hybrid $180^\circ/0^\circ$ splitter/combiner is added to the standard 8510 configuration. This splitter generates the two RF signals needed to operate both test-sets simultaneously. The use of a $180^\circ/0^\circ$ splitter allows for the generation of both differential and common-mode stimuli. An RF switch is required to select between the two modes, and a driver for the switch is required to allow automatic control. The switch driver and test-set enable control lines are interfaced to a GPIB controllable digital switches (3488A with option 014). With this switch controller, the PMVNA can be completely automated.

4.2.2. Test-Set Construction

One of the most useful aspects of a PMVNA implemented as shown in Figure 4-3 is the straight-forward manner by which the differential and common-mode normalized power waves can be derived from the nodal power waves. Referring first to the basic PMVNA test-set of Figure 4-2, one can see that the calculation of the modal normalized waves is accomplished through four $180^\circ/0^\circ$ splitter/combiners. The calculation is done at RF with real (non-ideal) components, and so is subject to errors (see Chapter 8). A more practical and accurate method of constructing the differential and common-mode responses is through digital calculation of (3-38) and (3-39). This technique exploits the architecture of the standard 8510, which down-mixes and digitizes the normalized power

waves. Once the nodal waves are digitized, the differential and common-mode normalized power waves can be simply calculated in the control software.

In the PMVNA implemented for this work, the calculations of the normalized power waves are accomplished by using two standard two-port test-sets. The connection of this simplified PMVNA test-set is shown in Figure 4-4, which includes two standard (single-ended) 8517A s-parameter test-sets. These test-sets have all required RF circuitry to separate the different waves, and all of the down converter circuitry. No modifications to the RF portions of these test-sets are needed.

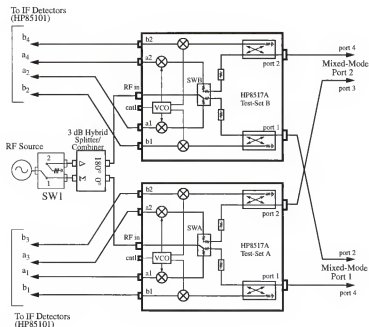


Figure 4-4. RF section of simplified PMVNA test-set.

A significant advantage of this test-set configuration is its symmetry. If the two test-sets are the same model (as they are for this work) then the RF paths of the PMVNA are well balanced. When the PMVNA is set to forward differential-mode, for example, both test-sets have the same switch configuration. The two RF paths that comprise the differential signal (one through test-set A, the other through test-set B) are identical (within manufacturing tolerances), and thus the phase and magnitude balance between the two paths is good. If the paths are poorly balanced, then high levels of mode-conversion will be generated in the PMVNA. Good balance is required to have sufficient raw dynamic range for accurate measurements. Again, the amount of tolerable imbalance must be determined by experience. The raw performance of the implemented PMVNA is examined in Section 6.2.1.

This simplified test-set configuration has one significant disadvantage, namely, the use of two independent voltage controlled oscillators (VCOs). Referring to Figure 4-4, one can see that each test-set contains a VCO. During measurements, this VCO is phase-locked to the RF input signal of the test-set (for details, see Appendix E). This VCO generates a signal that drives all four down-mixers in the test-set. As all mixers in a single test-set are driven by the same VCO, the phase relationship between the down-mixed a and b signals remains the same as it was at RF. However, as the PMVNA switches between the two test-sets, the phase relationship between the VCOs of the two test-sets is unknown. As a result, the straight-forward application of the measured power wave data will result in significant errors. This disadvantage can be removed, however, through a pre-calibration process that characterizes the phase offset between the two VCOs. This process is detailed in Section 6.3

Only the $180^\circ/0^\circ$ splitter/combiner and the RF switch for the source (SW1) limit the bandwidth of the simplified PMVNA. The 8517A test sets operate from 45 MHz to 50 GHz, and with relaxed requirements on the $180^\circ/0^\circ$ splitter/combiner, accurate measurements are possible from about 100 MHz to above 25 GHz with one hybrid [35]. A second hybrid allows accurate measurements from 45 MHz to above 5 GHz [36]. The factor limiting the frequency range of any splitter is the amount of imbalance that is tolerable in a PMVNA system. This imbalance leads to non-ideal mode generation, as will be shown in Chapter 8. This non-ideal mode generation can be tolerated and corrected through calibration (see Chapter 6) but only to a point. At some level of imbalance, the corrected dynamic range of one or more of the mixed-mode s-parameters becomes unacceptable. The frequency at which the level of imbalance is unacceptable generally occurs beyond the specified operation frequencies of the splitter (splitter frequency specifications are linked to specified levels of phase and magnitude imbalance), but the exact level of tolerable imbalance is usually found through experience.

With this PMVNA configuration, all mode responses, including mode conversion, can be measured. With all responses available, very accurate, repeatable calibrations and measurements are possible. Additionally, with the use of standard, readily available measurement equipment, the PMVNA can be easily and economically duplicated.

4.2.3. Detailed Operation

This section details the theory of operation of the PMVNA. The operation is presented as a sequence of high-level events that affect the measurement of a DUT by the analyzer. This discussion is meant to clarify the way raw data is collected and manipulated in the measurement of raw mixed-mode s-parameters. In general, each event

described in this section is comprised of many more elementary events which are not described here. The referenced elementary events are performed by the control software of the PMVNA which has been developed solely for this work. For more details on the PMVNA control software, see Section 4.2.4. Furthermore, there is a level of operation of the sub-systems that is even more fundamental. These low-level events, such as the locking of the main phase-lock loop, are accomplished by the operating system of the 8510 system, and are transparent to the PMVNA control software. This most basic level of operation is not described here, but can be found in 8510 documentation [43].

This section details only the measurement operation of the PMVNA. This operation is the foundation of the general operation of the PMVNA, and the output of this operation is raw (uncorrected) mixed-mode s-parameters of a DUT. Optionally, this operation can produce standard four-port raw s-parameters directly (in contrast to transformation of mixed-mode s-parameters). The calibration and subsequent error correction procedures, and all other functions of the PMVNA, are detailed in Section 4.2.4.

The basic operation of the PMVNA measures the differential and common-mode responses of a DUT to both a differential and a common-mode stimulus. Referring to the flow diagram in Figure 4-5, the PMVNA first measures the DUT with a differential stimulus, which is accomplished by setting SW1 to position one (see Figure 4-3). Forward operation of the DUT is measured by setting the RF port selection switches of both test-sets into forward position. This drives PMVNA ports (nodes) one and two with a nominal 180° phase difference. Normalized waves are measured at all down-mixers: $a_1, b_1, a_2, b_2, a_3, b_3, a_4, b_4$ (the reasons for measuring all possible normalized waves, even those that are apparently unneeded, are to correct for RF switch imperfections; see Section 6.2.4). This

configuration of the PMVNA is called the differential-forward mode (DF). Next, reverse operation of the DUT is measured by setting the RF port selection switches of both test-sets into reverse position. This drives PMVNA ports three and four with a nominal 180° phase difference. Again, normalized waves are measured at all down-mixers. This configuration of the PMVNA is called the differential-reverse mode (DR).

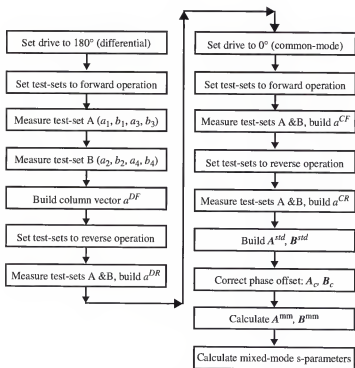


Figure 4-5. Flow chart of PMVNA measurement.

Next, the PMVNA measures the DUT with a common-mode stimulus, which is accomplished by setting SW1 to position two (Figure 4-3). The forward measurements are repeated in the same way as with the differential stimulus described above. This configuration is called the common-forward mode (CF). Similarly, the reverse measurements are repeated with the common-mode stimulus; this configuration of the PMVNA is called the common-reverse mode (CR).

The calculation of the mixed-mode normalized power waves is as follows. After all data from a DUT measurement has been collected, the raw a and b data are arranged into column vectors, where each vector corresponds to a single measurement mode (DF, DR, CF, CR), and the a and b data are collected into two corresponding vectors. In Figure 4-5, the arrangement of the a data is illustrated, where

$$\begin{matrix} \text{-DF} \\ a \end{matrix} = \begin{bmatrix} \text{DF} \\ a_1 \\ \text{DF} \\ a_2 \\ \text{DF} \\ a_3 \\ \text{DF} \\ a_4 \end{bmatrix} \quad \begin{matrix} \text{-DR} \\ a \end{matrix} = \begin{bmatrix} \text{DR} \\ a_1 \\ \text{DR} \\ a_2 \\ \text{DR} \\ a_3 \\ \text{DR} \\ a_4 \end{bmatrix} \quad \begin{matrix} \text{-CF} \\ a \end{matrix} = \begin{bmatrix} \text{CF} \\ a_1 \\ \text{CF} \\ a_2 \\ \text{CF} \\ a_3 \\ \text{CF} \\ a_4 \end{bmatrix} \quad \begin{matrix} \text{-CR} \\ a \end{matrix} = \begin{bmatrix} \text{CR} \\ a_1 \\ \text{CR} \\ a_2 \\ \text{CR} \\ a_3 \\ \text{CR} \\ a_4 \end{bmatrix} \quad (4-1)$$

and where the subscripts one through four correspond to the PMVNA port (node) numbers. Similarly, the b data are arranged into vectors \bar{b}^{DF} , \bar{b}^{DR} , \bar{b}^{CF} , and \bar{b}^{CR} . The data are placed in two matrices

$$\mathbf{A}^{\text{std}} = \begin{bmatrix} \text{-DF} & \text{-DR} & \text{-CF} & \text{-CR} \\ a & a & a & a \end{bmatrix} \quad \mathbf{B}^{\text{std}} = \begin{bmatrix} \bar{b}^{\text{DF}} & \bar{b}^{\text{DR}} & \bar{b}^{\text{CF}} & \bar{b}^{\text{CR}} \end{bmatrix} \quad (4-2)$$

where the superscript *std* indicates that the matrices are nodal data rather than mixed-mode data. The phase offset correction process, which will be described in detail in Section 6.3, is applied to the A and B-matrices, generated phase-corrected versions, A_c

and B_c , respectively. The mixed-mode normalized power waves are now calculated in matrix form

$$A^{mm} = MA^{std} \quad B^{mm} = MB^{std} \quad (4-3)$$

where the matrix M is the similarity operator described in (3-42). The designation of elements of the mixed-mode power wave matrix, A^{mm} is also composed of column vectors, one for each PMVNA configuration

$$A^{mm} = \begin{bmatrix} a^{-mmDF} & a^{-mmDR} & a^{-mmCF} & a^{-mmCR} \end{bmatrix} \quad (4-4)$$

and where

$$a^{-mmDF} = \begin{bmatrix} a_{d1}^{DF} \\ a_{d2}^{DF} \\ a_{c1}^{DF} \\ a_{c2}^{DF} \end{bmatrix} \quad (4-5)$$

with the subscript d referring to the differential-mode quantity, c to the common-mode, and the subscript numbers referring to the mixed-mode port numbers (in contrast to the single-ended node numbers). The remaining vectors of (4-4) are defined in the same fashion. Likewise, the mixed-mode B-matrix, B^{mm} , can be defined.

The calculation of raw mixed-mode s-parameters is examined in detail next. After calculation of the mixed-mode normalized power matrices A^{mm} and B^{mm} , the raw mixed-mode s-parameter matrix, S^{mm} , can be simply calculated

$$S^{mm} = B^{mm} (A^{mm})^{-1} \quad (4-6)$$

One of the added benefits of the PMVNA is that it can also be used to measure standard four-port s -parameters. The standard s -parameters can be calculated through the similarity transformation of (3-44), but they can also be calculated directly from raw A and B -matrices. With this method, the standard A and B -matrices of (4-3) are used to directly calculate the standard s -parameters

$$S^{\text{std}} = B^{\text{std}} (A^{\text{std}})^{-1} \quad (4-7)$$

The accuracy of these standard s -parameters must be considered carefully, however. As is shown in Chapter 5, the PMVNA has lower residual errors when measuring a differential device. By similar arguments, it can be shown that a standard four-port VNA (where only one test port is stimulated at a time) will have lower residual errors when measuring a device that exhibits no differential behavior. Stated another way, the four-port measurements of the PMVNA of a non-differential DUT have higher residual errors than measurements of the same device from a standard four-port VNA.

4.2.4. Control Software

The control software of the PMVNA was implemented in *LabVIEW*. *LabVIEW* is a graphical instrument control language which is well suited for the automation of the PMVNA [37]. The control software has many functions (1) general measurement control (2) VNA operation settings such as measurement frequencies, attenuation settings, etc., (3) PMVNA calibration, (4) general user interface, (5) data display, and (6) data input/output (I/O) in files.

The control software of the PMVNA represents a significant development effort. This software is highly specialized, and has been developed solely for this work. The program is graphically developed, so that wiring diagrams take the place of traditional

source-code listings. The control software represents more than 11.5 Mbytes of code, so including all diagrams is prohibitive. Instead, flow diagrams are presented to indicate the substance of the software.

This section reviews the control software at the highest level of functionality. For detailed descriptions of the various functions, see Appendix G. The basic flow of the software is indicated in Figure 4-6. The first step in using the PMVNA is to set the basic operating parameters of the analyzer. This includes the frequencies of measurement, the attenuator settings for all ports, the number of averages, RF source power level, and so on.

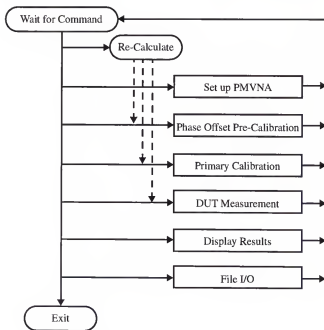


Figure 4-6. Top-level flow chart of PMVNA control software.

Next, a phase offset pre-calibration must be completed. This characterizes and allows for the correction of the phase offset between the two VCO signals in the test sets. For theoretical details on this calibration step, see Section 6.3. The primary calibration characterizes linear time-invariant errors in the PMVNA, allowing for error correction of measured data. The theoretical development of the PMVNA calibration is given in Chapter 6. The next step in the software flow is DUT measurement. This includes measurements as detailed in Section 4.2.3, and error correction of the measured DUT mixed-mode s -parameters. The final two steps in the software flow are optional, but are almost always used. The first of these is data display, which allows the user to examine the raw or corrected DUT and calibration standard s -parameters in a variety of formats. The last step is file IO which allows the user to save any of measured data to a file in CITI format [38]. Also, the software allows the user to re-calculate any portion calibration and error correction algorithms, which is used mainly for de-bugging purposes.

4.3. On-Wafer Measurements

The PMVNA can make measurements of devices with coaxial connectors, or devices that are meant to be probed at the wafer level. Wafer-level measurements, or on-wafer measurements, require special RF wafer probes to make good performance RF connections to integrated devices that are typically quite small (on the order of $300\mu\text{m}$ on a side). For the PMVNA, careful attention must be given to the signal launch from the probe tip to the wafer surface. As shown in Appendix C, the mixed-mode s -parameters of an arbitrary differential DUT can be accurately measured with uncoupled reference transmission lines (or ports), independent of any coupled modes of propagation that may exist in the DUT. This is achieved through the decomposition of any coupled-mode signals into

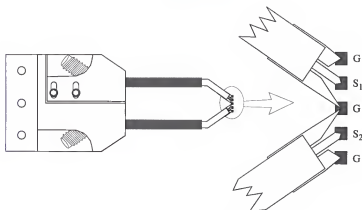


Figure 4-7. GGB dual-RF wafer probe, top view (not to scale).

uncoupled modes, which results in mixed-mode s -parameters that are normalized to the reference impedance of the uncoupled lines. Accordingly, the wafer probes that interface with a differential DUT can be composed of isolated single-ended probes.

In order to maintain a smooth transition to any coupled-modes, two single-ended probes are paired into a single mixed-mode probe. Each mixed-mode probe provides two RF measurement ports that are in reasonably close proximity, but are ideally uncoupled. Hence, a mixed-mode probe footprint of GS_1GS_2G is adopted. The PMVNA system, as implemented for this work, is fitted with a pair of $150\mu\text{m}$ pitch dual-RF probes manufactured by GGB Industries [39]. A dual-RF probe is illustrated in Figure 4-7, with a detail showing the probe contact configuration.

Wafer probes require special calibration standards. These standards are meant to be contacted directly by the probe, so that the calibration reference planes are at the probe

tips. These wafer probe-able standards are widely available for two-port VNAs. However, the unique nature of the PMVNA required custom wafer-probe standards to be designed and manufactured. These standards are discussed in detail in Section 6.2.7 of Chapter 6.

With the construction and operation of the PMVNA detailed, the measurement accuracy remains to be assessed. An important aspect of the PMVNA is its accuracy in the measurement of differential devices, relative to that of a more traditional VNA. This is the central issue that will be examined in the next chapter.

CHAPTER 5

ACCURACY OF THE PURE-MODE VECTOR NETWORK ANALYZER

As indicated in Section 3.1.3, mixed-mode s -parameters and standard four-port s -parameters are related by a linear similarity transform. This relationship suggests that a traditional four-port VNA (where only one measurement port is stimulated at a time) could be used to measure a differential DUT, and the resulting four-port s -parameters could be transformed to mixed-mode s -parameters for easy analysis. Instead, a specialized VNA has been constructed to directly measure mixed-mode s -parameters. These two approaches do not yield equally accurate mixed-mode s -parameters of differential devices, however. The PMVNA will be shown to be more accurate than a traditional four-port VNA while measuring a differential circuit. Mixed-mode s -parameters generated by transforming standard s -parameters measured by a traditional four-port VNA exhibit higher levels of uncertainty than those measured by a PMVNA. In particular, the uncertainties of transformed mode-conversion parameters, S_{dc} and S_{cd} , can be significantly larger than the actual device parameter magnitudes. The accuracy advantage of a pure-mode measurement system provides motivation for the development of this specialized measurement system for differential circuits.

In order to better understand the benefits and limitations of the PMVNA, the measurement accuracy of the system will be examined. The goal of this chapter is to quantify the error in mixed-mode s -parameters of differential devices as measured by a PMVNA. Since it has been earlier established that a linear transform exists between mixed-mode

s-parameters and standard s-parameters, a traditional four-port vector network analyzer (FPVNA) can theoretically be used to measure a differential device. Here, a traditional four-port network analyzer refers to a network analyzer that stimulates each port individually while un-stimulated ports are terminated with a matched load. If a FPVNA is to be considered for measurement of differential devices, it is important to understand the errors that result by transforming standard s-parameters into mixed-mode s-parameters. The accuracy of both systems must be compared to understand the advantages and disadvantages of each. To quantize the errors in both a PMVNA and a FPVNA, the analysis is divided into two important areas of consideration: probe-to-probe crosstalk and maximum measurement uncertainty. It will be shown that the PMVNA has a higher dynamic range than the FPVNA due to the $1/d^3$ and $1/d$ (d is distance) dependence of probe crosstalk, respectively. It will also be shown that the uncertainty of mode-conversion parameters is significantly lower for the PMVNA than for the FPVNA.

5.1. Probe-to-Probe Crosstalk

For a wafer-probe measurement system, the uncorrected probe-to-probe crosstalk is an important specification. This crosstalk can limit the dynamic range of the measurement system, making high dynamic range measurements impractical. An important example of such a high dynamic range measurement is the reverse isolation of an integrated RF amplifier. The unacceptable probe crosstalk of single-ended two-port VNA provided some of the original motivation for the development of the PMVNA. The differential mode of operation of the PMVNA is expected to have reduced probe crosstalk, due to the natural common-mode signal rejection characteristic of a differential circuit. This reduced crosstalk would allow higher dynamic range measurements than FPVNA. For

these reasons, the raw probe-to-probe crosstalk of the PMVNA and a traditional four-port VNA are first quantified. The examination of the crosstalk levels is based on electromagnetic simulations of probe tips. Measured probe-to-probe crosstalk is also provided as further evidence of the higher dynamic range of the PMVNA.

5.1.1. Simulated Probe Crosstalk

The mixed-mode probe is simulated as a ground-signal₁-ground-signal₂-ground (GS₁GS₂G) probe, as described in Section 4.3. The crosstalk of the four-port system is represented through simulations of ground-signal-ground (GSG) probes. The use of the two-port single-ended probes allows a consistent comparison between the crosstalk levels. For simulation, the probes are modeled as 50μm wide by 100μm long metal strips arranged in a 150μm pitch configuration, as shown in Figure 5-1. The strips are situated

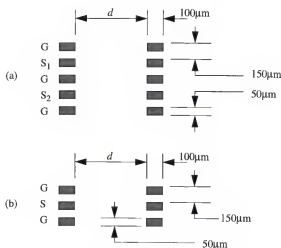


Figure 5-1. Probe crosstalk simulation layout.
 a) Mixed-mode probe layout. b) Single-ended probe layout.

on the surface of a 25mil substrate, and for purposes of this demonstration, the substrate relative dielectric constant has been chosen to be one. Under the substrate is an ideal ground plane. The probes are simulated in opposing pairs where the distance between probes is specified. The electromagnetic simulator used is Hewlett-Packard's Momentum, which is a method-of-moments simulator [40]. Multiple simulations of both the mixed-mode and single-ended structures have been executed over a range of distances between the probes tips.

The results of the multiple simulations are shown in Figure 5-2 to Figure 5-5. A direct comparison of the crosstalk in the differential mode of the PMVNA to that of the single-ended VNA is shown in Figure 5-2 as a function of probe separation at 1.0 GHz. The simulations show that the single-ended crosstalk maintains an approximate $1/d$ characteristic, whereas the differential crosstalk behaves as $1/d^3$. This different dependence on probe separation provides significant decrease in crosstalk for the differential mode with respect to the single-ended operation, and hence provides for greater dynamic range in the corresponding measurement. Also shown in Figure 5-2 is the common-mode crosstalk of the PMVNA. The common-mode shows nearly the same level of crosstalk as the single-ended system, as expected. This indicates that the common-mode measurements will have approximately the dynamic range as traditional single-ended measurements. This plot illustrates the dynamic range advantages of differential measurements over single-ended measurements. Figure 5-3 shows a comparison of the crosstalk of the PMVNA to that of the single-ended VNA 10.0 GHz. Figure 5-4 and Figure 5-5 show crosstalk as a function of frequency for single-ended and differential probes, respectively.

The previous figures assume perfect phase and magnitude balance in the PMVNA system. However, all real systems will have some degree of imbalance, degrading the modal purity of any stimulus signal. The effects of imbalances on probe-to-probe crosstalk can be quantified with the use to the same electromagnetic simulations. For example, a 5° phase imbalance from the ideal 180° differential results in a probe crosstalk level of -106 dB at 1.0 GHz and $1500\mu\text{m}$ separation, which reduces the dynamic range improvement over single-ended to approximately 34 dB. The phase imbalance of the present PMVNA is less than $\pm 5^\circ$ from 1 to over 5 GHz with very small magnitude imbalance.

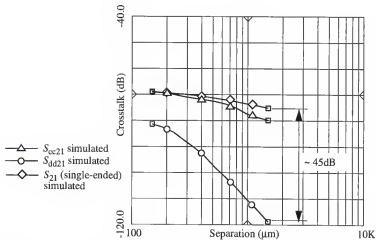


Figure 5-2. Simulated probe crosstalk vs. separation distance at 1.0 GHz.

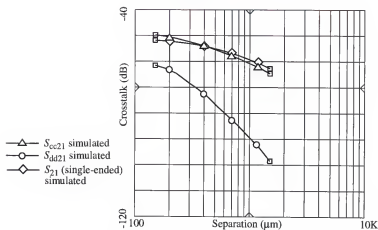


Figure 5-3. Simulated probe crosstalk vs. separation distance at 10 GHz.

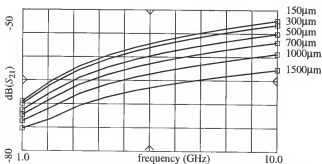


Figure 5-4. Simulated single-ended probe crosstalk vs. frequency for several probe separations.

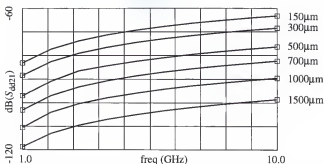


Figure 5-5. Simulated differential probe crosstalk vs. frequency for several probe separations.

5.1.2. Measured Probe Crosstalk

Measured probe-to-probe crosstalk for the PMVNA is shown in Figure 5-6 to Figure 5-8. This data was collected with GGB 150 μm -pitch dual RF probes (as discussed in Section 4.3), where the probe tips were suspended in air approximately 10 cm above a ground plane. Figure 5-6 shows the measured and simulated differential and common-mode crosstalk as a function of probe separation at 1.0 GHz. Figure 5-7 shows the same at 10.0 GHz. Figure 5-8 shows the measured differential crosstalk versus frequency for several probe separations.

From these figures, one can see that the measured crosstalk, regardless of mode, is generally higher than that of the simulated structures. The source of the difference is most likely due to the structural differences between the simulated structures and the actual probes. Despite the differences in the absolute level of crosstalk, the measured data shows similar trends versus probe separation. The measured data shows a 30 dB difference between the differential and common-mode crosstalk at 1.0 GHz and 1500 μm separation,

and 22 dB at 10.0 GHz (compared to simulated 40 dB and 30 dB, respectively). This difference in the crosstalk of the modes clearly indicates a higher dynamic range for the differential-mode in the PMVNA.

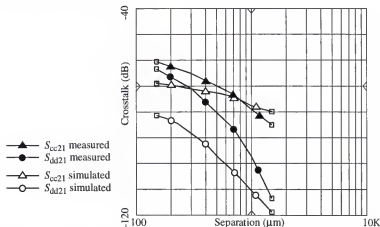


Figure 5-6. Measured probe crosstalk vs. separation distance at 1.0 GHz.

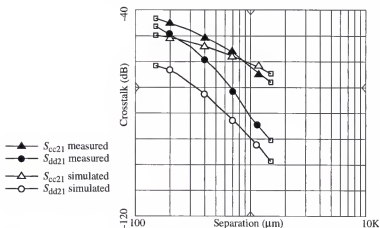


Figure 5-7. Measured probe crosstalk vs. separation distance at 10 GHz.

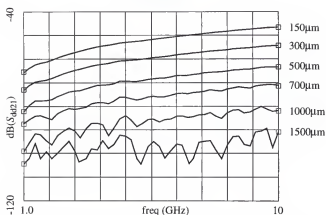


Figure 5-8. Measured differential probe crosstalk vs. frequency for several probe separations.

5.2. Uncertainty Calculations

A generally accepted quantification of error in VNA measurements is the maximum uncertainties in the magnitude and phase of a set of s-parameters [43]. This section seeks to quantify the error in a mixed-mode measurement, and compare that to the error in a standard four-port measurement.

All measurements have errors, and these (unknown) errors add uncertainty to the measurements. This uncertainty limits how accurately a DUT can be measured. VNA errors can be separated into raw and residual errors. Both types of errors can be further sorted into systematic (repeatable) and non-systematic (non-repeatable) errors. For a complete description of VNA errors, see Chapter 6. Residual errors are the errors that remain after calibration. During calibration, standards with known characteristics are

measured by the VNA, and the systematic errors of the VNA are quantified. Any measurement of a DUT can be corrected by mathematically removing the effects of the systematic errors (PMVNA calibration and error correction are examined in detail in Chapter 6). However, this correction process is not completely accurate. Limitations on how accurately the standards are known and non-systematic errors (in calibration and DUT data) cause the correction to be imperfect.

Measurement accuracy is specified as a certain level of maximum possible magnitude and phase error for a given DUT measurement, which is called maximum measurement uncertainty. The numerical values for these specifications arise from the combination of three elements: (1) detailed mechanical tolerances of the calibration standards (from the manufacturer of the standards) which lead to uncertainties in the standards electrical response, (2) raw instrumentation measurement errors, and (3) the precise VNA calibration process used [41]. All of these elements contribute to the actual measurement error.

To make the accuracy specifications independent from the DUT, the sources of error, from the three areas listed, are stated as a set of equivalent residual errors. These residual errors are based on an assumed error model. Since the actual error, produced by the three factors above, cannot be directly known, the residual error terms are expressed as maximum magnitudes. It is assumed that these residual errors can combine in a way to produce the maximum error in the corrected DUT s -parameters.

To ensure that a VNA is producing measurements within the accuracy limits set by the residual error terms, a verification process is typically employed [41]. This process involves measuring a set of verification standards (different than those used in calibra-

tion), and comparing the corrected s -parameters to NIST traceable measurements of the same verification standards (previously generated through a meteorology lab). These traceable measurement also have an associated maximum uncertainty, which has been calculated from the same three factors listed above (these uncertainties are typically smaller than those of a typical VNA due to extreme tolerances used in developing meteorology standards) [41]. The difference between the measured s -parameters and the traceable s -parameters represents the total measurement uncertainty. The effects of the uncertainty in the traceable data can be removed from the measurement data (in a worst-case fashion), leaving the VNA measurement uncertainty. From the established residual errors, an allowable maximum measurement uncertainty can be calculated for each of the verification standards, and the VNA measurement uncertainty must be less than this value to be considered to be operating within specifications [43].

For s -parameter measurements, uncertainty is usually expressed as a maximum magnitude uncertainty and a maximum phase uncertainty for each parameter. Maximum uncertainty is calculated by finding the phases for all residual errors that cause the maximum error in the corrected data, either in magnitude or phase. Furthermore, the uncertainties of a measurement are highly dependent on the actual s -parameters of the DUT. Because of this, maximum uncertainties are given with respect to a particular s -parameter value or specific DUT.

This study of uncertainty focuses on gaining a reasonable estimation of the maximum uncertainty of the PMVNA while measuring a differential device. The necessity of the estimation results from the lack of well established residual errors for the PMVNA, and the lack of appropriate mixed-mode verification standards through which measure-

ment uncertainties can be found. Another goal of this study is to estimate the maximum uncertainty of a FPNVA while measuring the same differential device. In particular, it is important to quantize the maximum uncertainty of transforming four-port s -parameters with uncertainty into mixed-mode s -parameters.

The calculation of maximum uncertainty is based upon a residual error model. The error model used for calculation of uncertainty of the FPNVA is shown in Figure 5-9. The figure shows the equivalent (composite) representation of several errors. The development of this model required several assumptions, but it is extended directly from accepted two-port residual error models. The basic assumptions of the model are discussed below, but a detail description is available in Section 5.2.2.

The basic assumptions used in the FPNVA are: (1) perfect port-to-port isolation. This is done primarily to simplify calculations. The effects of probe-to-probe crosstalk may limit accuracy of some parameters, but is considered in the earlier sections. (2) No drift errors are included, to simplify calculations. This error typically has only a minor effect. (3) No cable variation errors are considered, to simplify calculations. This error typically has only a minor effect. (4) No connector repeatability errors are considered, to simplify calculations. Again, this error typically has only a minor effect. (5) Forward and reverse error quantities are considered to be equal. This is done to simplify calculations, and from typical two-port residual errors, this is a good approximation. (6) Any source or load variations due to switching are geometrically averaged. Again, this is done to simplify calculations. This allows the development of a single error model instead of four, while allowing reasonable estimation of the effects of switching errors. (7) All residual error values are based on typical 8510C residual errors, TOSL sliding load calibration,

with 1024 averages [43] (see Table 5-1). The residual error model of the PMVNA is shown in Figure 5-10. It is essentially identical to that of the FPVNA.

The values of the maximum uncertainties have been found using a process of numerical calculation of many random trials, where all variables are considered to have a uniform probability distribution (this approach is generally called Monte-Carlo analysis). This analysis has been done with a *Mathematica* program. Since the error in any one s -parameter is in general a function of all DUT s -parameters and all error parameters, the direct solution of the worst-case error is extremely difficult without simplifying assumptions. The numerical technique allows the estimation of the worst-case errors without making any further simplifying assumptions. The following steps are taken in the monte-carlo calculation: (1) a set of actual DUT s -parameters are presumed. (2) The phase angles of the error terms are randomly set with a uniform distribution over 0° to 360° , and (3) the resulting “measured” s -parameters are calculated by an embedding process (the inverse function of error correction). (4) The error between the magnitudes of the actual and “measured” s -parameters are calculated, likewise for errors in phases. (5) Many random trials are run, and the maximum errors in magnitudes and phases are collected for each parameter.

Numerical calculations are based on the s -parameters of an example differential RF amplifier as the DUT. The s -parameters, given in (5-1), are the 1.0 GHz mixed-mode s -parameters of an RF pre-amp. The values of the error terms used in the calculation are given in Table 5-1. For this study, the number of random trials is one million.

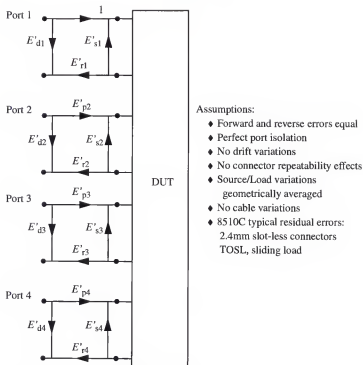


Figure 5-9. Equivalent four-port uncertainty model.

Table 5-1. Typical 8510C residual error magnitudes.

<i>Freq</i> (GHz)	E_d (dB)	E_r (\pm dB)	E_s (dB)	E_p (\pm dB)	E_{nl} (\pm dB)	A_b (\pm dB)	E_{ref} (dB)
.045-2	-41.90	0.00796	-41.90	0.00796	0.0009	0.0010	-99.3

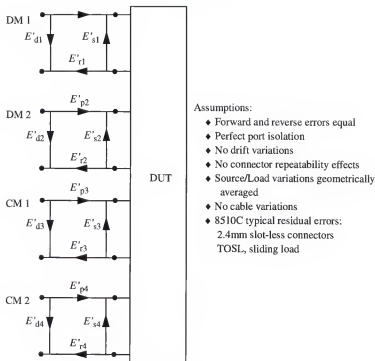


Figure 5-10. Equivalent mixed-mode uncertainty model.

$$|S_{DUT}^{mm}| = \begin{bmatrix} |S_{dd}| & |S_{dc}| \\ |S_{cd}| & |S_{cc}| \end{bmatrix} = \begin{bmatrix} 0.329 & 0.0007 & 0.0080 & 0.0019 \\ 1.24 & 0.973 & 0.0140 & 0.0190 \\ 0.0132 & 0.0013 & 0.286 & 0.0165 \\ 0.0351 & 0.0183 & 1.02 & 0.962 \end{bmatrix} \quad (5-1)$$

Calculations of maximum magnitude and phase uncertainties of the PMVNA and the FPNVA are presented below. In the following expressions, the superscript “mm” indicates the parameters are in mixed-mode format; the superscript “std” indicates standard

s-parameters. The vertical bars indicate the values are magnitude terms, and the angle sign, \angle , represents the phase of the parameter. The symbol Δ_{\max} indicates the maximum calculated error in magnitude or phase as appropriate. As the number of random trials increase, the maximum calculated error will approach the maximum uncertainty. For this work, it is assumed that the number of trials is sufficient so that the maximum calculated error is approximately equal to the maximum uncertainty, so the terms will be used interchangeably. The maximum magnitude uncertainty in the mixed-mode s-parameters of the amplifier, as measured by the PMVNA, are given in (5-2).

$$\Delta_{\max} |S_{\text{DUT}}^{\text{mm}}| = \begin{bmatrix} 9.35 \times 10^{-3} & 9.24 \times 10^{-6} & 7.23 \times 10^{-5} & 2.52 \times 10^{-5} \\ 1.47 \times 10^{-2} & 1.79 \times 10^{-2} & 4.06 \times 10^{-4} & 3.58 \times 10^{-4} \\ 1.00 \times 10^{-4} & 1.84 \times 10^{-5} & 9.45 \times 10^{-3} & 2.04 \times 10^{-4} \\ 7.05 \times 10^{-4} & 3.38 \times 10^{-4} & 1.25 \times 10^{-2} & 1.78 \times 10^{-2} \end{bmatrix} \quad (5-2)$$

It can be seen that the uncertainties are roughly proportional to the magnitude of the corresponding s-parameter. In all cases, the maximum uncertainties are more than one order of magnitude smaller than the magnitude of the parameter, illustrating good overall accuracy. This result is analogous to the behavior of two-port uncertainties.

The values of maximum magnitude uncertainty of mixed-mode s-parameters transformed from the FPVNA s-parameters is given in (5-3). This calculation has been accomplished during the monte-carlo calculation by first transforming the “measured” four-port s-parameters of each random trial into mixed-mode s-parameters, and then accumulating the maximum errors with respect to the actual DUT mixed-mode s-parameters. This order of calculation is indicated by explicitly showing the transformation (MSM^T)

before the uncertainty operator. An alternate order of calculation is discussed in Section 5.2.3 at the end of this chapter.

$$\Delta_{\max} |MS_{\text{DUT}}^{\text{std}} M^{-1}| = \begin{bmatrix} 9.38 \times 10^{-3} & 2.13 \times 10^{-5} & \mathbf{9.24 \times 10^{-3}} & \mathbf{7.82 \times 10^{-5}} \\ 1.51 \times 10^{-2} & 1.76 \times 10^{-2} & \mathbf{1.23 \times 10^{-2}} & \mathbf{1.71 \times 10^{-2}} \\ \mathbf{9.30 \times 10^{-3}} & \mathbf{1.48 \times 10^{-4}} & 9.15 \times 10^{-3} & 1.96 \times 10^{-4} \\ \mathbf{1.40 \times 10^{-2}} & \mathbf{1.69 \times 10^{-2}} & 1.19 \times 10^{-2} & 1.71 \times 10^{-2} \end{bmatrix} \quad (5-3)$$

In general, the uncertainties of the transformed four-port s-parameters are greater than those measured directly by the PMVNA. In the highlighted mode conversions terms (S_{dc} and S_{cd}) the uncertainties have increased significantly over those of the PMVNA, so that the uncertainties are approximately the same magnitude as the corresponding s-parameter. In these mode-conversions terms, the overall error is dominated by the largest error in the standard s-parameter terms. Consider the conversion parameter s_{cd21}

$$s_{cd21} = \frac{1}{2}(s_{31} - s_{32} + s_{41} - s_{42}) \quad (5-4)$$

In a typical differential device

$$|s_{31}| \gg |s_{32}| \quad |s_{41}| \gg |s_{42}| \quad |s_{31}| \approx |s_{41}| \quad (5-5)$$

so that the uncertainty in the transformed parameter is approximately

$$\Delta_{\max} |MS_{\text{DUT}}^{\text{std}} M^{-1}|_{cd21} \approx \Delta_{\max} |s_{31}| \approx |s_{31}| \quad (5-6)$$

With similar approximations, the differential gain of a device is

$$|s_{dd21}| = \frac{1}{2}|s_{31} - s_{32} - s_{41} + s_{42}| \approx |s_{31}| \quad (5-7)$$

$$\Delta_{\max} |MS_{\text{DUT}}^{\text{std}} M^{-1}|_{dd21} \approx \Delta_{\max} |s_{31}| \approx |s_{31}| \quad (5-8)$$

Therefore, the errors in the mode-conversion parameter will be in proportion to the gain of the device, rather than in proportion to the magnitude of the actual mode-conversion.

The maximum phase uncertainties of the mixed-mode s-parameters of the differential amplifier can also be calculated. The phase uncertainty of the directly measured mixed-mode parameters is shown in (5-9), and that of the transformed four-port data is given in (5-10), both in degrees.

$$\Delta_{\max} \angle S_{\text{DUT}}^{\text{mm}} = \begin{bmatrix} 1.63 & 0.756 & 0.516 & 0.755 \\ 0.679 & 1.05 & 1.67 & 1.08 \\ 0.433 & 0.816 & 1.89 & 0.707 \\ 1.15 & 1.06 & 0.705 & 1.06 \end{bmatrix} \quad (5-9)$$

$$\Delta_{\max} \angle (MS_{\text{DUT}}^{\text{std}} M^{-1}) = \begin{bmatrix} 1.63 & 1.75 & 180 & 2.34 \\ 0.696 & 1.04 & 61.7 & 63.8 \\ 44.6 & 6.59 & 1.83 & 0.680 \\ 23.5 & 67.2 & 0.672 & 1.02 \end{bmatrix} \quad (5-10)$$

The phase errors are of similar size, except in the mode-conversion parameters. The large phase errors in the conversion parameters of the transformed four-port data is directly related to the large magnitude errors in the same parameters.

5.2.1. Discussion of Accuracies

This study of uncertainties has demonstrated that the PMVNA has a higher accuracy than the FVPNA when measuring a differential device. When a differential device is measured by a PMVNA, the pure-mode parameters (S_{dd} and S_{cc}) have about one-half of the magnitude error of the corresponding parameters of transformed four-port s-parameters measured by a FVPNA. The mode-conversion parameters (S_{dc} and S_{cd}) as measured by a PMVNA can have substantially lower error than those measured by a FVPNA.

A practical example of where such errors can be important is in the calculation of the common-mode rejection of a radio receiver. In a differential-in-differential-out amplifier, the common-mode rejection ratio is essentially the mode-conversion parameters. In a case of a strong common-mode signal, errors in the mode-conversion parameters can lead to errors in the calculation of the amount of spurious differential response of the amplifier. Consider a 0 dBm common-mode signal at the input of the amplifier in (5-1). Assuming 50 Ω terminations for ease, the actual differential signal at the output of the amp is $20\text{Log}(s_{dc21}) = -37.1$ dBm. The signal level predicted by the PMVNA measurements would be, at worst, -36.2 dBm. In contrast, the signal predicted by the FPVNA could be between -31.6 dBm and -55.4 dBm.

The mode-conversion parameters represent important behavior in the analysis and design of differential circuits. A fundamental advantage of differential circuits is increased noise immunity when compared to single-ended circuits. Here, noise immunity means the rejection of common-mode signals of all type. Typical examples of such common-mode noise include interfering signals, known as electromagnetic interference (EMI), from clocks, VCOs, etc. Also, even-order distortion products are rejected in an ideal differential circuit. The ability of a real circuit to achieve the rejection of these signals is directly linked to the degree of balance in the differential circuit. The mode-conversion parameters are direct measurements of the degree of imbalance in a differential circuit. Thus, errors in the measured mode-conversion limit the ability to analyze and ultimately realize the advantages of differential topologies.

5.2.2. Uncertainty Model Derivation

The uncertainty error models of Figure 5-9 and Figure 5-10 are developed by extending the basic concepts of the well established two-port uncertainty model. The two-port model is typically developed in terms of separate forward and reverse models. These models are shown, in simplified form, in Figure 5-11, neglecting drift, cables, and connectors. The four-port models have simply applied two different two-port models. The major differences are two fold. First, the forward and reverse models have been combined into a single effective error model. Second, the two different two-port error models that compose the four-port model can not be considered to be independent. In other words, the increase in the number of ports requires additional error terms so that each port has a relative error path with respect to all other ports. In general, with the assumption of perfect port isolation, an n -port VNA will require $n^2 - 1$ error paths and one unity-valued path.

The models in Figure 5-11 show several cascaded blocks, each with multiple error terms. These blocks are reduced to a single block representing the composite error paths containing the appropriate error terms. For simpler calculation, the composite error block is represented in terms of chaining scattering parameters, known as t -parameters (see Appendix H). The error block, T_E , is partitioned into four-by-four sub-matrices

$$T_E = \begin{bmatrix} T_{E11} & T_{E12} \\ T_{E21} & T_{E22} \end{bmatrix} \quad (5-11)$$

The "measured" s -parameters, including errors, can be calculated by

$$S_m = (T_{E11}S_a + T_{E12})(T_{E21}S_a + T_{E22})^{-1} \quad (5-12)$$

where S_a is that actual s -parameter matrix of the DUT. For a complete discussion of the concepts leading to this equation, see Section 6.2.

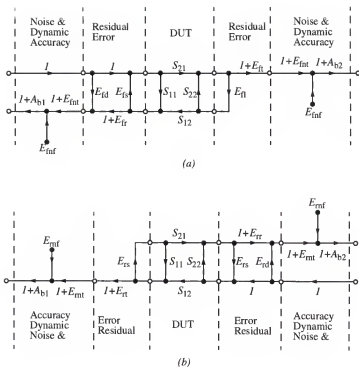


Figure 5-11. Two-port uncertainty model.

a) Forward uncertainty model. b) Reverse uncertainty model.

The above development is applicable to both standard and mixed-mode s-parameters. The uncertainty models of the PMVNA and FPNVA are essentially the same, but the corresponding s-parameter expressions are slightly different, due to their respective definitions. However, it can be shown (see Appendix I), that under the condition of the no-leakage

model (i. e. perfect isolation) the appropriate conversions of the two different s-parameter matrices results in identical t-parameter expressions, that is

$$T_E^{mm} \Big|_{\text{no-leakage}} = T_E^{\text{std}} \Big|_{\text{no-leakage}} \quad (5-13)$$

As a result, the remaining development applies equally to the FPNVA and the PMVNA uncertainty models.

The partitions of the T-matrix can now be related to the residual error terms in Figure 5-11. For perfect port isolation, the partitions, T_{Eij} , are diagonal matrices, and have the form

$$\begin{aligned} T_{E11} &= \text{Diag}(X_{1i}) \\ T_{E12} &= \text{Diag}(X_{2i}) \\ T_{E21} &= \text{Diag}(X_{3i}) \\ T_{E22} &= \text{Diag}(X_{4i}) \end{aligned} \quad i \in \{1, 2, 3, 4\} \quad (5-14)$$

where the subscript i indicates a term associated with a particular measurement port, and X_{ji} are intermediate variables. These terms are related to the error terms by

$$\begin{aligned} X_{1i} &= E_{ri} - \frac{E_{di}E_{si}}{E_{pi}} & X_{2i} &= \frac{E_{di}}{E_{pi}} \\ X_{3i} &= \frac{E_{si}}{E_{pi}} & X_{4i} &= \frac{1}{E_{pi}} \end{aligned} \quad (5-15)$$

The primed quantities are further expanded as

$$\begin{aligned} E_{ri} &= (1 + E_r)D_d & E_{si} &= E_s \\ E_{di} &= E_dD_d & E_{pi} &= 1 + E_p \end{aligned} \quad (5-16)$$

The ports are assumed to have the same residual error magnitudes, so the error terms are identical for all ports i . The noise and dynamic range errors, D_d , are expanded as

$$D_d = (1 + E_{nt} + E_{nf})(1 + A_b) \quad (5-17)$$

As stated earlier the effects switching between ports have been estimated to provide a single error model for the entire VNA. The estimation is accomplished by geometrically averaging the quantities that change as the port switches change. Since the FPNVA and PMVNA uncertainty models are derived from two-port VNA models, the switching estimation is done with respect to the two-port model of Figure 5-11. For example, the source impedance error of the FPNVA is assumed to be equal for all ports and constant, regardless of which port is being stimulated. The value of this error is estimated as the geometric mean of the source match error and the load match error of a two-port VNA. This same estimation is used for response/tracking errors and dynamic range errors

$$E_r = \sqrt{E_{fr}E_{ft}} \quad E_s = \sqrt{E_{fs}E_{fl}} \quad A_b = \sqrt{A_{b1}A_{b2}} \quad (5-18)$$

Furthermore, the numerical values used are assumed to be equal in forward and reverse directions

$$E_*|_{\text{forward}} = E_*|_{\text{reverse}} = E_* \quad (5-19)$$

where * represents any error term designator (e. g. d , s , r).

As discussed earlier in this section, additional error terms are required to describe the relative error between ports of the FPNVA and PMVNA. In absence of actual four-port residual errors, it is assumed that the port-to-port error will be similar in magnitude to the average response error

$$E_p = E_r \quad (5-20)$$

The error matrix, T_E , has fifteen non-unity composite error terms. However, it contains thirty-one independent error variables (E_r , E_d , etc.). To reduce the number of

independent variables, the composite error terms in T_E are considered as the variables for the monte carlo analysis. The maximum magnitudes of the composite error terms must be used since the individual error terms are independent, and they are found to be

$$\begin{aligned} |X_{1i}| &\leq (1 + |E_r|)|D_{\max}| + \frac{|E_d||E_s||D_{\max}|}{1 - |E_p|} \\ |X_{2i}| &\leq \frac{|E_d||D_{\max}|}{1 - |E_p|} \quad |X_{3i}| \leq \frac{|E_s|}{1 - |E_p|} \\ |X_{4i}| &\leq \frac{1}{1 - |E_p|} \quad (X_{41} = 1) \end{aligned} \quad (5-21)$$

with

$$|D_{\max}| = (1 + |E_{nt}| + |E_{nt}|)(1 + |A_b|) \quad (5-22)$$

The fact that the error terms are magnitudes only is emphasized by explicitly showing magnitude bars on all error terms.

The random variables of the composite error terms are constructed from the magnitudes of (5-21) where the phase of the error is the randomly varied quantity.

$$\begin{aligned} \tilde{X}_{1i} &= 1 + (|X_{1i}| - 1)e^{j\tilde{\Phi}_{1i}} & \tilde{X}_{2i} &= |X_{2i}|e^{j\tilde{\Phi}_{2i}} & \tilde{X}_{3i} &= |X_{3i}|e^{j\tilde{\Phi}_{3i}} \\ \tilde{X}_{4i} &= 1 + (|X_{4i}| - 1)e^{j\tilde{\Phi}_{4i}} & (\tilde{X}_{41} &= 1) \end{aligned} \quad (5-23)$$

where \tilde{X} indicated a random variable.

From the composite error terms in (5-23), the maximum uncertainties can be calculated. Each trial of the monte-carlo calculation set the random phases and the error matrix, T_E , is calculated by (5-14). From this, the "measured" s-parameters are calculated from (5-12), and the magnitude errors are found by

$$\Delta|S_a| = |S_m| - |S_a| \quad (5-24)$$

and the phase error can be calculated by [43]

$$\Delta\angle S_a = \sin^{-1}\left(\frac{\Delta|S_a|}{|S_a|}\right) \quad (5-25)$$

5.2.3. Order of Uncertainty Calculations

The order of calculation has been carefully considered, as there is an alternative approach. The maximum errors could first be accumulated in the four-port s-parameters, and then the maximum errors of each mixed-mode parameter could then be calculated. This last method requires that the uncertainties of the appropriate standard s-parameter be combined in a way to maximize the resulting mixed-mode uncertainty. This approach, although simpler to calculate, is not used as the primary method of calculation because it contains two levels of error maximization, and might unnecessarily inflate the uncertainties of the transformed s-parameters. In practice, the method of calculation makes little difference, as seen in (5-26).

$$\Delta_{\max} \left| M \left[\Delta_{\max} |S_{\text{DUT}}^{\text{std}}| \right] M^{-1} \right| = \quad (5-26)$$

$$\begin{bmatrix} 1.03 \times 10^{-2} & 2.38 \times 10^{-4} & 1.03 \times 10^{-2} & 2.38 \times 10^{-4} \\ 1.75 \times 10^{-2} & 2.01 \times 10^{-2} & 1.75 \times 10^{-2} & 2.01 \times 10^{-2} \\ 1.03 \times 10^{-2} & 2.38 \times 10^{-4} & 1.03 \times 10^{-2} & 2.38 \times 10^{-4} \\ 1.75 \times 10^{-2} & 2.01 \times 10^{-2} & 1.75 \times 10^{-2} & 2.01 \times 10^{-2} \end{bmatrix}$$

The similarity in the uncertainties of (5-6) and (5-26) indicates that the transform provides no advantage in reducing uncertainties. A particular random trial may produce correlated errors in the four-port s-parameters, and these correlations may reduce errors in

the transformed s -parameters. However, another random trial exists that, when the resulting four-port s -parameters are transformed, again produces an error that is as large as approach indicated in (5-26).

5.3. Conclusions on Accuracy

This study of uncertainties has demonstrated that the PMVNA has a higher accuracy than the FPVNA when measuring a differential device. The PMVNA has the advantage of the natural noise suppression of differential circuits. This results in greatly enhanced dynamic range in differential measurement with respect to traditional VNA measurements. Consideration of residual error in an practical VNA system has shown that, when measuring a differential device, the pure-mode parameters from the PMVNA have about one-half of the magnitude error of the corresponding parameters of transformed four-port s -parameters measured by a FPVNA. Most importantly, the mode-conversion parameters as measured by a PMVNA can have substantially lower error than those measured by a FPVNA. These findings indicate that the PMVNA has a clear accuracy advantage in the measurement of differential devices.

With the advantages of the PMVNA clear, the calibration and error correction of the PMVNA is next required for the measurement of RF differential circuits. The accuracy conclusions of this chapter are based, in part, on a assumed level of calibration accuracy. Care must be taken to ensure the completeness of the PMVNA calibration to ensure the accuracy advantages are maintained.

CHAPTER 6 CALIBRATION OF THE PURE-MODE VECTOR NETWORK ANALYZER

6.1. Types of VNA Measurement Errors

All VNA measurements have errors which can be grouped into several major categories. The most common groupings are: linear systematic errors, linear non-systematic (non-repeatable) errors, non-linear errors, source frequency errors. A further source of error, which is important, but not relevant to this discussion, is human operator error. Some of these errors are further sub-divided, such as non-systematic errors divided into random and drift errors. A representation of the classes of errors is shown in Figure 6-1.

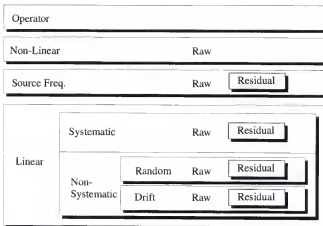


Figure 6-1. Types of VNA measurement errors.

Some errors will not be considered here. In particular, non-linear errors, and source frequency errors will not be treated. Non-linear errors include errors such as non-linear performance in the analog-to-digital converters in the VNA [41] and undesired non-linear behavior in down-mixers. Source frequency errors include absolute and relative (drift) errors in the frequency of the RF signal generated in the VNA source. Both of these types of errors can have serious impact on measurement accuracy. However, these errors are essentially set by the test equipment architecture, and are generally not improvable by the equipment user. For this reason, these errors will be assumed as residual, uncorrectable errors, and not treated in the calibration process.

Systematic errors include all static (repeatable) errors, and non-systematic errors include noise, drift, and other time variant errors. Theoretically, the effects of all static linear systematic errors can be mathematically removed if the errors are known. This process, called calibration, involves measuring certain well known devices, called standards, with the non-ideal VNA. These measurements, in combination with the known responses of the standards, can be used to solve for all systematic errors. After calibration, the systematic VNA errors can be removed from the measurements of any unknown device; this is called error correction.

The calibration of the PMVNA is separated into two major divisions: the primary calibration and the phase offset pre-calibration. The primary calibration characterizes linear systematic errors, as described above. This is done in with the traditional method of measuring a set of well known standards. The phase offset pre-calibration is the process by which the phase relationship between the VCOs of the two test-sets is characterized. This process is much different than the primary calibration in that very little needs to be

known about the standards associated with the pre-calibration. After a full description of these calibration steps, the step-by-step calibration process implemented for this work will be detailed. This final section of this chapter will explain the mechanics by which all of the previous theoretical development of the chapter is used to make a practical, accurate calibration of the PMVNA.

6.2. Primary PMVNA Calibration

6.2.1. Raw Performance

The raw performance of any VNA is important as it will effect the ultimate calibrated measurement accuracy. As an indication of the raw accuracy, the measured raw data of two devices are presented. The first presented device is the match, where matched 50Ω terminations are placed on all ports. The second device is a pair of through connections. Together, these devices give an indication of the raw dynamic range of the PMVNA. For instance, the ratio of the raw transmission of the through connection to the residual transmission of the match gives a measure of the raw dynamic range of that particular parameter. Other measures of raw performance might be proposed, such as non-matched impedance levels, but it is felt that no other definition has a particular advantage.

Furthermore, the raw dynamic range does not indicated directly the dynamic range of the corrected VNA. The corrected dynamic range of the VNA will typically be significantly greater than the raw dynamic range. The exact level of enhancement by calibration depends on the accuracy of the calibration, the stability of the VNA, and other conditions. However, the raw performance of the VNA will ultimately influence the corrected accuracy of the VNA.

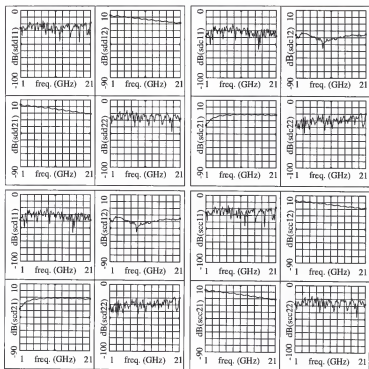


Figure 6-2. Raw measured mixed-mode s-parameters of a pair of through connections (coaxial) between ports one and three, and ports two and four. Note that scales of the parameters are different.

The uncorrected through connection data are shown in Figure 6-2. The through is accomplished by connecting the mixed-mode ports together with coaxial cables. (Specifically, ports one and three are connected together, and ports two and four are connected, where the port numbers are indicated in Figure 3-1) The figure shows $|S_{21}|$ and $|S_{11}|$ in dB for differential-to-differential (dd), common-mode-to-differential (dc), differential-to-

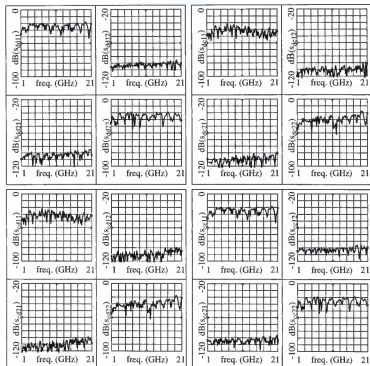


Figure 6-3. Raw measured mixed-mode s-parameters of matched loads (coaxial) at all ports. Note that scales of the parameters are different.

common-mode (cd) and common-mode-to-common-mode (cc) responses. The raw data shows a return loss of about 20 dB from 1 GHz to 21 GHz for the dd and cc responses, which is commensurate with the raw performance of a standard 8510 VNA. The raw dd and cc transmission show typical 8510 performance. The cd and dc transmission is less than -20 dB, which indicates a reasonably low level of imbalance in the raw system. The uncorrected mixed-mode s-parameters of measured matched loads is shown in Figure 6-3.

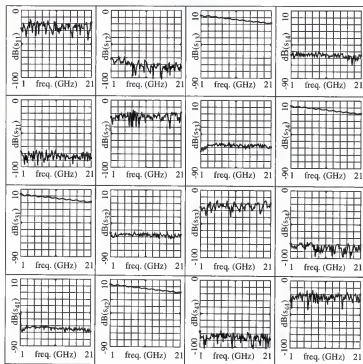


Figure 6-4. Raw measured four-port s-parameters of a pair of through connections (coaxial) between ports one and three, and ports two and four. Note that scales of the parameters are different.

Examination of the transmission parameters gives an indication of the port-to-port leakage. The measured leakage (whether due to actual leakage or to the noise floor of the instrument) can be considered to be the practical limit for the dynamic range of the PMVNA. Most of the transmission parameters have approximately -110 dB dynamic range. This range can be extended through use of measurement averaging, which reduces the effects of random noise. These measurements were made with 1024 averages. For ref-

erence, the raw four-port s-parameter data of the throughs and matches are shown in Figure 6-4 and Figure 6-5, respectively. These show that the transformed four-port data also have good dynamic range. These and other raw measurements indicate good raw system performance, which should result in good calibrated performance.

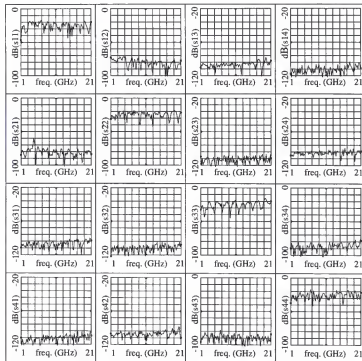


Figure 6-5. Raw measured four-port s-parameters of matched loads (coaxial) at all ports. Note that scales of the parameters are different.

6.2.2. PMVNA Error Model

The calibration and correction of linear systematic errors must be pursued only in the context of an assumed error model. The error model dictates the which errors of a VNA will be admitted to consideration and correction. For many years, the generally accepted approach to a VNA error model has been to propose an equivalent error model. In such a model, the total effect of all linear systematic errors (there may be many hundreds of sources of error in a VNA) is combined into a simpler set of equivalent error terms [42]. This equivalent error model may have only a few error terms, but, if properly constructed, it exactly reproduces the errors in the VNA. An analogy exists between this equivalent error model and a Thévenin's equivalent network. Just as a simple two parameter Thévenin's equivalent exists for a linear circuit [22], regardless of its complexity, so does a simple equivalent error model exists for a complex VNA system with many sources of linear errors. A more direct argument can be drawn from signal flow graph reduction techniques, where the flow graph of the entire VNA, with all errors included, can be reduced to a small set of equivalent signal paths [23].

A large body of work has been published in the literature over the past thirty years in the area of VNA calibration. The error models proposed have tended to become more general, but the question of the number of appropriate error terms and the number and types of calibration standards has been the subject of considerable debate. The de facto standard in VNA calibration for the past fifteen years is the so-called twelve-term error model for the two-port VNA. The reason for its prominence is primarily due to its use in the HP8510 VNA. This error model [43], shown for reference in Figure 6-6, is actually two independent half error models, one for forward operation of the test set, the other for

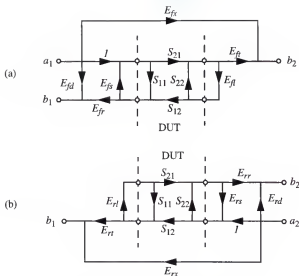


Figure 6-6. Twelve-term two-port VNA error model.
a) Forward error model. b) Reverse error model.

reverse. This error model is typically evaluated through a calibration procedure known as Through-Open-Short-Load (TOSL)¹. It can also be adapted to more sophisticated calibration techniques [44] such as Through-Line-Reflect (TRL) [45] and Line-Reflect-Match (LRM) [46]. Although not considered optimal due to the requirement of four standards, the twelve-term error model is well adapted to treating test-set switching errors, since each half model applied to only one port selection switch position (see Section 6.2.4 for more details on switching errors). One limitation of the twelve-term error model is its treatment of port-to-port crosstalk. The error model assumes that only two error terms, E_{fx} and E_{rx} ,

1. Or by some other permutation of the standard names, such as SOLT.

are required to characterize crosstalk under all test conditions. This assumption has been shown to be inaccurate under certain conditions [47], and must be recognized as a limitation of this error model.

The calibration and correction of the PMVNA begins by adopting an error model that departs from the traditional twelve-terms model. Due to its unique architecture, the PMVNA required a very general error model for accurate calibration development. The model used is the generalized error model for an n -port network analyzer, including all port-to-port leakage errors, which has been introduced by Speciale [48]. The error model, shown in Figure 6-7, employs a single error network with $2n$ ports, and the error network is an equivalent representation of all linear systematic errors. The error network is expressed with chaining scattering parameters, called t -parameters. These t -parameters are mathematically related to s -parameters, and they have the property where the resulting t -parameters of a series of cascaded networks is equal to the matrix product of the t -parameters of the individual networks [23] (similar to ABCD-parameters). The t -param-

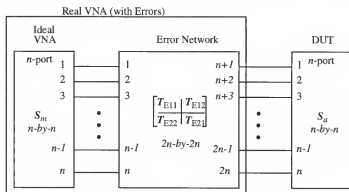


Figure 6-7. Generalized error model for the n -port VNA.

eters are typically defined only for two-port networks, so a definition of a $2n$ -port t-matrix is found in Appendix H.

All linear systematic errors in the PMVNA can be represented with this generalized error model, where n is equal to four. In the case of the PMVNA, the error network is a mixed-mode representation, as defined in Figure 3-1. A similarity transform relates the error matrices of the two-port PMVNA and the standard four-port VNA (see Appendix I), thus the applicability of the error model of Figure 6-7 is assured. Due to this transformation, the calibration theory of the PMVNA parallels that of a standard four-port VNA.

Each signal path in the error network represents an unknown error term. The error model of Figure 6-7 includes all possible error terms, including all port-to-port leakage paths. For a n -port VNA, there are $4n(n-1)$ leakage terms out of a total of $(2n)^2$ error terms. It is important to address the PMVNA calibration problem in the most general

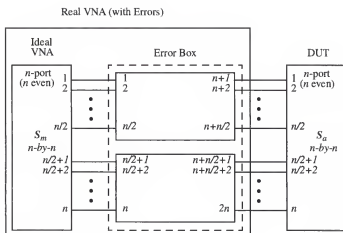


Figure 6-8. Half-leakage error model for general VNA.

terms, but there are some simplifications of the error model that are also of interest where some of the leakage paths are neglected.

One useful simplification splits the measurement ports into two groups, and neglects all error terms connecting the two groups while preserving all error terms of each group, as shown in Figure 6-8. This unique simplification arises because a single mixed-mode port is comprised of two single-ended ports. This simplification particularly applies when the PMVNA is used in wafer-level measurements. Typically, the port-to-port leakage in a wafer-probe system must be neglected, despite the fact the leakage can be significant, since the leakage is a strong function of probe placement and is not a static error. (Attempting to correct for leakage between probes can lead to significant errors in corrected measurements if the relative position of the probes are moved after calibration.) As implemented in Chapter 4, this error model is applicable, as each PMVNA wafer probe

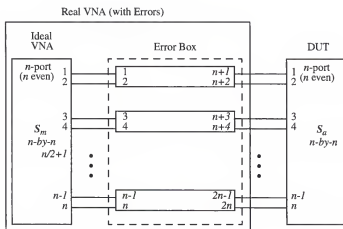


Figure 6-9. Pair-leakage error model for general VNA.

[35] is a static component with two single-ended probes. This error model, which will be called the half-leakage model, is a special case of the full model. With the half-leakage model, there is a total of $2n^2$ error terms (note that n must be even for this model to apply).

Another useful simplification splits the measurement ports into pairs, and neglects all error terms connecting the two groups while preserving all error terms of each pair, as shown in Figure 6-9. This simplification is similar to the half-isolation model, but is more appropriate for mixed-mode measurements with more than two mixed-mode ports. This simplifications similarly applies when the PMVNA is used in wafer-level measurements. This error model, which will be called the pair-leakage model, is a special case of the full model. With the pair-leakage model, there is a total of $8n$ error terms (note that n must again be even for this model to apply). For the two mixed-mode ports of the PMVNA, the pair-leakage and the half-leakage models are identical.

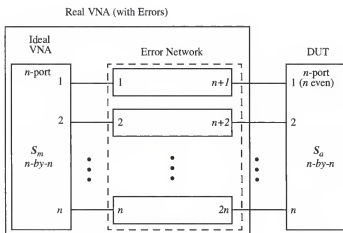


Figure 6-10. No-leakage error model for general VNA.

The second simplification of the error model neglects all leakage between ports. This greatly reduces the number of error terms in the model, leading to a simpler calibration problem. This simplified error model, shown in Figure 6-10, will be called the no-leakage model. The no-leakage model can be applied when the leakage levels in the measurement system are insignificant (compared to the DUT), such as a system using coaxial connector measurement interfaces. Such systems have significantly less crosstalk between ports than wafer probe interfaces. The no-leakage model must also be used if none of the leakage errors are static, such as with independently moving wafer probes. The no-leakage model, also a special case of the full model, leaves a total of $4n$ error terms.

6.2.3. Development of Calibration Equation

The development of the calibration procedure for the PMVNA continues with the development of the fundamental relation that describes the calibration problem. This so called calibration equation describes the relationship between measured s -parameters, actual s -parameters, and error terms. A general formulation of the calibration has been introduced by Speciale [48], and this section will initially follow this published work. The development will start with variable definitions as illustrated in Figure 6-11: S_m are the measured s -parameters (with linear systematic errors), T_E (S_E) are the t -parameters (s -parameters) of the error network, and S_d are the actual (error-less) s -parameters of a DUT. Note that the normalized waves have been expressed as n -dimensional vectors, as

described in Appendix H. As further explained in Appendix H, the matrix equation for T_E may be expanded in terms of the partitions

$$\begin{aligned}\bar{b}_1 &= T_{E11}\bar{a}_2 + T_{E12}\bar{b}_2 \\ \bar{a}_1 &= T_{E21}\bar{a}_2 + T_{E22}\bar{b}_2\end{aligned}\quad (6-1)$$

where T_{Eij} are the four n -by- n partitions of T_E , and a_i and b_i are the n -dimensional a and b -wave vectors, respectively. Similarly, $b_{1a} = S_a a_{1a}$, but from Figure 6-11, it can be seen that $a_{1a} = b_2$ and $b_{1a} = a_2$, so $a_2 = S_a b_2$. By substituting this last expression into (6-1), one finds

$$\bar{b}_1 = (T_{E11}S_a + T_{E12})\bar{b}_2 \quad (6-2)$$

$$\bar{a}_1 = (T_{E21}S_a + T_{E22})\bar{b}_2 \quad (6-3)$$

The last equation can be re-arranged to find

$$\bar{b}_2 = (T_{E21}S_a + T_{E22})^{-1}\bar{a}_1 \quad (6-4)$$

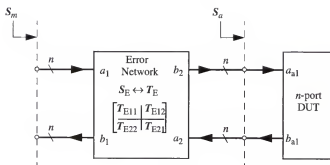


Figure 6-11. Vector equivalent of generalized error model for the n -port VNA.

Combining (6-4) and (6-2)

$$\bar{b}_1 = (T_{E11}S_a + T_{E12})(T_{E21}S_a + T_{E22})^{-1}\bar{a}_1 \quad (6-5)$$

However, it is true that $b_1 = S_m a_1$, so, by observation,

$$S_m = (T_{E11}S_a + T_{E12})(T_{E21}S_a + T_{E22})^{-1} \quad (6-6)$$

By a series of matrix multiplications and inversions, (6-6) can be expressed as

$$T_{E11}S_a + T_{E12} - S_m T_{E21}S_a - S_m T_{E22} = 0 \quad (6-7)$$

This equation is the fundamental relationship, call the calibration equation, on which the PMVNA calibration will be developed.

From the calibration equation, the basic concept of VNA calibrations can be readily observed. By measurement (S_m) of known devices called standards (S_{ax}), the unknown error terms (T_E) can be mathematically found. In general, VNA calibrations require the application of multiple calibration standards. Each standard is measured by the VNA (S_{mi}), and the actual s-parameters of the standards are assumed to be known (S_{axi} for the i -th standard). For each standard, the calibration equation (6-7) applies. In terms of an n -port VNA, the error network is represented by a $2n$ -by- $2n$ unknown network, and each s-parameter matrix is an n -by- n matrix. The matrix equation (6-7) can be expanded, and the resulting scalar equations are linear in the elements of T_E . The set of all scalar equations can then be re-written as

$$A_E \cdot \hat{t}_E = \bar{0} \quad (6-8)$$

where t_E is a column vector comprised of the elements of T_E [46, 47]. Given that m different calibration standards are applied, the coefficient matrix, A_E , has dimensions $(m n^2)$ -by-

$(2n)^2$, and t_E has dimensions $(2n)^2$ -by-1. The mathematical solution of (6-8) now becomes the key step in the PMVNA calibration process.

6.2.4. Switching Errors and Non-Pure Mode Generation

The development of the calibration equation (6-7) is predicated on the assumption that the error model remains static throughout the calibration process and through any subsequent measurements. Referring to Figure 4-4, one can see an RF switch to set the stimulus mode, as well as two HP8517 test sets, where each test set uses an RF switch to set forward or reverse operation [43]. By means of these three switches, the PMVNA has four distinct modes of operation: differential forward, differential reverse, common-mode forward, and common-mode reverse. The changing of the switch positions violates the primary assumption of the error model, however. By changing the switch positions, the error model also changes, and is no longer static. While in a single switch state, the error model is static, so the errors caused by switches are called quasi-static. These quasi-static errors must be effectively removed before the error model from the previous section can be applied to a calibration.

Another issue with the measurement of raw mixed-mode s -parameters with the PMVNA is imperfections in the generation of a pure-mode stimulus. As shown in Figure 4-5, the PMVNA generates the differential and common-mode stimuli from a $0^\circ/180^\circ$ hybrid power splitter. It has been shown that any imbalances in the splitter, together with any phase and magnitude imbalance in the paths of the HP8517 test sets, will generate a spurious mode simultaneously with the desired mode (see Chapter 8). These imbalances can cause spurious modes of significant amplitude. If the mode imperfections are neglected, and the measured response of a device to be attributed to the nominal mode

only, then significant inconsistencies can occur in the raw mixed-mode s-parameters. For accurate calculation of raw mixed-mode s-parameters, any imperfections in the stimulus must be characterized. Additionally, the changes in switch positions cause changes in the amount of imbalance in the stimuli. Again, these switch effects also violate the static requirement of the error model.

The removal of the switching effects and the stimulus imbalance can be achieved through the application of all eight samplers in the PMVNA. This approach is an extension of two-port VNA techniques [44]. The traditional model for the effects of imperfect switches is shown in Figure 6-12 for a two-port VNA. The model assumes that all systematic errors have been represented in the error network, so the directional couplers can be considered to be ideal, or error-free. The switch is typically said to have some non-matched terminating impedance, causing it to be non-ideal. By measuring a_1 , a_2 , b_1 , and b_2 with the four down-mixers of the test-sets at both switch positions, the raw s-parameters can be calculated. Traditionally, this approach of using all four down-mixer measure-

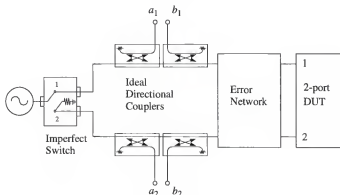


Figure 6-12. Physical model for switching error in a two-port VNA.

ments is only used during certain steps in a TRL or LRM calibration. After the calibration is complete, the TRL/LRM error coefficients are translated to the traditional twelve-port error model [49] of Figure 6-6. With this approach, only three down-mixers are used during DUT measurements (a_1, b_1, b_2 for forward and a_2, b_1, b_2 for reverse).

The PMVNA, as illustrated in Figure 4-3, is equipped with two HP8517A test sets, each having four down-mixers, for a total of eight down-mixers. A generalized model for all switching errors and imbalance errors is shown in Figure 6-13. This model can be used to model any systematic errors that change as a function of switch selection. By using measurements at all samplers for each switch position, the effects of both switching errors and mode imbalance can be removed from the measured s-parameters. Collecting all a and b data into matrices

$$A = \begin{bmatrix} a_1^{DF} & a_1^{DR} & a_1^{CF} & a_1^{CR} \\ a_2^{DF} & a_2^{DR} & a_2^{CF} & a_2^{CR} \\ a_3^{DF} & a_3^{DR} & a_3^{CF} & a_3^{CR} \\ a_4^{DF} & a_4^{DR} & a_4^{CF} & a_4^{CR} \end{bmatrix} \quad B = \begin{bmatrix} b_1^{DF} & b_1^{DR} & b_1^{CF} & b_1^{CR} \\ b_2^{DF} & b_2^{DR} & b_2^{CF} & b_2^{CR} \\ b_3^{DF} & b_3^{DR} & b_3^{CF} & b_3^{CR} \\ b_4^{DF} & b_4^{DR} & b_4^{CF} & b_4^{CR} \end{bmatrix} \quad (6-9)$$

where the superscript indicates differential (D) or common-mode (C) drive and forward (F) or reverse (R) drive, and the subscripts indicate port number (1, 2, 3, 4). Expressed with the vector notation of Appendix H, (6-9) becomes

$$A = \begin{bmatrix} a^{DF} & a^{DR} & a^{CF} & a^{CR} \end{bmatrix} \quad B = \begin{bmatrix} b^{DF} & b^{DR} & b^{CF} & b^{CR} \end{bmatrix} \quad (6-10)$$

With these matrices, the raw s-parameters can be calculated as

$$S_m = BA^{-1} \quad (6-11)$$

Equation (6-11) is the solution to a system of sixteen equations with the sixteen raw s-parameters as unknowns, through which the raw s-parameters of the DUT are separated from the effects of the imperfect switches and imperfect stimulus generation. By applying this approach to every calibration standard measurement, a single static error model can be applied, and the calibration equation (6-7) can be used. Additionally, all subsequent DUT measurements are also made using equations (6-9) and (6-11).

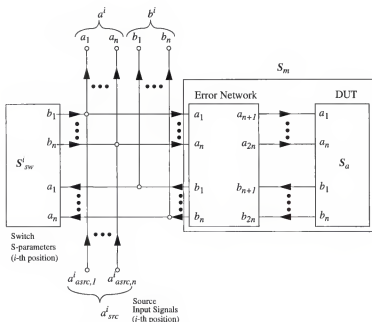


Figure 6-13. General switching error model signal flow graph.

6.2.5. Solution of the Calibration Problem

The construction of the calibration equation (6-8), and its subsequent solution, are the heart of calibration process. The conditions under which a solution to (6-8) can be found will first be presented in terms of a general n -port problem. These conclusions will then be applied to the calibration of the PMVNA.

There has been a variety of statements made in the literature about the minimum number of standards required for a calibration of a VNA. In the original presentation of the general n -port error model, it is said that only three n -port standards are required to solve all error terms, including all leakage terms [48], but is later changed to five [50]. In 1991, the minimum number is stated as four standards required to solve the general error model with (apparently) all leakage paths on a two-port VNA [47]. Many other calibration techniques for VNAs with two, three and four ports have been published in the last decade with a the number of standards use varying from three to ten [51 - 53]. This section attempts to resolve the ambiguity surrounding the number of standards required for a solution to the calibration equation.

For purposes of this examination, a solution is valid for calibration only if it is unique within one arbitrary scalar. That is, if t_S is a valid solution vector of (6-8), then the only other solution vectors that exist are αt_S , where α is any complex scalar. In other words, the Null-space of A_E must be of dimension one [31]. For ease, this type of solution will be called an ordinary solution. Furthermore, this section will consider only the general error model of Figure 6-7, with all leakage paths included, and the three special cases illustrated in Figure 6-8 to Figure 6-10. For an n -port calibration, a single standard will be considered to always have n -ports, regardless of actual construction of the physical stan-

dard. For example, an n -port match standard may be constructed of a group of n independent one-port match loads, but for purposes of discussion the group will be considered as a single standard. Due to the special cases of the error models, calibration standards will be considered to be either a reflection standard or a full standard. A reflection standard is defined as a group of n one-port reflection standards (such as the n -port match example above); a full standard is defined to have transmission between at least two ports. For the general error model, both types of standards are treated the same, but in the case of the half-leakage, pair-leakage or no-leakage models, the reflection standards generate fewer sets of measurement data (hence, fewer equations) than the full standards.

The determination of the number of required standards for calibration is based on consideration of the rank of the coefficient matrix, A_E . For an ordinary solution to (6-8), matrix A_E must have a rank of exactly $(2n)^2 - 1$. Recall that with m standards, A_E has dimensions $(m n^2)$ -by- $(2n)^2$. For the full error model, each standard generates n^2 equations. It has been found that A_E will have rank of exactly $(2n)^2 - 1$ only with five or more n -port standards. This means that $5n^2$ equations are generated for the solution of $4n^2$ error terms, so the system of equations (6-8) is over-determined. (The over-determined nature of the system of equations can be used to reduce the number of known s -parameters of S_{ax} , which can give significant accuracy advantages.) Furthermore, with four standards the matrix A_E is square (same number of equations and error terms), but the rank of A_E is $4n^2 - n$. Similar conclusions can be made about the special cases of half-leakage, pair-leakage and no-leakage models. All conclusions are summarized in Table 6-1.

Table 6-1. Calibration summary.

Error Model Type	Number of Unknowns	Eqns from Stds		Min. Std w/ Square A_E		Min. Stds for Ordinary Solution
		Full	Reflect	No. Std	Rank(A_E)	
Full-leakage	$4n^2$	n^2	n^2	4	$4n^2 - n$	5
Half-leakage (n even)	$2n^2$	n^2	$n^2/2$	2	$2n^2 - n$	3
Pair-leakage (n even)	$8n$	n^2	$2n$	depends on n	depends on n	depends on n
No-leakage	$4n$	n^2	n	depends on n	depends on n	depends on n

Conclusions about the pair-leakage and no-leakage model are not as general, since the minimum number of required standards depends on the number of ports, n . For example, with the no-leakage model, if n is four (as for the PMVNA) at least two full standards are required for rank of $4n - 1 = 15$. This is again over-determined, with one full standard giving a square A_E matrix with rank of fourteen. In contrast, if n equals two, at least three standards are required (for example: LRM [46] and TRL [45]).

These properties have been found through the use of numerical simulations. The simulations have been performed with a program written in *Mathematica* [54]. The program allows generation of a coefficient matrix, A_E , based on postulated error terms and calibration standards, for any number of ports, standards, and leakage model. With randomly generated error terms and calibration standards (for $n=2, 3, 4$ and 5), the previous conclusions about n -port calibrations have been found inductively. For more information about this process, see Appendix J.

Of course, the rank of the coefficient matrix, A_E , is affected by the type of each standard used in calibration. It has been found that at least one of the standards must be constructed so that at least $n-1$ non-zero transfer functions exist between its ports. In other words, such a standard interconnects all of the VNA's measurement ports simultaneously. Hence, this standard will be called a generalized through standard. It is important to note that the generalized through does not necessarily provide low loss interconnection between the ports. Without a generalized through standard as one of the minimal set of standards, the rank of the coefficient matrix will not be sufficient for an ordinary solution to the calibration equation.

As its name implies, the generalized through is a generalization of the through standard of two-port VNA calibrations. For a two-port VNA, the through provides transfer between all ports. However, with more than two ports, the generalized through standard is less familiar. It can be shown that one or more two-port through, used as a single n -port standard, is not sufficient for an ordinary solution to (6-8). Furthermore, use of

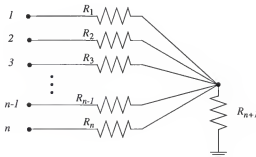


Figure 6-14. Preferred embodiment of n -port generalized through standard.

multiple pairs of throughs, each connecting different ports, will not provide sufficient rank in A_E for an ordinary solution.

With three or more ports, the implementation of a generalized through standard is no longer straight forward. The suggested implementation of a complete n -port standard is shown in Figure 6-14. This network provides the required connections between all measurement ports. This type of network will be called a star network. The star network is particularly practical to implement for wafer-probe standards (See Section 6.2.7). By isolating the ground connection of the network, the value of each resistor can be measured directly with a two terminal Ohmmeter. This property is important during fabrication of star standards when trimming individual resistors is necessary.

6.2.6. Coaxial Calibration Standards

The PMVNA calibration has been implemented with the application of the above conclusions about general VNA calibrations. With n being four, the PMVNA calibration standards can be defined in physical terms. For this section, calibration standards with 3.5mm coaxial connectors are used. Five standards are combined to create the calibration kit: (1) a four-port match (four 50Ω loads), (2) a four-port short (four offset shorts), (3) a four-port open (four offset opens), (4) a pair of zero-length through lines (by connecting test cable of ports one to three and two to four), and (5) a four-port resistive star network as the generalized through. The star network is constructed from two resistive power dividers [55] connected as shown in Figure 6-15.

To use the star network as a calibration standard, its s -parameters must be accurately known. The star network, as shown in Figure 6-15, has been characterized through a series of two-port s -parameter measurements, with the unused ports terminated with

50 Ω loads. By making six two-port measurements, all of the four-port s -parameters of the star network can be found. For this process, the VNA (operated as a standard two-port VNA) is calibrated with the Hewlett-Packard 85052B precision 3.5mm calibration kit [56] using the Through-Short-Open-Load (TOSL) technique with sliding loads. When making the two-port measurements of the star network, the remaining ports are terminated with the 50 Ω loads from the 85052B kit, and these are assumed to be perfect matched loads. These loads have return loss of no less than 35dB, and this assumption limits the accuracy of the four-port s -parameters of the star network. There are published methods that can remove this assumption [57], but for this work the assumption of perfect matched loads is reasonable.

Traditionally, calibration standards are modeled by simple equivalent circuits with a small set of parameters which allow calculation of the standards' s -parameters at any

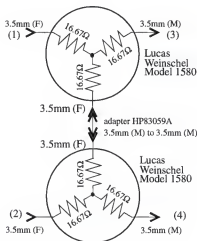


Figure 6-15. Schematic of coaxial star network standard.

frequency. The star network has more complex behavior than traditional standards, and accurate modeling would require a complex equivalent circuit with many parameters. To avoid this difficulty, interpolation between measured s-parameters is used to generate the star network's s-parameters at an arbitrary frequency point. The interpolation is done through a tenth order polynomial fit, over a range of nine frequency points about the desired frequency, for the real and imaginary parts of each s-parameter. This interpolation process is implemented in *LabVIEW*, and represents a useful general capability for calibrations that allows a simple means to incorporate non-traditional standards.

The remaining standards are treated with traditional models [43]. The calibration parameters of the shorts and opens used for the PMVNA calibration are provided by the manufacturer [58, 59]. With the published parameters, theoretical s-parameters (S_{ax}) of the short and open can be calculated. The through-lines are assumed perfect zero-length throughs, and the S_{ax} is defined accordingly. The S_{ax} of the star network is generated through interpolation as described above. The 50Ω load S_{ax} is also generated through interpolation of measurements of the load standards done with sliding load calibrations.

6.2.7. On-Wafer Calibration Standards

Calibration standards for the PMVNA have also been constructed for on-wafer measurements. These standards have been designed so the plane of calibration is the wafer probe tips. The standards are thin-film metal-on-ceramic structures, and two versions have been designed and fabricated, one for $150\mu\text{m}$ pitch probes, and another for $500\mu\text{m}$ pitch probes. Both have been fabricated with thin-film gold ($4\mu\text{m}$ thick $\pm 0.25\mu\text{m}$) on a polished alumina substrate ($\epsilon_r = 9.9$, $\tan\delta = 0.001$). The resistive layer is a nickel-chrome (NiCr) metal approximately 400\AA thick, with a sheet resistance of about 40

Ω /square. After fabrication, the resistors were tuned to the desired DC values ($\pm 0.1\%$) with a laser. All photo-masks required for fabrication have been generated in the University of Florida Microelectronics Laboratory, and all fabrication has been done in the Motorola Thin-Film Research Laboratory in Plantation, Florida.

In accordance with Section 6.2.5, five types of standards have been fabricated: (1) a four-port match (four 50Ω loads), (2) a four-port short (four offset shorts), (3) a four-port open (four offset opens), (4) a pair of zero-length through lines (by connecting test cable of ports one to three and two to four), and (5) a four-port resistive star network as the generalized through. The layouts of the $150\mu\text{m}$ pitch standards are shown in Figure 6-16 to Figure 6-20.

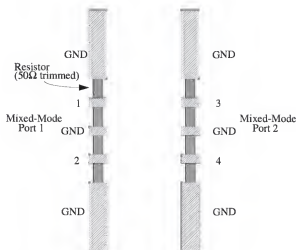


Figure 6-16. Physical layout of $150\mu\text{m}$ pitch four-port match standard.

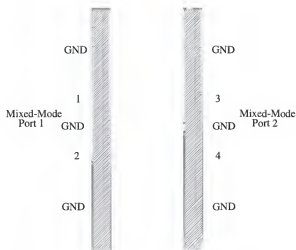


Figure 6-17. Physical layout of 150µm pitch four-port short standard.

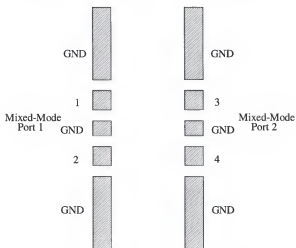


Figure 6-18. Physical layout of 150µm pitch four-port open standard.

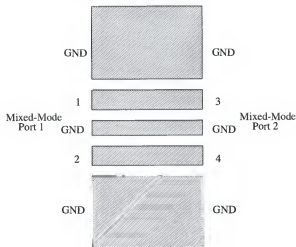


Figure 6-19. Physical layout of 150 μ m pitch pair-of-throughs standard.

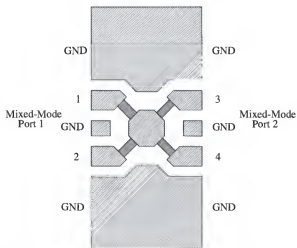


Figure 6-20. Physical layout of 150 μ m pitch four-port star standard.

For both sets of on-wafer calibration standards, the theoretical s -parameters (S_{arr}) are calculated by electromagnetic simulation. The simulator used is Hewlett-Packard's *Momentum* [40]. The simulations assumed a substrate with a relative dielectric constant of 9.9 and a loss tangent of 0.001. The gold was assumed to be $4\mu\text{m}$ thick with a conductivity of 5.8×10^7 S/m. The resistive layers were assumed to be infinitely thin resistor material with a defined sheet resistance of the nominal design value of $50\Omega/\text{square}$. After simulation, the resulting s -parameters have been used to generate the theoretical s -parameters of the calibration standards, S_{arr} , through the interpolation process described in Section 6.2.6.

The star standard of Figure 6-20 has special usefulness in the calibration of a PMVNA. This standard can help enhance the accuracy of the sensitive mode-conversion parameters. Theoretically, the accuracy of a calibration is limited by the accuracy to which the standards are known. However, due to noise, repeatability limitations, and numerical and/or measurement dynamic range limitations, the accuracy of a calibration is greatest in the neighborhood of the standards. In other words, a corrected DUT measurement will have greatest accuracy if its response is nearly that of at least one of the standards. PMVNA can measure the conversion between modes, such as differential-to-common-mode conversion. Different devices can have dramatically different levels of mode conversion, making accurate error correction difficult for the mode conversion responses.

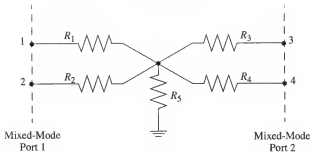


Figure 6-21. Possible embodiment of mode conversion standard.

The basic advantage of the star standard is that it allows the design of calibration standards with specified amount of mode-conversion. The basic network for this standard is the four-port resistive star, and its circuit diagram is given in Figure 6-21.

By choosing the appropriate values of the resistors in the star network, the mode-conversion parameters of the network can be varied over a wide range. Practical implementations of this standard have been able to reliably achieve mode-conversion magnitudes from -6 dB to less than -80 dB.

6.3. Phase Offset Pre-Calibration

A unique aspect of the PMVNA as implemented for this work is the unknown phase relationship between the VCOs in the two test-sets, as described in Section 4.2.2. The phase offset between the test-sets is not a systematic error in the strict sense because it changes as the RF switch positions change. Furthermore, direct application of switching error models, such as Figure 6-13, are insufficient to overcome the problem of an

unknown phase relation between the VCOs. Use of (6-9) and (6-11) with the raw a and b data from implemented PMVNA results in incorrect calculation of the raw s -parameters. This is due to the fact that there is an unknown phase offset between the data from test-set A and test-set B for each set of RF switch positions.

However, the phase offset relationship can be characterized and corrected. The process operates on the raw a and b data from both test-sets, and is independent of the primary calibration process. Furthermore, the phase offset correction must be applied to all a and b data in the primary calibration. For these reasons, the phase offset calibration process is called a pre-calibration procedure.

The phase offset between the test sets is actually a function of s -parameters of the DUT. As a result, the phase offset pre-calibration is broken into two steps. The first step calculates the phase offset for each of several so called offset standards. The second step uses these results to calculate the parameters that will describe the phase offset of an arbitrary DUT.

6.3.1. Phase Offset Standards

A phase offset standard is a device that is measured to allow calculation of the test-set phase offsets. It is significantly different from the type of standards used in the primary calibration, in that its actual s -parameters do not need to be known. The offset standard does have some restrictions in its general characteristics, as will be discussed. Conceptually, a offset standard is a device that allows one test-set to measure the response of the other test-set.

6.3.1.1. First Principles

The entire phase offset pre-calibration is based upon two observations about the PMVNA as implemented in Figure 4-3. The first of these is that, for a particular PMVNA test-set RF switch configuration, the phase offset is highly repeatable. This means that, for example, when PMVNA is switched into differential-forward (DF) mode, the phase offset between the VCO in test-set A and that of test-set B is always the same within a high degree of accuracy (as long as the DUT remains unchanged).

The second important observation is that the PMVNA test set has four additional RF switch configurations that have not been used to this point. Referring to Figure 4-4, one can see there are three independent RF switches (SW1, SWA and SWB) each having two positions, giving a total of eight possible switch configurations. Four of these positions represent the fundamental operation of the PMVNA (i. e. DF, DR, CF, and CR). The remaining four positions are not used in the normal PMVNA operation, and together these positions are called secondary operation.

Measuring a device (in this case a offset standard) in both the fundamental and secondary modes should give the same set of four-port (or mixed-mode) s-parameters, within the dynamic range of the PMVNA. Symbolically,

$$S_{mf} = S_{ms} \quad (6-12)$$

where S_{mf} is the raw s-parameters measured under fundamental operation, and S_{ms} is the raw s-parameters measured under secondary operation. This equality holds only if the data from the eight down-mixers of the PMVNA have no relative phase offset. Therefore, equation (6-12) can be used to calculate any unknown phase offsets. This important approach, based on (6-12), shall be called the principle of equality of operation. It is

important to note that (6-12) contains only raw uncorrected s -parameters; this allows the offset pre-calibration to be performed independently of the primary calibration as the error terms of the PMVNA do not need to be known.

6.3.1.2. Offset Model

The VCO in a 8517 test-set phase-locks to a particular phase point on the RF signal input (see Figure 4-4). For example, if the PMVNA is in DF mode, where ports one and three are driven 180° out of phase, the VCO in test-set A is phase-locked to a_1^{DF} . The down-mixed a_1^{DF} data will always have a phase that corresponds to a particular phase of the RF a_1^{DF} signal. For example, if the VCO is locked to a_1^{DF} , then the 0° point of the down-mixed data will always correspond to the same phase point of the RF signal, say 0° . The actual phase points are arbitrary, but the correspondence always holds. The two test-sets will lock to their appropriate phase points, and their sampled data will indicate a fixed phase difference between the two drive signals (a_1^{DF} and a_2^{DF} for this example), regardless of the actual phase difference between them.

Before proceeding, a mathematical model of the phase offset must be established. The simplest way of describing such an offset is by stating that, for a given measured a or b -wave, the actual quantity is equal to the measured quantity multiplied by an unknown complex scalar. For example

$$a_{1c}^{\text{DF}} = a_{1m}^{\text{DF}} X_1^{\text{DF}} \quad (6-13)$$

where the subscript c indicates the corrected quantity, and m indicates the measured quantity. The model of (6-13) allows both a phase and magnitude offset, but actual offsets found from measured data (as will be describe later) have unity magnitudes. In general the A matrix becomes

$$A_c = \begin{bmatrix} \text{DF}_1 & \text{DF}_1 & \text{DR}_1 & \text{DR}_1 & \text{CF}_1 & \text{CF}_1 & \text{CR}_1 & \text{CR}_1 \\ a_1 & x_1 & a_1 & x_1 & a_1 & x_1 & a_1 & x_1 \\ \text{DF}_2 & \text{DF}_2 & \text{DR}_2 & \text{DR}_2 & \text{CF}_2 & \text{CF}_2 & \text{CR}_2 & \text{CR}_2 \\ a_2 & x_2 & a_2 & x_2 & a_2 & x_2 & a_2 & x_2 \\ \text{DF}_3 & \text{DF}_3 & \text{DR}_3 & \text{DR}_3 & \text{CF}_3 & \text{CF}_3 & \text{CR}_3 & \text{CR}_3 \\ a_3 & x_3 & a_3 & x_3 & a_3 & x_3 & a_3 & x_3 \\ \text{DF}_4 & \text{DF}_4 & \text{DR}_4 & \text{DR}_4 & \text{CF}_4 & \text{CF}_4 & \text{CR}_4 & \text{CR}_4 \\ a_4 & x_4 & a_4 & x_4 & a_4 & x_4 & a_4 & x_4 \end{bmatrix} \quad (6-14)$$

This can be simplified with the use of the Haddamard matrix product [61] (also known as the entry-wise product)

$$A_c = A_m \bullet X \quad (6-15)$$

where

$$X = \begin{bmatrix} \text{DF}_1 & \text{DR}_1 & \text{CF}_1 & \text{CR}_1 \\ x_1 & x_1 & x_1 & x_1 \\ \text{DF}_2 & \text{DR}_2 & \text{CF}_2 & \text{CR}_2 \\ x_2 & x_2 & x_2 & x_2 \\ \text{DF}_3 & \text{DR}_3 & \text{CF}_3 & \text{CR}_3 \\ x_3 & x_3 & x_3 & x_3 \\ \text{DF}_4 & \text{DR}_4 & \text{CF}_4 & \text{CR}_4 \\ x_4 & x_4 & x_4 & x_4 \end{bmatrix} \quad (6-16)$$

No assumptions have been made at this point as to which a or b data have actual phase offsets. If no offset exists, the corresponding offset variable, x , will be unity. Similar expressions can be stated for the b data

$$B_c = B_m \bullet X \quad (6-17)$$

Applying (6-15) and (6-17) to the equality of operation equation (6-12), and re-arranging one finds

$$(B_{mf} \bullet X_f)(A_{mf} \bullet X_f)^{-1} - (B_{ms} \bullet X_s)(A_{ms} \bullet X_s)^{-1} = 0 \quad (6-18)$$

where X_f and X_s are the phase offset matrices for the fundamental and secondary modes of operation, respectively. In general, the matrices are not equal.

By solving equation (6-18) for X_f and X_r , the phase offsets for each a and b -wave can be found. However, the solution of this equation is not easily found, as it is non-linear in the elements of X_f and X_r . For this reason, the approach presented above has been modified to allow a simpler solution to the problem. This modified approach is presented in the next section.

6.3.1.3. Modified T-Matrix Solution

The enabling simplification begins with the observation that a single test-set has no phase offset between its corresponding a and b data. For example, a_1^{DF} and a_3^{DF} have no phase offset since they are measured by the same test-set. By using this fact, together with the concept of t-parameters, (6-18) can be restated as a linear equation.

Grouping ports one and three as a pair and two and four as another, a new T-matrix can be defined in a similar fashion as in Appendix H. The new T-matrix can be developed by considering an arbitrary four-port matrix, where the a - and b -waves are related by

$$\begin{bmatrix} b_1 \\ b_2 \\ b_3 \\ b_4 \end{bmatrix} = \begin{bmatrix} s_{11} & s_{12} & s_{13} & s_{14} \\ s_{21} & s_{22} & s_{23} & s_{24} \\ s_{31} & s_{32} & s_{33} & s_{34} \\ s_{41} & s_{42} & s_{43} & s_{44} \end{bmatrix} \begin{bmatrix} a_1 \\ a_2 \\ a_3 \\ a_4 \end{bmatrix} \quad (6-19)$$

The column of b -waves is the "output" vector, and the column of a -waves is the "input" vector. By re-arranging the a - and b -waves, a new set of "input" and "output" vectors are defined as

$$\vec{u}' = \begin{bmatrix} a_1 \\ a_3 \\ b_1 \\ b_3 \end{bmatrix} \quad \vec{v}' = \begin{bmatrix} b_2 \\ b_4 \\ a_2 \\ a_4 \end{bmatrix} \quad (6-20)$$

where the primed quantities denote the new port grouping (in contrast to that described in Appendix H which is used throughout the primary calibration). The new T-matrix equation becomes

$$\vec{v}' = T' \vec{u}' \quad (6-21)$$

The new T-matrix, T' , can be expressed in terms of the original s-parameters of the network, but the actual s-parameters are not of interest. In a similar fashion as the A and B matrices, one can define

$$U_f' = \left[\begin{array}{cccc} a_1^{DF} & a_1^{DR} & a_1^{CF} & a_1^{CR} \\ a_3^{DF} & a_3^{DR} & a_3^{CF} & a_3^{CR} \\ b_1^{DF} & b_1^{DR} & b_1^{CF} & b_1^{CR} \\ b_3^{DF} & b_3^{DR} & b_3^{CF} & b_3^{CR} \end{array} \right]_f \quad V_f' = \left[\begin{array}{cccc} b_2^{DF} & b_2^{DR} & b_2^{CF} & b_2^{CR} \\ b_4^{DF} & b_4^{DR} & b_4^{CF} & b_4^{CR} \\ a_2^{DF} & a_2^{DR} & a_2^{CF} & a_2^{CR} \\ a_4^{DF} & a_4^{DR} & a_4^{CF} & a_4^{CR} \end{array} \right]_f \quad (6-22)$$

or, more simply

$$U_f' = \left[\vec{u}^{DF} \vec{u}^{DR} \vec{u}^{CF} \vec{u}^{CR} \right]_f \quad V_f' = \left[\vec{v}^{DF} \vec{v}^{DR} \vec{v}^{CF} \vec{v}^{CR} \right]_f \quad (6-23)$$

In these matrices, the subscript f denotes fundamental operation of the PMVNA. For secondary U_s and V_s similarly defined (but have different numerical values). The full matrix expressions of (6-21) are

$$V_f' = T_f' U_f' \quad V_s = T_s' U_s \quad (6-24)$$

The phase offset in the measured a and b data can be treated in the same fashion as the previous section. The phase-corrected a and b data can be expressed as

$$U_{cf} = \left[\begin{array}{cccc} \text{DF} & \text{DF} & \text{DR} & \text{DR} \\ a_1 & x_1 & a_1 & x_1 \\ \text{CF} & \text{CF} & \text{CR} & \text{CR} \\ a_1 & x_1 & a_1 & x_1 \end{array} \right]_f \quad (6-25)$$

$$V_{cf} = \left[\begin{array}{cccc} \text{DF} & \text{DF} & \text{DR} & \text{DR} \\ b_2 & x_2 & b_2 & x_2 \\ \text{CF} & \text{CF} & \text{CR} & \text{CR} \\ b_2 & x_2 & b_2 & x_2 \end{array} \right]_f \quad (6-26)$$

or more compactly

$$U_{cf} = U_{mf} \bullet X_{1f} \quad V_{cf} = V_{mf} \bullet X_{2f} \quad (6-27)$$

where the X_{1f} and X_{2f} are the new offset matrices, and are defined as

$$X_{1f} = \left[\begin{array}{cccc} \text{DF} & \text{DR} & \text{CF} & \text{CR} \\ x_1 & x_1 & x_1 & x_1 \\ \text{DF} & \text{DR} & \text{CF} & \text{CR} \\ x_3 & x_3 & x_3 & x_3 \\ \text{DF} & \text{DR} & \text{CF} & \text{CR} \\ x_1 & x_1 & x_1 & x_1 \\ \text{DF} & \text{DR} & \text{CF} & \text{CR} \\ x_3 & x_3 & x_3 & x_3 \end{array} \right]_f \quad X_{2f} = \left[\begin{array}{cccc} \text{DF} & \text{DR} & \text{CF} & \text{CR} \\ x_2 & x_2 & x_2 & x_2 \\ \text{DF} & \text{DR} & \text{CF} & \text{CR} \\ x_4 & x_4 & x_4 & x_4 \\ \text{DF} & \text{DR} & \text{CF} & \text{CR} \\ x_2 & x_2 & x_2 & x_2 \\ \text{DF} & \text{DR} & \text{CF} & \text{CR} \\ x_4 & x_4 & x_4 & x_4 \end{array} \right]_f \quad (6-28)$$

Notice that X_{1f} contains only phase terms from test-set A, and X_{2f} contains only phase terms from test-set B. In a given configuration (e. g. fundamental DF), the relative phase offset in the a and b data from a single test-set will be zero. As a result, X_{1f} and X_{2f} simplify to a single offset variable for each row

$$X_{1f} = \begin{bmatrix} \text{DF} & \text{DR} & \text{CF} & \text{CR} \\ x_1 & x_1 & x_1 & x_1 \\ \text{DF} & \text{DR} & \text{CF} & \text{CR} \\ x_1 & x_1 & x_1 & x_1 \\ \text{DF} & \text{DR} & \text{CF} & \text{CR} \\ x_1 & x_1 & x_1 & x_1 \\ \text{DF} & \text{DR} & \text{CF} & \text{CR} \\ x_1 & x_1 & x_1 & x_1 \end{bmatrix}_f \quad X_{2f} = \begin{bmatrix} \text{DF} & \text{DR} & \text{CF} & \text{CR} \\ x_2 & x_2 & x_2 & x_2 \\ \text{DF} & \text{DR} & \text{CF} & \text{CR} \\ x_2 & x_2 & x_2 & x_2 \\ \text{DF} & \text{DR} & \text{CF} & \text{CR} \\ x_2 & x_2 & x_2 & x_2 \\ \text{DF} & \text{DR} & \text{CF} & \text{CR} \\ x_2 & x_2 & x_2 & x_2 \end{bmatrix}_f \quad (6-29)$$

Since only the relative phase offset between the two test-sets is important, either test-set may be considered as the phase reference. Accordingly, X_{1f} can be chosen arbitrarily. The Haddamard identity matrix, I , is chosen, where all the elements are unity (where $U_{mf} \bullet I = U_{mf}$). As a result,

$$U_{cf} = U_{mf} \quad (6-30)$$

Dropping the numeric subscript, and using f to denote fundamental operation, the remaining offset matrix is defined as

$$X_{2f} = \begin{bmatrix} \text{DF} & \text{DR} & \text{CF} & \text{CR} \\ x_f & x_f & x_f & x_f \\ \text{DF} & \text{DR} & \text{CF} & \text{CR} \\ x_f & x_f & x_f & x_f \\ \text{DF} & \text{DR} & \text{CF} & \text{CR} \\ x_f & x_f & x_f & x_f \\ \text{DF} & \text{DR} & \text{CF} & \text{CR} \\ x_f & x_f & x_f & x_f \end{bmatrix} = \begin{bmatrix} \bar{x}_f \text{DF} & \bar{x}_f \text{DR} & \bar{x}_f \text{CF} & \bar{x}_f \text{CR} \end{bmatrix} \quad (6-31)$$

Similarly for secondary operation,

$$U_{cs} = U_{ms} \quad V_{cs} = V_{ms} \bullet X_{2s} \quad (6-32)$$

where

$$X_{2s} = \begin{bmatrix} x_s^{DF} & x_s^{DR} & x_s^{CF} & x_s^{CR} \\ x_s^{DF} & x_s^{DR} & x_s^{CF} & x_s^{CR} \\ x_s^{DF} & x_s^{DR} & x_s^{CF} & x_s^{CR} \\ x_s^{DF} & x_s^{DR} & x_s^{CF} & x_s^{CR} \end{bmatrix} = \begin{bmatrix} \tilde{x}_s^{DF} & \tilde{x}_s^{DR} & \tilde{x}_s^{CF} & \tilde{x}_s^{CR} \end{bmatrix} \quad (6-33)$$

It must be remembered that the phase offset for the fundamental operation is not generally equal to that of the secondary operation. Furthermore, the switch configuration descriptors (e. g., DF) do not have the normal meaning in secondary operation. Combining (6-24) through (6-33), one finds

$$T'_f = (V_{mf} \bullet X_{2f})U_{mf}^{-1} \quad T'_s = (V_{ms} \bullet X_{2s})U_{ms}^{-1} \quad (6-34)$$

The principle of equality of operation (6-12) can now be restated as

$$T'_f = T'_s \quad (6-35)$$

or, with the unknown phase offsets, X'_{2f} and X'_{2s} , as

$$(V_{mf} \bullet X'_{2f})U_{mf}^{-1} - (V_{ms} \bullet X'_{2s})U_{ms}^{-1} = 0 \quad (6-36)$$

Provided that T'_f and T'_s exist, then (6-36) is linear in the elements of X'_{2f} and X'_{2s} . This equation can be expanded, and re-written as

$$A_p \tilde{x}_p = \tilde{0} \quad (6-37)$$

where

$$\tilde{x}_p = \begin{bmatrix} x_f^{DF} & x_f^{DR} & x_f^{CF} & x_f^{CR} & x_s^{DF} & x_s^{DR} & x_s^{CF} & x_s^{CR} \end{bmatrix}^T \quad (6-38)$$

and A_p is the coefficient matrix of (6-36). Equation (6-37) can now be solved with a numerical technique known as singular value decomposition (SVD) [60]. This technique

finds a solution vector, t_S , that minimizes the product $A_E t_S$ in a least-squares sense. The SVD approach is useful for the solution of the calibration equation where real data is used, where the real data has both random errors due to noise, drift, etc. and residual systematic errors due to imperfectly known standards. SVD is also used in the same way in the primary calibration (see Section 6.4).

Once a solution is found the offsets of the A and B matrix, defined in (6-16), can be directly found as

$$X = \begin{bmatrix} 1 & 1 & 1 & 1 \\ x_f^{DF} & x_f^{DR} & x_f^{CF} & x_f^{CR} \\ 1 & 1 & 1 & 1 \\ x_f^{DF} & x_f^{DR} & x_f^{CF} & x_f^{CR} \end{bmatrix} \quad (6-39)$$

The offset-corrected A_c and B_c matrix can be found by (6-15) and (6-17). For examples of actual offset data, calculated from measured data, see Appendix L.

As indicated, T'_f of the offset standard must exist for equation (6-36) to have a solution. This requirement has important implications on the general characteristic of offset standards. Referring to the matrix conversion between s-parameters and t-parameters, one can find that a T-matrix will exist only if S_{21}^{-1} exist. This is true if $|S_{21}| \neq 0$. With the new definition of the T-matrix for the phase offset calibration, this restriction can be stated in terms of the offset standard's s-parameters as

$$s_{21}s_{43} \neq s_{41}s_{23} \quad (6-40)$$

Physically, this restriction means that "cross-over" transmission, $s_{41}s_{23}$, must be distinguishable from "straight-through" transmission, $s_{21}s_{43}$. For a reciprocal offset standard, the restriction (6-40) means that either $s_{41}s_{23} = 0$ or $s_{21}s_{43} = 0$. Simply stated, an

acceptable offset standard will connect ports one and two and ports three and four, or it will connect ports one and four and ports two and three, while all other transmission is essentially eliminated. These two types of devices are illustrated in Figure 6-22.

6.3.2. Phase Offset Of An Unknown DUT

As mentioned earlier, the phase offset between the two test-sets is actually a function of the s -parameters of the DUT. As a result, the fundamental mechanics of this variable offset must be described and characterized so that the phase offset of an arbitrary, unknown device can be calculated.

6.3.2.1. Variable Offset Model

The reason for the variation of the phase offset can be found by examination of Figure 6-13. This figure has been simplified, and presented in terms of vector a and b -waves, in Figure 6-23. With the RF switches of the test-sets in the i -th configuration, the switches can be collectively described by an s -parameter matrix S_{sw}^i . The systematic errors of the PMVNA are included with the s -parameters of the DUT in S_m . With the i -th configuration, a particular stimulus condition is generated, \tilde{a}_{src}^i . For the moment assuming that all a and b data is sampled without phase errors, it can be shown that

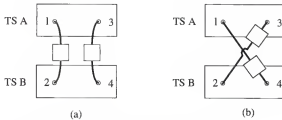


Figure 6-22. Schematic of types of acceptable offset standards.
a) Straight-through. b) Cross-over.

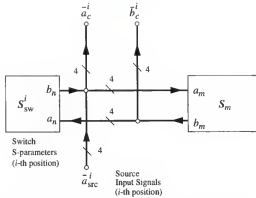


Figure 6-23. Simplified general switching error model signal flow graph.

$$\bar{a}_c^i = (I - S_{sw}^i S_m)^{-1} \bar{a}_{src}^i \quad (6-41)$$

$$b_c^i = S_m (I - S_{sw}^i S_m)^{-1} \bar{a}_{src}^i \quad (6-42)$$

This clearly indicates that the actual a and b data vary with the DUT raw s -parameters.

Referring to (6-41), one can see that the actual phase difference between the components of the a -waves is a function of the s -parameters of the DUT, S_m . Since the VCOs are always locked to the same phase point of the actual a -waves, the phase offset in the sampled a data is also a function of S_m . As a result, the switch s -parameter matrix, S_{sw}^i , and the source vector, \bar{a}_{src}^i , must be found for every switch position, i , to allow the calculation of the phase offset for an arbitrary DUT.

6.3.2.2. Using Multiple Offset Standards

The calculation of S_{sw}^i and \bar{a}_{src}^i is accomplished through the use of multiple offset standards. For each offset standard, the actual phase offset is calculated as described in

Section 6.3.1.3. The raw a and b data for each offset standard is corrected with the corresponding phase offset, giving the actual a and b data for each offset standard. Combining (6-41) and (6-42), it is found that

$$S_{sw}^i \bar{b}_c^i + \bar{a}_{src}^i = \bar{a}_c^i \quad (6-43)$$

Grouping the actual a and b data from each offset standard into matrices for each switch configuration, (6-43) becomes

$$S_{sw}^i B_c^i + A_{src}^i = A_c^i \quad (6-44)$$

This can be expanded into a non-homogeneous system of equations that are linear in the elements of S_{sw}^i and \bar{a}_{src}^i . This can be expressed as

$$A_T^i \bar{x}_T^i = \bar{a}_T^i \quad (6-45)$$

where A_T^i is the coefficient matrix for the i -th position, \bar{a}_T^i is a column vector of the elements of A_c^i , and \bar{x}_T^i is a column vector of the unknown elements of S_{sw}^i and \bar{a}_{src}^i . This system of equations can be solved via SVD. Of course, this process must be done for all switch positions, $i = \{DF, DR, CF, CR\}$.

6.3.2.3. Calculating the Offset of an Arbitrary DUT

Now that the fundamental mechanism for the phase offset has been characterized, the actual phase offset for an arbitrary DUT can be calculated. For any device measurement, the raw a and b data, are collected into a column vector for each switch position. The offset vector for this position, \bar{x}^i , can be calculated by the linear expression

$$S_{sw}^i (\bar{b}_m^i \bullet \bar{x}^i) + \bar{a}_{src}^i = \bar{a}_m^i \bullet \bar{x}^i \quad (6-46)$$

After calculating \bar{x}^i for all switch positions, the offset matrix can be constructed by

$$X_f = \begin{bmatrix} \tilde{x}_f^{\text{DF}} & \tilde{x}_f^{\text{DR}} & \tilde{x}_f^{\text{CF}} & \tilde{x}_f^{\text{CR}} \end{bmatrix} \quad (6-47)$$

From this offset corrected data, the raw s-parameters of the DUT can be accurately calculated by

$$S_m = (B_{mf} \bullet X_f)(A_{mf} \bullet X_f)^{-1} \quad (6-48)$$

This process is not restricted in the type of DUT that can be corrected. The limitations of the offset standards, namely that the T-matrix exists, does not apply to (6-46).

6.3.2.4. Diagonalized Form

In practice, equation (6-46) can be further simplified. This is due to the fact that S_{sw}^i is a diagonal matrix, within practical limits. That is

$$S_{sw}^i = \text{DiagonalMatrix}(\begin{bmatrix} \Gamma_1^i & \Gamma_2^i & \Gamma_3^i & \Gamma_4^i \end{bmatrix}) \quad (6-49)$$

where

$$\tilde{\Gamma}^i = \begin{bmatrix} \Gamma_1^i & \Gamma_2^i & \Gamma_3^i & \Gamma_4^i \end{bmatrix}^T \quad (6-50)$$

By recognizing this fact, (6-46) can be simplified to

$$\tilde{\Gamma}^i \bullet \tilde{x}^i \bullet \tilde{b}_m^i = \tilde{x}^i \bullet \tilde{a}_m^i - \tilde{a}_{src}^i \quad (6-51)$$

With this simplification, the vector offset can be symbolically found as

$$\tilde{x}^i = \frac{\tilde{a}_{src}^i}{\tilde{a}_m^i - \tilde{\Gamma}^i \bullet \tilde{b}_m^i} \quad (6-52)$$

where the division is the Haddamard (entry-wise) division. Now, the offset matrix can be constructed according to (6-47), and the raw s-parameters are calculated by (6-48).

6.4. Calibration Procedure

The calibration process for the PMVNA is summarized as follows. First the phase offset pre-calibration is completed. Several offset standards are measured during this process. These standards are generated with the use of a pair of resistive splitters [55] in combination with various terminations. The test-port cables from ports one and four (one and two) are connected to one resistive splitter, and ports two and three (three and four) are connected to the other resistive splitter. The remaining ports of the resistive splitters are terminated with a variety of one-port devices, such as opens and shorts. This combination of splitters and terminations provide a simple means of generating a large variety of offset standards. The offset pre-calibration is always executed at the coaxial interface, regardless of the type of primary calibration that will follow (i. e., on-wafer or coaxial). The offset pre-calibration is independent of the reference plane of the primary calibration.

The primary calibration is accomplished next. Each calibration standard is connected to the PMVNA, and all down-mixers are measured for each stimulus mode and direction. The raw A and B data matrices are constructed as shown in (6-9). The phase offset of each standard is calculated via (6-47), and the raw measured s-parameters (S_{mx}) are calculated as shown in (6-48). The measured s-parameters and the corresponding theoretical s-parameters (S_{ax}) of all standards are used to generate the coefficient matrix, A_E , via equation (6-7). Finally, the calibration equation (6-8) is solved, and the error matrix, T_{ES} , is constructed.

For the PMVNA, the solution of the calibration equation (6-8) is implemented with a numerical technique known as singular value decomposition (SVD) [60]. SVD is an technique that finds a solution vector, t_S , that minimizes the product $A_E t_S$ in a least-

squares sense. The SVD approach is useful for the solution of the calibration equation where real data is used, where the real data has both random errors due to noise, drift, etc., and residual systematic errors due to imperfectly known standards. The SVD solution provides the best least-square-error solution to the calibration data. Since the solution to the calibration problem by this method is actually an estimate of the actual error network, T_E , the notation T_{ES} is adopted to make a clear distinction. For this work the SVD solution algorithm was integrated into *LabVIEW* so calibration and correction could be accomplished within the control software. The basic *LabVIEW* application does not include a SVD algorithm. As a result, a custom C-code routine (from [60]) for SVD has been integrated into *LabVIEW* for this work.

After the error matrix, T_{ES} , is found, any subsequent device measurements can be corrected through the application of (6-7). First the DUT offset corrected a and b data is found via (6-47), and the raw DUT s -parameters are calculated by (6-48). Then, the error matrix, T_{ES} , is partitioned as discussed earlier, and then (6-7) is solved for S_a ,

$$S_a = (T_{ES11} - S_m T_{ES21})^{-1} (S_m T_{ES22} - T_{ES12}) \quad (6-53)$$

which now represents the corrected s -parameters of the DUT. For the PMVNA, the s -parameters are expressed in terms of mixed-mode s -parameters, but the corrected s -parameters can be transformed into standard four-port s -parameters if desired. For more details on the calibration software, see Appendix G.

CHAPTER 7

VERIFICATION OF THE PMVNA

To provide a verification of the accuracy of the PMVNA calibration it is required to measure some standard other than those used in calibration. By comparing the corrected s -parameters from the PMVNA to the theoretical s -parameters of the verification standard, one can get a measure of the accuracy of the calibration. It is desirable to find verification standards where the theoretical s -parameters are as independent as possible from the PMVNA measurement system (and calibration standards used). It is also desirable to use devices that are representative of typical differential device performance. Although verification sets are commercially available for two-port VNAs, there are no such differential verification standards (with NIST traceable measurements provided).

For this reason, the verification standards used here are provided by a Hewlett-Packard 85057B verification kit [62]. This kit contains four two-port standards, each accompanied with NIST traceable s -parameter measurements (these measurements have associated maximum uncertainties, also provided). For verification of the PMVNA, various combinations of two verification standards are measured, and the corrected measurements are compared to the provided s -parameters. While combinations of two-port devices do not represent a general differential device that the PMVNA is designed to measure, the 85057B kit provides a readily available means of accuracy verification.

The 85057B verification kit contains a 20 dB attenuator, and 40 dB attenuator, a 50 Ω air-dielectric transmission line, and a 25 Ω air-dielectric transmission line. The stan-

dards have 2.4mm coaxial connectors, but the PMVNA uses 3.5mm connectors. These devices are used despite this incompatibility since they are readily available to the author. As a result of the connector incompatibility, adapters are used between the connectors of the PMVNA (representing the calibration reference plane) and the verification standards. The corrected s -parameters of the verification device and adapters are manipulated to de-embed the adapters, after which the s -parameters can be compared directly to the provided verification s -parameters. The s -parameters of the adapters needed for the de-embedding

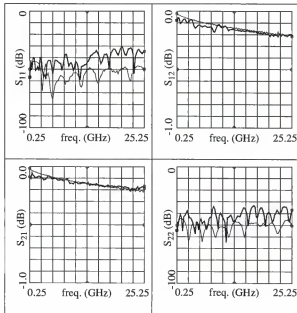


Figure 7-1. Measured s -parameters with adapters de-embedded (bold) and verification s -parameters of the 50Ω air-dielectric transmission line, connected between ports one and three while the 25Ω air-dielectric transmission line is connected between port two and four.

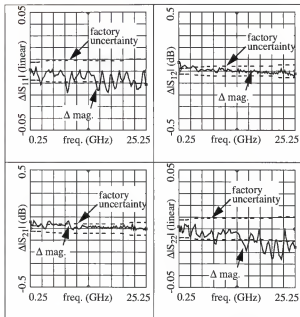


Figure 7-2. Differences between measured s-parameters and verification s-parameters of Figure 7-1 (solid) and factory uncertainty of verification s-parameters (dashed). Errors in S_{11} and S_{22} expressed as the difference of the linear magnitudes of the respective data. Errors in S_{12} and S_{21} are expressed as the difference in dB of magnitudes in dB.

are found through a series of one-port measurements. The adapters are placed on a calibrated (TOSL, sliding load) 3.5mm measurement port, and 2.4mm calibration standards (open, short, load, sliding load from a HP 85056A 2.4mm calibration kit [63]) are placed on the remaining end of the adapter. The sliding load algorithm has been implemented according to [64] in *Mathematica*. With these measurements of the adapter and standards, and the corresponding calibration coefficients of the 85056A kit, the s-parameters of each adapter can be calculated.

The verification measurements are made by the PMVNA which has been calibrated using all five standards described earlier, with perfect isolation between the port assumed. All measurements (calibration and verification) are made with 1024 averages. The first verification standard measurement is the simultaneous measurement of the 50 Ω air-dielectric transmission line and the 25 Ω air-dielectric transmission line. The 50 Ω transmission line is connected between ports one and three, while the 25 Ω transmission line is connected between ports two and four. The measured s-parameters of the 50 Ω

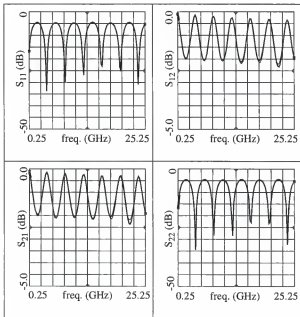


Figure 7-3. Measured s-parameters with adapters de-embedded (bold) and verification s-parameters (light: present but not distinguishable) of the 25 Ω air-dielectric transmission line, connected between ports two and four while the 50 Ω air-dielectric transmission line is connected between port one and three.

transmission line are shown in Figure 7-1 together with the s-parameters provided with the verification kit. The agreement between the two sets of data is quite good; the error between the sets of data is shown in Figure 7-2. The agreement of S_{21} and S_{12} is good in both phase and magnitude. The error in the parameter magnitudes, with respect to the verification s-parameters, is less than ± 0.05 dB over the entire measurement band, where the error is defined as $\Delta|S_{ij}| = 20\log|S_{ij}^{\text{verif}}| - 20\log|S_{ij}^{\text{meas}}|$. Also shown in Figure 7-2, is the maximum uncertainty of the provided s-parameters of the verification standards. For most

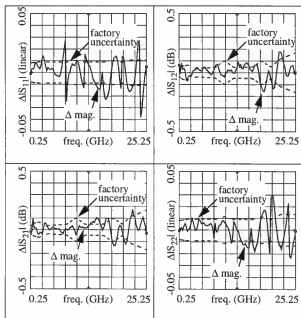


Figure 7-4. Differences between measured s-parameters and verification s-parameters of Figure 7-3 (solid) and factory uncertainty of verification s-parameters (dashed). Errors in S_{11} and S_{22} expressed as the difference of the linear magnitudes of the respective data. Errors in S_{12} and S_{21} are expressed as the difference in dB of magnitudes in dB.

of the measurement band, the errors fall within the uncertainty window of the verification data, indicating that the measurements are reasonably accurate. The phase agreement of the transmission parameters is also very good, but due to space limitations, the phase of the s-parameters are not shown. The phase error for the transmission parameters less than 2° , where $\Delta \angle S_{ij} = \angle S_{ij}^{\text{verif}} - \angle S_{ij}^{\text{meas}}$. The agreement between S_{11} and S_{22} is not as good, but the reflections represented are very small (-40 dB to -50 dB), so errors of these magnitudes are not overly objectionable. Furthermore, the adapter de-embedding process will effectively mask return losses greater than that of the adapters, which is in the 40 dB

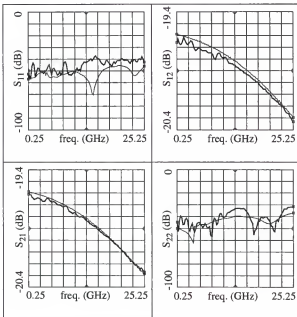


Figure 7-5. Measured s-parameters with adapters de-embedded (bold) and verification s-parameters of the 20 dB attenuator, connected between ports one and three while the 40 dB Attenuator connected between port two and four.

range. The error for these reflections are represented in Figure 7-2 in terms of a (non-relative) difference between the magnitudes of the measured and verification data, where $\Delta|S_{ii}| = |S_{ii}^{\text{verif}}| - |S_{ii}^{\text{meas}}|$. When compared to the uncertainty of the verification data, the errors of the reflection parameters are not excessive. Had the de-embedding process not been necessary, the errors would undoubtedly compared more favorably with the uncertainty bounds. The phase errors of S_{11} and S_{22} (not shown) vary rapidly over the measurement band. However, the uncertainty of verification data for these parameters is $\pm 180^\circ$.

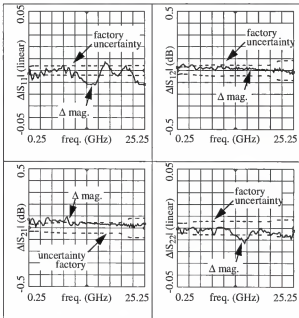


Figure 7-6. Differences between measured s-parameters and verification s-parameters of Figure 7-5 (solid) and factory uncertainty of verification s-parameters (dashed). Errors in S_{11} and S_{22} expressed as the difference of the linear magnitudes of the respective data. Errors in S_{12} and S_{21} are expressed as the difference in dB of magnitudes in dB.

The diminishing magnitudes of S_{11} and S_{22} cause the phase error of these parameters to be of little significance.

From the same PMVNA measurement, the s -parameters of the 25 Ω transmission line are also determined, and they are shown in Figure 7-3 together with the s -parameters provided with the verification kit. Again the agreement is quite good, and the two sets of data overlay each other so well as to make the verification traces barely discernible. The errors are shown in Figure 7-4 in the same format as discussed above. The errors of S_{11} and S_{22} are less than about ± 0.04 , which is good considering the large variation in the

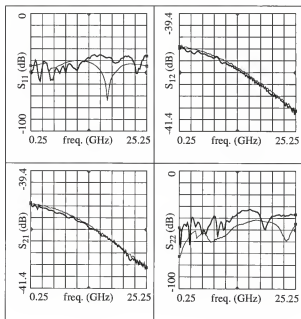


Figure 7-7. Measured s -parameters with adapters de-embedded (bold) and verification s -parameters of the 40 dB attenuator, connected between ports two and four while the 20 dB Attenuator connected between port one and three.

magnitudes of the parameters. The transmission parameters, S_{21} and S_{12} , which also vary significantly over the measurement, have less than ± 0.2 dB magnitude error, which compares reasonably to the uncertainties, and no more than 5° phase error with respect to the s-parameters provided with the verification kit.

The second verification standard measurement is the simultaneous measurement of the 20 dB attenuator and the 40 dB attenuator. The 20 dB attenuator is connected between ports one and three of the PMVNA, while the 40 dB attenuator is connected

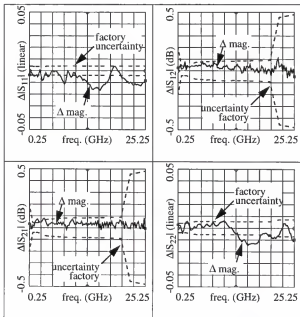


Figure 7-8. Differences between measured s-parameters and verification s-parameters of Figure 7-7 (solid) and factory uncertainty of verification s-parameters (dashed). Errors in S_{11} and S_{22} expressed as the difference of the linear magnitudes of the respective data. Errors in S_{12} and S_{21} are expressed as the difference in dB of magnitudes in dB.

between ports two and four. The measured s -parameters of the 20 dB attenuator are shown in Figure 7-5 together with the s -parameters provided with the verification kit. The differences are again quite small, as shown in Figure 7-6. The reflection parameters S_{11} and S_{22} show similar behavior to that of the 50 Ω transmission line, as is expected since the attenuator is a well matched device. The transmission parameters, S_{21} and S_{12} , agree well with less than ± 0.1 dB magnitude error and less than 4° phase error.

From the same PMVNA measurement, the measured s -parameters of the 40 dB attenuator are also found, and they are shown in Figure 7-7 together with the s -parameters provided with the verification kit. Again the agreement is quite good, as seen in the errors, shown in Figure 7-8. The reflection parameters S_{11} and S_{22} show similar behavior to other well matched devices. The errors of S_{21} and S_{12} are less than ± 0.1 dB in magnitude and less than 4° in the phase.

The calibration of the PMVNA has been shown to be accurate in terms independent of the PMVNA. Strictly speaking, the accuracy of the calibration has been established for only the specific verification standards measured. These verification standards are meant to represent some extremes of possible DUT performance, so it is argued that the accuracy of the measurements of any DUT can be reasonably assured. The verification standards as shown do not exercise all of the sixteen s -parameters measurable. However, many other combinations of the same verification standards have been made. The combinations include connecting the standards between different ports, such as one to two or one to four, and many combinations of different standards, such as the 50 Ω air-dielectric transmission line with the 40 dB attenuator. These measurements have not been shown due to space limitations, but all compare to verification data with the same general

level of accuracy. It is argued that these many measurements verify the accuracy of all sixteen s -parameters measured by the PMVNA.

Even with the acceptable accuracy indicated, the actual accuracy of the PMVNA calibration is further argued to be higher than what is indicated through the discussed measurements. The de-embedding process of the adapters from the measured verification devices must be recognized as a significant source of error. The s -parameters of the adapters include any residual errors from the 3.5mm calibrations compounded with any errors in the 2.4mm calibration process. The residual error of the basic PMVNA is argued to be something less than what is indicated through this verification process. The errors shown here are felt to be over-estimations of the actual errors of the PMVNA calibration, but are useful as conservative measures of accuracy.

The calibration of the PMVNA has been successfully completed in the theoretical framework of a general VNA calibration. The appropriateness of this approach has been established through theoretical arguments and validated through measured results. The requirements for a solution of a general calibration problem have been clarified, and new approaches to calibration standards and models have proved accurate.

CHAPTER 8

POWER SPLITTER AND COMBINER ANALYSIS

The fundamental concepts of mixed-mode scattering parameters have been established by the preceding chapters. The methods of measurement of mixed-mode s-parameters has also been thoroughly explored, and a specialized measurement system has been described. The error correction and measurement accuracy of the mixed-mode measurement system have been demonstrated. Now, the tools of mixed-mode s-parameter theory and the measurement system will be applied to the analysis of some important RF devices, structures, and circuits. This chapter will focus on power splitters and combiners, and the mixed-mode s-parameters will provide new insight into the performance of such components. Chapter 9 and Chapter 10 will focus on the analysis of several RF differential applications, and Chapter 11 will provide some important mixed-mode design concepts.

Power splitters and combiners are indispensable components in RF and microwave systems, being used in mixers, balanced amplifiers, baluns, phase shifters, and many other applications. Some of the more commonly used splitters/combiners include 180° hybrid rings [66 - 70] and 90° branch-line couplers [71 - 73]. There are many other varieties of these components such as tightly coupled microstrip [74, 75]. Some recent developments have focused on use of uniplanar transmission line to simplify MMIC implementations [76 - 79]. Recent MMIC applications include active splitters with an arbitrary phase relationship [80], baluns for double-balanced mixers [81], and linear vector modulators [82].

The performance of power splitters and combiners, particularly phase and magnitude balance, can have a strong influence on the performance of some systems. Systems such as a balanced s-parameter measurement system [83] rely on phase and magnitude relationships in power splitters/combiners to make accurate measurements. However, practical splitters/combiners, such as 3dB hybrids, have varying amounts of phase and magnitude imbalance over their bandwidth which leads to system performance degradation or measurement errors. Typically, splitter/combiner imbalance is specified across a bandwidth in terms of maximum magnitude and phase variation [66 - 82]. Manufacturers of splitters/combiners also specify imbalance with this method. For example, a typical specification of a 1.0 GHz to 12.4 GHz 180° 3 dB hybrid splitter is ± 0.8 dB amplitude imbalance and $\pm 10^\circ$ phase imbalance [35].

This chapter presents an analysis of imbalances in power splitters and combiners in terms of differential and common-modes. Portions of this work has been published by the author [84]. The analysis yields approximate expressions for the differential and common-mode normalized waves as a function of magnitude and phase imbalance. These expressions demonstrate that splitter/combiner imbalance can be represented in terms of differential and common-mode responses, and provide insight into the nature of such responses. The combined differential and common-mode analysis represents a more complete way of quantifying imbalance, and new performance metrics are suggested to simultaneously characterize phase and magnitude imbalance. These metrics promote a fundamental understanding of the physical performance of non-ideal splitters and combiners which is useful in the design and analysis of sensitive differential circuits and systems.

8.1. Splitters

Consider a splitter, such as a hybrid splitter, which has a single input and two outputs. The relationships between the two outputs can be described in several ways, but this analysis will use the total voltages and currents at the outputs in terms of differential and common-mode voltages and currents. The definitions of these quantities for a two output system are defined in Section 3.1.1, and are repeated below.

$$v_d(x) \equiv v_1 - v_2 \quad (8-1)$$

$$i_d(x) \equiv \frac{1}{2}(i_1 - i_2) \quad (8-2)$$

$$v_c(x) \equiv \frac{1}{2}(v_1 + v_2) \quad (8-3)$$

$$i_c(x) \equiv i_1 + i_2 \quad (8-4)$$

where v_1 and v_2 are the voltages at outputs one and two, respectively, and i_1 and i_2 are the currents flowing into the outputs one and two, respectively. From these voltages and currents, the differential and common-mode normalized waves have been shown to be

$$b_d = \frac{1}{\sqrt{2}}(b_1 - b_2) \quad (8-5)$$

$$b_c = \frac{1}{\sqrt{2}}(b_1 + b_2) \quad (8-6)$$

where b_1 and b_2 are normalized output waves at ports one and two, respectively.

To continue the analysis, a specific type of splitter/combiner will be used, say a 180° 3 dB hybrid in a splitter configuration. A simplified signal flow graph of this device is shown in Figure 8-1, neglecting port mismatch and the output-to-output signal path.

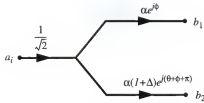


Figure 8-1. Simplified signal flow graph of 180° 3dB splitter with phase and amplitude imbalance.

Included in this flow graph is the amplitude imbalance (Δ), phase imbalance (θ), balanced loss (α) and balanced phase shift (ϕ). Note, the outputs of the splitter are ideally of equal magnitude and 180° out of phase.

From (8-5) and Figure 8-1, the differential-mode normalized output can be found to be

$$b_d = \frac{\alpha a_i e^{j\phi}}{2} (1 + (1 + \Delta) e^{j\theta}) \quad (8-7)$$

where a_i is the normalized input wave. Similarly, from (8-6) the common-mode normalized output can be found to be

$$b_c = \frac{\alpha a_i e^{j\phi}}{2} (1 - (1 + \Delta) e^{j\theta}) \quad (8-8)$$

If the phase imbalance is small ($|\theta| \ll 1$) then the complex exponential can be approximated by

$$e^{j\theta} \approx 1 + j\theta \quad (8-9)$$

Applying this approximation to (8-7), the differential-mode normalized output can be approximated as

$$b_d = \frac{\alpha a_i e^{j\phi}}{2} (2 + \Delta + j\theta(1 + \Delta)) \quad (8-10)$$

which can be expressed as

$$b_d = \frac{\alpha a_i e^{j\phi}}{2} \sqrt{(2 + \Delta)^2 + \theta^2(1 + \Delta)^2} \exp(j \cdot \tan^{-1}(\frac{\theta(1 + \Delta)}{2 + \Delta})) \quad (8-11)$$

which can be further approximated by

$$b_d = \frac{\alpha a_i e^{j\phi}}{2} \sqrt{(2 + \Delta)^2 + \theta^2(1 + \Delta)^2} e^{j\theta(\frac{1 + \Delta}{2 + \Delta})} \approx \frac{\alpha a_i e^{j\phi}}{2} (2 + \Delta) e^{j(\theta/2)} \quad (8-12)$$

where the final approximation assumes the imbalances to be small ($|\theta| \ll 1$, $\Delta \ll 1$). In a similar fashion, the common-mode normalized output wave (8-8) from the splitter can be approximated by

$$b_c = \frac{-\alpha a_i e^{j\phi}}{2} \sqrt{\Delta^2 + \theta^2(1 + \Delta)^2} e^{j(\frac{\theta(1 + \Delta)}{\Delta})} = \frac{-\alpha a_i e^{j\phi}}{2} \sqrt{\Delta^2 + \theta^2} e^{j(\theta/\Delta)} \quad (8-13)$$

In the case of a 180° splitter, the common-mode wave can be considered to be an unintended signal, and its magnitude is directly proportional to magnitude imbalance of the splitter. The phase imbalance has a second order effect on the magnitude of the common-mode wave, but it has a more significant effect on the phase of the common-mode signal. As can be seen from (8-12), the magnitude of the differential-mode wave is affected primarily by the magnitude imbalance of the splitter. However, since $\Delta \ll 1$, one can see the splitter imbalance is a small error in the desired output signal.

The common-mode rejection ratio can be adapted from differential circuit concepts as a measure of the imbalance in a splitter. The common-mode rejection ratio (CMRR) [4] can be adapted to normalized waves by the definition

$$\text{CMRR} = \left| \frac{b_d}{b_c} \right| \quad (8-14)$$

which, in the case of a 180° splitter, can be approximated by

$$\text{CMRR} = \sqrt{\frac{(2 + \Delta)^2 + \theta^2(1 + \Delta)^2}{\Delta^2 + \theta^2(1 + \Delta)^2}} = \frac{2 + \Delta}{\sqrt{\Delta^2 + \theta^2}} \quad (8-15)$$

This quantity gives a single measure of the effects of both magnitude and phase imbalance in a splitter.

The relation between CMRR and the traditional measures of imbalance can be examined by plotting contours of constant CMRR from (8-14) as a function of θ and $1 + \Delta$, as shown in Figure 8-2. By plotting θ and $1 + \Delta$ in rectangular coordinates, these contours form ellipses, and by choosing units of degrees and dB for phase and magnitude imbalance, respectively, the specifications can be plotted on the same plane as horizontal and vertical lines. The phase and magnitude imbalance specification lines define a rectangle in the imbalance plane. The lowest CMRR in this rectangle, the result of maximum phase and maximum magnitude imbalance occurring simultaneously, is indicated by the ellipse which intersects the corners of the rectangle.

Another significant ellipse is the one which is entirely contained in the specification rectangle. This ellipse represents the highest CMRR that can occur while one of the imbalances is at its maximum specified limit. In Figure 8-2, such an ellipse is limited by the magnitude imbalance, indicating the worst-case best performance is limited by magnitude imbalance. The shaded regions in Figure 8-2 indicate performance that is within the traditional specification limits, but has relatively poor CMRR.

Had the phase specifications been made such that their representative lines were also tangent to the smallest dashed ellipse, areas of lower CMRR would still exist in the corners of the resulting rectangle. These regions illustrate the advantage of specifying minimum CMRR over maximum magnitude and phase imbalance. Two splitters with the same magnitude and phase specifications may have different minimum CMRR. However, if minimum CMRR is specified, no such ambiguity exists, and the CMRR ellipse indicates the maximum simultaneous phase and magnitude imbalance.

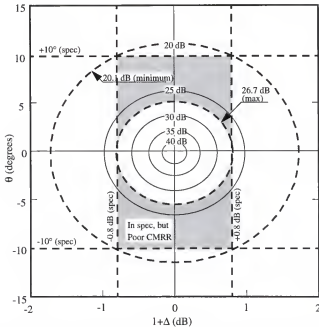


Figure 8-2. Loci of constant CMRR (dB) in the plane of phase imbalance, θ (degrees), versus magnitude imbalance, $1+\Delta$ (dB). Dashed lines indicate manufacturer's specifications, and dashed ellipses indicate worst-case and best-case CMRR interpretation of specifications. Shaded regions indicate performance within specification with poor CMRR.

To illustrate the use of above analysis, the s-parameters of a 180° 3dB hybrid splitter/combiner (Merrimac, part number HJM-4R-6.5G [35]) were measured. The measurements were made on a standard HP8510C two-port VNA with 3.5mm coaxial connectors, with a sliding-load TOSL calibration. In this case, a “round-robin” method was used to determine the multi-port s-parameters of the splitter. This method employs multiple two-port measurements of the device, with remaining ports of the device terminated in precision 50Ω loads. A total of three two-port s-parameter sets were generated as the three ports were measured two at a time, with the remaining port terminated. The errors due to any imperfect termination of the free port were considered to be negligibly small. The

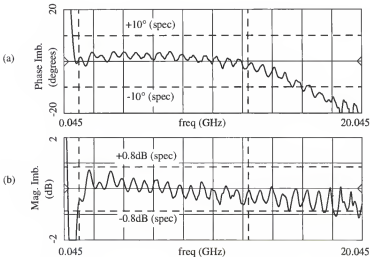


Figure 8-3. Measured imbalance of a 180° 3dB hybrid power splitter with dashed lines indicating manufacturer's specifications.

a) Measured magnitude imbalance in dB. b) Measured phase imbalance in degrees.

overall three-port s -parameters of the splitter were constructed from the appropriate elements of the three two-port s -parameter sets.

A direct measurement of the output magnitude imbalance is shown in Figure 8-3(a). This power splitter is specified to have no more than ± 0.8 dB magnitude variation from 1 GHz to 12.4 GHz. The measured phase imbalance is shown in Figure 8-3(b). Over its bandwidth, this splitter should have a maximum phase variation of $\pm 10^\circ$. As can be seen from these figures, the splitter is within specification.

The differential and common-mode responses of the splitter were calculated from the measured s -parameters. With the definitions $S_{1i} = b_1/a_i$, and $S_{2i} = b_2/a_i$, and the use of (8-5) and (8-6), it is easily shown that

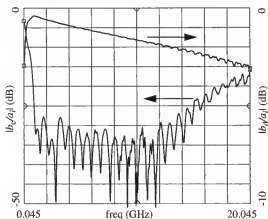


Figure 8-4. Ratio in dB of normalized common-mode-to-input waves and normalized differential-mode-to-input waves of a 180° 3dB hybrid power splitter. Data is derived from measured data. Note the different vertical scales.

$$S_d = \frac{b_d}{a_i} = \frac{1}{\sqrt{2}}(S_{1i} - S_{2i})$$

$$S_c = \frac{b_c}{a_i} = \frac{1}{\sqrt{2}}(S_{1i} + S_{2i}) \quad (8-16)$$

which are readily calculated from measured data. The magnitude of these differential and common-mode s-parameters are shown in Figure 8-4. This figure clearly shows the generation of a common-mode signal at the output of the splitter. Outside of the splitter's intended bandwidth, the common-mode response becomes large in magnitude, and the differential-mode response shows ripple in its magnitude.

The CMRR of the splitter can also be easily calculated from measured s-parameters. With the use of (8-14) and (8-16)

$$\text{CMRR} = \left| \frac{S_d}{S_c} \right| = \left| \frac{S_{1i} - S_{2i}}{S_{1i} + S_{2i}} \right| \quad (8-17)$$

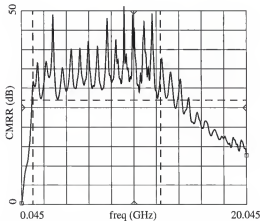


Figure 8-5. Common-mode rejection ratio (magnitude) in dB of a 180° 3dB hybrid power splitter. Data is derived from measured data.

The calculated CMRR magnitude is shown in Figure 8-5. In the specified bandwidth, the splitter has approximately 30 dB CMRR, decreasing rapidly out of band. The minimum measured CMRR is 27.2 dB.

The measured imbalance is plotted on the imbalance plane of θ and $1+\Delta$ in Figure 8-6 over the specification bandwidth of 1.0 GHz to 12.4 GHz. The data is entirely contained within the 27.2 dB ellipse, which falls within the limits of the highest possible CMRR specification of 26.7 dB (see Figure 8-2).

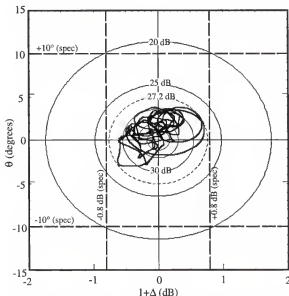


Figure 8-6. Measured imbalance of 180° 3dB hybrid power splitter (1.0 GHz to 12.4 GHz) plotted in the plane of phase imbalance, θ (degrees), versus magnitude imbalance, $1+\Delta$ (dB), with loci of constant CMRR (dB). Dashed lines indicate manufacturer's specifications, and dashed ellipse indicates minimum measured CMRR.

8.2. Combiners

The effect of magnitude and phase imbalance on power combiners can also be analyzed in terms of differential and common-mode normalized waves. In a typical hybrid power splitter/combiner, two signals will be combined in two fashions simultaneously, producing two outputs. For example, the 3 dB hybrid 180° splitter/combiner will produce the sum of two input signals at one output and the difference of the signals at the second output. The combiner can be analyzed as two single output combiners, each delivering the sum or difference signal as appropriate. Therefore, only a 180° combiner will be considered, with generalizations to any phase of combining. The simplified signal flow graph of a 180° combiner is similar to that of the splitter, and is shown in Figure 8-7. A linear combination of differential and common-mode waves is assumed at each input

$$a_1 = \frac{a_c + a_d}{\sqrt{2}} \quad a_2 = \frac{a_c - a_d}{\sqrt{2}} \quad (8-18)$$

which can be found by solving the forward wave relations similar to (8-5) and (8-6) for a_1 and a_2 . The total output of the combiner is then a function of a_d , a_c and imbalances Δ and θ . The 180° combiner has an output

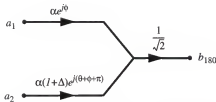


Figure 8-7. Simplified signal flow graph of 180° 3dB combiner with phase and amplitude imbalance.

$$b_{180} = \frac{\alpha e^{j\phi}}{2} [(a_c + a_d) - (1 + \Delta)e^{j\theta}(a_c - a_d)] \quad (8-19)$$

A rejection ratio can not be directly applied to combiners. However, a common-mode combiner response ratio (RCM_{comb}) can be defined as

$$RCM_{\text{comb}} = \left| \frac{b_{180}}{a_c} \right| \bigg|_{a_d=0} \quad (8-20)$$

which can be shown to be approximately

$$RCM_{\text{comb}} = \frac{\alpha}{2} \sqrt{\Delta^2 + \theta^2(1 + \Delta)^2} \quad (8-21)$$

Equations (8-19) and (8-21) indicate that, due to imbalance, the output of the combiner is clearly influenced by the presence of a common-mode signal at the inputs.

In addition to a response from an undesired mode, imbalance in the combiner also causes error in the combining of the desired mode. To illustrate this, consider the differential-mode response ratio (RDM_{comb}) of the 180° combiner defined as

$$RDM_{\text{comb}} = \left| \frac{b_{180}}{a_d} \right| \bigg|_{a_c=0} = \frac{\alpha}{2} \sqrt{(2 + \Delta)^2 + \theta^2(1 + \Delta)^2} \quad (8-22)$$

This illustrates the error in the combination of the desired mode is a function of imbalance. It is interesting to note that the ratio of (8-22) and (8-21) is equal to the CMRR of the splitter in (8-15).

The measured s -parameters of the example splitter of Section 8.1 can also be examined for combiner performance. The response ratios of (8-20) can be related to the measured s -parameters by

$$\text{RCM}_{\text{comb}} = \left| \frac{b_3}{(a_1 + a_2)/\sqrt{2}} \right| = \sqrt{2} \left| \frac{a_1}{b_3} + \frac{a_2}{b_3} \right|^{-1} = \sqrt{2} \left| \frac{1}{S_{31}} + \frac{1}{S_{32}} \right|^{-1} \quad (8-23)$$

where port three is the output and ports one and two are the inputs. Similarly, the response ratios of (8-22) can be related to the measured s-parameters by

$$\text{RDM}_{\text{comb}} = \sqrt{2} \left(\frac{1}{S_{31}} - \frac{1}{S_{32}} \right)^{-1} \quad (8-24)$$

Plots of these ratios are not included since they are closely related to the splitter performance shown in Figure 8-5.

8.3. Extensions to Arbitrary Phase

The above combined differential and common-mode analysis suggests an alternate, and useful, way of interpreting the imbalances in a splitter/combiner. The measured s-parameters of a practical power splitter further illustrate the combined-mode, or mixed-mode, concepts. From the application of these concepts, CMRR is found to quantify the effects of both magnitude and phase imbalance in power splitters. The above analysis considers only a 180° power splitter, but the analysis is easily extended to an arbitrary phase relation. For an arbitrary phase splitting the CMRR is exactly

$$\text{CMRR} = \left| \frac{1 - (1 + \Delta)e^{j(\Omega + \Theta)}}{1 + (1 + \Delta)e^{j(\Omega + \Theta)}} \right| \quad (8-25)$$

where Ω is the phase of the split (e. g., 0°, 180°). With first order approximations, (8-25)

has been simplified for three common angles, and these results are summarized in

Table 8-1. A study of errors resulting from the approximations ($|\Theta| \ll 1$, $\Delta \ll 1$) indicates both forms to be quite accurate over practical values of phase and magnitude imbalance.

For a CMRR of 25 dB, both approximations have a maximum error of less than ± 0.2 dB.

Note that when Ω is not 180° , CMRR does not have the traditional meaning or value, so that its name is misleading. For example, with $\Omega = 0^\circ$ CMRR is ideally zero since the differential-mode output is ideally zero. For 0° splitters/combiners another metric is more conceptually natural, namely differential-mode-rejection-ratio (DMRR) which can be defined as $DMRR=1/CMRR$. For 90° , and other angles, neither DMRR nor CMRR is interpreted in a typical fashion. The use of the single metric CMRR for all phases of splitters is both simple and accurate, if its meaning is properly interpreted for each phase splitter.

Table 8-1. Splitter CMRR for common values of Ω

Ω	CMRR (1 st approx.)	CMRR (2 nd approx.)	Ideal Value
0°	$\sqrt{\frac{\Delta^2 + \theta^2(1 + \Delta)^2}{(2 + \Delta)^2 + \theta^2(1 + \Delta)^2}}$	$\frac{\sqrt{\Delta^2 + \theta^2}}{2 + \Delta}$	0
90°	$\sqrt{\frac{(1 + \theta(1 + \Delta))^2 + (1 + \Delta)^2}{(1 - \theta(1 + \Delta))^2 + (1 + \Delta)^2}}$	$\sqrt{\frac{1 + \Delta + \theta}{1 + \Delta - \theta}}$	1
180°	$\sqrt{\frac{(2 + \Delta)^2 + \theta^2(1 + \Delta)^2}{\Delta^2 + \theta^2(1 + \Delta)^2}}$	$\frac{2 + \Delta}{\sqrt{\Delta^2 + \theta^2}}$	∞

The effects of magnitude and phase imbalance in power combiners have also been described through a mixed-mode analysis. Response ratios such as RDM and RCM quantify these effects. The combiner analysis considers only a 180° power combiner, but the analysis is easily extended to an arbitrary phase relation. For an arbitrary phase combining these responses are exactly

$$\begin{aligned} \text{RDM} &= \frac{\alpha}{2} |1 - (1 + \Delta)e^{j(\Omega + \theta)}| \\ \text{RCM} &= \frac{\alpha}{2} |1 + (1 + \Delta)e^{j(\Omega + \theta)}| \end{aligned} \quad (8-26)$$

To a first order approximation, (8-26) has been simplified for three common angles, and these results are summarized in Table 8-2.

The impact on systems using power splitters and combiners can now be considered in terms of differential and common-mode responses. The effects of an undesired signal mode, such as common-mode, can be investigated with simple network theory, and limits on such undesired signals can be set through the use of CMRR.

Table 8-2. Combiner RDM and RCM for common values of Ω

Ω	RDM	RCM
0°	$\frac{\alpha}{2} \sqrt{\Delta^2 + \theta^2(1 + \Delta)^2}$	$\frac{\alpha}{2} \sqrt{(2 + \Delta)^2 + \theta^2(1 + \Delta)^2}$
90°	$\frac{\alpha}{2} \sqrt{(1 + \theta(1 + \Delta))^2 + (1 + \Delta)^2}$	$\frac{\alpha}{2} \sqrt{(1 - \theta(1 + \Delta))^2 + (1 + \Delta)^2}$
180°	$\frac{\alpha}{2} \sqrt{(2 + \Delta)^2 + \theta^2(1 + \Delta)^2}$	$\frac{\alpha}{2} \sqrt{\Delta^2 + \theta^2(1 + \Delta)^2}$

CHAPTER 9

THIN-FILM METAL-ON-CERAMIC STRUCTURES

This chapter examines a series of RF differential structures that are fabricated on ceramic substrates. The structures are designed to provide examples of the use of mixed-mode s -parameter concepts in the measurement and analysis of RF differential structures. The test results are from differential transmission structures. These structures provide important information about practical differential implementation of one of the most basic RF components, the transmission line. These experiments examine the performance of various differential transmission line in terms of (1) mode-specific transmission behavior and (2) line-to-line crosstalk (coupling).

All structures are fabricated on an IC scale, and they are all designed to be directly probed with $150\mu\text{m}$ pitch probes. The structures are thin-film metal-on-ceramic structures, fabricated with thin-film gold ($4\mu\text{m}$ thick $\pm 0.25\mu\text{m}$) on a polished alumina substrate ($\epsilon_r \approx 9.9$, $\tan\delta \approx 0.001$). Resistors are fabricated with a resistive layer of a nickel-chrome (NiCr) metal approximately 400\AA thick, with a sheet resistance of about $40\ \Omega/\text{square}$. In this case, the resistors were left un-tuned at their fabricated values. All photo-masks required for fabrication have been generated in the University of Florida Microelectronics Laboratory, and all fabrication has been done in the Motorola Thin-Film Research Laboratory in Plantation, Florida. All measurements presented in this chapter were made with 1024 averages and half-leakage correction using the methods presented in Chapter 6.

9.1. Differential Transmission Lines

9.1.1. Uniform Differential Transmission Line

The first structure presented is a simple coplanar wave guide (CPWG) transmission line pair. The constituent transmission lines are placed close together so that the pair can be considered a single differential transmission line. Their closeness causes the individual transmission lines to be coupled, so that they act as a single differential transmission line. The transmission line, shown in Figure 9-1, has a constant cross-section over its length, and is therefore called a uniform differential transmission line. Each constituent transmission line was designed to have a nominal 50Ω characteristic impedance¹. The signal conductors are $104\mu\text{m}$ wide, and the spaces between the edge of the signal conductors and the edge of the ground planes are $58\mu\text{m}$. The ground strip between the signal conductors is $80\mu\text{m}$ wide. The signal conductors are $4000\mu\text{m}$ long, and the outer ground planes are $400\mu\text{m}$ wide. The shaded regions, $400\mu\text{m}$ wide, represent strips of resistor material which have been added to reduce parasitic resonances of the structure at high frequencies.

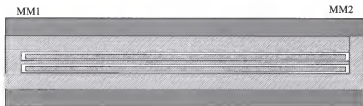


Figure 9-1. Layout of uniform differential transmission line with intermediate ground.

1. The design of each line was a single signal conductor design neglecting any coupling between the two adjacent transmission lines and the effects of the truncated ground planes. In other words, the design assumed uncoupled transmission lines. Thus the even- and odd-mode characteristic impedances are assumed to be 50Ω during the design process.

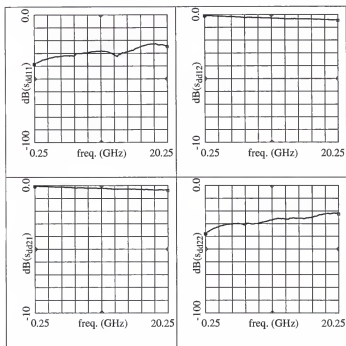


Figure 9-2. Measured pure differential s-parameters (DD) of structure of the uniform differential transmission line, magnitude in dB.

The measured mixed-mode s-parameters of the uniform differential transmission line are shown in Figure 9-2 to Figure 9-5. The magnitudes in dB of the pure differential-mode responses (DD) are plotted versus frequency in Figure 9-2. From this figure, one can see that the structure behaves as a matched, low-loss transmission line to the differential mode signals. The structure has better than 20 dB differential return loss at 20 GHz, and less than 4 dB differential insertion loss at 20 GHz. The actual differential character-

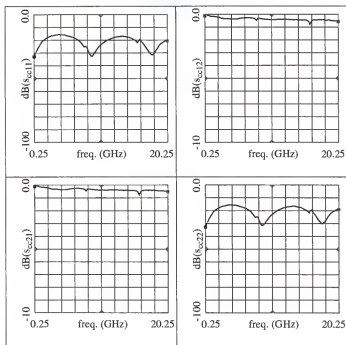


Figure 9-3. Measured pure common-mode s-parameters (CC) of structure of the uniform differential transmission line, magnitude in dB.

istic impedance is approximately 101Ω , which is slightly more than twice the nominal single-ended impedance of the individual lines. The small deviation from the nominal single-ended impedance indicates the individual lines are loosely coupled.

The magnitudes in dB of the pure common-mode responses (CC) are plotted versus frequency in Figure 9-3. These measurements indicate that the structure is good transmission line to the common-mode, but it is not as well matched as to the differential-

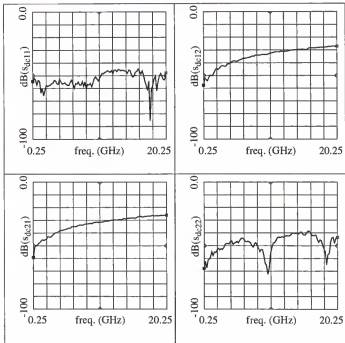


Figure 9-4. Measured common-to-differential mode-conversion s-parameters (DC) of structure of the uniform differential transmission line, magnitude in dB.

mode. The periodic variations in the common-mode return loss indicate an impedance miss-match, although slight. The actual common-mode characteristic impedance is approximately 29Ω . Note, however, that the two reflection parameters are nearly indistinguishable, indicating a high level of port symmetry, as is expected from the layout.

The magnitudes in dB of the mode-conversion responses (DC and CD) are plotted versus frequency in Figure 9-4 and Figure 9-5. These plots show a reasonably low level of

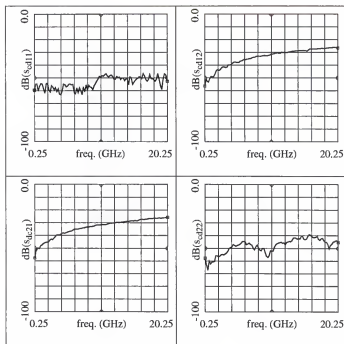


Figure 9-5. Measured differential-to-common mode-conversion s-parameters (CD) of structure of the uniform differential transmission line, magnitude in dB.

mode-conversion in reflection (in the -40 dB to -50 dB range), but indicate more significant levels of conversion in the transmission parameters as frequency increases. These mode-conversions are most likely due to the combined effect of probe-to-probe crosstalk and raw imbalance in the PMVNA.

9.1.2. Balanced Step Differential Transmission Line

The second structure presented is a differential transmission line with a change in the width of both signal conductors. This change in the width is equal for both conductors, and is therefore called a balanced, or symmetric, step in width. Referring to Figure 9-6, the section of transmission line with the wide signal conductors is cascaded between two sections of narrower line. Both end sections are of the same dimensions as the nominal 50Ω single-ended characteristic impedance (conductors $104\mu\text{m}$ wide, spaces $58\mu\text{m}$ wide) as examined in Section 9.1.1. The middle section has conductors $140\mu\text{m}$ wide and spaces $40\mu\text{m}$ wide, and is $2000\mu\text{m}$ long. Both end sections are $1000\mu\text{m}$ long, making the entire transmission line $4000\mu\text{m}$ long.

The measured pure differential-mode (DD) results from the balanced step-in-width transmission line are shown in Figure 9-7, as magnitudes in dB. The differential return loss has a distinctive periodic variation with frequency. Furthermore, the transmission parameters also have a slight periodic variation. These plots, together with polar plots of the differential data (not shown) indicate a step in the differential characteristic impedance. In other words, a differential-mode signal encounters a transmission line system with impedance first of Z_1 , then Z_2 , then back to Z_1 . This type of transmission line system is often

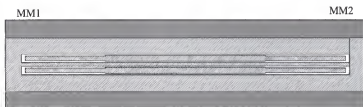


Figure 9-6. Layout of differential transmission line with symmetrical step in conductor widths.

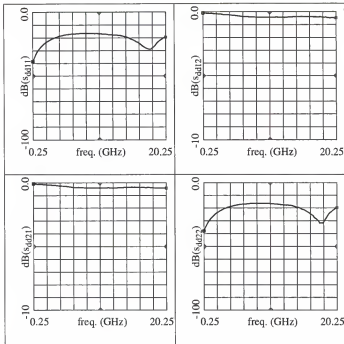


Figure 9-7. Measured pure differential s-parameters (DD) of structure of the balanced step differential transmission line, magnitude in dB.

called a Beatty standard [85]. This behavior of the differential transmission line of Figure 9-6 is not surprising since the constituent single-ended transmission lines each embody a Beatty standard. Analysis shows the differential characteristic impedance of the center section to be 81Ω , while both end sections are 101Ω .

The pure common-mode response (CC) of Figure 9-6 is shown in Figure 9-8 as magnitudes in dB. The periodic nature of the common-mode response is more evident than that of the differential-mode. Clearly the common-mode response of the transmis-

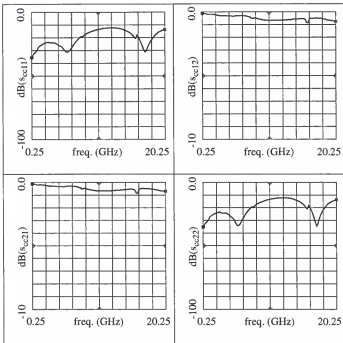


Figure 9-8. Measured pure common-mode s-parameters (CC) of structure of balanced step differential transmission line, magnitude in dB.

sion line is also that of a Beady standard. Analysis shows the common-mode characteristic impedance of the center section to be 23Ω , while both end sections are 29Ω .

Furthermore, the return loss minima occurs at lower frequencies in the balanced step system than in the uniform transmission line. This downward shift indicates that the common-mode electrical length of the balanced step section is longer than that of an equal length of uniform transmission line. This difference is due to the quasi-TEM nature of

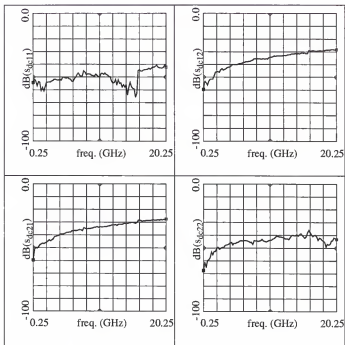


Figure 9-9. Measured common-to-differential mode-conversion s-parameters (DC) of structure of balanced step differential transmission line, magnitude in dB.

CPWG, where the velocity of propagation is a function of the transmission line cross-section. It is also interesting to note that minima in the differential return loss occur at about twice the frequency of the corresponding common-mode minima. This indicates that the overall structure has a differential electrical length that is about half that of the common-mode.

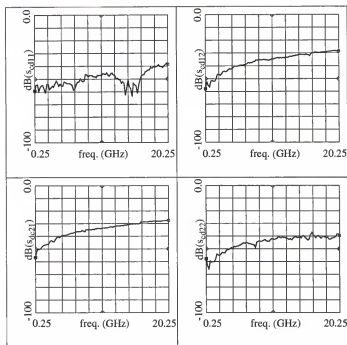


Figure 9-10. Measured differential-to-common mode-conversion s-parameters (CD) of structure of balanced step differential transmission line, magnitude in dB.

The measured mode-conversions responses (DC and CD) are shown in Figure 9-9 and Figure 9-10. Despite the step in the conductor widths, the mode-conversion levels are essentially the same as the uniform transmission line of Figure 9-1. It can be observed that, at any distance along the line, the signal conductors are of equal width. This type of structure can be said to have electromagnetic field symmetry (that is the even and odd-mode exist in contrast to the c and π -modes). As a result of this symmetry, the structure

has a high degree of balance, that is, there is low levels of mode-conversion. The relationship between field symmetry and mode-conversion will be further examined in the following sections.

9.1.3. Unbalanced Step-Up Differential Transmission Line

The third structure presented has a change in the width of only one signal conductor. As shown in Figure 9-11, this structure is similar to that of the previous section, but in this case only one of the signal conductors have a step in width. Like the previous transmission line, the section of transmission line with the wide signal conductors is cascaded between two sections of narrower line. Both end sections are of the same dimensions as the nominal 50Ω single-ended characteristic impedance (conductors $104\mu\text{m}$ wide, spaces $58\mu\text{m}$ wide) as examined in Section 9.1.1. The middle section has one signal conductor $140\mu\text{m}$ wide and spaces $40\mu\text{m}$ wide, but the other signal conductor is $104\mu\text{m}$ wide with $58\mu\text{m}$ wide spaces. Again the middle section is $2000\mu\text{m}$ long, and both end sections are $1000\mu\text{m}$ long, making the entire transmission line $4000\mu\text{m}$ long.

Since the middle section does not have signal conductors of equal width, the differential transmission line is considered to be unbalanced. As discussed in Section 3.1.1, the structural asymmetry in the coupled transmission lines leads to a lack of field symme-

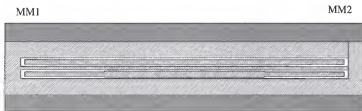


Figure 9-11. Layout of differential transmission line with unbalanced step-up in conductor width.

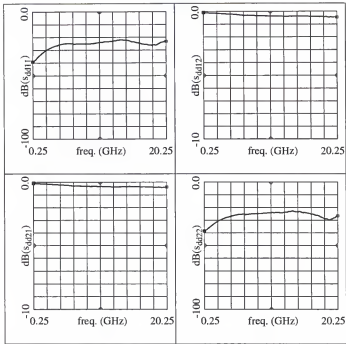


Figure 9-12. Measured pure differential s -parameters (DD) of structure of the unbalanced step-up differential transmission line, magnitude in dB.

try. Hence, the even and odd-modes are no longer defined, being replaced by the more general c and π -modes.

The measured pure differential-mode (DD) responses are shown in Figure 9-12. The structure acts as a reasonably good differential-mode transmission line, despite its unbalanced nature. The differential return loss is quite good (especially when compared to that of the uniform transmission line of Section 9.1.1), but it does show some periodic

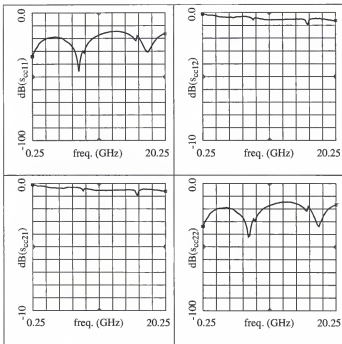


Figure 9-13. Measured pure common-mode s -parameters (CC) of structure of the unbalanced step-up differential transmission line, magnitude in dB.

variations indicating a Beady-like effect. The minima in the differential return loss of the unbalanced structure are at slightly higher frequencies than the balanced step system. This difference indicates that the differential-mode electrical length of the unbalanced section is less than that of the balanced section of the same physical length. Recall that the differential and common-modes do not actually exist on asymmetrical structures, but that

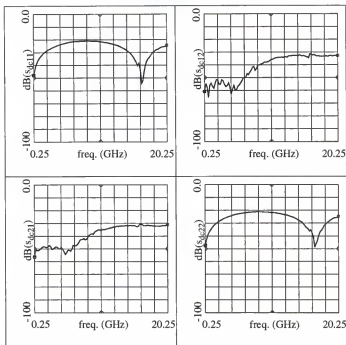


Figure 9-14. Measured common-to-differential mode-conversion s-parameters (DC) of structure of the unbalanced step-up differential transmission line, magnitude in dB.

related differential and common-mode responses can be defined (or measured) by use of a zero-length symmetric reference transmission line (see Appendix C).

The measured pure common-mode (CC) responses are shown in Figure 9-13. The common-mode response of the unbalanced step line is very similar to that of the balanced step system. The most notable differences are in the reflection parameters, particularly at low frequencies. The common-mode return loss minima occur at very slightly higher fre-

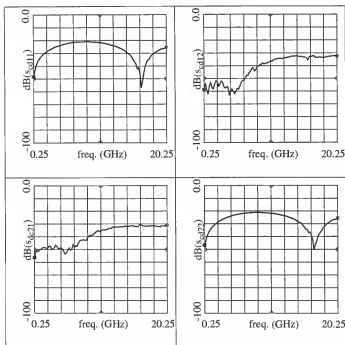


Figure 9-15. Measured differential-to-common mode-conversion s-parameters (CD) of structure of the unbalanced step-up differential transmission line, magnitude in dB.

quencies in the unbalanced system, again indicating that the common-mode electrical length of the unbalanced section is less than that of the balanced section.

The measured mode-conversions responses (DC and CD) of the unbalanced structure are shown in Figure 9-14 and Figure 9-15. The level of conversion is higher in this structure than in the uniform or balanced step transmission lines (particularly in the reflection parameters). The mode-conversion in reflection is particularly strong. These reflec-

tion parameters exhibit behavior that is very similar to that of a traditional Beady standard. Furthermore, the mode-conversion reflections are very similar to the pure differential-mode reflections. However, the minima in the mode-conversion reflections occur at lower frequencies than the differential-mode. This indicates an effective mode-conversion electrical length that is higher than the differential-mode. Alternatively, the effective velocity of propagation of the mode-conversion is less than that of the differential-mode. Furthermore, the common-mode propagation velocity is about half of the differential mode. Hence, the mode-conversion equivalent propagation velocity is greater than the common-mode, but less than the differential mode. This relationship is consistent with the concepts of mode-conversion. The mode-conversion response can be considered to be one mode for some of its propagation, and the other mode for the remainder. As a result the effective propagation velocity of the mode-conversion response will be some sort of average of the velocities of the two pure modes.

Also note that the two directions of mode-conversion are equal for this structure. The differential-to-common-mode conversion (CD) is equal to the common-to-differential-mode conversions (DC).

9.2. Comparison Between Measurements and Simulations

To illustrate the on-wafer measurement accuracy of the PMVNA, two simple differential structures have been measured and compared to simulated results. These structures have been chosen because they provide good examples of mixed-mode behavior, such as mode conversion. Furthermore, these structures can be simulated with a reasonably high degree of confidence in the accuracy of the results. The results of this section have been published, along with a description of the PMVNA [34].

9.2.1. Unbalanced Step Differential Transmission Line

The first device, shown in Figure 9-16, is an unbalanced stepped impedance transmission line pair. In contrast to the structures presented in Section 9.1, this device does not possess port symmetry. In other words, the ports are not interchangeable, as the equivalent impedance seen by mixed-mode port one is different than that of mixed-mode port two. As in Section 9.1 the structure is fabricated with thin-film gold ($4\mu\text{m}$ thick $\pm 0.25\mu\text{m}$) on a polished alumina substrate ($\epsilon_r = 9.9$, $\tan\delta = 0.001$). The structure has three sections of different impedances, where Lines A and C are pairs of nominally (single-ended) 69Ω transmission lines, and Line B provides a pair of transmission lines with different impedances (one 72Ω , the other 40Ω). The lengths of the three sections are shown in Figure 9-16, and are known $\pm 1\mu\text{m}$. The vertical dimensions of the structure are shown in Figure 9-17. The fabrication tolerance on the spaces between the conductors is $\pm 1\mu\text{m}$.

The structure of Figure 9-16 has been simulated in Hewlett-Packard's Microwave Design System (MDS) [32]. The simulation employs the five conductor coupled micro-

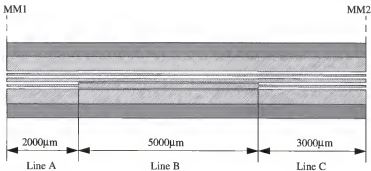


Figure 9-16. Layout of unbalanced step differential transmission line for comparison between measured and simulated results.

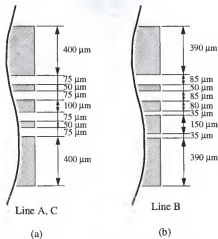


Figure 9-17. Detail layout of Figure 9-16 showing critical dimensions.
 a) Detail of Lines A and C.
 b) Detail of Line B.

trip transmission line model incorporated within MDS with the first, third and fifth conductor grounded. See Figure 9-18 for the schematics of this circuits. The transitions between the sections of line are modeled with the MDS microstrip step-in-width model, but the coupling between each step is not modeled. The simulation makes a quasi-static approximation, but includes metal losses ($\sigma = 4.1 \times 10^7 \text{ S/m}$) and dielectric losses. The nominal values for all dimensions and physical properties are used in all simulations, with the exception of the end sections (Lines A, C). The lengths of these sections are reduced by the distance the probes overlap the end of the structures. It is assumed that the overlap is 25 μm at each end, but the actual probe overlap can vary, causing discrepancies between measured and simulated data. The simulations generate standard s-parameters which are converted to mixed-mode s-parameters through the transformation (3-44).

The corrected measured and simulated mixed-mode s-parameters of the asymmetrically stepped transmission line pair are plotted in Figure 9-19 through Figure 9-22. The agreement between the measured and simulated data is quite good across the entire bandwidth. The measured and simulated data share many of the unusual fine features of the responses. For example, the measured S_{cc12} has several abrupt increases in insertion loss at about 6.1 GHz, 12.2 GHz and 18.3 GHz; likewise, the simulated data shows similar responses, although at slightly lower frequencies. Additionally, the device demonstrates a strong level of mode-conversion (S_{dc} , S_{cd}), and the agreement between measured and simulated mode-conversion indicates that the effects of imbalance in the PMVNA are largely removed through calibration.

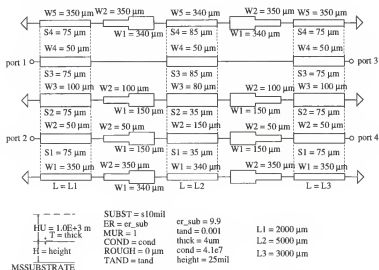


Figure 9-18. MDS schematic of unbalanced step differential transmission line of Figure 9-16 for comparison between measured and simulated results.

Note that both the measured and simulated pure differential parameters (S_{dd}), common-mode parameters (S_{cc}), and mode-conversion parameters (S_{dc} , S_{cd}) all show approximately periodic variations across frequency. As discussed in Section 9.1, these variations are analogous to the effects of a single transmission line with a step in impedance. Hence, each partition of the mixed-mode s-parameter matrix (S_{dd} , S_{cc} , S_{dc} , S_{cd}) can be interpreted as an effective single transmission line with stepped impedance.

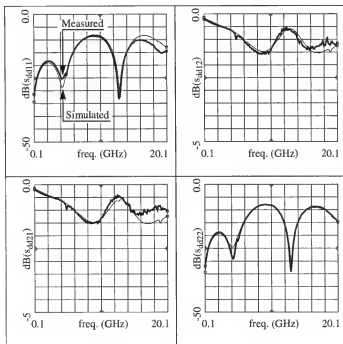


Figure 9-19. Measured (heavy) and simulated (light) pure differential s-parameters (DD) of structure of the unbalanced step differential transmission line of Figure 9-16, magnitude in dB.

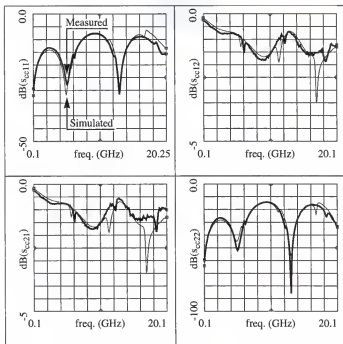


Figure 9-20. Measured (heavy) and simulated (light) pure common-mode s -parameters (CC) of structure of the unbalanced step differential transmission line of Figure 9-16, magnitude in dB.

By close examination of Figure 9-19 through Figure 9-22, it is found that only ten of the mixed-mode s -parameters are clearly unique². This is a property of reciprocal devices. In contrast, the devices of Section 9.1 possessed only six unique mixed-mode s -parameters. This difference is due to the fact that the devices of Section 9.1 all possessed

2. Random noise and measurement errors make each parameter unique to some degree. In the context of this discussion, a unique parameter is one that is substantially different than all other parameters.

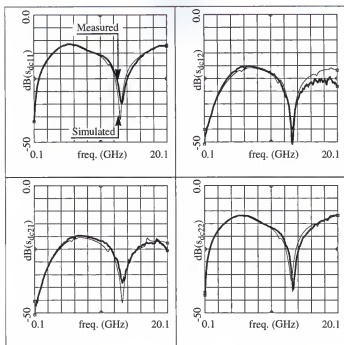


Figure 9-21. Measured (heavy) and simulated (light) common-to-differential mode-conversion s-parameters (DC) of structure of the unbalanced step differential transmission line of Figure 9-16, magnitude in dB.

port symmetry, where the device of Figure 9-16 does not. In general, it can be shown that for a mixed-mode reciprocal device, $S^{mm} = (S^{mm})^T$. Further consideration of the properties of mixed-mode s-parameters will be made in Chapter 11.

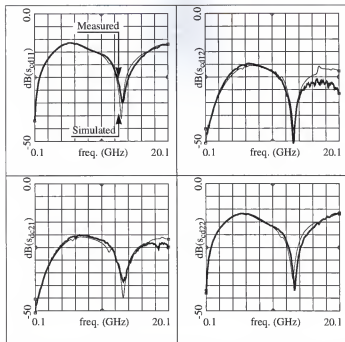


Figure 9-22. Measured (heavy) and simulated (light) differential-to-common mode-conversion s-parameters (CD) of structure of the unbalanced step differential transmission line of Figure 9-16, magnitude in dB.

9.2.2. Balanced Step Differential Transmission Line

The second device, shown in Figure 9-23, is an balanced stepped impedance transmission line pair. Like the previous structure, this device does not possess port symmetry. The fabrication details for this device are the same as those of the previous device. The structure again has three sections of different impedances, where Lines D and F are pairs of nominally (single-ended) 69Ω transmission lines, and Line E provides a pair of trans-

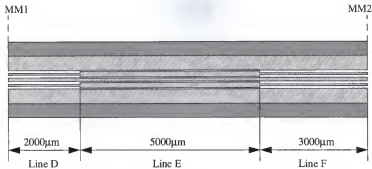


Figure 9-23. Layout of balanced step differential transmission line for comparison between measured and simulated results.

mission lines with equal impedances (40Ω). The vertical dimensions of the structure are shown in Figure 9-24.

The corrected measured and simulated mixed-mode s-parameters of the balanced step transmission line pair are plotted in Figure 9-25 through Figure 9-28. Again, the agreement between measured and simulated data is good. Like the unbalanced structure, the balanced structure demonstrates the periodic responses analogous to a single transmission line with a step in impedance. The balanced structure supports only differential and common-mode, and hence no significant mode-conversion occurs. Referring to Figure 9-27 and Figure 9-28, the measured mode-conversion s-parameters are small, and are most likely generated by probe crosstalk and residual errors in the calibration.

From these two structures, one can see that the measured mixed-mode s-parameters compare well to the simulated parameters. This is indication that the PMVNA on-wafer calibration is accurate. Of course, the conclusion of accurate measurement results here rests on the assumption of simulation accuracy. The accuracy of the simulations can

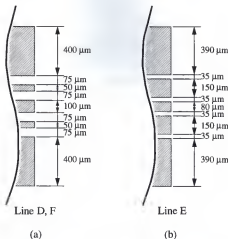


Figure 9-24. Detail layout of Figure 9-23 showing critical dimensions.
 a) Detail of Lines A and C.
 b) Detail of Line B.

be assumed, at least for this comparative exercise, since the models are based on well-established electromagnetic solution methods. With the assumption of accurate simulation results, the good correlation of the measured data becomes only necessary, but not sufficient, evidence of calibration accuracy. Due to the lack of traceable metrology standards at the wafer level (particularly four-port standards), this sort of relative measures are the only means of assessing on-wafer measurement accuracy of the PMVNA.

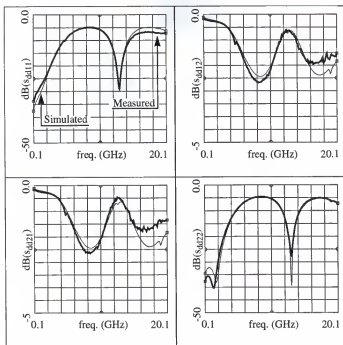


Figure 9-25. Measured (heavy) and simulated (light) pure differential s-parameters (DD) of structure of the balanced step differential transmission line of Figure 9-23, magnitude in dB.

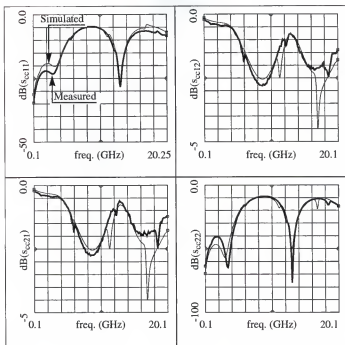


Figure 9-26. Measured (heavy) and simulated (light) pure common-mode s-parameters (CC) of structure of the balanced step differential transmission line of Figure 9-23, magnitude in dB.

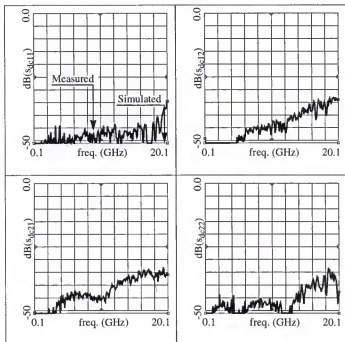


Figure 9-27. Measured (heavy) and simulated (light) common-to-differential mode-conversion s-parameters (DC) of structure of the balanced step differential transmission line of Figure 9-23, magnitude in dB.

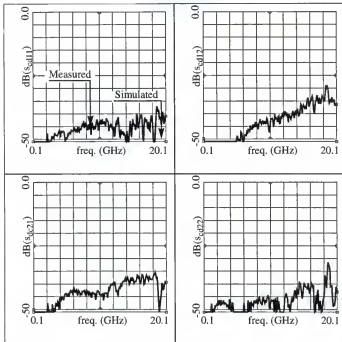


Figure 9-28. Measured (heavy) and simulated (light) differential-to-common mode-conversion s-parameters (CD) of structure of the balanced step differential transmission line of Figure 9-23, magnitude in dB.

9.3. Crosstalk Between Differential Transmission Lines

One of the primary motivations for the use of differential circuits is the inherent immunity of such circuits to interfering signals. In particular, differential circuits exhibit reduced crosstalk between adjacent circuits with respect to single-ended circuits. As illustrated in Section 5.1, the crosstalk between adjacent circuits is not eliminated by use of differential topologies; rather it is reduced.

Unintentional transmission line coupling is a major concern in high density integrated circuits. The application of differential transmission line should reduce this coupling. However, it is important to quantify the levels of residual crosstalk between differential interconnections. Such knowledge is important for understanding the limitations on differential circuit-to-circuit isolation at maximum integration levels, or alternatively, the minimum separation between differential circuits for a desired level of isolation.

The PMVNA provides a unique capability for the measurement and analysis of differential circuits. This capability can be directly applied to make accurate measurement of differential crosstalk. Such measurements have not been possible before the advent of the PMVNA. As a result, analysis of differential crosstalk has been previously limited to indirect (and usually ambiguous) measurements, or to overly simplistic electromagnetic simulations. The PMVNA allows direct measurement of crosstalk of differential systems in a practical circuit implementation. Furthermore, the PMVNA also provides increased measurement dynamic range over traditional single-ended equipment, particularly for on-wafer measurements.

To begin the study of differential transmission line crosstalk, several experiments have been fabricated on ceramic substrates. These structures are generally larger than IC implementations, but they provide insight nevertheless. The experiments are primarily a series of pairs of adjacent differential transmission lines, with the separation between the differential transmission lines is varied. The experiments are divided into two groups: (1) pairs of balanced differential transmission lines, and (2) pairs of unbalanced transmission lines.

9.3.1. Balanced Differential Transmission Lines

These experiments are a series of pairs of differential transmission lines with varying separations between the two transmission lines. Each differential transmission line is terminated with a load of nominal values of 100Ω differentially and 25Ω common-mode. By terminating two adjacent differential transmission lines at opposite ends, the overall structure becomes a two-port mixed-mode device which can be measured with the PMVNA. The goal of these experiments is to quantify the level of crosstalk between balanced differential transmission lines. It is a further goal to find the dependence on transmission line separation for crosstalk.

This series of experiments are based on the differential transmission line shown in Figure 9-29. This structure is meant to approximate a practical differential transmission line in an IC implementation, where ground planes are not interposed between the two signal conductors. As can be seen in Figure 9-29, the signal conductors of the transmission line are of equal width, so the line is balanced. The signal conductors are designed to be $100\mu\text{m}$ wide with $100\mu\text{m}$ spaces between the signal conductors and grounds, which results in a differential characteristic impedance of approximately 100Ω . No attempt was made to set the common-mode characteristic impedance. The tapered separation of the



Figure 9-29. Layout of simple balanced differential transmission line without intermediate ground.

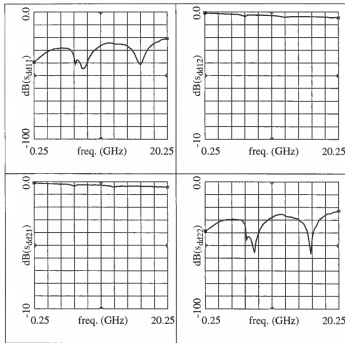


Figure 9-30. Measured pure differential s-parameters (DD) of structure of the simple balanced differential transmission line, magnitude in dB.

signal conductors at both ends of the transmission line is required to allow connection with $150\mu\text{m}$ pitch dual RF probes. The transmission line is $4000\mu\text{m}$ long.

The measured results of this transmission line are shown in Figure 9-30 through Figure 9-33. The pure differential-mode response, shown in Figure 9-30, indicates the structure is a reasonably good differential transmission line. By the periodic variation of the differential return loss, it is clear that the characteristic impedance of the line is not

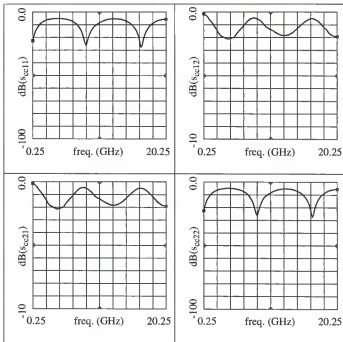


Figure 9-31. Measured pure common-mode s-parameters (CC) of structure of the simple balanced differential transmission line, magnitude in dB.

precisely 100Ω , but it is less than -20dB to above 20GHz which is acceptable. The actual differential characteristic impedance is approximately 97Ω . Also, the differential insertion loss is less than 0.5dB over the entire measurement band.

The pure common-mode response is shown in Figure 9-31. As can be seen, the structure does not provide a well-matched common-mode transmission line. This is not a concern, as practical IC implementation of differential transmission line will generally

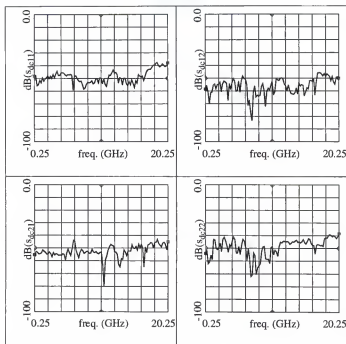


Figure 9-32. Measured common-to-differential mode-conversion s-parameters (DC) of structure of the simple balanced differential transmission line, magnitude in dB.

exhibit common-mode characteristic impedances far from the match value of 25Ω . The actual common-mode characteristic impedances of the structure is 45Ω .

The mode-conversions responses are shown in Figure 9-32 and Figure 9-33. These measurements indicate that the structure is well balanced. The mode-conversion levels, both in transmission and reflection, are in the -40dB to -50dB range. These levels could result from probe-to-probe crosstalk or from residual errors in the calibration.

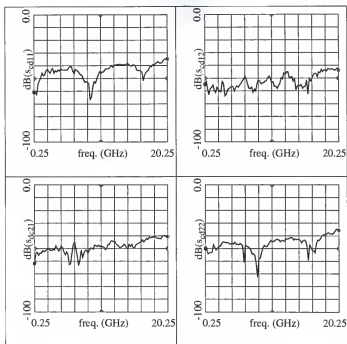


Figure 9-33. Measured differential-to-common mode-conversion s-parameters (CD) of structure of the simple balanced differential transmission line, magnitude in dB.

In the crosstalk experiments the transmission line of Figure 9-29 is resistively terminated at one end. A test structure of such a device has been fabricated, as shown in Figure 9-34. The terminating resistors, made of thin NiCr, are design for nominal values of 100Ω for the differential mode and 25Ω for the common-mode. The fabricated resistors have not been tuned, so the actual values are about 10% low.

The structure of Figure 9-34 has been measured as a mixed-mode one-port, and the results are plotted in Figure 9-35. From this measurement, one can see that the structure is

terminated reasonably well in the differential-mode. This indicates that the actual values of the terminating resistor are close to their nominal values. The common-mode response indicates a mismatched transmission line, as expected. The mode-conversion responses show that the balance of the structure has been preserved.

The crosstalk experiments are constructed through the use of two of the terminated transmission lines of Figure 9-34. The first of these experiments is shown in Figure 9-36. The two differential transmission lines are separated by $600\mu\text{m}$, measured from the center of the signal conductor space of the top transmission line to that of the bottom. Since it is desirable to make the results as general as possible, the transmission line separation is reported as a normalized value, where the separation distance is divided by the signal conductor width. This choice of normalization does not make the results completely independent of the physical dimensions of the structures, however. For example, the substrate height, relative to the conductor width, will also influence the responses of these structures, particularly the common-mode responses. The separation ratio of Figure 9-36 is six. The remaining crosstalk experiments are shown in Figure 9-37 through Figure 9-39. The separation ratios of these structures are ten, fifteen, and twenty.



Figure 9-34. Layout of terminated simple balanced differential transmission line without intermediate ground.

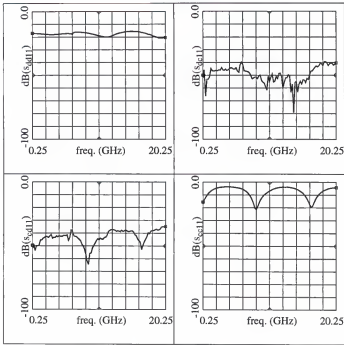


Figure 9-35. Measured one-port mixed-mode reflection s-parameters of structure of the terminated simple balanced differential transmission line, magnitude in dB.

The measured mixed-mode s-parameters from these four structures are presented in Figure 9-40 through Figure 9-43. The s-parameters of the four structures are overlaid in each of the figures. Figure 9-40 contains the pure differential-mode response of the four crosstalk experiments. The differential transmission, S_{dd21} and S_{dd12} , represents the crosstalk level between the transmission lines (in the differential-mode only). The differential crosstalk clearly indicates a dependence on the separation ratio, as expected, with

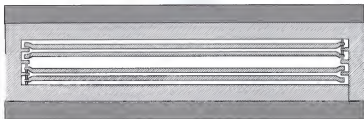


Figure 9-36. Layout of differential-to-differential crosstalk experiment with simple differential transmission line (without intermediate ground) and transmission lines separated by $600\mu\text{m}$ ($D/W=6$).

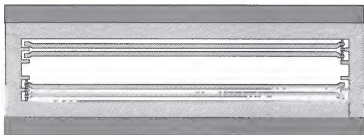


Figure 9-37. Layout of differential-to-differential crosstalk experiment with simple differential transmission line (without intermediate ground) and transmission lines separated by $1000\mu\text{m}$ ($D/W=10$).

the closest transmission lines having the highest levels of crosstalk. The differential reflection parameters, S_{dd11} and S_{dd22} , show a very slight dependence on the separation ratio (note the difference in scales). The reflection response of the widest separation is essentially equal to that of the single terminated transmission line of Figure 9-34. The lack of a strong dependence of the reflection parameters of the separation indicates that, even with a small separation, the differential transmission lines are only weakly coupled.



Figure 9-38. Layout of differential-to-differential crosstalk experiment with simple differential transmission line (without intermediate ground) and transmission lines separated by 1500μm ($D/W=15$).



Figure 9-39. Layout of differential-to-differential crosstalk experiment with simple differential transmission line (without intermediate ground) and transmission lines separated by 2000μm ($D/W=20$).

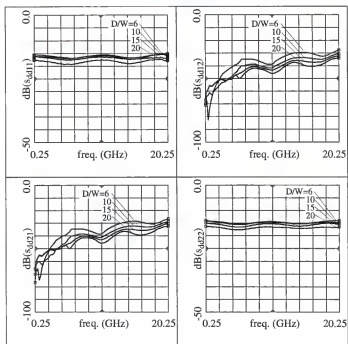


Figure 9-40. Measured pure differential s-parameters (DD) of structures of Figure 9-36 to Figure 9-39, magnitude in dB. Note the different scales.

It is important to note that the transmission parameters represent the crosstalk of the structure only while terminated with reference impedances. The effect of termination impedances on crosstalk can be found by calculating the transducer power gain (or voltage gain if desired) with the pure-differential s-parameters. More details of this type of calculation will be given in Chapter 11.

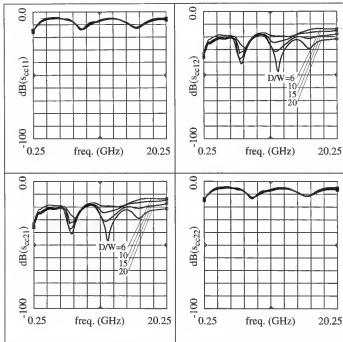


Figure 9-41. Measured pure common-mode s-parameters (CC) of structures of Figure 9-36 to Figure 9-39, magnitude in dB.

The pure common-mode responses of the crosstalk experiments are shown together in Figure 9-41. The common-mode transmission, S_{cc21} and S_{cc12} , represents the common-mode crosstalk between the transmission lines with reference terminations. In a practical differential circuit, the common-mode crosstalk physically represents the extent to which an undesired common-mode signal (such as noise from a power supply) can be coupled into an adjacent differential circuit (as a common-mode signal). Several observations can be made about the common-mode crosstalk. First, it is generally at a higher

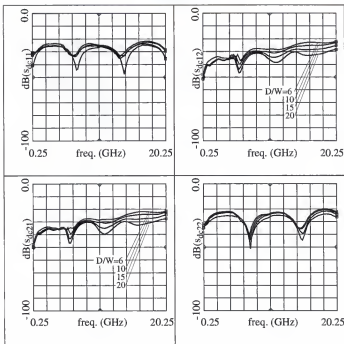


Figure 9-42. Measured common-to-differential mode-conversion s-parameters (DC) of structures of Figure 9-36 to Figure 9-39, magnitude in dB.

level than the differential mode crosstalk. Second, the periodic nature of both the transmission and reflection illustrate the dependence of crosstalk on impedance levels. Variations in magnitudes of common-mode reflections indicate impedance levels along the transmission line are also changing. Corresponding to these impedance changes are also changes in the common-mode crosstalk.

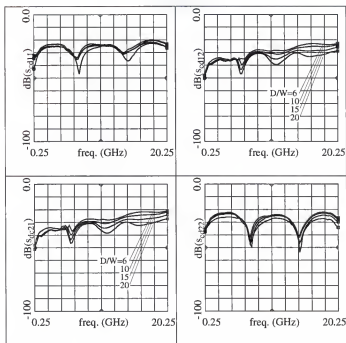


Figure 9-43. Measured differential-to-common mode-conversion s-parameters (CD) of structures of Figure 9-36 to Figure 9-39, magnitude in dB.

The mode-conversion responses of the crosstalk experiments are plotted in Figure 9-42 and Figure 9-43. The levels of mode-conversion exhibited by the crosstalk experiments is significantly higher than those of the single differential transmission line structure of Figure 9-29. This difference is due to an imbalance that has been introduced in the crosstalk experiments. In the crosstalk experiment structures, the differential transmission lines have a ground plane near only one of the signal conductors. In contrast, the

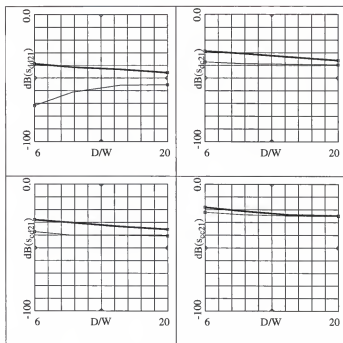


Figure 9-44. Measured mixed-mode transmission s-parameters (S_{21}) as a function of separation distance, at 10 GHz (heavy) and 1.0 GHz (light), of structures of Figure 9-36 to Figure 9-39, magnitude in dB.

single differential transmission line in Figure 9-29 has ground planes equal distances from each signal conductor. This oversight in the crosstalk experiment design results in erroneously high mode-conversion levels. As a result, it is difficult to make any quantitative conclusions about the effects of mode-conversion on crosstalk. Nevertheless, it is instructive to consider the physical meaning of transmissive mode-conversion in crosstalk situations. Consider the common-to-differential conversion, S_{dc21} . This term represents the

level at which a common-mode (undesired) signal on one transmission line is converted into a differential signal on an adjacent line. This type of conversion is particularly undesirable since the differential circuit is designed to respond to differential signals. When a common-mode interfering signal is converted into a differential-mode signal, the interfering signal is effectively injected into the adjacent differential circuit. This injection of the interfering signal negates the isolation advantages of differential topologies to some extent. As it has been demonstrated, imbalance in a differential system generates mode-conversion. Therefore, imbalance can greatly reduce the isolation effectiveness of differential transmission lines.

To better understand the relationship of circuit separation to crosstalk strength, the four unique transmission parameters of the crosstalk experiments, S_{dd21} , S_{cc21} , S_{dc21} and S_{cd21} , have been plotted as a function of the separation ratio, D/W , in Figure 9-44. These crosstalk parameters have been plotted for 1 GHz and 10 GHz. In all but one case, the magnitudes of the crosstalk parameters decrease monotonically with increasing separation ratio, as is expected. The one exception is the differential crosstalk at 1 GHz, which increases as the separation increases. By inspecting Figure 9-40, it is observed a deep minimum occurs in S_{dd21} near 1 GHz. This null is most likely due to some unexpected parasitic behavior of the structures. Quantitative conclusions about crosstalk near the null are not reliable.

In general, it can be seen that the differential crosstalk at higher frequencies does decrease as a function of separation. However, the rate of decrease with separation is not at the rate one might expect, particularly in light of the measurements of Section 5.1. In Section 5.1, it was shown that probe-to-probe crosstalk has a $1/d^3$ dependence on separa-

tion. The differential transmission line systems of this section show a much weaker dependence on separation. The cause of this difference is found in the means by which the coupling occurs. The probe-to-probe coupling is a high impedance effect; that is, the coupling mechanism is primarily the electric field. With the adjacent differential transmission lines, the primary coupling mechanism is the magnetic field (low-impedance effects). Each differential transmission line creates a relatively large loop through which magnetic fields pass. This magnetic field coupling, in combination with the residual electric field coupling, and the distributed nature of transmission lines, result in an overall crosstalk profile that is weaker than the expected $1/d^3$ dependence on separation. This behavior in differential transmission lines has given rise to the so-called twisted-pair transmission line, which greatly reduces the magnetic coupling between adjacent differential transmission lines [5]. This suggests the need for analogous "twisted" differential transmission line structures for IC applications.

Despite the magnetic coupling, the differential transmission lines still provide isolation advantage over single-ended transmission line systems. By comparing the pure differential-mode transmission to that of the common-mode (S_{cc2t}), one can see the crosstalk advantages of the untwisted differential transmission system. The common-mode crosstalk is essentially the same as single-ended crosstalk. Care must be taken in this comparison, however, since crosstalk in any interconnection system is a function of termination impedances. The behavior of S_{cc2t} versus separation shows that single-ended transmission line crosstalk decreases slower than differential crosstalk, so that at $D/W=20$, the differential system has a 30 dB advantage at 1 GHz and 20 dB at 10 GHz. Therefore,

it can be concluded generally that the untwisted differential transmission line systems have lower crosstalk than single-ended systems.

9.3.2. Unbalanced Differential Transmission Lines

To study the effects of imbalance on differential transmission line crosstalk, a series of experiments have been designed with unbalanced differential transmission lines. Like the previous section, these experiments are a series of pairs of differential transmission lines with varying separations between the two transmission lines. In this case, one of the transmission lines have an unbalanced step-up in signal conductor width. The unbalanced transmission line in these experiments is shown in Figure 9-45. The wide section is $125\mu\text{m}$ wide, leaving a space between signal conductors of $87\mu\text{m}$. All other dimensions are the same as in the previous section.

The measured mixed-mode s-parameters of the unbalanced step are shown in Figure 9-46 through Figure 9-49. From these figures, it can be seen that the step in width has strongly effected the pure-common mode and mode-conversion responses and the pure differential-mode response to a lesser extent. The most pertinent changes are in the mode-conversion parameters which clearly show the imbalance of the transmission line.



Figure 9-45. Layout of simple differential transmission line with an unbalanced step in conductor width, without intermediate ground.

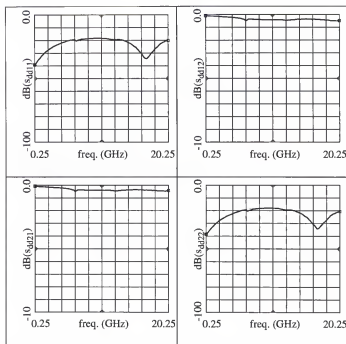


Figure 9-46. Measured pure differential s-parameters (DD) of structure of the simple differential transmission line with an unbalanced step in conductor width, magnitude in dB.

Comparing the mode-conversion responses of Figure 9-48 and Figure 9-49 to Figure 9-44, one can see the mode-conversion of the unbalanced transmission line are on the same order as those of the crosstalk experiments with balanced transmission lines in the previous section. The mode-conversion of the balanced transmission experiments is caused by unintentional imbalances in the layouts. The crosstalk experiments, shown in Figure 9-50 to Figure 9-53, have the same unintentional imbalances, which will cause

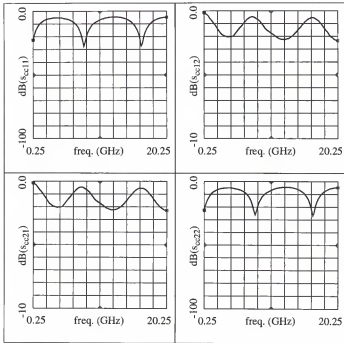


Figure 9-47. Measured pure common-mode s-parameters (CC) of structure of the simple differential transmission line with an unbalanced step in conductor width, magnitude in dB.

similar levels of mode-conversion. This indicates that the crosstalk effects of the intentional imbalance will be masked by those of the unintentional imbalances.

Nevertheless, the four unique transmission parameters of the crosstalk experiments, S_{dd21} , S_{cc21} , S_{dc21} and S_{cd21} , have been plotted as a function of the separation ratio, D/W , in Figure 9-54. Like the previous section, the crosstalk parameters have been plotted for 1 GHz and 10 GHz. The masking of the intention mode-conversion effects is evident

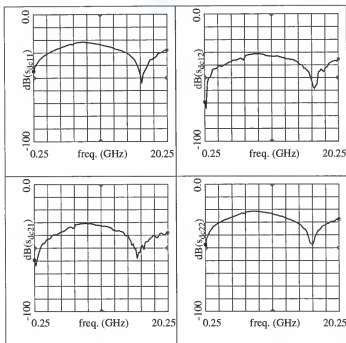


Figure 9-48. Measured common-to-differential mode-conversion s-parameters (DC) of structure of the simple differential transmission line with an unbalanced step in conductor width, magnitude in dB.

by comparing the conversion parameters of Figure 9-54 to those of Figure 9-44. Despite the imbalance in the transmission line signal conductors, the mode-conversion levels in the crosstalk experiments are unchanged. Due to these difficulties no quantitative conclusions can be drawn about the dependence of mode-conversion crosstalk upon separation.

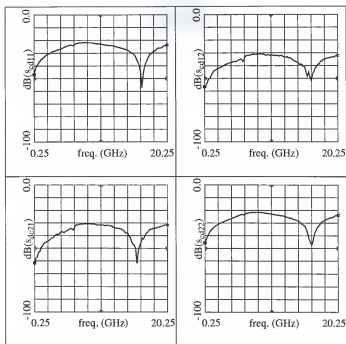


Figure 9-49. Measured differential-to-common mode-conversion s-parameters (CD) of structure of the simple differential transmission line with an unbalanced step in conductor width, magnitude in dB.

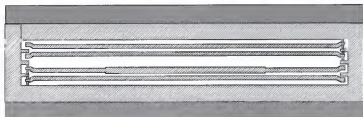


Figure 9-50. Layout of differential-to-differential crosstalk experiment with simple differential transmission line with an unbalanced step in conductor width (without intermediate ground) and transmission lines separated by $600\mu\text{m}$ ($D/W=6$).



Figure 9-51. Layout of differential-to-differential crosstalk experiment with simple differential transmission line with an unbalanced step in conductor width (without intermediate ground) and transmission lines separated by $1000\mu\text{m}$ ($D/W=10$).



Figure 9-52. Layout of differential-to-differential crosstalk experiment with simple differential transmission line with an unbalanced step in conductor width (without intermediate ground) and transmission lines separated by $1500\mu\text{m}$ ($D/W=15$).



Figure 9-53. Layout of differential-to-differential crosstalk experiment with simple differential transmission line with an unbalanced step in conductor width (without intermediate ground) and transmission lines separated by $2000\mu\text{m}$ ($D/W=20$).

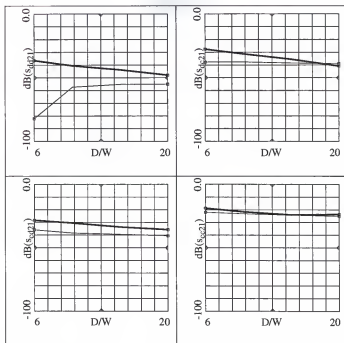


Figure 9-54. Measured mixed-mode transmission s-parameters (S_{21}) of the simple differential transmission line with an unbalanced step in conductor width as a function of separation distance, at 10 GHz (heavy) and 1.0 GHz (light), of structures of Figure 9-50 to Figure 9-53, magnitude in dB.

Regardless of the problems with the experiments of this section and Section 9.3.1, several important conclusions about differential transmission line crosstalk can be made. First, the PMVNA provides a means by which the crosstalk of differential systems can be directly and accurately measured. Second, with PMVNA measurements, S_{dd21} represents the differential crosstalk. This type of crosstalk is usually the most important in differen-

tial circuit applications. Third, S_{cc21} is the transmission level of an undesired common-mode signal from one differential transmission line to an adjacent line. Fourth, mode-conversion crosstalk, S_{cd21} and S_{dc21} , can significantly reduce the isolation effectiveness of differential systems. This is done by converting an undesired common-mode signal from one differential transmission line to an undesired differential signal on an adjacent line (in the case of S_{dc21} , and the reverse in the case of S_{cd21}). Fifth, the transmission parameters (S_{dd21} , S_{cc21} , etc.) are equal to the actual crosstalk in a system only when that system is terminated at the source and load with the reference impedances. If the actual circuits have other termination impedances, the actual crosstalk can be calculated with the use of the mixed-mode s -parameters.

CHAPTER 10

PASSIVE INTEGRATED CIRCUIT STRUCTURES

This chapter presents a series of RF differential structures that are fabricated with a silicon IC process. The structures are designed to provide practical examples of RF IC interconnections for differential circuits. Moreover, this chapter provides original studies of IC interconnection crosstalk using mixed-mode s-parameter concepts in measurement and analysis. The majority of presented experiments are based on transmission lines structures, including traditional single-ended transmission lines and a variety of differential transmission lines. These experiments are designed primarily to assess the line-to-line coupling of such transmission lines on a silicon IC, but some consideration is also given the mode-specific transmission performance of these structures. Finally, the coupling between probe pads will be studied a function of two dimensions.

All structures were fabricated on a silicon substrate using the IC processing facilities of the University of Florida Microelectronics Laboratory. All design, mask generation, and IC processing was done by the author. The IC process is shown schematically in cross-section of Figure 10-1. The final wafer has two metal layers, polysilicon diffused resistors, and an implanted substrate surface. The original substrate was three inches in diameter, and had a resistivity of approximately $100\ \Omega\text{-cm}$. Ion implantation (dose of $3.3 \times 10^{15}\ \text{cm}^{-2}$ of boron at 30 KeV) decreased the surface resistivity to approximately $0.1\ \Omega\text{-cm}$. A first layer of oxide was thermally grown on the implanted surface. After all processing, this oxide was approximately $1\ \text{\AA}$. Substrate contacts were defined by wet

etching a photo-lithographically defined opening in the thermal oxide. A resistor layer was implemented with a layer of doped polysilicon (with a sheet resistance of approximately $50 \Omega/\text{square}$). A second layer of oxide, $5 \text{ K}\text{\AA}$ thick, was deposited on top of the photo-defined polysilicon layer. The first metal layer was formed by electron beam evaporation of aluminum, $5 \text{ K}\text{\AA}$ thick, directly on to the photo-defined polysilicon layer. A

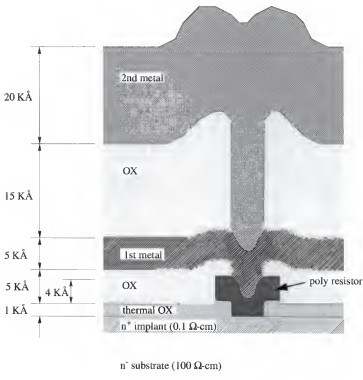


Figure 10-1. Cross section of IC structure. (Not to scale)

third layer of oxide, 15 KÅ thick, was deposited on top of the photo-defined first metal layer. Contacts to the first metal were also defined by wet etching photo-defined vias through the third oxide. The second metal layer was formed by electron beam evaporation of aluminum, 20 KÅ thick, on to the third oxide layer.

It was assumed that sufficient ohmic metal-to-silicon and metal-to-metal contacts were established through physical contact of the materials during fabrication. This assumption is clearly not optimal, but its adoption was dictated by processing limitations. The risk of poor inter-layer contacts was particularly high for the first-to-second-metal contact, where a thin oxide readily forms on the surface of bare aluminum when exposed to air. These risks were accepted due to processing limitations, and efforts were made to reduce the oxidation of the aluminum (such as storing the wafers in a small air-tight container between processing steps, and minimizing the time between critical processing steps). Despite these efforts, the finished wafers exhibited poor contact resistance for both the first-to-second-metal contact and the first-metal-to-polysilicon contact. The contact resistance for a small via (20µm by 20µm) was on the order of 100KΩ. This high contact resistance rendered some experiments unusable.

The problems with inter-layer contacts being foreseen, several experiments were designed to be useful even with poor contacts. These experiments are constructed either entirely from one metal layer or from two metal layers where interconnections are not required. These structures were successfully fabricated, and the results are presented in the following sections. All measurements presented in this chapter were made with 256 averages and half-leakage correction.

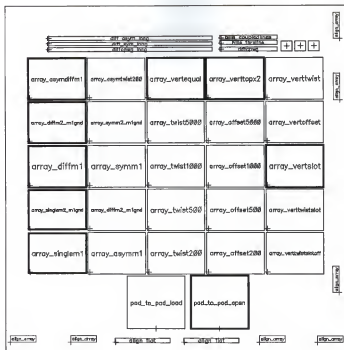


Figure 10-2. Map of wafer with groups of experiment shown as rectangles, and measured experiments indicated with heavy lines.

The layout of the entire wafer is summarized in Figure 10-2. Each rectangle represents a series of experiments on a particular transmission line structure. The transmission line experiments consist primarily of a pair of terminated transmission lines with varying line-to-line separation. The layout cell name is shown in each rectangle. For example, “array_diffm1” is the series of experiments using simple uniform differential transmis-

sion lines formed in first metal. The heavy lines of some rectangles indicate that these experiments have been measured, and the results are summarized in this chapter.

The structures presented in this chapter are grouped into several categories. The first presented are transmission line structures without a metal ground plane. This is followed by a study of similar structures with ground metal ground planes. The effect of unbalanced transmission lines on crosstalk is next examined. A series of new structures, called vertical differential transmission lines is then presented. The chapter is concluded with a study of crosstalk between probe pads.

10.1. Transmission Lines without Metal Ground Planes

This set of experiments examines the crosstalk performance of transmission lines when only the semi-conductor substrate is available for a ground plane. These structures are termed "without metal ground planes" in contrast to the series of experiments in the following section (Section 10.2). This type of transmission line is very common in today's ICs, where a single metal runner is used as an interconnection. With these structures, the semi-conductor substrate unavoidable becomes part of the transmission line. These experiments examine the basic RF transmission performance of such single-ended transmission line using the substrate as the ground plane, as well as the line-to-line crosstalk of such structures. These single-end structures are contrasted to differential transmission line structures, also without a metal ground plane.

10.1.1. Single-Ended Transmission Lines

The layouts of the experiments of single-ended transmission lines without metal ground planes are shown in Figure 10-3. Each transmission line is 10 mm long (not including the 100 μm square probe pads), and the signal conductors are 20 μm wide. For

this experiment, the signal conductors are formed in first metal. The crosstalk experiments are formed from two terminated transmission line placed with a certain separation. The separation is measured from the center of one transmission line conductor to the center of that of the adjacent transmission line. This center-to-center distance is divided by the conductor width to create a normalized separation distance (D/W). The transmission lines were intended to be terminated to the substrate via a 50Ω polysilicon resistor, but contact problems render the terminations as open-circuits. This deviation from the design goal does not invalidate the experiments, however. Rather, the results of these experiments are valid, but must be interpreted in the context of high impedance terminations.

For the crosstalk experiments, the separation ratio is varied through the series of structures, and the crosstalk between the transmission lines has been measured with the PMVNA. In this case, four-port s-parameters have been generated, and the data associated with the unused pads has been ignored. A single-ended transmission line has been provided with both ends connected to probe pads. The basic RF transmission performance

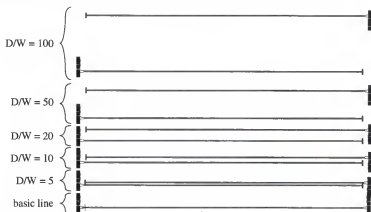


Figure 10-3. Layout of test structures for single-ended transmission lines.

can be established through direct measurement of the single-ended transmission line without a metal ground plane.

The measured results of these single-ended experiments are summarized in Figure 10-4, Figure 10-5, and Figure 10-9. Figure 10-4 shows the magnitude in dB of the two-port s-parameters of the transmission line from 45 MHz to 5 GHz. Figure 10-5 shows the s-parameters in polar form, indicating linear magnitudes and phases as a function of

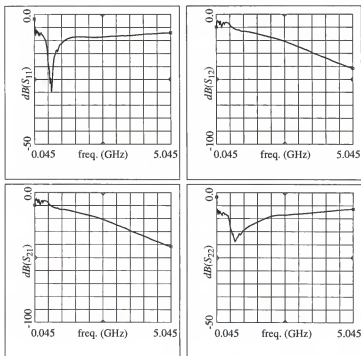


Figure 10-4. Measured s-parameters of single-ended transmission line, magnitude in dB versus frequency.

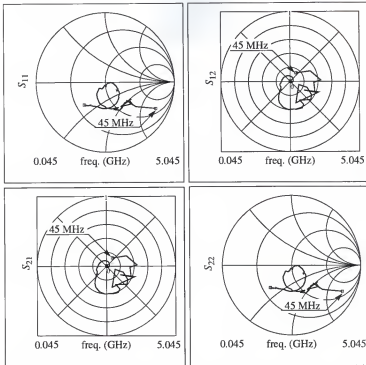


Figure 10-5. Measured s-parameters of single-ended and differential transmission line, linear magnitudes and phase versus frequency in polar plots.

frequency. From these two figures, it is apparent that this structure has very poor RF transmission qualities. Poor substrate contact may be a contributing factor in the structure's poor performance, but it is most likely primarily due to poor ground plane conductivity at RF. It is concluded that the use of the silicon substrate as a ground plane is the primary source of the poor performance. This conclusion is supported by the literature [87]. The structure of the single-ended transmission line with a doped silicon semi-con-

ducting substrate causes complex behavior as a function of substrate resistivity and frequency. This structure supports three distinct modes: the skin-effect mode, the slow-wave mode, and dielectric quasi-TEM mode [87]. These mode do not necessarily have desirable transmission line performance. The modes can occur in various combinations as the frequency of operation changes for a given structure, thus causing unexpected and abrupt changes in the effective transmission line characteristic impedance, propagation velocity, and loss. As a result, single conductors over a silicon substrate do not generally make reasonable RF transmission lines.

The results of the line-to-line crosstalk for the single-ended transmission line are summarized in Figure 10-9 of the next section. As can be seen, this single-ended structure exhibits very high levels of crosstalk. The crosstalk magnitude decreases about 15 dB over a decade of separation increase. This indicates that crosstalk between single-ended lines has dependence on separation approximately proportional to $1/d$.

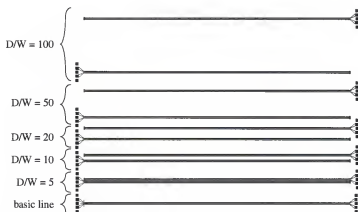


Figure 10-6. Layout of test structures for simple uniform differential transmission lines.

10.1.2. Simple Uniform Differential Transmission Line

The layouts of the experiments of simple uniform differential transmission lines without metal ground planes are shown in Figure 10-6. Like the prior structures, each transmission line is 10 mm long. The signal conductors are each 20 μm wide with a 20 μm space between conductors. The signal conductors are formed in first metal, so there is no metal ground plane under the differential transmission lines. Additionally, the transmission lines have a constant cross-section over their length. The lack of a distinct

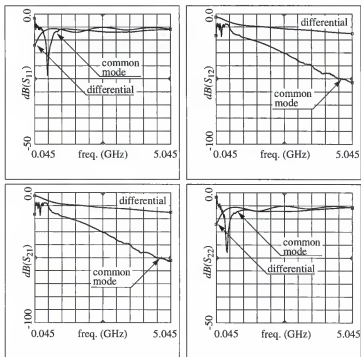


Figure 10-7. Measured s-parameters of a simple uniform differential transmission line.

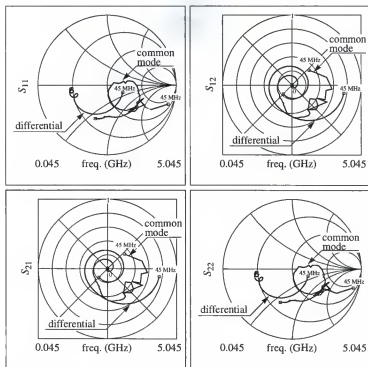


Figure 10-8. Measured s-parameters of a simple uniform differential transmission line, magnitudes and phase.

ground plane, and the uniform structure of these lines warrant the name of “simple uniform” differential transmission lines.

A directly measurable differential transmission line has also been provided in this series of experiments. The response of this structure, as measured by the PMVNA, is illustrated in Figures 10-7 and 10-8. Figure 10-7 shows the magnitudes in dB of the pure differential-mode and pure common-mode s-parameters. Figure 10-8 shows the same

parameters in polar form. The mode-conversion responses of the transmission line are not shown, but the conversions magnitudes are less than -20 dB, indicating a reasonable degree of balance. Both of these figures illustrate the basic advantage of differential transmission lines as IC interconnections. The differential RF performance of the line, despite the lack of a discernible ground plane, is acceptable. In this case, the differential characteristic impedance is approximately 32Ω . The differential-mode also shows low dispersion and low loss (in comparison to the common-mode). In contrast, the common-mode behavior is poor and not useful in RF applications. The behavior of the common-mode is very similar to that of the single-ended transmission line, and is influenced by the same physical factors. In particular, the lack of a distinct ground plane has caused the common-mode RF transmission performance to be poor.

The crosstalk experiments are formed from two terminated differential transmission lines placed with a certain separation. In this case, the separation is measured from the center of the space between the conductors of one differential transmission line to that of the adjacent differential transmission line. This center-to-center distance is divided by the width of a single conductor to create the normalized separation distance (D/W). The transmission lines were intended to be terminated with a 100Ω polysilicon resistor, but contact problems also rendered these as open-circuits. Again, the results of these experiments must be interpreted in the context of high impedance terminations.

The measured line-to-line crosstalk of the simple uniform differential transmission line is summarized in Figure 10-9. This figure shows the differential-mode and common-mode crosstalk at 1.0 GHz as a function of the normalized line separation. Like the previous chapter, crosstalk is measured as the magnitude of the transmission between the adja-

cent lines (i. e. S_{dd21} , S_{cc21} , etc.) Also shown in Figure 10-9 is the line-to-line crosstalk of the single-ended transmission line without a metal ground plane. This plot clearly shows the reduction of crosstalk in the differential-mode in comparison to the common-mode and the single-ended line. At larger separation ratios (greater than 20), the differential crosstalk decreases about 50 dB per decade of separation increase. This rate of decrease indicates a functional dependence on separation nearly equal to the theoretical limit of $1/d^3$. The common-mode crosstalk, although not monotonic, decreases at a rate of approximately 20 dB per decade of separation increase. The common-mode crosstalk is again similar to that of the single-ended transmission line.

The differential transmission line, even without a distinct ground plane, has significant crosstalk advantages for IC interconnections. At a separation ratio of one hundred, the differential-mode crosstalk is nearly 60 dB less than the common-mode, and nearly

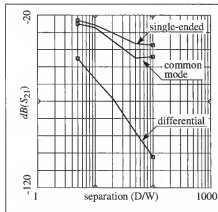


Figure 10-9. Measured line-to-line crosstalk, at 1.0 GHz, for single-ended and simple uniform differential transmission lines (both without ground planes) as a function of line separation.

70 dB less than that of the single-ended transmission line. The differential transmission line retains crosstalk advantages at small separations. Even at a separation ratio of five (which corresponds to 40 μm edge-to-edge separation between adjacent transmission lines, equal to twice the conductor spacing of a differential transmission line), the differential-mode crosstalk is 20 dB less than the crosstalk between two single-ended transmission lines.

This measured evidence is in contrast to the results of Section 9.3. The structures of Section 9.3 provided only slight reduction of crosstalk in the differential mode compared to that of the common-mode. The reason for this discrepancy is two-fold. First, the structures of Section 9.3 have significant imbalances and parasitic responses so that effectiveness of the differential structures in decreasing crosstalk is impaired. Second, the structures of Section 9.3 are limited to small separation ratios (six to twenty). Furthermore, the transmission lines of Section 9.3 have cross-sectional dimensions five times larger than those of this chapter. The theoretical decrease in crosstalk for differential-modes is based on approximations that the conductor widths and spaces of each differential transmission line are much smaller than the separation between adjacent lines. The larger dimensions of Section 9.3 cause these approximations to be less accurate, and hence the increase the actual differential crosstalk.

10.2. Transmission Lines with Ground Metal Ground Planes

This set of experiments examines the crosstalk performance of integrated transmission lines where a metal ground plane is used. These structures are the same as those in Section 10.1, except that first metal is used for a ground plane, and the transmission lines are formed from second metal. This type of transmission line is not common in

today's ICs, but could be easily implemented. With these structures, the effects of semiconductor substrate are substantially removed from the transmission line performance.

These experiments examine the basic RF transmission performance of such single-ended transmission line, as well as the line-to-line crosstalk of such structures. These single-ended structures are contrasted to differential transmission line structures, both with a metal ground plane.

10.2.1. Single-Ended Transmission Lines

The layouts of the experiments of single-ended transmission lines with metal ground planes are shown in Figure 10-10. Like the prior structures, each transmission line is 10 mm long, with signal conductors 20 μm wide. The signal conductors are formed in second metal, and the ground plane under the transmission lines is formed in first metal. Referring to Figure 10-1, the height between the signal conductor and the ground plane is approximately 15 $\text{K}\text{\AA}$. The crosstalk experiments of this section are a function of the nor-

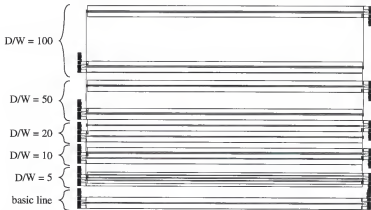


Figure 10-10. Layout of test structures for single-ended transmission line with metal ground plane.

malized separation, measured the same as the single-ended transmission lines of Section 10.1.1. Similarly, these experiments are terminated with open-circuits.

The measured results of the single-ended transmission lines with metal ground plane are shown in Figures 10-12 and 10-13 of the next section. With a metal ground plane, the single-ended transmission line has good RF performance. The characteristic impedance of this line is approximately 27Ω , and is essentially constant across the measurement band. In contrast, the line without a metal ground plane exhibits a characteristic impedance that varies rapidly over frequency. Furthermore, the losses of the single-ended line with the metal ground plane are significantly less than without a metal ground plane.

The measured line-to-line crosstalk of the single-ended transmission lines with metal ground plane is summarized in Figure 10-14, also of the next section. The magnitude of the crosstalk between single-ended transmission lines is significantly reduced by the use of the metal ground plane. The ground plane reduces the crosstalk between adjacent transmission line by nearly 45 dB at small separations and more than 60 dB at large separations. Clearly, the use of metal ground planes with single-ended interconnections has significant advantages for RF transmission line performance and reduced crosstalk.

10.2.2. Uniform Differential Transmission Lines

The layouts of the experiments of simple uniform differential transmission lines with metal ground planes are shown in Figure 10-11. Each transmission line is again 10 mm long. The signal conductors are each $20\text{ }\mu\text{m}$ wide with a $20\text{ }\mu\text{m}$ space between conductors, like the differential lines of Section 10.1.2. The signal conductors are formed in second metal, with a first metal ground plane beneath. Due to the constant cross-section, these line are called uniform differential transmission lines.

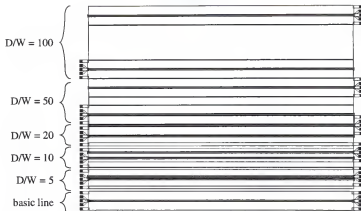


Figure 10-11. Layout of test structures for uniform differential transmission line with metal ground plane.

The measured response of the uniform differential transmission line with a metal ground plane is summarized in Figures 10-12 and 10-13. Figure 10-12 shows the magnitudes in dB of the pure differential-mode and pure common-mode s-parameters. Figure 10-13 shows the same parameters in polar form. The mode-conversion responses of the transmission line again are not shown, but the conversions magnitudes are less than -20 dB, indicating a reasonable degree of balance. Also shown of these figures is the response of the single-ended transmission line with a metal ground plane.

The differential and common-mode responses are virtually indistinguishable from one another and from the single-ended transmission line response. This similarity of the responses indicates that the signal conductors comprising the differential transmission line are essentially uncoupled. With uncoupled conductors, the differential and common-mode behavior degenerate into identical modes, which are equal to that of a single-ended

transmission line (see Section 3.1.1). The physical construction of the differential line supports the conclusion that the signal conductors are uncoupled. The two conductors are $20\text{ }\mu\text{m}$ apart, but they are only $15\text{ K}\text{\AA}$ ($1.5\text{ }\mu\text{m}$) above the ground plane. Relative to the height above the ground plane, a conductor over ten times farther away has essentially no effect on another signal conductor.

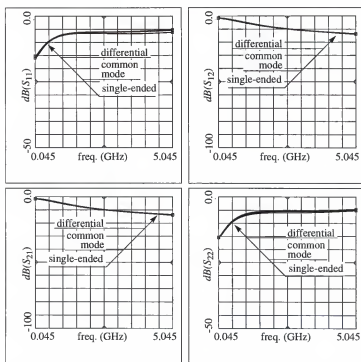


Figure 10-12. Measured s-parameters of single-ended and uniform differential transmission lines, both with metal ground planes.

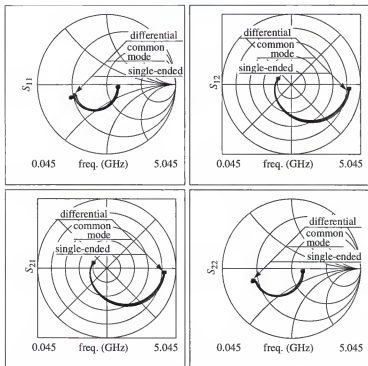


Figure 10-13. Measured s-parameters of single-ended and differential transmission line, both with ground planes, magnitudes and phase.

The crosstalk experiments of this section are again function of the normalized separation. The separation between adjacent lines is measured by the ratio of center-to-center distance and a signal conductor width, which is the same as in Section 10.1.2. Similarly, these experiments are terminated with open-circuits. The line-to-line crosstalk of both the differential and common-modes are summarized in Figure 10-14. Like previous sections, the crosstalk is quantified by the transmission s-parameters, as measured by the PMVNA.

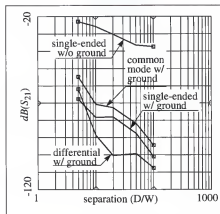


Figure 10-14. Measured line-to-line crosstalk, at 1.0 GHz, for single-ended and differential transmission lines with metal ground planes, as a function of line separation.

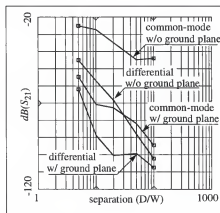


Figure 10-15. Measured line-to-line crosstalk, at 1.0 GHz, for differential transmission lines, with and without metal ground planes, as a function of line separation.

The ground plane under the differential transmission line has substantially reduced the amount of crosstalk for both differential and common-modes. Notice that the common-mode crosstalk is approximately 6 dB higher than the single-ended crosstalk, particularly as the separation increases. This difference is in accordance with the approximate results expected with uncoupled lines. The overall decrease in crosstalk is illustrated in Figure 10-15. For the differential line, the differential-mode crosstalk is reduced between 20 dB to 40 dB by the presence of the ground plane. The common-mode crosstalk is reduced 30 dB to 50 dB by the ground plane. This reduction is a result of the small height of the signal conductors over the ground plane. In this case, the metal ground plane confines electromagnetic fields, causing significantly less coupling (crosstalk) compared to the same structures without the ground plane.

Clearly the use of metal ground planes for RF IC interconnections has several advantages over structures without ground planes. By establishing a distinct ground plane, single-ended interconnections become good RF transmission lines. In IC implementations, the separation between metal layers is typically small compared to signal conductor widths. This small separation between ground planes and signal conductors has the effect of significantly reducing the crosstalk between interconnections. The addition of a ground plane also benefits the differential transmission line. The nearness of the ground plane further reduces differential-mode crosstalk. With such differential structures, a very high degree of circuit-to-circuit isolation can be achieved, even on high density ICs.

10.3. Unbalanced Differential Transmission Lines

This set of experiments examine the effects of imbalance on crosstalk between differential IC interconnections. These differential structures are the same as those in

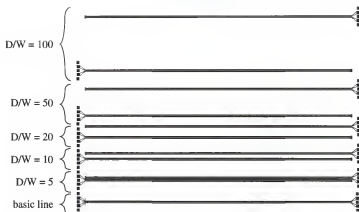


Figure 10-16. Layout of test structures for unbalanced differential transmission lines.

Section 10.1.2, except that imbalance is intentionally introduced. Like Section 10.1.2, these transmission lines have no metal ground plane. The layouts of the experiments of simple uniform differential transmission lines without metal ground planes are shown in Figure 10-16. Like the prior structures, each transmission line is 10 mm long. The first metal signal conductors are each nominally $20\text{ }\mu\text{m}$ wide with a $20\text{ }\mu\text{m}$ space between conductors. The imbalance is introduced by a step in the width of one of the signal conductors of the differential transmission lines. The width of this unbalanced conductor is $40\text{ }\mu\text{m}$ wide with a length of 5 mm.

The measured response of the unbalanced differential transmission is summarized in Figures 10-17 and 10-18. Figure 10-17 shows the magnitudes in dB of selected pure differential-mode and pure common-mode s-parameters. Also shown in the figure are the same parameters for the (balanced) simple uniform differential line of Figure 10-6. Since

the structures are port-symmetric, only S_{11} and S_{12} are shown. Figure 10-18 shows the magnitudes in dB of selected mode-conversion parameters of the same structures. Due to the reciprocal nature of the devices, only four mode-conversion s-parameters are unique (see Chapter 11), so only S_{dc} is shown. From these figures, it is seen that the step-in-width has little effect on the differential lines. The pure-mode responses are very similar, with only the insertion loss of the unbalanced line increasing slightly (about 1 dB at 5 GHz). The imbalance has a more perceptible impact on the mode-conversion s-parameters. All

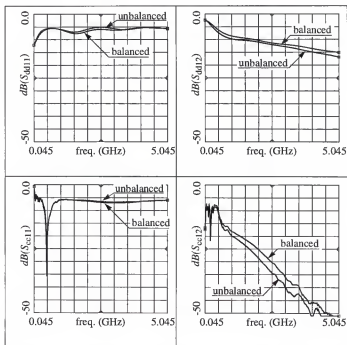


Figure 10-17. Measured differential and common-mode s-parameters of unbalanced and simple uniform (balanced) differential transmission lines.

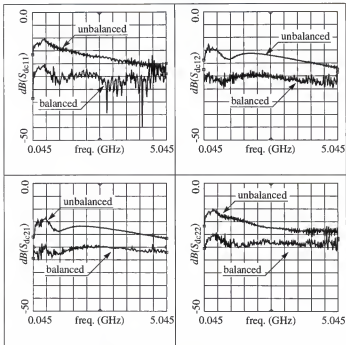


Figure 10-18. Measured mode-conversion s-parameters of unbalanced and simple uniform (balanced) differential transmission lines.

mode-conversion s-parameters increased about 10 dB with the unbalanced transmission line. The magnitudes of the mode-conversion are relatively small (near -10 dB to -20 dB), but still significant.

The crosstalk experiments with the unbalanced lines are function of the normalized separation between two differential transmission lines. Only one of the lines is unbalanced; the other is the same as the balanced simple uniform differential transmission lines of Section 10.1.2. The separation between adjacent lines is measured by the ratio of cen-

ter-to-center distance and a signal conductor width, which is the same as in Section 10.1.2. Similarly, these experiments are terminated with open-circuits. The line-to-line crosstalk of the pure modes is summarized in Figure 10-19. Included in this figure is the pure mode crosstalk of the simple uniform differential transmission lines of Section 10.1.2. From this figure, there is very little meaningful change in the magnitude of crosstalk between the balanced and unbalanced differential transmission lines. However, contrary to expectations, the common-mode crosstalk of the balanced line is slightly higher than the unbalanced line, over most of the range of line separations. This is due to different common-mode losses for the two transmission lines. Referring to Figure 10-17, the common-mode insertion loss of the unbalanced line is greater than that of the balanced line. Because there is no significant difference in the return loss of the two lines, it can be concluded that

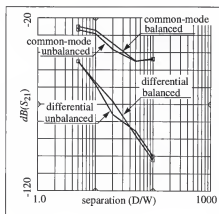


Figure 10-19. Measured line-to-line crosstalk, at 1.0 GHz, for uniform and unbalanced and simple uniform (balanced) differential transmission lines, as a function of line separation.

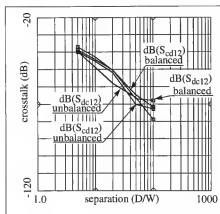


Figure 10-20. Measured line-to-line mode-conversion crosstalk, at 1.0 GHz, for uniform and unbalanced and simple uniform (balanced) differential transmission lines, as a function of line separation.

the ohmic losses of the unbalanced line are higher than the balanced line. The common-mode crosstalk of the unbalanced lines will naturally be lower due to these losses.

The mode-conversion crosstalk of the unbalanced differential line is summarized in Figure 10-20. Again included for comparison is the mode-conversion crosstalk of the simple uniform differential transmission lines of Section 10.1.2. The mode-conversion crosstalk of the unbalanced transmission line is very near that of the balanced line. This figure confirms that, in this case, the intentionally introduced physical imbalances of the unbalanced differential transmission line do not cause a significant increase in mode-conversion.

10.4. Vertical Differential Transmission Lines

This section examines the characteristics of an uncommon type of differential transmission line for IC applications. This transmission line is formed by stacking the two signal conductors in the vertical direction, rather than in the horizontal direction as seen in previous sections. This vertical stacking gives the structure the name of “vertical” differential transmission line. The vertical differential line is essentially a broad-side coupled pair transmission line [14]. This structure requires about one-third less surface area to construct compared to a typical horizontal differential transmission line, which is an advantage in RF IC applications. Specifically, this section considers three varieties of vertical differential transmission lines. The first structure has equal width top and bottom conductors. The second variation has a top conductor width twice that of bottom. The third type of vertical line also has a double width top conductor, but the top conductor

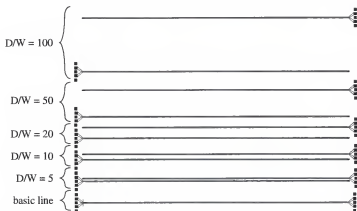


Figure 10-21. Layout of test structures for vertical differential transmission line, with equal widths of top and bottom conductors.

additionally has long open slots down the center. In this section, a set of experiments examines the RF transmission line performance, and the crosstalk behavior, of these vertical differential transmission lines.

The layout for the three types of vertical differential transmission lines are shown in Figures 10-21, 10-22, and 10-23. Figure 10-21 shows the layout of the vertical lines with equal top and bottom conductor widths. The layout of the vertical transmission lines with the top conductor width twice the bottom is shown in Figure 10-22. Figure 10-23 shows the layout of the final variety of vertical differential transmission line, where the double width top is slotted down its length. A detail of the layout of one slotted transmission line is shown in Figure 10-24.

Like previous sections, these experiments include a series of pairs of terminated transmission lines for the measurement of crosstalk. These lines were intended to be

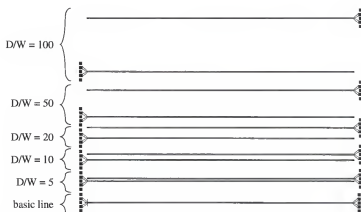


Figure 10-22. Layout of test structures for vertical differential transmission line, with width of top conductor twice the width of the bottom conductor.

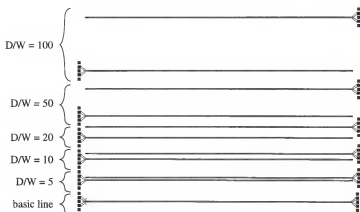


Figure 10-23. Layout of test structures for vertical differential transmission line, with top conductor with slots and width of top conductor twice the width of the bottom conductor.

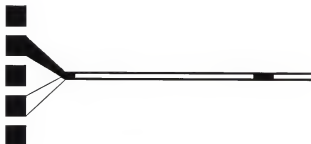


Figure 10-24. Detail of layout of test structures for vertical differential transmission line, with top conductor with slots and width of top conductor twice the width of the bottom conductor.

terminated with 100 Ω resistors, but, like previous experiments, processing problems have left the lines terminations open. In all cases, the separation between transmission lines is measured from the center of the bottom conductor of one line to the center of the bottom conductor of the adjacent line. This distance is divided by the width of the bottom conductor to calculate the separation ratio (D/W). Also included is a structure for direct measurement of the RF performance of each type of vertical differential transmission line.

Each variation of the vertical transmission line is designed to address a certain performance issue. The design process is illustrated by the cross-sectional sketch of the three vertical differential transmission lines in Figure 10-25. The simple vertical differential line is meant to maintain low crosstalk while increasing the integration density of differential IC interconnections. The vertical line with twice the top conductor width is designed to improve the balance of the vertical line. The top conductors of the simple vertical line

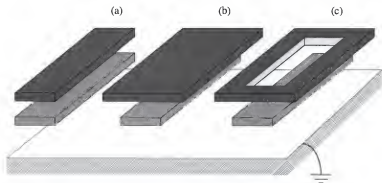


Figure 10-25. Cross section of vertical differential transmission lines.

- a) Equal width top and bottom conductors.
- b) Top width twice the bottom.
- c) Top with slot.

(a) have unequal parasitic capacitances to ground. The nearness of the bottom conductor to ground results in a larger capacitance than that of the top conductor. This unequal capacitance generates an unbalanced differential transmission line. By increasing the width (b), the capacitance of the top conductor to ground is increased. The design goal of this structure is to balance the parasitic capacitances of the two conductors. The actual width of the top conductor required for complete balance is a function of the location of the ground and the height between the conductors of the vertical transmission line. While the calculation of the width of the top conductor is straight-forward with a distinct ground plane, it is difficult when only the semi-conductor substrate is used under the vertical transmission line. As the IC process used for these experiments is limited to two metal layers, no metal ground plane could be used under the vertical lines. As a result, the design of the width of the top conductor is best accomplished through empirical methods. For this work, the width of the top conductor has been set at twice that of the bottom conductor as a baseline for future work. For this work, the top conductor is made 40 μm wide, and the bottom conductor is 20 μm wide. The total transmission line length is 10 mm.

The design of the third variation of vertical differential transmission line is one with a slotted top conductor, as illustrated in Figure 10-25(c). This transmission line is designed to further improve the balance for the vertical transmission line. As a consequence of its greater width, the top conductor of Figure 10-25(b) is expected to exhibit lower series resistance than the bottom conductor. This unequal resistance will again generate imbalance in the differential transmission line. To compensate for this decreased resistance, a slot is formed in the top conductor. The slot is long and narrow, made down

the center of the top conductor. Ideally, this slot should increase the series resistance of the top conductor, while maintaining the balanced capacitance to ground, while having minimal impact on the transmission performance of the structure. The actual amount of increased balance, and the proper design of the slot, is again left to empirical methods.

For this work, the slot is made 20 μm wide in the center of the 40 μm top conductor. The length of each slot is 900 μm , followed by a 100 μm long section of transmission line

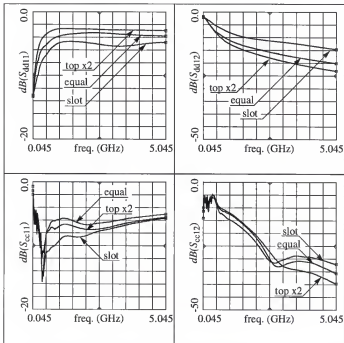


Figure 10-26. Measured differential and common-mode s-parameters of the three types of vertical differential transmission lines.

without a slot. This 1000 μm cycle is repeated of the length of the line. The bottom conductor is again 20 μm wide. The total transmission line length is 10 mm.

The mixed-mode s-parameters of these three vertical differential transmission lines are summarized in Figures 10-26 and 10-27. Figure 10-26 shows selected pure-mode responses of all three vertical lines. Due to port-symmetry, only S_{11} and S_{12} are shown for each mode. From this figure, it is clear that all three lines have acceptable differential transmission characteristics. In contrast, the common-mode characteristics of all three

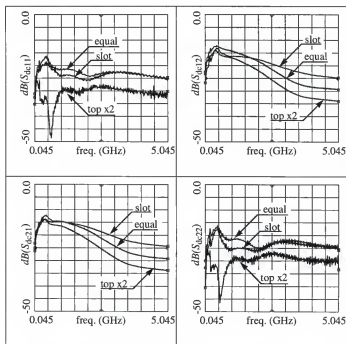


Figure 10-27. Measured mode-conversion s-parameters of the three types of vertical differential transmission lines.

vertical lines are poor. The common-mode behavior is due to the lack of a distinct ground plane, and is very similar to the results of Section 10.1. The transmission line with equal width conductors has a differential characteristic impedance of about 20Ω . For comparison, the simple uniform (horizontal) differential transmission line has a differential characteristic impedance of 32Ω . The small height between the top and bottom conductors ($15\text{ K}\text{\AA}$) has decreased the differential characteristic impedance of the vertical transmission line.

The transmission line with the double width top conductor has a differential characteristic impedance of about 15Ω . The increase of the width of the top conductor has increased the capacitance to the bottom conductor, which decreases the differential characteristic impedance of the structure. This decrease largely accounts for the higher insertion loss of this structure with respect to the equal width vertical line. The increased insertion loss is primarily due to miss-match losses, as supported by the increased reflection magnitude.

The transmission line with the slotted top conductor has a differential characteristic impedance of approximately 29Ω . In addition to raising the series resistance, the slot decreased the capacitance between the top and bottom conductors. This decrease results in an increased differential characteristic impedance, which further results in lower insertion loss and lower reflection magnitudes.

The mode-conversion behavior of the three vertical transmission line is summarized in Figure 10-27. Again, only four mode-conversion parameters are shown due to symmetry considerations. The mode-conversion levels of all three vertical transmission line are relatively high when compared to the simple uniform differential line. Further-

more, the magnitudes of mode-conversion in transmission apparently run counter to the intended behavior of the three transmission lines. The slotted line has the highest mode-conversion magnitudes, despite the most extensive efforts to balance the structure. The apparent increase in mode-conversion is due to the different characteristic impedances of the three transmission lines. The slotted line, with its differential characteristic impedance closest to 50Ω is better matched than the other vertical lines. The better match of the slotted line increases the amount of signal that can be delivered to the load. This better match increases the magnitude of differential transmission, s_{dd12} , as well as the mode-conversion transmission, s_{dc12} and s_{cd12} . Inspection of Figure 10-27 reveals the relative strengths of the transmission mode-conversion correspond to the relative magnitudes of the differential characteristic impedances of the three vertical transmission lines. With the change in

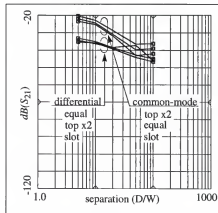


Figure 10-28. Measured line-to-line crosstalk (pure mode), at 1.0 GHz, for the three vertical differential transmission lines, as a function of line separation.

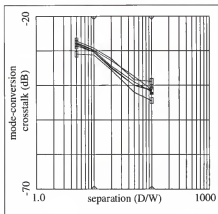


Figure 10-29. Measured line-to-line crosstalk (mode-conversion), at 1.0 GHz, for the three vertical differential transmission lines, as a function of line separation. Note different scale from previous figures.

characteristic impedances considered, no significant difference can be seen in the imbalance of the three vertical transmission lines.

The crosstalk behavior of the three vertical transmission lines is summarized in Figure 10-28. The crosstalk magnitudes between vertical transmission lines are significantly higher than in the horizontal differential lines of Section 10.1. This increase in crosstalk is due to the large magnitude of mode-conversion in the vertical transmission lines. Despite the general increase in its magnitude, the differential-mode crosstalk characteristic still retains an advantage over the common-mode crosstalk. The three variations of vertical lines exhibit similar levels of differential-mode crosstalk, but have consistent, but small, differences in common-mode crosstalk. The large imbalance in all three vertical lines is illustrated in Figure 10-28. Because of the similarity of the responses, the indi-

vidual traces on the plot are not identified. This figure clearly shows that all three lines possess a large degree of imbalance. This imbalance is responsible for the increased line-to-line crosstalk in these structures.

It is concluded that the mode-conversion of the vertical transmission lines is a result of IC processing issues. The series resistance of the first metal layer is higher than that of the second metal. For example, in terms of standard *s*-parameters, at 1.0 GHz the vertical differential line with equal width conductors has about 7.7 dB of insertion loss in the top conductor, but about 17 dB loss in the bottom conductor. This difference is large enough to generate significant mode-conversion. The mode-conversion produced by the resistance imbalance is much larger than the imbalances generated by unequal capacitance of the conductors to ground. As a result, the effects of the balancing techniques used on the vertical lines are masked by the dominating effect of the unbalanced metal resistance. This type of problem will typically dominate most IC implementation of vertical differential transmission lines. For the advantages of this structure to be realized, care must be taken to compensate the vertical transmission line for unequal resistance in the constituent metal layers.

10.5. Pad-to-Pad Crosstalk

This set of experiments examines the crosstalk between probe pads as a function distance. Pads are relatively large (compared to other integrated devices), typically square, metal structures used for both wafer-probe or wire-bond connections. In many applications, signal coupling through pads can be a significant problem. This is due to the fact that pads can be large with respect to other IC features, and can sometimes capacitively couple signals into the substrate at relatively high levels. Pure differential and com-

mon-mode coupling between probe pads is examined, as well as mode-conversion coupling. Unlike the simple study of Section 5.1, this set of experiments quantify pad-to-pad crosstalk for a practical silicon IC. Furthermore, these experiments map the pad-to-pad crosstalk as a two-dimensional function of position of the pads.

As discussed in Section 4.3, the PMVNA uses ground-signal₁-ground-signal₂-ground (GSGSG) probes, so the pads for the experiments in this section (and throughout the chapter) are constructed accordingly. The construction of GSGSG pads is illustrated in Figure 10-30. The GSGSG pads are placed in a grid to form the coupling experiments of this section, as shown in Figure 10-31. The rows of pads are spaced 500 μm center-to-center, and the columns are spaced 1000 μm center-to-center. The origin of the array is defined to be at the center set of pads in the bottom row. With the wafer probe of mixed-

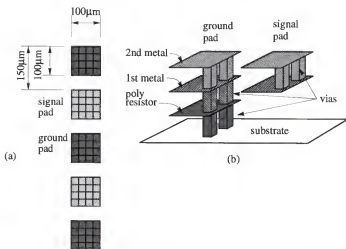


Figure 10-30. Probe pad construction. a) Top view of GSGSG pads. b) Cross-sectional view of process layers in signal and ground pads.

mode port one fixed at the origin of the pad array, the probe of mixed-mode port two has been placed at various pads in the array, where the PMVNA has measured the mixed-mode s -parameters. Like other experiments, the various transmission s -parameters quantify crosstalk between the pads. Treating the pads as sample points in a continuous domain, contours of constant crosstalk magnitudes can be constructed from the measured mixed-mode s -parameters.

The contours of constant crosstalk are two dimensional maps of the coupling between two differential structures. This contour map of coupling can provide insight into how signals from one circuit on an IC are coupled into others on the same IC. The maps show the crosstalk level of the differential-mode between two differential circuits, as well as the common-mode crosstalk. Additionally, the maps can also show the mode-conversion crosstalk between two differential circuits as a function of position. This two-dimensional mapping of the mode-conversion illustrates how mode-conversion crosstalk can occur between two otherwise balanced differential circuits.

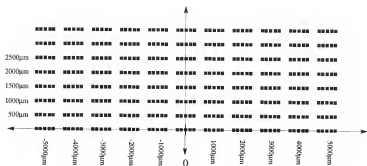


Figure 10-31. Layout of test structure for pad-to-pad crosstalk.

The measured crosstalk results are summarized in Figures 10-32 to 10-35. These figures are contour plots of measured mixed-mode transmission. Figure 10-32 is the pure differential-mode crosstalk between pads at 1.0 GHz and 2.0 GHz. The measured s_{dd21} between each pair has been used to interpolate the contours of constant crosstalk over the surface of the IC. This figure shows the crosstalk decreases rapidly as the radial distance

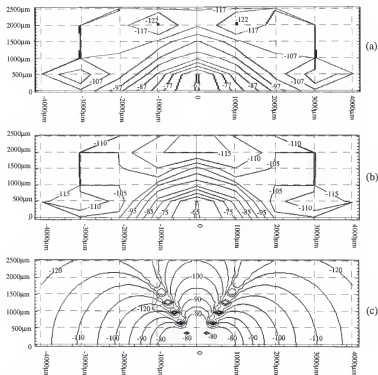


Figure 10-32. Constant crosstalk magnitudes contours (s_{dd21} in dB) of pad-to-pad test structure.

a) Crosstalk at 1.0 GHz. b) Crosstalk at 2.0 GHz. c) Analytical approximation of crosstalk.

from the origin increases. This indicates that the differential crosstalk decreases as a function between two differential circuits increase, as has been demonstrated earlier.

Figure 10-33 is the pure common-mode crosstalk between pads at 1.0 GHz and 2.0 GHz.

Similarly to the previous figure, the measured s_{cc21} between each pair has been used to interpolate the contours of constant crosstalk over the surface of the IC. Compared to the

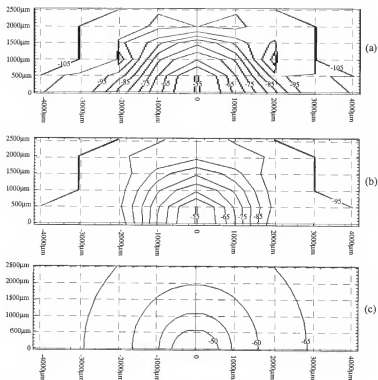


Figure 10-33. Constant crosstalk magnitudes contours (s_{cc21} in dB) of pad-to-pad test structure.
a) Crosstalk at 1.0 GHz. b) Crosstalk at 2.0 GHz. c) Analytical approximation of crosstalk.

differential crosstalk map, the common-mode crosstalk decreases slower than differential crosstalk with increasing radial distance. Figure 10-34 is the common-to-differential crosstalk between pads at 1.0 GHz and 2.0 GHz. In this case, the measured s_{dc21} between each pair has been used to interpolate the contours of constant crosstalk over the surface of the IC. Finally, the differential-to-common crosstalk is shown in Figure 10-34 at 1.0 GHz

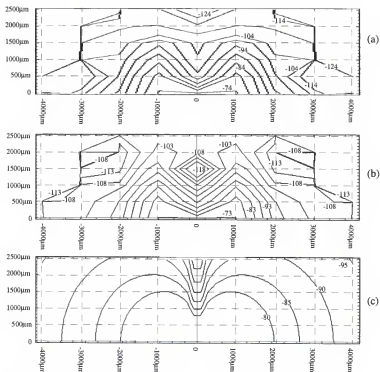


Figure 10-34. Constant crosstalk magnitudes contours (s_{dc21} in dB) of pad-to-pad test structure.
 a) Crosstalk at 1.0 GHz. b) Crosstalk at 2.0 GHz. c) Analytical approximation of crosstalk.

and 2.0 GHz. In this case, the measured s_{cd21} between each pair has been used to interpolate the contours of constant crosstalk over the surface of the IC. Both of the mode conversion crosstalk maps have minimal crosstalk along the y-axis.

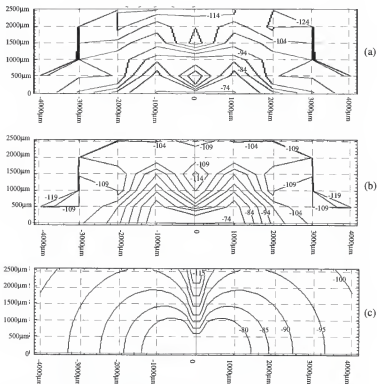


Figure 10-35. Constant crosstalk magnitudes contours (s_{cd21} in dB) of pad-to-pad test structure.
 a) Crosstalk at 1.0 GHz. b) Crosstalk at 2.0 GHz. c) Analytical approximation of crosstalk.

With some approximations, the crosstalk behavior exhibited in these pad experiments can be theoretically explained. The theoretical development of the pad crosstalk illuminates the basic principles leading to circuit-to-circuit crosstalk. By assuming that a probe pad is much smaller than a wavelength, the pad can then be approximated as a lumped element, neglecting distributed circuit effects. The structure can be further simplified by assuming the pads can be approximated by small conductive sphere at some potential. This sphere has a radius, a , where a is the smallest radius that completely encloses the pad (and a is much smaller than a wavelength). To greatly simplify the following expressions, the loading of the pads will be neglected. In other words, the characteristic source and load impedances of the PMVNA will be assumed to have no effect on the crosstalk. This is a coarse approximation, but it provides expression that are easily interpreted. Furthermore, the predicted crosstalk maintains the same qualitative behavior as the measured data. Neglecting the PMVNA ports impedances is the same as assuming the pads are part of a high impedance circuit, where current is negligible.

By neglecting the PMVNA port impedances, the crosstalk can be approximated with a simple electrostatic approximation. With two pads, each approximated as a sphere,

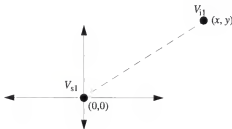


Figure 10-36. Model of single-ended circuit-to-circuit crosstalk.

the electric potential between the spheres can be easily calculated as a function of distance. For example, consider two single-ended pads, as illustrated in Figure 10-36. One pad, radius a , is located at the origin, and the other pad, radius a , is located at a point in the xy -plane, (x, y) . The electric potential of a charged sphere is known to be [88]

$$\begin{aligned} V(r) &= \frac{Q_s}{4\pi\epsilon} \frac{1}{r} & (r > a) \\ V(r) &= \frac{Q_s}{4\pi\epsilon a} & (r \leq a) \end{aligned} \quad (10-1)$$

where r is radial distance from the center of the sphere. If the sphere at the origin is defined to have a potential of V_{s1} , then the surface charge can be found to be

$Q_s = (4\pi\epsilon a)V_{s1}$, so that the potential of the sphere can be stated as

$$V(r) = aV_{s1} \frac{1}{r} \quad (r > a) \quad (10-2)$$

The potential at a point in the x - y plane, outside of the sphere, can be expressed as

$$V(x, y) = aV_{s1} \frac{1}{\sqrt{x^2 + y^2}} \quad (10-3)$$

The radius of the second pad will be neglected, so that its potential is simply expressed by (10-3), so that $V_{i1}(x, y) = V(x, y)$. The crosstalk between the two pads will be defined as the ratio of the potentials of the pads.

$$\text{Crosstalk} = \left| \frac{V_{i1}}{V_{s1}} \right| = \frac{a}{\sqrt{x^2 + y^2}} = \frac{a}{r} \quad (10-4)$$

From (10-4), the $1/r$ proportionality of single-ended crosstalk is readily observed.

This same approach can be applied to two sets of differential probe pads, and the pure differential, common-mode, and mode-conversion crosstalk can be approximated.

Referring to Figure 10-37, the pair of differential pads can be modeled by four small

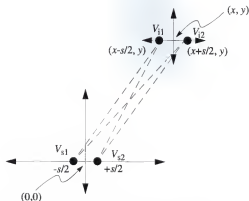


Figure 10-37. Model of differential circuit-to-circuit crosstalk.

spheres. Two spheres on the x -axis represent the “source” pads. These pads, are at $(-s/2, 0)$ and $(+s/2, 0)$, where s is the pad-to-pad separation of the differential pad set, and these pads have electric potentials of V_{s1} and V_{s2} , respectively. The potentials at the other two pads, located at $(x-s/2, y)$ and $(x+s/2, y)$, are approximated by

$$V_{i1}(x, y) = \frac{a V_{s1}}{\sqrt{x^2 + y^2}} + \frac{a V_{s2}}{\sqrt{(x-s)^2 + y^2}} \quad (10-5)$$

$$V_{i2}(x, y) = \frac{a V_{s1}}{\sqrt{(x+s)^2 + y^2}} + \frac{a V_{s2}}{\sqrt{x^2 + y^2}} \quad (10-6)$$

Differential-mode operation of the source pads is set by driving the pads with equal but opposite potentials, $V_{s1} = -V_{s2} = V_0$. Common-mode is set with equal potential sources, $V_{s1} = V_{s2} = V_0$. The differential signal at the output pads is the difference of the potentials of the two pads

$$V_{id} = V_{i1}(x, y) - V_{i2}(x, y) \quad (10-7)$$

and the common-mode output is the average potential

$$V_{ic} = \frac{V_{i1}(x, y) + V_{i2}(x, y)}{2} \quad (10-8)$$

The pure differential-mode crosstalk is defined as

$$Cr_{dd} = \left| \frac{V_{i1}(x, y)|_{V_{s1} = -V_{s2} = V_0} - V_{i2}(x, y)|_{V_{s1} = -V_{s2} = V_0}}{2aV_0} \right| \quad (10-9)$$

The pure common-mode crosstalk is defined as

$$Cr_{cc} = \left| \frac{\frac{1}{2} \left(V_{i1}(x, y)|_{V_{s1} = V_{s2} = V_0} + V_{i2}(x, y)|_{V_{s1} = V_{s2} = V_0} \right)}{aV_0} \right| \quad (10-10)$$

The differential-to-common-mode crosstalk is defined as

$$Cr_{cd} = \left| \frac{\frac{1}{2} \left(V_{i1}(x, y)|_{V_{s1} = -V_{s2} = V_0} + V_{i2}(x, y)|_{V_{s1} = -V_{s2} = V_0} \right)}{aV_0} \right| \quad (10-11)$$

The common-to-differential-mode crosstalk is defined as

$$Cr_{dc} = \left| \frac{V_{i1}(x, y)|_{V_{s1} = V_{s2} = V_0} - V_{i2}(x, y)|_{V_{s1} = V_{s2} = V_0}}{2aV_0} \right| \quad (10-12)$$

Using equations (10-9) through (10-12), in combination with (10-5) and (10-6), the various types of crosstalk can be approximated everywhere in the xy -plane. These expressions have been used to generate approximate contour maps of the pad-to-pad crosstalk. These maps are included in Figures 10-32 to 10-35. Comparing the measured pure differential-mode crosstalk in Figure 10-32, strong similarities can be seen. Along

both the x -axis and the y -axis, a rapid decline in the crosstalk with increasing distance can be seen. The theoretical relationship of the on-axis behavior can be readily derived from earlier approximations. Setting the y ordinate to zero, (10-9) can be written

$$Cr_{dd} = \frac{\left| aV_0 \left(\frac{1}{x} - \frac{1}{x-s} \right) - aV_0 \left(\frac{1}{x+s} - \frac{1}{x} \right) \right|}{2aV_0} = \left| \frac{-s^2}{x^3 - s^2x} \right| \quad (10-13)$$

As the distance between pad sets becomes much greater than the space between the individual pads of a differential pair, $x \gg s$, and (10-13) becomes

$$Cr_{dd} \approx \frac{s^2}{x^3} \quad (10-14)$$

With these approximations, the $1/d^3$ characteristic of differential crosstalk becomes clear. However, the analysis also indicates that the differential crosstalk will have this desired behavior only as the distance between circuits is large compared to the dimensions of the differential circuits.

Returning to Figure 10-32, both measured and theoretical differential crosstalk decreases approximately proportional to the inverse of the cube of the distance between pads (or -60 dB per decade of distance). The theoretical contour map shows unexpected behavior along radii approximately $\pm 40^\circ$ from the y -axis. At these locations, the theoretical map shows a series of deep nulls in the differential crosstalk. This effect is caused when the four paths (see Figure 10-37) are precisely balanced, forcing the coupled differential signal to vanish. This phenomenon illustrates the limitation of differential circuits in general. Differential circuits, in general, can only approximately reject interfering signals. This is due to the fact that interfering signals will be at slightly different strengths at each of the two conductors of a differential circuit. Only at the points where the interfer-

ing signal strength is precisely equal at the two conductors will the differential circuit completely reject the signal. This behavior is not clearly indicated in the measured data. The measurements are limited to a coarse grid, and rapidly changing features, such as the deep nulls, will likely be missed. Nevertheless, some evidence of the nulls can be seen in the measured data. The data at 1.0 GHz has symmetrical minima at a pair of points near the expected locations. Furthermore, the contours near the y -axis are nearly triangular, which approximates the theoretical contours. In general, the theoretical calculations of the probe-to-probe crosstalk match the measured data, despite the crude approximations applied.

Comparing the measured pure common-mode crosstalk in Figure 10-33, strong similarities can be again be seen. Both the measured and theoretical behavior are nearly independent of the angle of rotation in the xy -plane. The common-mode crosstalk level is approximately proportional to the inverse of the radial distance between the pads. In common-mode, the pairs of pads essentially behave as a single pads. As a result, the common-mode coupling characteristic closely follows that of a single-ended pad, as described in (10-4).

The approximate theoretical mode-conversion crosstalk maps are shown in Figure 10-34 and Figure 10-35. The measured mode-conversion responses are very similar for differential-to-common and common-to-differential. This is expected due to the port symmetry of the test structures. The theoretical maps show contours that are very similar to the measured data. The differences between the two theoretical mode-conversion maps are due to neglecting the radius of one pair of pads. Nevertheless, the measured data corresponds well to the theoretical predictions. Both show the mode-conversion lev-

els decreasing very rapidly near the y-axis. The off-axis mode-conversion of the pads is due to the difference in path lengths between the four individual pads. Consider differential-to-common mode conversion, for example. The distance from one of the pads in a differential pair to a point on the y-axis equal to that of the other pad in the differential pair. Thus, a differential signal on the pair of pads at the origin creates a zero potential on the y-axis. If a pair of non-source pads are symmetrical about the y-axis, the average voltage coupled to these pads is also zero. The voltage difference between the pads is not zero, however, so the pure differential crosstalk is non-zero. As the output pads are moved off of the y-axis, the path lengths are increasingly asymmetric, leading to mode-conversion. The effect of this asymmetry is reduced as the radial distance between the pads increase, causing the difference in path lengths to be small relative to the overall length. Along the x-axis, it can be shown that the mode-conversion crosstalk is

$$C_{r_{cd}} = C_{r_{dc}} = \frac{s}{x^2} \quad (10-15)$$

if $x \gg s$. Thus, mode-conversion displays a crosstalk characteristic that is proportional to the inverse of the square of distance (or -40 dB per decade of distance). This indicates that, in some cases, mode-conversion crosstalk can become stronger than differential crosstalk, even in differential circuits that are otherwise perfectly balanced. This conversion crosstalk can be a serious limitation in the effectiveness of differential IC interconnects.

These pad-to-pad experiments have provided the means for insight into circuit crosstalk on ICs. The coarse approximations lead to analytical relations that qualitatively follow the actual crosstalk. These relations represent the fundamental mechanisms of cir-

circuit crosstalk, but did not provide accurate quantitative prediction of the strength of crosstalk. Many improvements in the accuracy of the expressions can be made by removing or improving the applied approximations. These improvements lead to increasingly complex analytic expressions, obscuring the meaning of the expressions. Accuracy of the analytic expressions can be significantly improved by including the effects of termination impedances. Other effects, such as inductive coupling can also be included. Ultimately, full electromagnetic analysis of the structures can be accomplished. Regardless of the degree of completeness, the accuracy of theoretical crosstalk predictions can be improved. These predictions can be used as a tool in IC design to reduce crosstalk between circuits.

In concluding this chapter, it is important to emphasize the enabling role that the PMVNA plays in the study of IC crosstalk, particularly for differential circuits. With this instrument, empirical validation of the basic crosstalk theory is achieved. Furthermore, the advantages and limitations of differential circuits on practical silicon ICs have been demonstrated. Several important conclusions can be made from this study. Even with minimal separation, the application of differential IC interconnections significantly reduces circuit-to-circuit crosstalk with respect to single-ended interconnections. The use of metal ground planes beneath interconnections greatly reduces crosstalk and improves the RF performance of interconnections, for both single-ended and differential topologies. The limitations of differential circuits have been demonstrated also. The ability of differential circuits to reject crosstalk is generally dependent on the separation between adjacent circuits. The general rule of $1/d^3$ applies only as separations are large with respect to the cross-sectional dimensions of the differential circuit. At smaller separations, the crosstalk is stronger than that predicted by the $1/d^3$ rule. The most important limitation is perhaps

the significant level of mode-conversion crosstalk that can exist between otherwise balanced differential circuits, due simply to the relative spatial arrangement of the circuits.

The next chapter will defined properties and methods to aid in the design of differential circuits. With the use of mixed-mode s -parameters, the design of differential circuits can be accomplished in a straight-forward manner. These tools will allow efficient differential IC design which, with the application of the finding of this chapter, will lead to significant reduction in circuit-to-circuit crosstalk.

CHAPTER 11

PROPERTIES OF MIXED-MODE S-PARAMETERS

Mixed-mode s-parameters have been developed for the accurate measurement and analysis of differential RF devices and circuits. In particular, mixed-mode s-parameters of two-port differential devices provide mode-specific interpretations that are analogous to traditional (single-ended) two-port device analysis. However, some of the well-known properties of traditional s-parameters are yet to be formulated in terms of mixed-mode s-parameter. This chapter will derive the mixed-mode counterparts of some of the most basic, and useful, properties of traditional s-parameters. In addition, some important new properties of mixed-mode s-parameters will be discussed. The first section will examine symmetry properties of mixed-mode s-parameters. The next section defines a balanced differential device, and considers its implications. The following section will define the indefinite mixed-mode s-parameter matrix, and derive the properties associated with it. The final section of the chapter examines mode-specific gain calculations, and basic design methods.

11.1. Symmetry of Reciprocal Devices

11.1.1. General

Provided that all ports are normalized by the same reference impedance, the traditional s-parameter matrix of an n -port device can be shown to be symmetric if the device is reciprocal [89]. For a reciprocal device, the standard s-parameters have the property

$$S^{\text{std}} = (S^{\text{std}})^T \quad (11-1)$$

Equivalently, the property can be expressed in terms of the elements of the s-parameter matrix as $s_{ij} = s_{ji}$. By direct calculation of the mixed-mode s-parameters with

$$S^{\text{mm}} = MS^{\text{std}}M^{-1} \quad (11-2)$$

it can be shown that

$$S^{\text{mm}} = (S^{\text{mm}})^T \quad (11-3)$$

In other words, a reciprocal device has a symmetric mixed-mode s-parameter matrix. In terms of the mode-specific responses of a reciprocal device, it follows directly from (11-3) that

$$\begin{aligned} S_{dd} &= S_{dd}^T & S_{cc} &= S_{cc}^T \\ S_{cd} &= S_{dc}^T \end{aligned} \quad (11-4)$$

Thus, a reciprocal differential device has symmetric pure-mode s-parameter partitions. The reciprocal differential device has differential s-parameters that behave like a traditional reciprocal device. Similarly, common-mode s-parameters also behave as reciprocal device. In contrast, the mode-conversion parameters do not behave as reciprocals devices in the traditional sense. Rather, a reciprocal differential device has complementary mode-conversion. For the case of a two-port mixed-mode device, the differential-to-common-mode forward transmission, s_{cd21} , is equal to the common-to-differential reverse transmission, s_{dc12} . This does not imply that the differential-to-common mode forward transmission, s_{cd12} , is equal to either of the previous terms. In this sense, the conversion process is fixed with respect to the ports, but reciprocal with respect to the modes.

11.1.2. Port-Symmetric Reciprocal Devices

An additional class of reciprocal devices has played an important role in previous chapters. This device is one that possess differential port symmetry. This type of symmetry is not widely discussed in traditional two-port devices. However, the motivation for defining this type of symmetry arises from two-port applications. A traditional two-port network can be said to have port-symmetry when the ports can be interchanged without affecting the response. For a two-port device to have port symmetry, the reflection parameters of the ports must be equal, and the transmission parameters must also be equal. This type of symmetry is more restrictive than reciprocity since the reflection parameters are encompassed. Physically, a port-symmetric device is one where there is an axis of symmetry perpendicular to the direction of propagation (see Figure 11-1).

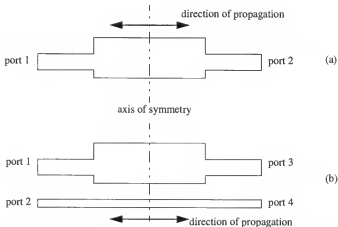


Figure 11-1. Port-symmetric devices. a) Traditional two-port device. b) Mixed-mode two-port device.

Extending the definition of port-symmetry to differential devices relies on the concept of an axis of symmetry. In particular, when an axis of symmetry is perpendicular to the direction of propagation of the differential-mode, for example, the differential device can be said to possess port-symmetry. This does not require that the two constituent single-ended ports of a differential port be identical (see Figure 11-1).

Under port-symmetry, it can be shown that the mixed-mode s -parameters have some important properties. Significantly, the mode-conversion partitions are equal

$$S_{cd} = S_{dc} \quad (11-5)$$

The device is also reciprocal, so $S_{cd} = S_{dc}^T$ still holds. This means the mode-conversion parameters behave as reciprocal devices. The condition of port-symmetry has further implication for mixed-mode s -parameters. Each of the four two-by-two partitions of the mixed-mode parameters contain only two unique parameters: one for transmission and one for reflection. That is

$$\begin{bmatrix} s_{dd11} & s_{dd12} & s_{dc11} & s_{dc12} \\ s_{dd12} & s_{dd11} & s_{dc12} & s_{dc11} \\ s_{cd11} & s_{cd12} & s_{cc11} & s_{cc12} \\ s_{cd12} & s_{cd11} & s_{cc12} & s_{cc11} \end{bmatrix} \leftrightarrow \begin{bmatrix} s_{11} & s_{12} & s_{13} & s_{14} \\ s_{12} & s_{22} & s_{14} & s_{24} \\ s_{13} & s_{14} & s_{11} & s_{12} \\ s_{14} & s_{24} & s_{12} & s_{22} \end{bmatrix} \quad (11-6)$$

Hence, the partitions of the mixed-mode s -parameters are each port-symmetric.

11.2. Balanced Devices

This type of device is defined in terms of a mixed-mode representation. By definition, a balanced differential device has no mode-conversion

$$S_{dc} = S_{cd} = 0 \quad (11-7)$$

This definition can apply to any type of differential device: passive, active, reciprocal, and so on. Under balanced conditions, the device can be separated into two independent networks, one for the differential response and one for the common-mode response. These two network can be separated in both analysis and design.

The condition of balance has some implications for the traditional s-parameters that are useful to consider. By applying the transformation

$$S^{\text{sid}} = M^{-1} S^{\text{mm}} M \quad (11-8)$$

one finds

$$\begin{bmatrix} s_{dd11} & s_{dd12} & 0 & 0 \\ s_{dd21} & s_{dd22} & 0 & 0 \\ 0 & 0 & s_{cc11} & s_{cc12} \\ 0 & 0 & s_{cc21} & s_{cc22} \end{bmatrix} \leftrightarrow \begin{bmatrix} s_{11} & s_{12} & s_{13} & s_{14} \\ s_{12} & s_{11} & s_{14} & s_{13} \\ s_{31} & s_{32} & s_{33} & s_{34} \\ s_{32} & s_{31} & s_{34} & s_{33} \end{bmatrix} \quad (11-9)$$

This gives some insight into the meaning of balance with respect to traditional parameters. In such terms, a balanced device has identical signal paths on each "side" of the differential circuit. For example, the transmission from port one to port three (on, say, the "positive side" of a differential circuit) is equal to the transmission from port two to port four (on the "negative side" of the differential circuit). In this way balance in the device is achieved.

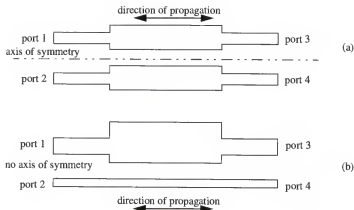


Figure 11-2. Balance in devices. a) Balanced device illustrating propagation symmetry. b) Unbalanced device without propagation symmetry.

An alternative interpretation of circuit balance can be given in terms of symmetry. Examining the form of the traditional four-port s -parameters in (11-9), and comparing it to those of the port-symmetric device in (11-6), one can see that balance is related to symmetry in direction of propagation. Specifically, balance in a device is possible when there is an axis of symmetry parallel with direction of propagation. This type of symmetry, which can be called propagation symmetry, is illustrated in Figure 11-2. Such symmetry generally is physical (as in symmetry of physical dimensions), but must also be electrical response symmetry. For example, active differential circuits can be physically symmetric, but care must be taken in the balance of electrical operation of the active devices (bias, device area matching, etc.) so that balanced operation is maintained.

11.3. Indefinite Mixed-Mode S-Parameters

Indefinite s-parameter matrices are typically used in active devices. In terms of traditional single-ended circuits, the indefinite s-parameter matrix relates the s-parameters of a transistor with one terminal grounded to the s-parameters of the same device with a different port grounded. For example, the s-parameters of a bipolar transistor in common-base (CB) connection can be related to the s-parameters of the same device in common-emitter (CE) connection. The indefinite s-parameters of a device are defined as those found when all terminals of the device are used as measurement ports. The name “indefinite” is derived since no terminal is grounded as a definite reference [23]. Thus, a three terminal device, like a typical bipolar transistor, has a three-port indefinite s-parameter matrix.

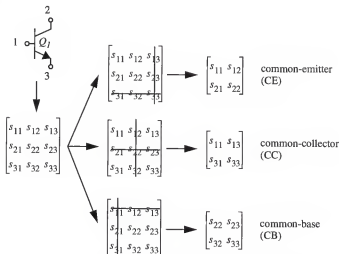


Figure 11-3. Use of traditional indefinite s-parameter matrix of a bipolar transistor.

The indefinite s -parameter matrix is useful since the s -parameters of all possible referenced configurations of a device can be derived from it by observation. For example, let port one of the indefinite matrix corresponds to the base of a bipolar transistor, port two to the collector, and port three to the emitter. Then the s -parameters of the device in common-collector (CC) configuration can be immediately found by striking the third row and third column of the indefinite s -parameter matrix. The remaining parameters form the two-port s -parameters of the device in CC configuration.

Direct measurement of the indefinite s -parameter matrix of a device requires a three-port VNA. (This is a possible application of the PMVNA.) However, the true utility of the indefinite s -parameter matrix is that it can be readily found from the s -parameters of one of the definite configurations. The indefinite s -parameter matrix has the property that each row and column sum to one [23]. As a result, the indefinite s -parameter matrix can be found from any configuration. For example, the CE s -parameters of a device can be measured, and the indefinite s -parameter matrix calculated. The s -parameter of any other configuration can now be found. (This approach can have practical difficulties at RF. The parasitic effects of the grounding and biasing elements can make each of the configurations differ. Care must be taken when applying the indefinite s -parameter matrix method for RF operation.)

The concepts of the indefinite s -parameter matrix can be extended to differential circuits and mixed-mode s -parameters. The fundamental differential device must be defined, however. The basic unit in traditional indefinite s -parameter matrices is the single three-terminal transistor. By analogy, a pair of matched transistors will be defined as the basic differential device. This basic device is illustrated in Figure 11-4, showing port

numbering conventions to be used in the following developments. From this basic differential device, a large variety of practical differential circuits can be constructed. These differential circuits can have any of the mixed-mode ports grounded. For example, grounding mixed-mode port three will result in a simple differential amplifier (essentially, two single-ended CE amplifiers in parallel). By connecting the terminals of mixed-mode port three together, and grounding them through a single resistor, a more familiar differential amplifier is constructed. By knowledge of the indefinite s -parameter matrix of the basic differential pair, the s -parameters of these specific amplifier configurations can be easily found.

Now that the basic differential active device has been defined, it is important to find the relationships that govern its indefinite s -parameter matrix. With these established, the indefinite s -parameter matrix can be readily found from a single measurement of the basic differential pair. The relationships that are required can be derived from con-

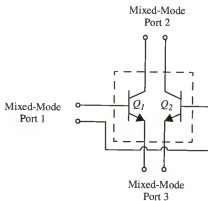


Figure 11-4. Schematic of basic differential gain block for indefinite s -parameter definition.

which, when combined with (11-11), becomes

$$\hat{i}_{11}^+ - \hat{i}_{11} + \hat{i}_{12}^+ - \hat{i}_{12} - \hat{i}_{21} - \hat{i}_{22} - \hat{i}_{31} - \hat{i}_{32} = 0 \quad (11-13)$$

When the pair is stimulated with a pure differential-mode signal at port one,

$$\hat{i}_{11}^+ = -\hat{i}_{12}^+ \quad (11-14)$$

which causes (11-13) to become

$$\hat{i}_{11} + \hat{i}_{12} + \hat{i}_{21} + \hat{i}_{22} + \hat{i}_{31} + \hat{i}_{32} = 0 \quad (11-15)$$

However, from the fundamental definitions of common-mode currents of (3-4),

$$\hat{i}_{c1} = \hat{i}_{11} + \hat{i}_{12} \quad \hat{i}_{c2} = \hat{i}_{21} + \hat{i}_{22} \quad \hat{i}_{c3} = \hat{i}_{31} + \hat{i}_{32} \quad (11-16)$$

equation (11-15) becomes

$$\hat{i}_{c1} + \hat{i}_{c2} + \hat{i}_{c3} = 0 \quad (11-17)$$

Dividing by the differential input current, \hat{i}_{d1}^+ , (11-17) becomes

$$\frac{\hat{i}_{c1}}{\hat{i}_{d1}^+} + \frac{\hat{i}_{c2}}{\hat{i}_{d1}^+} + \frac{\hat{i}_{c3}}{\hat{i}_{d1}^+} = 0 \quad (11-18)$$

By definition of s-parameters

$$S_{jk} = \frac{\hat{i}_j}{\hat{i}_k^+} \quad (11-19)$$

so equation (11-18) can be stated as

$$S_{cd11} + S_{cd21} + S_{cd31} = 0 \quad (11-20)$$

Similar results can be found when driving other ports. In general, it can be said that the sums over each column of S_{cd} equals zero

$$\sum_{j=1}^n S_{cdij} = 0, \forall i \quad (11-21)$$

In the same fashion, it can be shown that the sum over each row of S_{cd} equals zero

$$\sum_{i=1}^n S_{cdij} = 0, \forall j \quad (11-22)$$

By summing the currents entering Q_1 , it can be shown

$$S_{dd11} + S_{dd21} + S_{dd31} + \frac{1}{2}(S_{cd11} + S_{cd21} + S_{cd31}) = 1 \quad (11-23)$$

But from (11-20), this can be written as

$$S_{dd11} + S_{dd21} + S_{dd31} = 1 \quad (11-24)$$

So, in general, the sum over each column of S_{dd} equals one

$$\sum_{j=1}^n S_{ddij} = 1, \forall i \quad (11-25)$$

Similarly, it can be shown that the sum over each row of S_{dd} equals one

$$\sum_{i=1}^n S_{ddij} = 1, \forall j \quad (11-26)$$

With similar arguments, can also be shown that the sum over each row of S_{cc} equals one

$$\sum_{i=1}^n S_{ccij} = 1, \forall j \quad (11-27)$$

sum over each column of S_{cc} equals one

$$\sum_{j=1}^n S_{ccij} = 1, \forall i \quad (11-28)$$

sum over each row of S_{dc} equals zero

$$\sum_{i=1}^n S_{dcij} = 0, \forall j \quad (11-29)$$

sum over each column of S_{dc} equals zero

$$\sum_{j=1}^n S_{dcij} = 0, \forall i \quad (11-30)$$

The important relationships governing the indefinite mixed-mode s-parameter matrix can be summarized with the following statements. (1) Each row and column of the pure-mode s-parameters sum to one. (2) Each row and column of the mode-conversion parameters sum to zero. These relationships apply regardless of the balance between transistors Q_1 and Q_2 . With these relationships, the indefinite mixed-mode s-parameter matrix can be easily calculated from the mixed-mode s-parameters of a basic differential pair measured with a specific configuration. For example, the simple differential pair of Figure 11-4 can be grounded at the emitters. The resulting device is a differential two-port, and can be measured with the PMVNA. From these measurements, the indefinite mixed-mode s-parameter matrix can be calculated. With the use of the indefinite mixed-mode s-parameter matrix, the overall s-parameters of many practical differential amplifiers can be easily found from the measurements of a simple differential pair.

11.4. Device Mode Specific Gains of Ideally Balanced Differential Circuit

One of the primary goals in developing mixed-mode s -parameters is to aid the analysis and design of differential circuits. With traditional two-port devices, many well established analysis and design methods have been developed for use with s -parameters. Examples of such techniques are stability analysis, maximum gain calculations, and source and load terminations for maximum gain. These methods are typically applied to active devices for amplifier design, but are equally valid for use with passive networks. This section will demonstrate how mixed-mode s -parameters can be teamed with traditional two-port techniques to produce useful design and analysis tools for differential circuits.

By representation with mixed-mode s -parameters, the responses of a differential circuit are explicitly stated in terms of the desired modes of operation, the differential and common-modes. A two-port differential device has a two-port pure differential response, and likewise for the pure common-mode and mode-conversions responses. The two-port differential circuit can then be considered as four two-port devices. For example, a differential amplifier can be represented as four two-port amplifiers, as shown in Figure 11-6. With this interpretation, each of the four networks can be analyzed as a two-port network with traditional two-port methods. Under certain conditions, the traditional two-port methods can be directly applied to each of the modal partitions. The condition, which will be assumed throughout the rest of this chapter, is that of an ideally balanced differential circuit. As discussed in Section 11.2, a balanced differential circuit has identically zero mode-conversion responses. Under this condition, the pure-mode responses can be treated as independent networks, but care must be taken with reference impedances. The

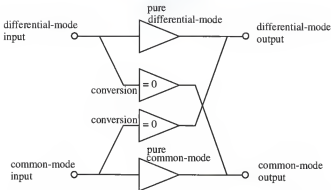


Figure 11-6. Representation of mixed-mode response of ideally balanced differential amplifier.

differential-mode ports typically have a 100Ω reference impedance, whereas the common-mode ports have a 25Ω reference impedance. The analysis and design of differential RF circuits can now be demonstrated.

11.4.1. Transducer Power Gains

With this interpretation, the differential-mode gain of an amplifier (or loss through a passive device) can now be calculated. One widely accepted gain definition for RF and microwave circuits is the transducer power gain [23]. The traditional definition of this gain can be extended to the differential-mode as

$$G_{\text{Tdd}} = \frac{\text{differential power delivered to the differential-mode load}}{\text{differential-mode power available from the source}} \quad (11-31)$$

The differential-mode power available from the source is calculated from the differential normalized power waves defined in (3-24)

$$P_{\text{AVS(d)}} = |a_{d1}|^2 \quad (11-32)$$

The power delivered to the differential-mode load is calculated by

$$P_{2(d)} = |b_{d2}|^2 - |a_{d2}|^2 \quad (11-33)$$

The differential transducer power gain is a function of the source and load terminations. If the differential source impedance is expressed as a differential reflection coefficient, Γ_{sd} , then

$$\Gamma_{sd} = \frac{Z_{sd} - Z_{0d}}{Z_{sd} + Z_{0d}} \quad (11-34)$$

where Z_{0d} is the differential reference impedance. Likewise, the differential load impedance is defined as

$$\Gamma_{Ld} = \frac{Z_{Ld} - Z_{0d}}{Z_{Ld} + Z_{0d}} \quad (11-35)$$

These definitions are straight-forward extensions of traditional reflection coefficient definitions [23]. With these source and load reflection coefficients, the differential transducer power gain (or loss) can be expressed as

$$G_{Tdd} = \frac{1 - |\Gamma_{sd}|^2}{|1 - \Gamma_{INd} \Gamma_{sd}|^2} |s_{dd21}|^2 \frac{1 - |\Gamma_{Ld}|^2}{|1 - s_{dd22} \Gamma_{Ld}|^2} \quad (11-36)$$

where

$$\Gamma_{INd} = s_{dd11} + \frac{s_{dd12}s_{dd21}\Gamma_{Ld}}{1 - s_{dd22}\Gamma_{Ld}} \quad (11-37)$$

Again, these expressions are straight-forward extensions of traditional two-port expressions [23] with the differential parameters replacing the single-ended parameters. With equations (11-36) and (11-37), the pure differential transducer power gain can be directly calculated from the pure differential s-parameters. Again, these expressions apply only

when the mode-conversion is approximately zero (or when the common-mode ports are terminated in the reference impedance).

Similarly, the common-mode power gain can be defined. The transducer power gain can be defined for the common-mode response as

$$G_{Tcc} = \frac{\text{common-mode power delivered to the common-mode load}}{\text{common-mode power available from the source}} \quad (11-38)$$

The common-mode power available from the source is calculated from the common-mode normalized power waves defined in (3-25)

$$P_{AVS(c)} = |a_{c1}|^2 \quad (11-39)$$

The power delivered to the common-mode load is calculated by

$$P_{2(c)} = |b_{c2}|^2 - |a_{c2}|^2 \quad (11-40)$$

The common-mode source impedance is expressed as a differential reflection coefficient

$$\Gamma_{sc} = \frac{Z_{sc} - Z_{0c}}{Z_{sc} + Z_{0c}} \quad (11-41)$$

where Z_{0c} is the common-mode reference impedance. The common-mode load impedance is defined as

$$\Gamma_{Lc} = \frac{Z_{Lc} - Z_{0c}}{Z_{Lc} + Z_{0c}} \quad (11-42)$$

With these source and load reflection coefficients, the common-mode transducer power gain (or loss) can be expressed as

$$G_{Tcc} = \frac{1 - |\Gamma_{sc}|^2}{|1 - \Gamma_{INc} \Gamma_{sc}|^2} |s_{cc21}|^2 \frac{1 - |\Gamma_{Lc}|^2}{|1 - s_{cc22} \Gamma_{Lc}|^2} \quad (11-43)$$

where

$$\Gamma_{\text{INc}} = s_{\text{cc}11} + \frac{s_{\text{cc}12}s_{\text{cc}21}\Gamma_{\text{Lc}}}{1 - s_{\text{cc}22}\Gamma_{\text{Lc}}} \quad (11-44)$$

Thus, the common-mode power gain can be simply calculated from the pure common-mode s -parameters. Like the differential response, the pure common-mode response is treated as a traditional two-port device. Again, these expressions apply only when the mode-conversion is approximately zero (or when the differential-mode ports are terminated in the reference impedance).

11.4.2. Maximum Power Gains

With the developments of the previous section as a guide, many more useful analysis and design tools established for traditional two-port networks can be applied to differential circuits with the use of mixed-mode s -parameters. One key design tool is the method for achieving maximum power gain through choice of source and load impedances. A related issue is stability analysis of a device. Both of these methods form the foundations of RF amplifier design for traditional two-port devices. These fundamental design methods can be applied to differential circuits by substituting the appropriate mixed-mode s -parameters in the traditional expressions. Again, for direct application of the two-port expression, the mode-conversion responses must be zero. The differential maximum power gain will be developed as an example.

Following traditional development [23], it is known that maximum power gain in a two-port device occurs when both ports are simultaneously conjugately matched. In the case of a differential device, maximum differential power gain occurs when both ports are simultaneously conjugately matched differentially. From two-port theory, it is known that the condition of simultaneously conjugately match is possible only when the device is

unconditionally stable. The stability of the differential response can be found with the use of the following adapted differential quantities

$$\Delta_{dd} = s_{dd11}s_{dd22} - s_{dd12}s_{dd21} \quad (11-45)$$

$$K_{dd} = \frac{1 - |s_{dd11}|^2 - |s_{dd22}|^2 + |\Delta_{dd}|^2}{2|s_{dd12}s_{dd21}|} \quad (11-46)$$

For the differential response to be stable for all possible (passive) combinations of differential source and load terminations, the following must be true

$$K_{dd} > 1 \quad (11-47)$$

and

$$|\Delta_{dd}| < 1 \quad (11-48)$$

If this is the case, then differential source and load terminations exist to result in a simultaneously conjugate match (differentially). Continuing the adaptation of traditional development [23], these optimum terminations can be expressed as

$$\Gamma_{Msdd} = \frac{B_{1dd} - \sqrt{B_{1dd}^2 - 4|C_{1dd}|^2}}{2C_{1dd}} \quad (11-49)$$

$$\Gamma_{MLdd} = \frac{B_{2dd} - \sqrt{B_{2dd}^2 - 4|C_{2dd}|^2}}{2C_{2dd}} \quad (11-50)$$

where

$$B_{1dd} = 1 + |s_{dd11}|^2 - |s_{dd22}|^2 - |\Delta_{dd}|^2 \quad (11-51)$$

$$B_{2dd} = 1 + |s_{dd22}|^2 - |s_{dd11}|^2 - |\Delta_{dd}|^2 \quad (11-52)$$

$$C_{1dd} = s_{dd11} - \Delta_{dd}^* s_{dd22} \quad (11-53)$$

$$C_{2dd} = s_{dd22} - \Delta_{dd}^* s_{dd11}^* \quad (11-54)$$

By terminating the differential device with the differential impedances represented in equations (11-49) and (11-50), the maximum differential power gain of the device can be achieved. With these terminations, the transducer power gain is found to be

$$G_{Tmax(dd)} = \frac{s_{dd21}}{s_{dd12}} \left(K_{dd} - \sqrt{K_{dd}^2 - 1} \right) \quad (11-55)$$

Through very similar developments, the common-mode simultaneously conjugate match can be derived (provided the common-mode response is unconditionally stable). In most applications, however, maximizing the common-mode gain is not a design goal. Additionally, it is possible to calculate the simultaneously conjugate match impedances for the mode-conversion responses. Increasing mode-conversion is generally contrary to the design goals of a differential device.

To illustrate the use of the concepts in this section, some calculations on a representative differential RF amplifier are presented below. The amplifier circuit is shown

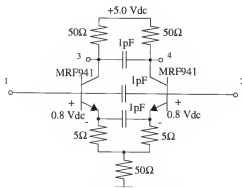


Figure 11-7. Schematic of simulated RF balanced differential amplifier.

in Figure 11-7 (note that this is very similar to Figure D-1 of Appendix D, except the emitter resistor are now balanced). The mixed-mode s -parameters are generated through simulations of the circuit in MDS. Using the simulated mixed-mode s -parameters, the maximum differential power gain can be calculated. The stability of the differential response is determined by applying (11-45) and (11-46). The conditions (11-47) and (11-48) are true, indicating that the amplifier is unconditionally stable over the entire frequency band examined. Figure 11-8(a) shows the differential stability factor, K_{dd} , versus frequency. Since the device is differentially stable, the maximum power gain can be calculated via (11-55). This maximum gain is also plotted in Figure 11-8(a). At 1.0 GHz, for example, the maximum differential power gain from the amplifier is 10.3 dB. The optimum differential source and load terminations (simultaneous conjugate match terminations) are shown in Figure 11-8(b) in terms of reflection coefficients. The values at 1.0 GHz are $\Gamma_{Msd} = 0.853\angle 105^\circ$ ($Z_{Msd} = 12.6 + j76.0 \Omega$) for the differential source termi-

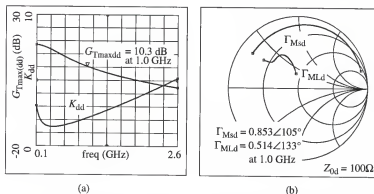


Figure 11-8. Maximum differential power gain of simulated differential amplifier. a) Maximum differential power gain in dB and stability factor versus frequency. b) Optimum differential terminations versus frequency.

nation and $\Gamma_{MLd} = 0.514 \angle 133^\circ$ ($Z_{MLd} = 37.4 + j38.3 \Omega$) for the differential load termination. When the amplifier is terminated with these differential impedances, the differential gain will be equal to the calculated maximum gain (10.3 dB at 1.0 GHz).

Similarly, the maximum common-mode gain can be calculated. The common-mode response of the amplifier is also unconditionally stable. The common-mode stability factor, K_{cc} , and the maximum common-mode power gain are plotted versus frequency in Figure 11-9(a). These values are calculated through expressions analogous to equations (11-45) through (11-55) with the common-mode quantities substituted for the differential quantities. At 1.0 GHz, the maximum common-mode power gain from the amplifier is 4.3 dB. The optimum differential source and load terminations (simultaneous conjugate match terminations) are shown in Figure 11-9(b) in terms of reflection coefficients. The values at 1.0 GHz are $\Gamma_{Msc} = 0.971 \angle 18.3^\circ$ ($Z_{Msc} = 14.4 + j154 \Omega$) for the common-mode source termination and $\Gamma_{MLc} = 0.487 \angle 119^\circ$ ($Z_{MLc} = 11.2 + j12.5 \Omega$) for the common-

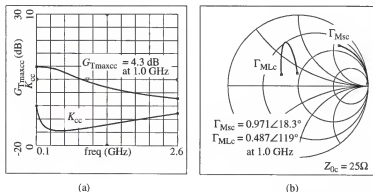


Figure 11-9. Maximum common-mode power gain of simulated differential amplifier. a) Maximum common-mode power gain in dB and stability factor versus frequency. b) Optimum common-mode terminations versus frequency.

mode load termination. When the amplifier is terminated with these common-mode impedances, the common-mode gain will be equal to the calculated maximum common-mode gain.

11.4.3. Power Gain Circles

A fundamental property of the mixed-mode representation of a differential circuit with no significant mode-conversion is that the differential and common-mode gains can be set independently. This property allows the design of the differential and common-mode responses of a circuit to be pursued to independent design goals. In the previous example, both the differential and common-mode power gains have been maximized. Alternatively, one could design matching impedances that maximize differential gain while simultaneously greatly reducing the common-mode power gain.

To aid in the design of non-maximum gain responses, mode-specific power gain circles will now be introduced. Power gain circles, for traditional two-port networks, are contours of constant gain as a function of termination impedances [23]. These circles allow a particular gain (less than maximum) to be achieved through intentionally mismatching the amplifier. The circles indicate all possible termination impedances that will produce the desired gain. Typically, a mis-matched amplifier design is begun by de-coupling the source and load match problems. In gain circles, this de-coupling translates into the use of power gains other than the transducer gain. One method of miss-matched amplifier design is based on available power gain. This power gain is calculated assuming the output of the device is always conjugately matched as the input match is varied. As a result, the available gain is independent of the load termination. For the pure differential response, this gain is defined as

$$G_{A(dd)} = \frac{\text{differential power available from the device output}}{\text{differential power available from the source}} \quad (11-56)$$

Another method of miss-matched amplifier design is based on operating power gain. This power gain is calculated assuming the input of the device is always conjugately matched as the output match is varied. As a result, the operating gain is independent of the source termination. For the pure differential response, this gain is defined as

$$G_{P(dd)} = \frac{\text{differential power delivered to the load}}{\text{differential power input to the device}} \quad (11-57)$$

The gain circles for both of these differential power gains are developed directly from the traditional two-port expression [23]. These circles have been plotted for the example differential amplifier, at 1.0 GHz, in Figure 11-10. The smallest circles on these plots correspond to nearly maximum gains (the actual maximum are points near the centers of the smallest shown circles). The gains corresponding to smallest circles are very close to the

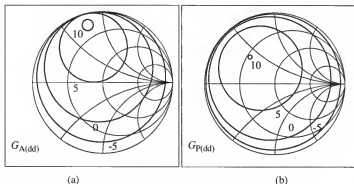


Figure 11-10. Constant differential power gain circles of simulated differential amplifier.
a) Available differential-mode power gain circles in dB at 1.0 GHz.
b) Operating differential-mode power gain circles in dB at 1.0 GHz

maximum transducer gain values. In fact the maximum values of all three types of gains are equal, corresponding to simultaneously conjugate matches.

The common-mode power gain circle can be similarly developed. Both the available and operating common-mode power gain circles are plotted, at 1.0 GHz, in Figure 11-11. From these plots, it is possible to choose common-mode termination impedances that reduce the common-mode gain of the amplifier. For example, if a common-mode load termination is chosen to be $\Gamma_{Lc} = 0.95 \angle -90^\circ$, then the common-mode gain of the amplifier is, at best, only -12 dB. In fact, by also miss-matching the source to $\Gamma_{sc} = 0.95 \angle -90^\circ$, the common-mode power transducer gain is reduced to -31 dB. The miss-matching of the common-mode response has no effect on the differential response. Thus, by setting the differential terminations to the optimum values ($\Gamma_{sd} = 0.853 \angle 105^\circ$ and $\Gamma_{Ld} = 0.514 \angle 133^\circ$) a differential gain of 10.3 dB is achieved.

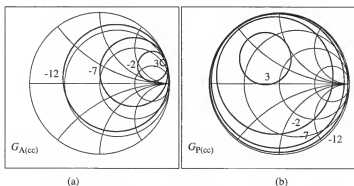


Figure 11-11. Constant common-mode power gain circles of simulated differential amplifier. a) Available common-mode power gain circles in dB at 1.0 GHz. b) Operating common-mode power gain circles in dB at 1.0 GHz

These termination values can be translated into equivalent networks at the input and output of the amplifier. The differential and common-mode terminations can simultaneously be generated by either a “tee” or “pi” network [10]. For example, the output load can be shown to be equivalent to the circuit shown in Figure 11-12. The relations between differential/common-mode impedances and the elements in the “pi” network can be shown to be

$$\begin{aligned} Z_1 &= 2Z_c \\ Z_3 &= \frac{4Z_c Z_d}{4Z_c - Z_d} \end{aligned} \quad (11-58)$$

Optionally, the “tee” network elements, as shown in Figure 11-13, can be shown to be

$$\begin{aligned} Z_1 &= \frac{Z_d}{2} \\ Z_3 &= Z_c - \frac{Z_d}{4} \end{aligned} \quad (11-59)$$

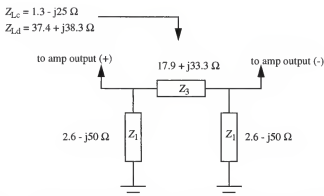


Figure 11-12. Equivalent load network providing specified differential and common-mode load impedances.

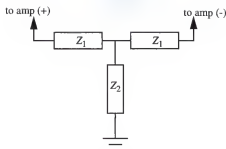


Figure 11-13. Equivalent "tee" network providing specified differential and common-mode termination impedances.

Matching networks can be designed to generate the desired impedances at the input and output of the device, given source and load impedance. The design of these networks can proceed along traditional lines with the separate design tasks for the differential and common-mode matching networks.

The properties discussed in this chapter make mixed-mode s -parameters very useful in the analysis and design of RF differential circuits. This chapter has illustrated how some of the most useful concepts of traditional s -parameters are embodied in mixed-mode s -parameters. In particular, the utility of mixed-mode parameters is founded in their ability to isolate the response of a device to a single-mode signal. This ability allows separation of the design and analysis of each mode response, so that these tasks can proceed along traditional lines.

CHAPTER 12

CONCLUSIONS

This work has provided a way to accurately measure, analyze, and design RF and microwave differential circuits. The motivation for this work is the drive to higher levels of circuit integration and decreasing power supply voltage. Historic applications of differential topologies promise that integrated RF differential circuits can reduce unwanted circuit-to-circuit coupling and increase dynamic range. The inability to accurately measure, analyze, and design differential circuits at RF has impeded their wide spread use in IC applications.

The reasons for these problems have been enumerated in Chapter 2, showing several weaknesses in accepted engineering practices with respect to differential circuits. The traditionally accepted analog definitions of differential and common-mode voltages and currents are not appropriate for power calculations. Power-based quantities are a fundamental requirement of RF methods. No theory, prior to this work, was found for the accurate analysis of RF differential circuits. Furthermore, no measurement technique, existing prior to this work, is appropriate for accurate characterization of RF differential circuits.

The fundamental theory of mode-specific analysis of RF differential circuits was developed in Chapter 3. This original work is based on a new set of definitions for differential and common-mode voltages and currents which are appropriate for power calculations. With these new definitions, mode-specific scattering parameters, termed mixed-mode *s*-parameters, have been developed which completely describe the linear behavior of

an RF differential circuit. These mixed-mode s -parameters have been interpreted, and shown to be useful in understanding differential circuit operation. The relation between mixed-mode s -parameters and traditional s -parameters was established. This relation is useful for deriving mixed-mode s -parameters from traditional RF simulators. This relationship suggested a more general interpretation of multi-mode circuits. Following from this, a generalized development of mode-specific s -parameters was advanced which was not limited to differential circuits.

The measurement of RF differential circuits was successfully addressed in Chapter 4 with development of the pure-mode vector network analyzer (PMVNA). This new measurement instrument directly measures the differential-mode, common-mode, and mode-conversion responses of a two-port RF differential device. This specialized network analyzer was implemented with standard commercial test equipment, making it practical to reproduce. The PMVNA was shown to make accurate mixed-mode s -parameter measurements in Chapter 5. The PMVNA was further shown to have significantly increased dynamic range in its differential measurements, with respect to traditional single-ended measurements. Importantly, the PMVNA was shown to have significantly lower errors in the measurement of differential circuits than those of a traditional four-port VNA.

The calibration of the PMVNA was developed in detail in Chapter 6. This work was pursued from the perspective of a general n -port VNA calibration. Original work in this area has established a new class of calibration standard that is required for successful calibration of the PMVNA, as well as for a general n -port VNA. Special consideration was given to the correction of quasi-systematic phase errors in the PMVNA. This error

mechanism is unique to the specific implementation of the PMVNA of this work. The accuracy of the PMVNA was verified in Chapter 7. The PMVNA was used to measure NIST-traceable devices, and the corrected measurement data was shown to compare well to the specified uncertainties of the NIST data.

The remainder of the dissertation was devoted to the application of mixed-mode concepts for the measurement, analysis, and design of practical RF differential circuits. Chapter 8 examined power splitters and combiners, which are critical components in many differential systems. The application of mixed-mode concepts produced relationships between phase and magnitude imbalances and spurious mode responses in these devices.

Differential structures, fabricated with thin-film metal on ceramic substrates, were examined in Chapter 9. These structures provided a well-characterized environment in which to study the practical effects of balance and symmetry in differential structures. Selected structures were simulated with a commercial electromagnetic simulator, and compared with the measured mixed-mode data. The measured and simulated data correlated well.

Circuit-to-circuit crosstalk, an original motivation for the application of differential circuits, was studied in Chapter 10. This chapter examined structures implemented on a silicon IC. These studies provided insight into practical implementations of differential circuits in ICs. The PMVNA played an enabling role in the study of IC crosstalk, particularly for differential circuits. It was found that differential IC interconnections significantly reduced circuit-to-circuit crosstalk with respect to single-ended interconnections. Metal ground planes beneath interconnections greatly reduced crosstalk and improved the

RF performance of interconnections, for both single-ended and differential topologies. The limitations of differential circuits were also examined. It was found that mode-conversion crosstalk can exist at levels that degrade the overall crosstalk immunity of differential circuits. This mode-conversions can exist between otherwise balanced differential circuits, due simply to the relative spatial arrangement of the circuits.

Some basic design procedures were presented in Chapter 11. This chapter began by establishing some important properties of mixed-mode s -parameters. These properties are useful in many practical RF differential applications. The practical importance of mixed-mode s -parameters were demonstrated through design procedures. With mixed-mode s -parameters, the analysis and design of differential circuits can be divided into independent designs for the differential and common-modes. It was shown how design goals for each mode can be independently achieved.

This work has established the foundations for the accurate measurement, analysis, and design of RF differential circuits with respect to linear systematic behavior. Many important aspects of RF differential circuit performance remain to be developed. A complete theoretical description of the linear noise performance of RF differential circuits is needed. Future research in this area is of practical importance. Like single-ended circuits, many differential circuits must be designed for low noise applications. A complete treatment of noise in differential circuits must include self-consistent definitions for noise in multiple modes. A practical means of measuring the noise in differential devices, particularly at RF, is also needed. Finally, useful design procedures for noise performance are required for RF differential circuits. These items will likely share many of the aspects of the mixed-mode s -parameter theory. A general differential device or circuit is expected to

have both differential and common-mode noise sources. These sources can be expected to have some correlation. This should result in equivalent noise sources that are analogous to pure-mode and mode-conversion responses in mixed-mode s -parameter theory. The complete noise performance of an RF differential device is expected to depend on source terminations, including both pure-mode and mode-conversion terms. The measurement and design of differential noise will likely follow this basic direction.

Another important area of future research is the non-linear performance of a differential circuit. In particular, effects like intermodulation distortion (IMD) have great practical importance. Theoretical development is needed to better understand and predict IMD in RF differential circuits. Measurement methods and systems for non-linear behavior in differential circuits are also needed. Design methods limiting IMD are ultimately required. The basic multi-mode IMD theory is expected to have aspects analogous to pure-mode and mode-conversion responses. The relations between these responses may be quite complex, however. The most promising approach is the application of Volterra series analysis to differential circuits. This analysis method, already challenging in many simple single-ended circuits, may require significant work for differential applications. However, this may be the most reasonable approach to gain understanding of the basic mechanisms of distortion in differential circuits.

APPENDIX A

ANALOG HALF-CIRCUIT TECHNIQUES

Of particular interest in analog techniques is the method of differential and common-mode half-circuits. This technique allows circuit analysis simplification by considering separately the response of the circuit to a pure differential signal and a pure common-mode signal. This approach [4] can best be summarized by application to an emitter-coupled, or differential, pair. It is important to note that the example presented here is meant as an illustrative example only. As such, many important effects, like output resistance of the transistors and frequency effects, are neglected. Figure A-1 shows a differential pair with both differential and common-mode input signals. With the common-mode input set to zero, the small-signal equivalent circuit can be drawn as shown in Figure A-2. Because the circuit is symmetric, and because the input signals are equal but opposite, the voltage at the emitters does not vary. The emitters are at small-signal ground, and the circuit has two independent identical halves. One half of the circuit is redrawn in Figure A-3, and this is known as the differential half-circuit. The differential performance of the amplifier can be calculated from this much simplified circuit diagram.

$$\frac{v_{od}}{2} = -g_m R_C \frac{v_{id}}{2} \quad (\text{A-1})$$

$$A_d = \frac{v_{od}}{v_{id}} = -g_m R_C \quad (\text{A-2})$$

Next the differential input of Figure A-1 is set to zero, and the small-signal equivalent circuit drawn as in Figure A-4. Since both transistors have equal base-emitter voltages, the collector currents are equal. This ensures that the AC voltage at the emitters is non-zero, and the emitter resistor R_{EE} can be redrawn as the parallel combination of two resistors, each of value $2R_{EE}$. Furthermore, the symmetry in the circuit ensures that no current flows in the branch between the emitter resistors. This branch can be removed, again leaving two independent identical halves. One half of the circuit is redrawn in Figure A-5, and this is known as the common-mode half-circuit. The common-mode performance of the amplifier can be calculated from this simplified circuit diagram.

$$A_c = \frac{v_{oc}}{v_{ic}} = \frac{g_m R_C}{1 + 2g_m R_{EE} \left(1 + \frac{1}{\beta_0}\right)} \quad (\text{A-3})$$

From these analog techniques another important parameter can be defined. The common-mode rejection ratio (CMRR) of a differential amplifier is typically

$$\text{CMRR} = \left| \frac{A_d}{A_c} \right| \quad (\text{A-4})$$

CMRR is a measure of ability of a differential amplifier to reject a common-mode signal with respect to its differential-mode gain. From the half-circuit technique above, the CMRR of the simple differential pair is found to be

$$\text{CMRR} = 1 + 2g_m R_{EE} \left(1 + \frac{1}{\beta_0}\right) \quad (\text{A-5})$$

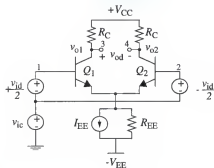


Figure A-1. Differential pair with differential and common-mode inputs.

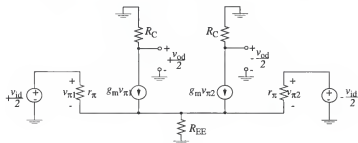


Figure A-2. Small-signal equivalent circuit of Figure A-1 with pure differential input.

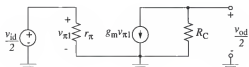


Figure A-3. Differential-mode half-circuit of Figure A-2.

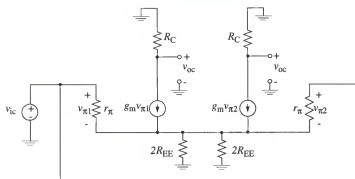


Figure A-4. Small-signal equivalent circuit of Figure A-1 with pure common-mode inp

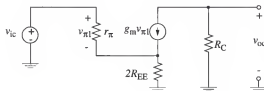


Figure A-5. Small-signal equivalent circuit of Figure A-4.

APPENDIX B

ANALOG MEASUREMENT TECHNIQUES

Certain parameters are widely used in analog circuit descriptions due to their intuitive relation to the traditional analog state variables of voltage and current. For example, a two-port z -parameter description of a circuit is

$$\begin{bmatrix} v_1 \\ v_2 \end{bmatrix} = \begin{bmatrix} z_{11} & z_{12} \\ z_{21} & z_{22} \end{bmatrix} \begin{bmatrix} i_1 \\ i_2 \end{bmatrix} \quad (\text{B-1})$$

The voltage-current derived parameters can be individually defined. For example, the z_{ij} parameter is

$$z_{ij} = \left. \frac{v_i}{i_j} \right|_{i_{k \neq j} = 0} \quad (\text{B-2})$$

The method of measurement of these parameters is implied in their definitions. For example, z -parameters are measured by leaving certain ports open-circuits, which satisfies (B-2). Z -parameters are therefore also known as open-circuit parameters.

Direct measurement of voltages and currents is the traditional measurement method for analog differential circuit. The main difficulty with analog differential measurements is the generation and reception of differential signals. Most test equipment uses single-ended (ground referenced) inputs and outputs in the form of coaxial connections. At analog frequencies, these single-ended connections are called unbalanced. These

unbalanced signals can be converted to balanced (differential) signals with a device known as a balun (balanced-unbalanced).

A balun is a reciprocal device that can convert a single-ended signal to differential or can convert a differential signal to single-ended. Regardless of their specific implementation, baluns can be modeled as a transformer with the primary winding grounded on one terminal and the secondary winding with a grounded center-tap. There are other types of differential-to-single-ended converters for analog use. Of note is the operational amplifier which can be used as an active, but unidirectional, balun.

With the use of baluns, the differential-mode response of a differential circuit can be measured. Common-mode measurements can be made by driving the inputs from a single source. (However, care must be taken so the DC operation of the circuit is not effected.) These two measurements require two distinct configurations. Furthermore, both measurements assume a pure mode input and output; any mode conversion is neglected. For these reasons, this type of measurement will be called single mode.

The primary instrument for analog measurements is the oscilloscope, while input signals are provided by a signal generator. The oscilloscope typically has high impedance inputs (usually $1\text{M}\Omega$), and is useful for measuring voltages [90]. This high impedance generally does not load the circuit. (In reality, the input impedance of the oscilloscope is the resistive load in parallel with a parasitic capacitance. The capacitance reduces the effective impedance level of the input as frequency increases, loading the circuit. This effect represents another basic limitation of analog measurements.) A schematic of an analog measurement is given in Figure B-1. Currents can be measured by measuring the

voltage across a series resistor of known value. Currents can also be measured with a current probe which inductively couples a signal proportional to a current.

An important feature of the described voltage-current measurement techniques is the embedding of the baluns into the test circuit. The resulting measurements are then of the combined system of the converters and differential circuit. There is no way, without significant characterization of the baluns, to remove the effect of the baluns from the measured data. Typically, the balun is assumed to be ideal, and for many analog applications this approximation is acceptable. Nevertheless, the inability to remove the effects of the baluns is a significant problem, and this problem becomes acute as operation frequency increases.

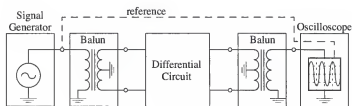


Figure B-1. Analog Differential Circuit Measurement.

APPENDIX C

TRANSMISSION OF MODES FROM COUPLED TO UNCOUPLED LINES

Consider a system where a pair of coupled transmission lines are connected in cascade with a pair of uncoupled transmission lines, as shown in Figure C-1. The coupled pair will be considered to be a reference line; hence, the coupled pair line is symmetric and low loss. The normalized waves at the outputs of the uncoupled lines will be investigated under the same assumptions, namely low loss and symmetry, which for the uncoupled case means the lines are identical. The voltages at a point x on the coupled pair lines are given by (3-19), rewritten here to explicitly show the complex exponentials

$$\begin{aligned}v_1(x) &= V_e^+ e^{-\gamma_e x} + V_e^- e^{\gamma_e x} + V_o^+ e^{-\gamma_o x} + V_o^- e^{\gamma_o x} \\v_2(x) &= V_e^+ e^{-\gamma_e x} + V_e^- e^{\gamma_e x} - V_o^+ e^{-\gamma_o x} - V_o^- e^{\gamma_o x}\end{aligned}\tag{C-1}$$

and the currents, also given by (3-19) are

$$\begin{aligned}i_1(x) &= \frac{V_e^+}{Z_e} e^{-\gamma_e x} - \frac{V_e^-}{Z_e} e^{\gamma_e x} + \frac{V_o^+}{Z_o} e^{-\gamma_o x} - \frac{V_o^-}{Z_o} e^{\gamma_o x} \\i_2(x) &= \frac{V_e^+}{Z_e} e^{-\gamma_e x} - \frac{V_e^-}{Z_e} e^{\gamma_e x} - \frac{V_o^+}{Z_o} e^{-\gamma_o x} + \frac{V_o^-}{Z_o} e^{\gamma_o x}\end{aligned}\tag{C-2}$$

With the uncoupled transmission lines, the voltages and currents at a point x are

$$\begin{aligned}v_{ui}(x) &= V_{ui}^+ e^{-\gamma_u x} + V_{ui}^- e^{\gamma_u x} \\i_{ui}(x) &= \frac{V_{ui}^+}{Z_u} e^{-\gamma_u x} - \frac{V_{ui}^-}{Z_u} e^{\gamma_u x}\end{aligned}\tag{C-3}$$

with $i = 1, 2$ and $Z_{u1} = Z_{u2} = Z_u$, $\gamma_{u1} = \gamma_{u2} = \gamma_u$. At the interface between the coupled pair and the uncoupled pair, ($x = 0$) the voltages and currents of the two systems must conform to the boundary conditions

$$\begin{aligned} v_{u1}(0) &= v_1(0) & i_{u1}(0) &= i_1(0) \\ v_{u2}(0) &= v_2(0) & i_{u2}(0) &= i_2(0) \end{aligned} \quad (\text{C-4})$$

Through the application of these boundary conditions and the simultaneous solution of equations (C-1), (C-2), and (C-3), the phasor coefficients on the uncoupled lines are found to be

$$\begin{aligned} V_{u1}^+ &= \frac{1}{2} \left[V_e^+ \left(1 + \frac{Z_u}{Z_e} \right) + V_e^- \left(1 - \frac{Z_u}{Z_e} \right) + V_o^+ \left(1 + \frac{Z_u}{Z_o} \right) + V_o^- \left(1 - \frac{Z_u}{Z_o} \right) \right] \\ V_{u1}^- &= \frac{1}{2} \left[V_e^+ \left(1 - \frac{Z_u}{Z_e} \right) + V_e^- \left(1 + \frac{Z_u}{Z_e} \right) + V_o^+ \left(1 - \frac{Z_u}{Z_o} \right) + V_o^- \left(1 + \frac{Z_u}{Z_o} \right) \right] \end{aligned} \quad (\text{C-5})$$

$$\begin{aligned} V_{u2}^+ &= \frac{1}{2} \left[V_e^+ \left(1 + \frac{Z_u}{Z_e} \right) + V_e^- \left(1 - \frac{Z_u}{Z_e} \right) - V_o^+ \left(1 + \frac{Z_u}{Z_o} \right) - V_o^- \left(1 - \frac{Z_u}{Z_o} \right) \right] \\ V_{u2}^- &= \frac{1}{2} \left[V_e^+ \left(1 - \frac{Z_u}{Z_e} \right) + V_e^- \left(1 + \frac{Z_u}{Z_e} \right) - V_o^+ \left(1 - \frac{Z_u}{Z_o} \right) - V_o^- \left(1 + \frac{Z_u}{Z_o} \right) \right] \end{aligned} \quad (\text{C-6})$$

The differential-mode voltage at the output of the uncoupled pair ($x = -d$) can be defined by (3-1) as

$$v_d(-d) = v_{u1}(-d) - v_{u2}(-d) \quad (\text{C-7})$$

which is found to be

$$v_d(-d) = V_d^+ e^{\gamma_u d} + V_d^- e^{-\gamma_u d} \quad (\text{C-8})$$

where

$$V_{d_u}^+ = V_{u1}^+ - V_{u2}^+ \quad V_{d_u}^- = V_{u1}^- - V_{u2}^- \quad (C-9)$$

The normalized forward differential-mode wave at the output of the uncoupled pair, similarly defined by (3-23), can also be shown as

$$a_{d_u} = \frac{V_{d_u}^+}{\sqrt{R_{d_u}}} \quad (C-10)$$

where R_{d_u} is the (approximately) purely real characteristic impedance of the differential-mode, defined between the uncoupled lines, and $R_{d_u} = 2R_u$ where R_u is the characteristic impedance of the each of the uncoupled lines. From (C-5), (C-6), (C-9), and (C-10) it is found that

$$a_{d_u} = \frac{1}{2} \sqrt{\frac{R_d}{R_{d_u}}} \left[a_d \left(1 + \frac{R_{d_u}}{R_d} \right) + b_d \left(1 - \frac{R_{d_u}}{R_d} \right) \right] e^{j\beta_u d} \quad (C-11)$$

where a_d and b_d is the differential-mode normalized forward and reverse waves of the coupled system at $x = 0$, and R_d is the approximately real characteristic impedance of the differential-mode on the coupled-pair. Similarly, the remaining differential and common-mode normalized waves can be shown to be

$$\begin{aligned} b_{d_u} &= \frac{1}{2} \sqrt{\frac{R_d}{R_{d_u}}} \left[b_d \left(1 + \frac{R_{d_u}}{R_d} \right) + a_d \left(1 - \frac{R_{d_u}}{R_d} \right) \right] e^{-j\beta_u d} \\ a_{c_u} &= \frac{1}{2} \sqrt{\frac{R_c}{R_{c_u}}} \left[a_c \left(1 + \frac{R_{c_u}}{R_c} \right) + b_c \left(1 - \frac{R_{c_u}}{R_c} \right) \right] e^{j\beta_u d} \\ b_{c_u} &= \frac{1}{2} \sqrt{\frac{R_c}{R_{c_u}}} \left[b_c \left(1 + \frac{R_{c_u}}{R_c} \right) + a_c \left(1 - \frac{R_{c_u}}{R_c} \right) \right] e^{-j\beta_u d} \end{aligned} \quad (C-12)$$

where b_d , a_c , and b_c are the normalized waves of the coupled system at $x = 0$. Therefore, the differential and common-mode normalized waves at the output of the uncoupled lines are equal to the corresponding coupled system waves with a phase-shift and a scaling/offset factor due to the different characteristic impedances. To the resulting mixed-mode s-parameters, the phase-shift and the scaling/offset factor represent an arbitrary reference plane shift and a re-normalization to the characteristic impedance of the uncoupled transmission lines, respectively. Because of this, the coupled pair reference line can be replaced with an uncoupled pair reference, and the resulting mixed-mode s-parameters are simply transposed to a different reference impedance by the uncoupled lines. Therefore, the mixed-mode s-parameters of an arbitrary n-port DUT can be measured with n pairs of uncoupled transmission lines.

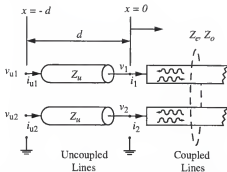


Figure C-1. Schematic of uncoupled pair in cascade with coupled-pair line.

APPENDIX D

SIMULATED S-PARAMETERS OF DIFFERENTIAL AMPLIFIER

To illustrate the difficulty of interpreting the standard four-port s-parameters of a differential amplifier, an example circuit has been simulated in Hewlett-Packard's MDS [32]. The schematic of the amplifier is shown in Figure D-1. The amplifier is a typical RF differential amplifier, with one exception. One of the emitter resistors is larger than the other to be representative of device mis-match. The mis-match is exaggerated to demonstrate the effects of mode conversion. Also included are some representative parasitic capacitances between various nodes. The transistor, a Motorola MRF941 silicon BJT, is by a typical RF device; the model of the device is provided in the MDS device model library. The simulated four-port s-parameters are shown in Figure D-2.

For contrast, one half of the differential amp has also been simulated as a single-ended amplifier, as shown in Figure D-3. The simulated two-port s-parameters are shown in Figure D-4. The two-port data shows the well known characteristics of a common emitter amplifier.

Examining the four-port data, one does not find any interpretation analogous to two-port s-parameters of an amplifier. In spite of the fact that the circuit is ideally meant to operate as a two-port (differential) amplifier, the full simulated s-parameters show no clear indication of the differential operation.

This example can be further examined with mixed-mode s-parameters as defined in Section 3.1.1. The mixed-mode s-parameters of the differential amplifier of Figure D-1

are shown in Figure D-5. With the application of mixed-mode s-parameters, the mixed-mode data becomes very similar to traditional two-port amplifier data. Each quadrant now exhibits characteristics that can be interpreted as a two-port amplifier. Note that both the differential and common-mode performance is that of an inverting amp. Even the cross-mode parameters display amplifier-like behavior.

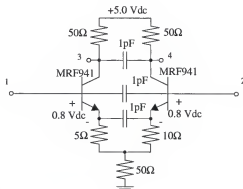


Figure D-1. Schematic of simulated RF differential amplifier.

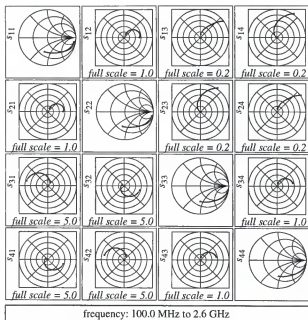


Figure D-2. Simulated four-port s-parameters of differential amp.

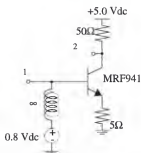


Figure D-3. Schematic of simulated single-ended amplifier.

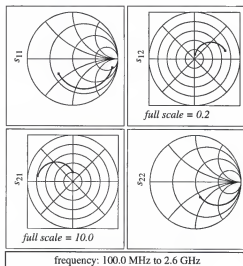


Figure D-4. Simulated two-port s-parameters of one-half of differential amp.

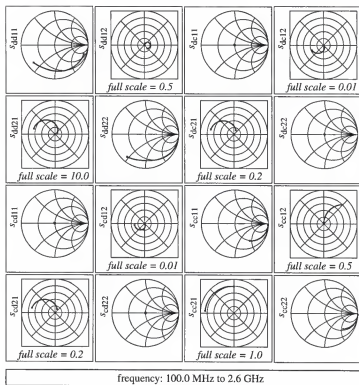


Figure D-5. Simulated mixed-mode s-parameters of differential amp.

APPENDIX E

DESCRIPTION OF HP8510 VNA SUB-SYSTEMS

This appendix summarizes the operation of a standard Hewlett-Packard 8510 VNA, and describes the sub-systems of the VNA. These sub-systems have been used to construct the PMVNA, so understanding their basic functions is important for understanding of the PMVNA operation. The basic configuration of the standard 8510 VNA is shown in Figure E-1. The 8510 has four major sub-systems, each corresponding to a sep-

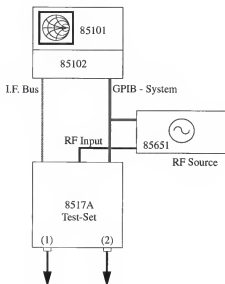


Figure E-1. Standard HP8510 two-port VNA system block diagram.

arate piece of test equipment. The four sub-systems are (1) the RF source (85651), (2) the test-set (8517), (3) the IF/detector (85102), and (4) the display/processor (85101). The basic function of these units is illustrated in a simplified view of a test signal path, shown in Figure E-2. Detail description of each sub-system is given below. The following information is adapted from the *HP8510C On-Site Service Manual* [43].

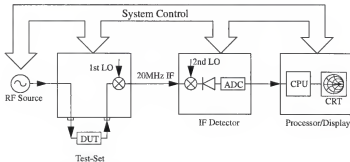


Figure E-2. Simplified test signal path of standard 8510 VNA. Adapted from [43].

E.1. RF Source

The RF source provides the RF stimulus for the s-parameter measurements made by the 8510 VNA system. The RF source is a broad-band, continuous-wave signal source. The processor controls the RF source, setting frequency start and stop points, as well as RF power levels.

The RF source used in the PMVNA is the 85651 synthesized sweeper. This particular source operates from 45 MHz to 50 GHz. Synthesized sweepers can operate in two modes: ramp and step sweeps. Both operations effect how the RF source is swept across

the desired operation frequency band. In ramp mode, the RF source is phase-locked only at the first frequency point of a measurement. After phase-locking, the frequency of the source is swept in a continuous fashion across the measurement frequencies. For averaging, the source is swept across the entire band a number of times equal to the averaging factor. The ramp mode has the advantage of being generally faster than the step mode (for small number of averages). The ramp mode has less frequency accuracy than the step mode, however.

The step mode of RF source operation allows phase-locking at each frequency point of the measurement. For averaging, multiple measurements are made at each frequency point. The source is swept across the frequency range only once. This mode of operation has higher frequency accuracy than the ramp mode. This mode also allows relatively high average factors with no significant increase in measurement time since the total sweep time is dominated by the phase-locking time.

E.2. Test-Set

Test-sets provide the signal separation functions for the VNA systems. In addition, the test-sets in the 8510 VNA system down-convert the separated signals to a first IF. Signal separation is the means by which the forward and reverse waves are measured at each test port. These separated signals are proportional to the normalized power waves, a and b .

The test-sets used in the PMVNA are the 8517A. A simplified block diagram of the 8517 is shown in Figure E-3. The input signal from the RF source provides the stimulus for the s -parameter measurements. The RF signal is routed first through a resistive divider/switch (SWA). This device provides signal separation for the incident normalized

power wave, a , through the resistive divider. It also provides a switch to allow forward and reverse measurement of the DUT. The two directional couplers provide signal separation for the transmitted and reflected normalized power waves, b . All of the normalized power waves are routed to four down-mixers. These down-mixers convert the a and b waves from RF to a first IF of 20 MHz. All four down-mixers are driven by the same VCO, which acts as the local oscillator (LO) signal. The VCO operating frequency is controlled by the 8510 processor via a phase-lock loop. This phase-lock loop ensures that the VCO is at the correct frequency as the RF source is swept through the measurement frequencies. The down-mixed signal maintain phase coherence, so that the relative phase relations between the normalized power waves at the first IF is the same as at RF.

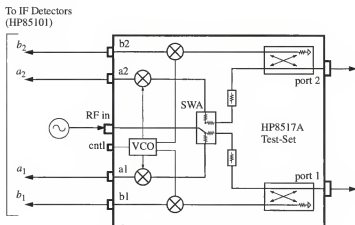


Figure E-3. Standard 8517 test-set block diagram.

E.3. IF/Detector

The 85102 IF/detector sub-system of the 8510 VNA performs many functions. First, it performs a down-conversion to a second IF frequency of 100 KHz. Next, it detects these signals with a synchronous detector so that the phase relations are preserved. The signals are then converted to digital information, so that the processor can operate on the data. This sub-system is also a part of the phase-lock loop. A simplified block diagram of the 85102 is shown in Figure E-4.

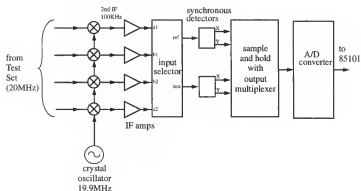


Figure E-4. Simplified HP85102 IF/Detector block diagram showing major sub-systems. (Adapted from [43]).

E.4. Display/Processor

The 85101 also performs several functions in the 8510 VNA system. It acts as the system controller, data processor and display unit. As a system controller, the 85101 controls the RF source (frequency and power output) during measurements. It also controls

the phase-locking sequence during measurement. Furthermore, the 85101 controls the test-set to select forward or reverse operation, and it controls the VCO operating frequency. The 85101 also controls the various operations of the 85102 IF/detector sub-system.

As a data processor the 85101 sub-system performs a number of operations of the measured data. Foremost, the unit provides means for calibration and data correction. A variety of math operations can be performed on measured data. The data then is displayed on the CRT. The 85101 can display uncorrected and corrected measured s-parameters. The processor unit also provides a GPIB interface, so that the 8510 operation can be computer controlled. Furthermore, the measured data from the 8510 system can be exported the external controller via the GPIB bus.

The 85101 can also provide unratiod measurements of the normalized power waves. These measurements are the (uncorrected) down-converted signals from the four mixers in the test-set. These digitized unratiod signals are the data on which the PMVNA operates.

E.5. System Phase Lock Operation

The 8510 system phase lock operation is a key element of the PMVNA performance. The phase lock sequence is now summarized to aid in the understanding of the PMVNA operation, particularly the phase-offset correction algorithm of Chapter 6. The pertinent aspects of the phase locking sequence can be better understood with the use of an overall block diagram of the 8510 VNA system, shown in Figure E-5. The components and signal/control paths that are part of the phase lock loop are highlighted with heavy lines. Every sub-system plays a role in the phase lock operation.

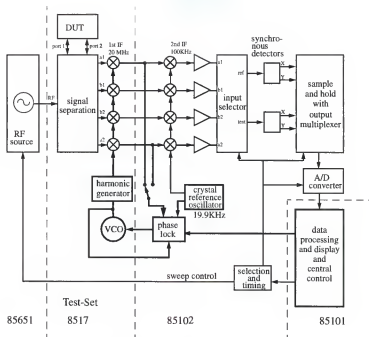


Figure E-5. Simplified HP8510C two-port VNA block diagram showing major subsystems. (Adapted from [41]).

For clarity, the phase lock loop components have been isolated in a simplified block diagram, shown in Figure E-6. The phase lock sequence has three main sections: (1) the pretune phase lock, (2) the pretune IF count, and (3) the main phase lock sequences. The pretune sequence is an open-loop coarse adjustment of the VCO operating frequency. The pretune IF count ensures that the coarse adjustment has brought the VCO frequency within locking range of the loop. The main phase lock is the closed-loop process by which the fine adjustment of the VCO operating frequency is achieved. When the

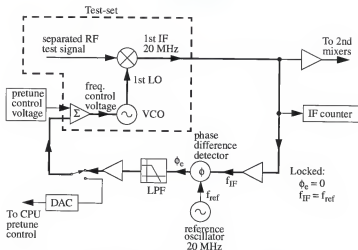


Figure E-6. Simplified HP8510C main phase lock loop. (Adapted from [43]).

main phase lock sequence is complete, the IF frequency is equal to the frequency of the 20 MHz crystal reference oscillator. Furthermore, under locked conditions, the phase difference between the IF signal and the reference oscillator has been driven to zero. This zero phase difference is very important to the phase offset calibration.

The phase lock loop characteristics, together with the synchronous detectors, allow for the phase offset calibration algorithm of Chapter 6 to be successful. Each time the 8510 system completes the entire phase lock sequence, the loop is locked to the same phase point on the separated RF test signal. For example, if the VNA is set to phase lock to a_1 , one can say that this separated signal has zero phase at the input to the down-mixer. With a locked loop, the phase of the down-converted a_1 signal might be ϕ_{if} . The loop forces this phase to be equal to that of the reference oscillator, ϕ_{ref} . It has been shown

experimentally, that this phase point of the of reference oscillator is constant. That is, the phase lock loop drives the phase of the down-converted a_1 signal to a certain absolute phase. This final absolute phase (which might be appropriately called the set-point phase) is constant for all phase locking sequences of a given test-set. Furthermore, the remaining down-conversion, synchronous detecting, and digitalization results in the same phase value in the unratiod data of a_1 (the actual value of the phase is irrelevant) for every locking sequence. Therefore, the two test-sets of the PMVNA will always indicate a constant phase difference between a_1 of test-set one and a_1 of test-set two, for example, regardless of the actual phase difference between the signals.

The constant set-point phase of each test-set ensures the phase offset between the two test-sets is repeatable. As a result, any offset between the RF sources of the two test-sets will result in an unknown, but repeatable phase offset in the digital data from the test-sets. Since the phase offset is repeatable, the offset can be characterized and corrected.

APPENDIX F

DETAILS OF HP8517 TEST-SET MODIFICATIONS

F.1. Disabling Test-Set Commands

As discussed in Chapter 4, the PMVNA test-set is constructed from two Hewlett-Packard 8517A test-sets. Both test-sets have been fitted with Option 001, a regular manufacturers' option, which allows selection between multiple test-sets. The option is an IF multiplexer board which works in coordination with features of the 8510 operating system. The operating system of the standard 8510 allows the selection of a test-set to be accomplished simply by changing the address of the active test-set (contained in a register in the 85101) to the address of the desired test-set. However, as developed by Hewlett-Packard, Option 001 allows the selection of one active test-set, and the deactivation of all other test-sets [91]. This deactivation includes the moving of the RF port selection switch to a terminated position, so that no RF signal is present at the ports of the deselected test-sets. Also upon deactivation, the variable attenuators in a test-set are re-set to 0 dB. The suppressing of the RF signal from the inactive test-sets and the change of attenuation setting are unwanted side effects. The PMVNA requires the use of the 8510 operating system routines to control the IF multiplexers, but the RF port selection switches and attenuator settings in both test-sets must remain unchanged. Both test-sets have been modified ensure that the RF port selector switch and attenuator settings remain unchanged as test-sets are deactivated.

The modification entails minor changes to the attenuator/switch driver boards of the test-sets. The modifications allow the masking of commands to change the position of the RF port selector switch or attenuators. The masking of system commands is achieved through a single digital control signal for each test-set. The digital control signals are generated by a Hewlett-Packard 3488A switch control unit [92]. The 3488A is fitted with a digital switch board (called option 014). This combination of the 3488/option 014 provides sixteen open-collector digital output lines whose states can be controlled via GPIB commands to the 3488A.

The schematics of the test-set attenuator/switch driver board are shown in a very simplified form in Figure F-1. This figure summarizes the means by which the attenuators

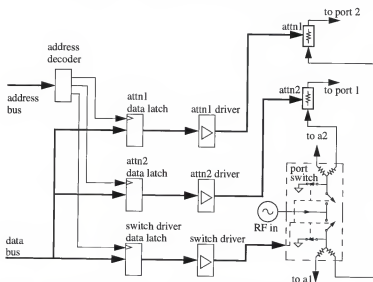


Figure F-1. Simplified schematic of 8517A test-set. Adapted from [93].

and port selection switch are changed. First, data is placed on the data bus by the 8510 operating system. This data contains the new settings for the switches and attenuators. When the appropriate address is placed on the address bus, the corresponding data latches are clocked, and the new data is forwarded to the drivers. Upon arriving at the drivers, the attenuators and switches are set according to the data on the data bus. When the active test-set address changes in the 8510 system, unwanted commands are sent to the de-activated test-sets. These commands follow the sequence just described.

The modifications to the test-set provide a means by which these unwanted commands can be blocked. This is done by preventing the latches from being clocked. By examining the detailed schematic of the address decoder, in Figure F-2, one can see that

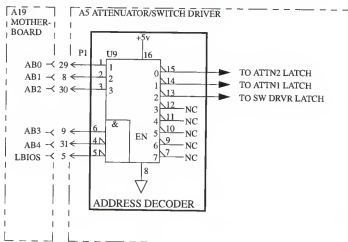


Figure F-2. Detailed schematic of 8517A test-set address decoder for attenuator drivers and RF switch driver. Adapted from [93].

the address decoder is implemented with a three-to-eight de-multiplexer (denoted as U9). This IC drives the clocks for both sets of attenuator drivers and the port selector switch. However, before U9 can clock the latches, it must be enabled. The IC has three enable lines (pins 4, 5, and 6) which must be satisfied (TTL low, low, high, respectively) before any latches can be clocked. By forcing the state of one of these enable signals, commands sent to the attenuator/switch driver board can either be blocked or accepted.

As explained earlier, the blocking (or masking) control signal is generated by a 3488A with a digital switch board installed. This piece of equipment provides several open collector switches that can be controlled via the GPIB. These open collector switches are typically used as active low logic signals, as illustrated in Figure F-3. When a switch is closed (active), the transistor, Q_1 , sinks enough current through the collector resistor to drive the collector voltage below the TTL logical low level. When the switch is opened, the resistor pulls the collector voltage to the TTL high level. Using the active low, open collector circuitry, the desired control function can be implemented.

The blocking of commands to the driver board is accomplished by modifying address bit four (AB4) signal at the address decoder of the driver board of each test-set.

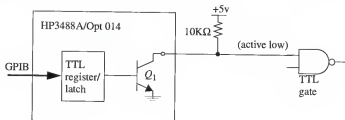


Figure F-3. Schematic of application of open collector output of 3488 with option 014.

The state of AB4 is forced to depend on the new masking signal, SW_EN. The truth table defining this dependence is shown in Figure F-4. Simply put, when the switch enable signal for a test-set is active (SW_EN = 1) then the new AB4 signal (called NAB4) is equal to the original AB4 signal; otherwise NAB4 is forced to be inactive, regardless of AB4. The new signal, NAB4, is routed to pin 4 of U9 (see Figure F-2), which is one of the decoder enable signals. When SW_EN is low, the address decoder never allows new data to the

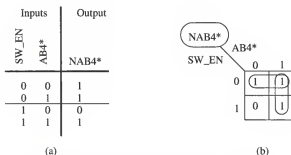


Figure F-4. Definition of digital behavior of control modifications.
 a) Truth table of desired control function. b) Karnaugh map of function described in (a). The * denotes active low signals.

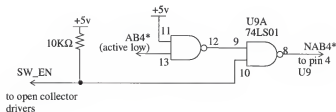


Figure F-5. Circuit implementation of desired control function of Figure F-4.

various drivers (thus blocking any such commands from the operating system). When SW_EN is high, the commands to the drivers are unaffected.

The logical implementation of the new control function is indicated in the Karnaugh map of Figure F-4(b). The physical implementation of this function is shown in Figure F-5. The function can be implemented with the addition of a single quad-NAND gate (74LS01) and a resistor. On the driver board, this IC has been piggy-backed on top of

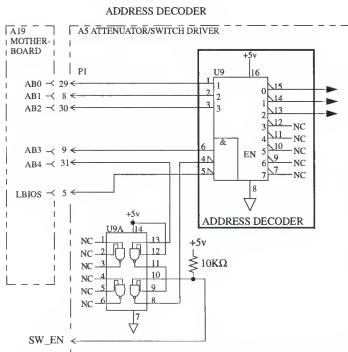


Figure F-6. Modification schematics of 8517A test-set, showing address decoder for attenuator drivers and RF switch driver.

the decoder IC. This allows for all electrical connections to be made with minimal changes to the driver board. Of course, the original connection of the AB4 line to pin four of U9 must be broken. The schematic of the modified address decoder is shown in Figure F-6.

This modification has been executed on both test-sets, and two masking signals (SW_EN1 for test-set one, and EN_SW2 for test-set two) have been provided via the 3488A/option 014 GPIB switch controller. The PMVNA software controls the states of these masking signals. When the state of the RF port selector switch or the attenuators is to be changed, the PMVNA software first sets the appropriate signal to high. Then the PMVNA software issues the appropriate standard 8510 commands. During a measurement when the PMVNA must switch from one test-set to the other, both SW_EN1 and SW_EN2 are set low, and the PMVNA issues the standard 8510 command to change the active test-set. In this case, the option 001 IF multiplexer boards switch the appropriate IF signals to the 85102 IF/detector sub-system, while the state of both test-sets remains constant.

F.2. DM/CM Switch Driver

The RF switch used to select between differential and common-mode has also been designed to be operated through PMVNA control software via the 3488A/option 014 digital switch. The RF switch used for this work is the Hewlett-Packard 8762C coaxial switch [94]. This switch is a single-pole, double-throw switch, with internal 50 Ω terminations that are connected to the inactive port. A simplified schematic for the switch is shown in Figure F-7.

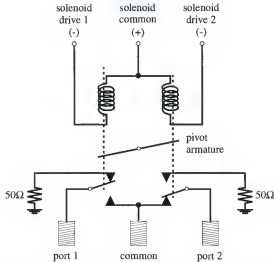


Figure F-7. Simplified schematic of HP8762 RF switch. Adapted from [94].

This switch requires a driver circuit for interfacing to standard TTL digital circuitry. The switch has two solenoids that operate change the RF connections. The switching is achieved by applying five volts DC to the common solenoid terminal, and grounding one of the two solenoid drive terminals. The solenoids require 400mA, which is much more than a typical TTL gate can sink. As a result, a switch driver circuit has been designed and built, as shown in Figure F-8. The driver circuit employs two 2N6038 NPN Darlington transistors, which provide sufficient current sinking capacity for the solenoids. The driver also uses a 74LS04 hex inverter to drive both solenoids from a single digital control signal. This digital signal is controlled by the PMVNA software via the 3488A/option 014. Also included in the switch driver circuitry are light-emitting diodes (LED) to indicate the state of the mode selector switch.

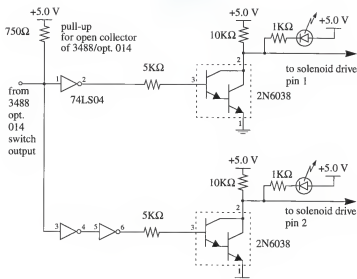


Figure F-8. Schematic of driver circuit for mode-selector switch.

APPENDIX G PMVNA CONTROL SOFTWARE

G.1. Top-Level Operation

The PMVNA control software is a custom coded operating system for the new analyzer. It has been developed in *LabVIEW*, which is a graphical programming language. The flow included in this appendix diagrams are meant as illustrations of the operation of the PMVNA software. Incorporation of the complete wiring diagrams, which are analogous to source code of more traditional programming languages, would make this appendix prohibitively long.

The top-level operation of the PMVNA control software is shown in Figure G-1. The construction of the software is such that the user can dictate the sequence of operation at a high level. Typically, the PMVNA begins from a power-up reset state, where a certain sequence must be followed by the user in order to achieve meaningful measurements. This power-up sequence is as follows: (1) initial set-up of the PMVNA, (2) phase offset pre-calibration, (3) primary calibration, (4) and DUT measurement. After this, the data can be plotted or saved to a file.

After an initial pass through the required sequence, the individual steps can be revisited if desired. The measured and calculated data from all main sections are stored in memory, and are available for re-calculations.

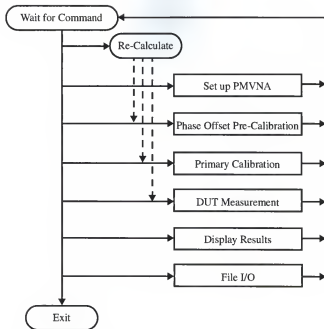


Figure G-1. Top-level flow chart of PMVNA control software.

G.1.1.1. PMVNA Initial Set-Up

This section of the software establishes the basic operating parameters of the PMVNA. This section is straight forward, so no flow chart is included. This section can be called by the user from the top level control at any time. This section sets the VNA hardware operating parameters, such as start frequency, stop frequency, and number of points in the frequency sweep. Also, the RF source power level, number of averages, sweep type, and attenuator settings are controlled here. Additionally, certain software

parameters are set in this section. GPIB addresses for all equipment used in the PMVNA is set (and kept as defaults) here.

G.1.2. Phase Offset Pre-Calibration

The phase offset pre-calibration portion of the control software is illustrated in Figure G-2. This flow chart represents both the measurement of the offset standards as

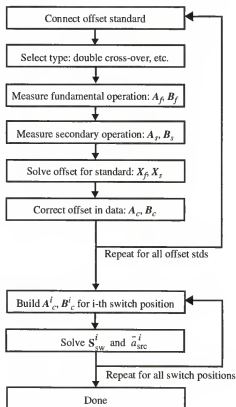


Figure G-2. Flow chart of the phase offset pre-calibration.

well as the solution method for phase offset calibration. This portion of the software implements the phase offset correction theory detailed in Section 6.4. In summary, the phase offset pre-calibration consists of the following steps: (1) multiple devices, called phase offset standards are measured under two different conditions (fundamental operation, detailed in Section G.2.7, and secondary operation, as detailed in Section G.2.8). (2) Using the two measurements, the phase offsets are found for each offset standard. (3) The raw a and b -data for each standard is phase corrected. (4) The corrected a and b -data for each PMVNA switch configuration (i. e. DF, DR, etc.) is collected from all offset standards. (5) Using the correct a and b -data from all standards, the switch impedance, S_{sw}^i , and the signal source vector, \bar{a}_{src}^i , are calculated for each of the switch configurations. With these correction terms, the phase offset of an arbitrary measurement can be calculated.

G.1.3. Primary Calibration

The flow chart of the portion of the PMVNA control software that implements the primary calibration algorithm is shown in Figure G-3. This section of the software control both the measurement and the calculation of the solution. The theory of the calibration algorithm implemented in this section is presented in detail in Section 6.2.

Each calibration standard is connected to the PMVNA, and all down-mixers are measured for each stimulus mode and direction. The raw A and B data matrices are constructed. The phase offset of each standard is calculated and corrected, and the raw measured s -parameters (S_{mx}) are calculated. The measured s -parameters and the corresponding theoretical s -parameters (S_{ax}) of all standards are used to generate the coefficient matrix, A_E , via equation (6-7). Finally, the calibration equation (6-8) is solved, and

the error matrix, T_{ES} , is found through SVD numerical techniques. SVD is a technique that finds a solution vector, t_S , that minimizes the product $A_E t_S$ in a least-squares sense. Since the solution to the calibration problem by this method is actually an estimate of the actual error network, T_E , the notation T_{ES} is adopted to make a clear distinction. The SVD solution algorithm was integrated into *LabVIEW* through a custom C-code routine.

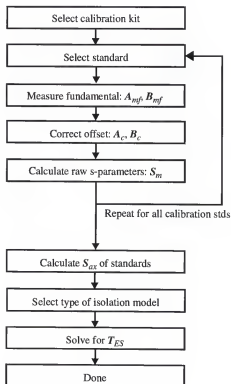


Figure G-3. Flow chart of primary calibration.

G.1.4. Measure DUT

The flow chart for the DUT measurement and correction portion of the PMVNA control software is shown in Figure G-4. Once the phase offset and primary calibrations are complete, an unknown DUT can be measured and the measured s-parameters can be corrected. The device is measured using raw a and b-data from all down-mixers. The phase offset is calculated and applied to the a and b-data. The final error correction is done according to (6-53) in Section 6.4.

G.1.5. Display Results

This portion of the software allows the user to display various data on demand. The user can view the raw or corrected s-parameters, of the DUT or any calibration standard. The s-parameters can be seen in mixed-mode or standard bases. The software also allows the user to plot the theoretical s-parameters of the calibration standards. This data

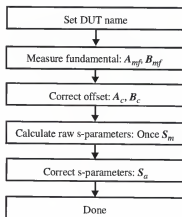


Figure G-4. Flow chart for DUT measurement and correction.

can be plotted in a variety of formats, including magnitude in dB, polar, and phase in degrees. This plotting software allows the user to interpret the various data in real-time, as it is measured. This capability is important in a practical measuring system.

G.1.6. File Input/Output

This section of the PMVNA software allows a variety of data to be written to computer files for long-term storage. The software can store the following data to file: raw a and b-data of the phase offset standards, the phase offset switch impedances and source vectors, the raw a and b-data of the primary calibration standards, the phase corrected raw s-parameters of the standards, the theoretical s-parameter of the calibration standards, the corrected measured s-parameters of the calibration standards, the primary calibration solution vector, the raw a and b-data of the DUT, the phase corrected raw s-parameters of the DUT, and the corrected measured s-parameters of the DUT.

All of this data is written in a standard file format called CITI format [38]. This format is used throughout Hewlett-Packard software and hardware. To be compatible with these products, most notably MDS, the PMVNA software reads and writes CITI data files.

G.2. Basic Sub-Routines

All of the top-level functions of the PMVNA software described in Section G.1 are composed of many sub-routines. Some of the most fundamental of these sub-routines are the equipment control routines. These important sub-routines are outlined in the sections that follow.

G.2.1. Set DM/CM Operation

The routine for the control of the stimulus mode of the PMVNA is shown in Figure G-5. The flow chart shows how the 3488A switch controller is used to open or close a digital switch (switch address 302, in this case) to set the desired state of an RF switch. This switch determines the phase of the power split, and hence the mode of the stimulus signal produced at the DUT ports.

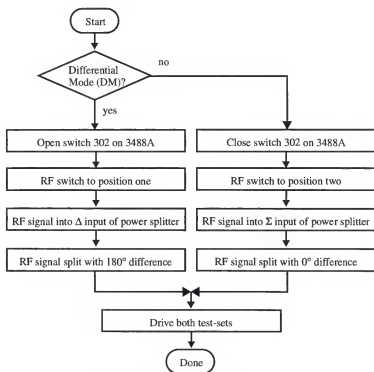


Figure G-5. Flow chart of setting of differential/common-mode operation.

G.2.2. Enable/Disable Test-Sets

The ability to disable certain low-level commands to the test-sets is a fundamental requirement for PMVNA functionality, as implemented for this work. As described in Chapter 4 and in Appendix F, the standard test-sets have been modified to block system commands to the port selector switches and attenuators. The blocking, also called disabling, is controlled by a digital signal. The software flow associated with the control of this signal is shown in Figure G-6. The flow chart shown is for test-set A, but a similar flow also describes the control of the enable signal of test-set B. In Figure G-6, the enabling signal is named SW_EN1, and its state is controlled by the PMVNA software via the 3488A GPIB switch controller.

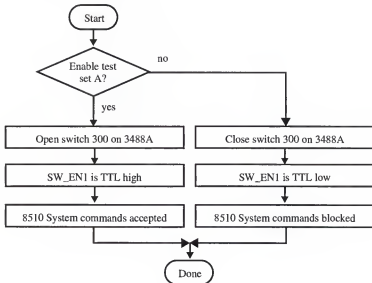


Figure G-6. Flow chart of enabling/disabling the operation of test-set A.

G.2.3. Activate Test-Sets

Another fundamental architectural feature of the PMVNA, as implemented in this work, is the use of the test-set multiplexing abilities of the standard 8510 VNA system. This ability allows the IF outputs of multiple test-sets to be multiplexed to a single 85102 detector unit. For use in the PMVNA, the test-sets must be modified (as described earlier) to avoid some unwanted side-effects of the standard IF multiplexing routines in the 8510 system.

With these modifications in place, the IF outputs of the test-sets are easily multiplexed by activating each test-set in turn. The flow of this portion of the PMVNA software is shown in Figure G-7.

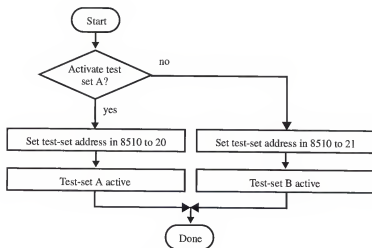


Figure G-7. Flow chart of activating test-sets.

G.2.4. General Measurement Operation

The general procedure a measurement is shown through Figure G-8 and Figure G-9. The first figure described the set-up procedure for the PMVNA test-sets, and

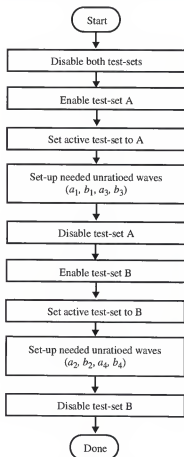


Figure G-8. Flow chart of the set-up procedure for the test-sets.

the second shows the actual measurement procedure. These procedures are followed for all measurement with the PMVNA (offset standards, primary calibration standards, and DUT).

The set-up of the test-sets for a given measurement is examined in detail in Figure G-8. This flow diagram shows how the modifications to the test-set control hardware are used in the measurement procedure. By asserting the enable test-set digital control line (as explained in Section 4.2.1) the system commands to the RF switch and the attenuators of the test-sets can be disabled. First, both test-sets are disabled to ensure the system is in a known state. Then test-set A is enabled, and it is then activated by loading

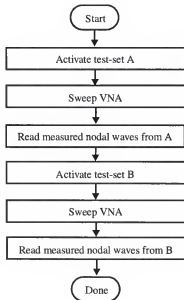


Figure G-9. Flow chart of measurement procedure.

the address of test-set A into the 85101. The appropriate unratiod wave measurements are set-up for each test-set (i.e. drive port one, phase-lock to port one, etc.). For more information on the details of the unratiod measurement set-up, see Section G.2.7 and Section G.2.8. The test-set is then disabled to keep the hardware state fixed. This procedure is repeated for test-set B, leaving the PMVNA ready to measure the prescribed parameters.

The basic flow of an *s*-parameter measurement is shown in Figure G-9. After the stimulus mode has been set, and the test-sets are set for the proper measurements, the PMVNA makes a measurement as shown in the flow chart. This flow is the same for all modes of measurement. In fundamental operation, for example, this procedure is repeated for DF, DR, CF, and CR measurements. A measurement is achieved by first activating test-set A by changing the active test-set address in the 8510. (Both test-set are disabled prior to entering this procedure, so that port selector switches and attenuator settings are not changed.) The PMVNA is triggered, and the measurements are made at the down-mixers in test-set A. This data is collected and stored by the PMVNA control software. Next, test-set B is activated by a change of address, and the PMVNA is swept again. The data from the down-mixers of test-set B is collected, completing the measurement.

G.2.5. Calculation of Mixed-Mode Normalized Power Waves

After all measurements of a device are made, the raw *a* and *b*-data must be used to calculate the mixed-mode *a* and *b*-data. This process is summarized in Figure G-10. This figure shows the calculation of the *a*-data only, but the same process is used for the *b*-data. In summary, the raw *a* and *b*-data is separated into the vectors corresponding to the measured data from each mode of stimulation (i. e. DF, DR, CF, CR). The vectors have a

dimension of four, where each element corresponds a physical test port. The four vectors (one from each stimulus mode) are joined as an A-matrix and a B-matrix. This data is corrected to account for the phase offset between the test-sets, via (6-52). These corrected matrices represent the measured unratioed normalized powers at all ports and under all measurement conditions in terms of single-ended (nodal) quantities. These quantities are used to calculate the corresponding mixed-mode quantities, as shown.

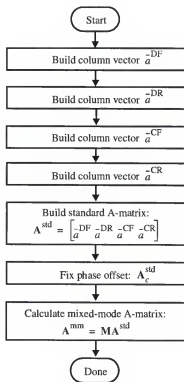


Figure G-10. Flow chart of mixed-mode normalized power wave calculation.

G.2.6. Calculate Raw S-Parameters

After all A and B-matrices are calculated, the raw measured s-parameters can be calculated. The PMVNA control software performs this calculations according to Figure G-11. This flow chart shows the straight-forward process by which raw (uncorrected) mixed-mode s-parameters are calculated from the phase corrected mixed-mode A and B-matrices.

The PMVNA also has the ability to optionally calculate the standard four-port s-parameters of a device. This process is shown in Figure G-12. For standard four-port s-parameter calculations, the single-ended (nodal) A and B-matrices are used.

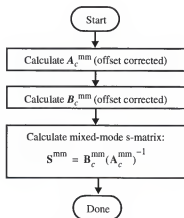


Figure G-11. Flow chart of raw mixed-mode s-parameter calculation.

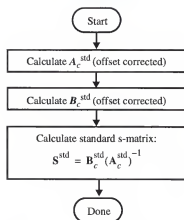


Figure G-12. Flow chart of optional raw standard four-port s-parameter calculation.

G.2.7. Measurements with Fundamental Operation

The specific flow of measurements with fundamental operation is shown in Figure G-13. This flow chart indicates the particular settings that are unique to fundamental operation of the PMNVA. The fundamental operation mode is the normal mode of operation of the PMVNA. This mode of operation drives ports one and two together, or ports three and four. With this operation, the primary calibration standards and the DUT measurements are made. The fundamental operation is divided into forward and reverse operation, so that the specific equipment setting of each can be described.

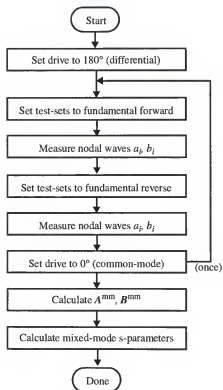


Figure G-13. Flow chart of PMVNA fundamental measurement operation.

G.2.7.1. Set Fundamental Forward Operation

The flows of the configuration of the test-sets of the PMVNA for fundamental forward measurements are shown in Figure G-14 and Figure G-15. The set-up of test-set A is detailed in Figure G-14. Each of the steps in this flow chart represent the equipment

configuration needed for the associated a or b-data. For example, with forward fundamental operation, the measured quantity of a_1 (the normalized incident wave at port one) is defined by "user parameter one" with certain settings. This user parameter allows the quantities to be measured to be defined at a basic level. Continuing the example, a_1 is

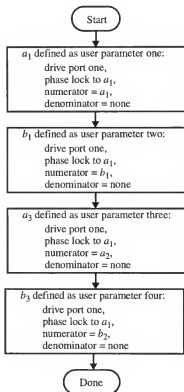


Figure G-14. Flow chart of the set-up of fundamental forward operation of test-set A.

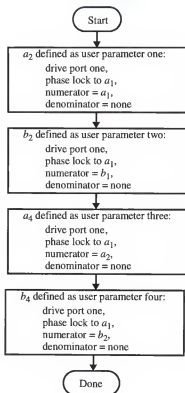


Figure G-15. Flow chart of the set-up of fundamental forward operation of test-set B.

defined by driving port one (i. e. set port selector switch to drive port one of the test-set), phase locking to a_1 (use the a_1 down-mixer in the phase-lock loop, see Figure E-5 in Appendix G), setting the numerator of the measured quantity to a_1 (the output of the down-mixer), and setting the denominator to none (an un-ratioed measurement).

For each test-set, four user parameters are defined. Each of these parameters corresponds to one of the four down-mixers in the test-set. The user parameters must be defined for both test sets. Figure G-14 describes the definitions for test-set A with forward fundamental operation, and Figure G-15 for test-set B.

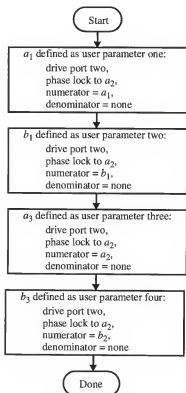


Figure G-16. Flow chart of the set-up of fundamental reverse operation of test-set A.

G.2.7.2. Set Fundamental Reverse Operation

The flows of the configuration of the test-sets of the PMVNA for fundamental reverse measurements are shown in Figure G-16 and Figure G-17. The fundamental reverse operation causes ports three and four to be driven simultaneously. The set-up of test-set A is detailed in Figure G-16, and test-set B in Figure G-17.

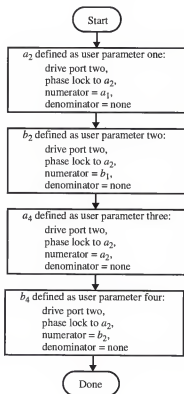


Figure G-17. Flow chart of the set-up of fundamental reverse operation of test-set B.

G.2.8. Measurements with Secondary Operation

The flow of measurements with secondary operation is shown in Figure G-18. Secondary operation mode is used in phase offset calibration measurements. This mode of operation drives ports one and four together, or ports two and three. Driving ports one and four together is called secondary forward, and driving ports two and three is called secondary reverse mode.

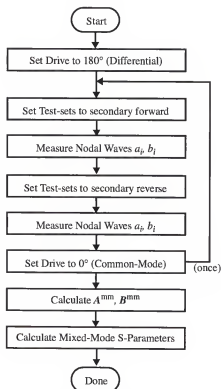


Figure G-18. Flow chart of PMVNA secondary measurement operation.

G.2.8.1. Set Secondary Forward Operation

The flows of the configuration of the test-sets of the PMVNA for secondary forward measurements are shown in Figure G-19 and Figure G-20. The secondary forward operation causes ports one and four to be driven simultaneously. The set-up of test-set A is detailed in Figure G-19, and test-set B in Figure G-20.

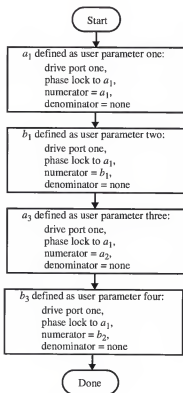


Figure G-19. Flow chart of the set-up of secondary forward operation of test-set one.

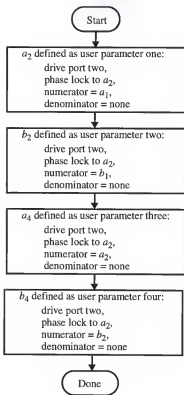


Figure G-20. Flow chart of the set-up of secondary forward operation of test-set two.

G.2.8.2 Set Secondary Reverse Operation

The flows of the configuration of the test-sets of the PMVNA for secondary reverse measurements are shown in Figure G-21 and Figure G-22. The secondary reverse operation causes ports one and four to be driven simultaneously. The set-up of test-set A is detailed in Figure G-21, and test-set B in Figure G-22.

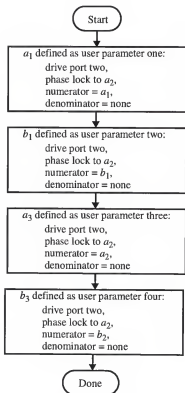


Figure G-21. Flow chart of the set-up of secondary reverse operation of test-set one.

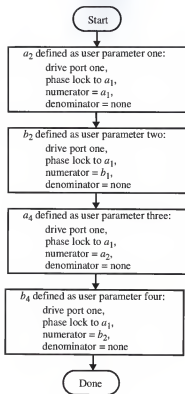


Figure G-22. Flow chart of the set-up of secondary reverse operation of test-set two.

APPENDIX H MULTI-PORT T-MATRIX DEFINITION

The development of the $2n$ -port t -matrix begins with the definition of the two-port case. The t -parameter definition [48] for the two-port case, in matrix form is

$$\begin{bmatrix} b_1 \\ a_1 \end{bmatrix} = \begin{bmatrix} t_{11} & t_{12} \\ t_{21} & t_{22} \end{bmatrix} \begin{bmatrix} a_2 \\ b_2 \end{bmatrix} \quad (\text{H-1})$$

Where a_i, b_i are the normalized input and output power waves at port i , respectively.

Some definitions swap the rows of the input and output waves, so the resulting definition is [23]

$$\begin{bmatrix} a_1 \\ b_1 \end{bmatrix} = \begin{bmatrix} t_{11} & t_{12} \\ t_{21} & t_{22} \end{bmatrix} \begin{bmatrix} b_2 \\ a_2 \end{bmatrix} \quad (\text{H-2})$$

Either definition is acceptable, as long as one is used consistently throughout a calculation. For this work the definition of (H-1) will be adopted.

To expand to more ports, a port numbering convention is set. The convention is illustrated in Figure H-1 with a $2n$ -port network. To define a T -matrix for a general network, it must have an even number of ports. This limitation is emphasized by the use of the $2n$ notation.

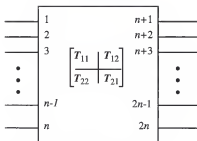


Figure H-1. Network definition for $2n$ -port T-matrix.

The definition of the $2n$ -port t-matrix is [48]

$$\begin{bmatrix} b_1 \\ \vdots \\ b_n \\ a_1 \\ \vdots \\ a_n \end{bmatrix} = \begin{bmatrix} t_{11} & \cdots & t_{1(2n)} \\ \vdots & \ddots & \vdots \\ t_{(2n)1} & \cdots & t_{(2n)(2n)} \end{bmatrix} \begin{bmatrix} a_{n+1} \\ \vdots \\ a_{2n} \\ b_{n+1} \\ \vdots \\ b_{2n} \end{bmatrix} \quad (\text{H-3})$$

The $2n$ -port t-matrix is analogous to the two-port. The b -waves from the left side of the network are grouped together, the a -waves from the left side, and so on. Following this analogy, the vector partitions can be defined

$$\bar{b}_1 = \begin{bmatrix} b_1 \\ \vdots \\ b_n \end{bmatrix} \quad \bar{a}_1 = \begin{bmatrix} a_1 \\ \vdots \\ a_n \end{bmatrix} \quad \bar{b}_2 = \begin{bmatrix} b_{n+1} \\ \vdots \\ b_{2n} \end{bmatrix} \quad \bar{a}_2 = \begin{bmatrix} a_{n+1} \\ \vdots \\ a_{2n} \end{bmatrix} \quad (\text{H-4})$$

so that the t-matrix definition of (H-3) becomes

$$\begin{bmatrix} \bar{b}_1 \\ \bar{a}_1 \end{bmatrix} = \begin{bmatrix} T_{11} & T_{12} \\ T_{21} & T_{22} \end{bmatrix} \begin{bmatrix} \bar{a}_2 \\ \bar{b}_2 \end{bmatrix} \quad (\text{H-5})$$

Where T_{ij} are the n -by- n partitions of the t -parameter matrix. In some cases, it is convenient to define the t -parameter "input" and "output" vectors as

$$\bar{v} = \begin{bmatrix} \bar{b}_1 \\ \bar{a}_1 \end{bmatrix} \quad \bar{u} = \begin{bmatrix} \bar{a}_2 \\ \bar{b}_2 \end{bmatrix} \quad (\text{H-6})$$

so that (H-5) becomes

$$\bar{v} = T\bar{u} \quad (\text{H-7})$$

Conversion between s -parameters and t -parameters is relatively simple for the two-port case, but becomes more difficult in the general $2n$ -port case. However, by using the partitions definitions in (H-4) and (H-5), the conversions can be made in a straightforward manner. First, the s -parameters for a $2n$ -port network are defined

$$\begin{bmatrix} b_1 \\ \dots \\ b_n \\ b_{n+1} \\ \dots \\ b_{2n} \end{bmatrix} = \begin{bmatrix} s_{11} & \dots & s_{1(2n)} \\ \dots & \dots & \dots \\ s_{(2n)1} & \dots & s_{(2n)(2n)} \end{bmatrix} \begin{bmatrix} a_{n+1} \\ \dots \\ a_{2n} \\ a_{n+1} \\ \dots \\ a_{2n} \end{bmatrix} \quad (\text{H-8})$$

This can be partitioned in a similar fashion

$$\begin{bmatrix} \bar{b}_1 \\ \bar{b}_2 \end{bmatrix} = \begin{bmatrix} S_{11} & S_{12} \\ S_{21} & S_{22} \end{bmatrix} \begin{bmatrix} \bar{a}_1 \\ \bar{a}_2 \end{bmatrix} \quad (\text{H-9})$$

Expanding the matrix equation (H-9) in terms of its partitions, one finds

$$\bar{b}_1 = S_{11}\bar{a}_1 + S_{12}\bar{a}_2 \quad (\text{H-10})$$

$$\bar{b}_2 = S_{21}\bar{a}_1 + S_{22}\bar{a}_2 \quad (\text{H-11})$$

Taking (H-11) and solving for a_1

$$\bar{a}_1 = S_{21}^{-1}\bar{b}_2 - S_{21}^{-1}S_{22}\bar{a}_2 \quad (\text{H-12})$$

Substituting this result into (H-10)

$$\bar{b}_1 = S_{11}S_{21}^{-1}\bar{b}_2 + (S_{12} - S_{11}S_{21}^{-1}S_{22})\bar{a}_2 \quad (\text{H-13})$$

Re-writing (H-12) and (H-13) as a single matrix equation

$$\begin{bmatrix} \bar{b}_1 \\ \bar{a}_1 \end{bmatrix} = \begin{bmatrix} S_{12} - S_{11}S_{21}^{-1}S_{22} & S_{11}S_{21}^{-1} \\ -S_{21}^{-1}S_{22} & S_{21}^{-1} \end{bmatrix} \begin{bmatrix} \bar{a}_2 \\ \bar{b}_2 \end{bmatrix} \quad (\text{H-14})$$

Therefore, the t-parameters of a $2n$ -port network can be found from the n -by- n partitions of the network s-parameters by

$$T = \begin{bmatrix} S_{12} - S_{11}S_{21}^{-1}S_{22} & S_{11}S_{21}^{-1} \\ -S_{21}^{-1}S_{22} & S_{21}^{-1} \end{bmatrix} \quad (\text{H-15})$$

Similarly, it can be shown that the s-parameters can be found from the t-parameters by

$$S = \begin{bmatrix} T_{12}T_{22}^{-1} & T_{11} - T_{12}T_{22}^{-1}T_{21} \\ T_{22}^{-1} & -T_{22}^{-1}T_{21} \end{bmatrix} \quad (\text{H-16})$$

APPENDIX I ERROR TERMS OF PMVNA AND FOUR-PORT VNA

I.1. General Relations

The relationship between the error boxes of a two-port PMVNA and a four-port VNA can be found by considering the relationship between standard and mixed-mode s -parameters. The transformation between mixed-mode s -parameters and standard s -parameters, as developed in Section 3.1.3, is

$$S^{\text{mm}} = MS^{\text{std}}M^{-1} \quad (\text{I-1})$$

where the superscripts indicate mixed-mode or standard quantities, and where

$$M = \frac{1}{\sqrt{2}} \begin{bmatrix} 1 & -1 & 0 & 0 \\ 0 & 0 & 1 & -1 \\ 1 & 1 & 0 & 0 \\ 0 & 0 & 1 & 1 \end{bmatrix} \quad (\text{I-2})$$

By combining equations (I-2) and (I-1), it can be shown

$$\begin{bmatrix} T_{11}^{\text{mm}} & T_{12}^{\text{mm}} \\ T_{21}^{\text{mm}} & T_{22}^{\text{mm}} \end{bmatrix} = \begin{bmatrix} M & \theta \\ \theta & M \end{bmatrix} \begin{bmatrix} T_{11}^{\text{std}} & T_{12}^{\text{std}} \\ T_{21}^{\text{std}} & T_{22}^{\text{std}} \end{bmatrix} \begin{bmatrix} M & \theta \\ \theta & M \end{bmatrix}^{-1} \quad (\text{I-3})$$

or, more compactly,

$$T^{\text{mm}} = (I_2 \otimes M)T^{\text{std}}(I_2 \otimes M)^{-1} \quad (\text{I-4})$$

where I_2 represents a two-by-two identity matrix, the \otimes operator is the Kroneker tensor product [65], and T^{mm} and T^{std} are the mixed-mode and standard error network representations, respectively.

The relationship between the two-port PMVNA error model and a standard four-port VNA error model is that the two error models are different representations of the same error network. The PMVNA uses a mixed-mode representation of the error network, and a standard VNA uses a standard representation of the same network. The two representation of the error network are related by a similarity transformation (I-4). Since the models are equivalent, and the mathematical treatment of the PMVNA and a four-port VNA is identical. Therefore the calibration equation (6-7) can be applied directly to a PMVNA, as well as a standard VNA, without any loss of generality.

I.2. Half-Leakage Error Model

This error network simplification is shown in Figure 6-8. Under this simplification, observation indicated that the four partitions of T^{std} are

$$T^{\text{std}}|_{\text{half-leakage}} = \begin{bmatrix} t_{11} & t_{12} & 0 & 0 & t_{15} & t_{11} & 0 & 0 \\ t_{21} & t_{22} & 0 & 0 & t_{11} & t_{26} & 0 & 0 \\ 0 & 0 & t_{33} & t_{34} & 0 & 0 & t_{37} & t_{38} \\ 0 & 0 & t_{43} & t_{44} & 0 & 0 & t_{47} & t_{48} \\ t_{51} & t_{52} & 0 & 0 & t_{55} & t_{56} & 0 & 0 \\ t_{61} & t_{62} & 0 & 0 & t_{65} & t_{66} & 0 & 0 \\ 0 & 0 & t_{73} & t_{74} & 0 & 0 & t_{77} & t_{78} \\ 0 & 0 & t_{83} & t_{84} & 0 & 0 & t_{87} & t_{88} \end{bmatrix} \quad (\text{I-5})$$

Applying (I-5) to (I-4), one finds T^{mm} has a different zero-pattern

$$T^{mm}|_{\text{half-leakage}} = \begin{bmatrix} t_{11}^{mm} & 0 & t_{13}^{mm} & 0 & t_{15}^{mm} & 0 & t_{17}^{mm} & 0 \\ 0 & t_{22}^{mm} & 0 & t_{24}^{mm} & 0 & t_{26}^{mm} & 0 & t_{28}^{mm} \\ t_{31}^{mm} & 0 & t_{33}^{mm} & 0 & t_{35}^{mm} & 0 & t_{36}^{mm} & 0 \\ 0 & t_{42}^{mm} & 0 & t_{44}^{mm} & 0 & t_{46}^{mm} & 0 & t_{48}^{mm} \\ t_{51}^{mm} & 0 & t_{53}^{mm} & 0 & t_{55}^{mm} & 0 & t_{57}^{mm} & 0 \\ 0 & t_{62}^{mm} & 0 & t_{64}^{mm} & 0 & t_{66}^{mm} & 0 & t_{68}^{mm} \\ t_{71}^{mm} & 0 & t_{73}^{mm} & 0 & t_{75}^{mm} & 0 & t_{77}^{mm} & 0 \\ 0 & t_{82}^{mm} & 0 & t_{84}^{mm} & 0 & t_{86}^{mm} & 0 & t_{88}^{mm} \end{bmatrix} \quad (1-6)$$

1.3. No-Leakage Error Model

This error network simplification is shown in Figure 6-10. Under this simplification, observation indicated that the four partitions of T^{std} are diagonal matrices.

$$T^{\text{std}}|_{\text{no-leakage}} = \begin{bmatrix} t_{11} & 0 & 0 & 0 & t_{15} & 0 & 0 & 0 \\ 0 & t_{22} & 0 & 0 & 0 & t_{26} & 0 & 0 \\ 0 & 0 & t_{33} & 0 & 0 & 0 & t_{37} & 0 \\ 0 & 0 & 0 & t_{44} & 0 & 0 & 0 & t_{48} \\ t_{51} & 0 & 0 & 0 & t_{55} & 0 & 0 & 0 \\ 0 & t_{62} & 0 & 0 & 0 & t_{66} & 0 & 0 \\ 0 & 0 & t_{73} & 0 & 0 & 0 & t_{77} & 0 \\ 0 & 0 & 0 & t_{84} & 0 & 0 & 0 & t_{88} \end{bmatrix} \quad (1-7)$$

Applying (1-7) to (1-4), one finds T^{mm} also has diagonal partitions. Furthermore, it can be easily shown that

$$T^{mm}|_{\text{no-leakage}} = T^{\text{std}}|_{\text{no-leakage}} \quad (1-8)$$

APPENDIX J

DEMONSTRATION OF COEFFICIENT MATRIX RANK

This appendix details the method by which the rank of the calibration coefficient matrix, A_E , is found under various conditions. Knowledge of the rank of A_E is critical for a meaningful solution to the calibration problem for the PMVNA. For a meaningful solution, A_E must have sufficient rank. By examining the rank of A_E from a theoretical standpoint, much can be learned about the calibration problem.

The rank of A_E depends on many factors. It is obviously effected by the number of ports on the VNA, as well as the number of standards used in calibration. The rank is also strongly effected by the types of standards used. Further, the rank is effected by the isolation model applied.

The rank of any matrix is a simple concept. The rank is equal to the dimension of the largest square sub-matrix with a non-zero determinant. In other words, the rank of a matrix is the dimension of it largest non-zero minor. Despite the simplicity of the concept, the rank of A_E is difficult to determine in practice, particularly as the number of VNA ports increases. As a result, the rank of A_E is examined through numerical methods. These methods assign values to required data, so that A_E becomes a purely numerical matrix. With this matrix, well established numerical methods can be applied to find the rank, even when A_E is quite large.

With this numerical approach, the number and nature of standards required for a successful calibration can be established. For example, one can determine the minimum

number of standards required for a four-port VNA with a no-leakage error model. Alternatively, one can establish whether a particular set of physical standards (such as shorts, opens, loads, and a pair of throughs) is sufficient for a calibration. This appendix first presents the numerical procedures by which the rank of A_E can be found for a particular circumstance, and then the results will be summarized in table form.

J.1. Numerical Calculation of Rank

The calculations of rank have been implemented in a *Mathematica* program. *Mathematica* allows both symbolic manipulation and numerical calculations required for this procedure. The method used for the calculation of rank of A_E is best illustrated as a list of steps. The steps are as follows:

1. Set the number of ports on the VNA, n , the number of calibration standards to be used, m , type of standards to be used, and isolation model type (e. g. full-leakage).
2. For the given n and m , symbolically expand the calibration equation (6-7).
3. For the given n and m , symbolically build the coefficient matrix A_E from results in step two.
4. For the given isolation model, remove the columns of A_E corresponding to the zero elements in the error box.
5. For the given n , set the numerical values of the error box. This is typically done by assigning random complex numbers to each of the elements in the error box. Some elements are zero-valued according to the chosen isolation model.
6. For the given n and m and type of standards chosen, set the numerical value of the actual s-parameters of the standards S_{axi} . This can be done in accordance with particular physical standards, or random s-parameters can be assigned.

7. Using the data from steps five and six, calculate the measured s-parameters of the standards, S_{mi} . This requires re-arranging (6-7) to solve for the measured s-parameters, thus producing an embedding equation.
8. Load the numerical values of S_{axi} , S_{mi} and the error box into the appropriate variables in the symbolic A_E from step four.
9. Remove any all zero rows from the resulting A_E . These rows are caused by certain types of standards in combination with certain isolation models. For example, using a reflection standard with a four-port no-leakage model gives sixteen rows. However, only four of these rows have any non-zero entries.
10. Perform SVD on A_E from step nine.
11. The number of non-zero singular values equal the rank of A_E .

1.2. Results of Rank Calculations

The procedure outlined in the previous section has been executed for many combinations of port numbers, standards, types of standards, and isolation models. The goal of these calculations is to establish general relations for the rank of A_E for an n -port VNA. These relationships provide important insight into the requirements for a successful calibration. The calculation of rank of A_E has been done for the four types of error models outlined in Chapter 6: full-leakage (the most general), half-leakage, pair-leakage and no-leakage models. Each of these models is examined for two types of calibration standards: full and reflection. For purposes of these calculations, a full standard is an n -port standard where all s-parameters are randomly assigned. However, these full standards have been restricted to reciprocal s-parameters, so that $S = S^T$, since practical standards will be recip-

rocal. A reflection standard is an n -port standard where only the diagonal elements of the s -parameter matrix is randomly assigned. All other s -parameters of the reflection standard are zero. In all cases, the number of ports is varied, so that a pattern can be established, and with this pattern, n -port conclusions can be drawn.

The results of the rank calculations for full-leakage model with full standards are summarized in Table J-1. The results with reflection standards are summarized in Table J-2. With this error model, the type of standard makes no difference in the dimensions of A_E . However, reflection standards alone can never produce an ordinary solution. The differences in rank resulting from the two types of standards are highlighted with heavy borders.

Table J-1. Calibration equation simulations, full-leakage correction, with full standards.

Ports n	Standards m	Unknowns $(2n)^2$	Arbitrary Variables	Dimensions A_E	Rank(A_E)
1	1	3	3	1 x 4	1
1	2	3	2	2 x 4	2
1	3	3	1	3 x 4	3
1	4	3	1	4 x 4	3
1	5	3	1	5 x 4	3
1	6	3	1	6 x 4	3
2	1	16	12	4 x 16	4
2	2	16	8	8 x 16	8
2	3	16	4	12 x 16	12
2	4	16	2	16 x 16	14
2	5	16	1	20 x 16	15
2	6	16	1	24 x 16	15
3	1	36	27	9 x 36	9

Table J-1. (Continued) Calibration equation simulations, full-leakage correction, with full standards.

Ports n	Standards m	Unknowns $(2n)^2$	Arbitrary Variables	Dimensions A_E	Rank(A_E)
3	2	36	18	18 x 36	18
3	3	36	9	27 x 36	27
3	4	36	3	36 x 36	33
3	5	36	1	45 x 36	35
3	6	36	1	54 x 36	35
4	1	64	48	16 x 64	16
4	2	64	32	32 x 64	32
4	3	64	16	48 x 64	48
4	4	64	4	64 x 64	60
4	5	64	1	80 x 64	63
4	6	64	1	96 x 64	63
5	1	100	75	25 x 100	25
5	2	100	50	50 x 100	50
5	3	100	25	75 x 100	75
5	4	100	5	100 x 100	95
5	5	100	1	125 x 100	99
5	6	100	1	150 x 100	99
n	m	$4n^2$	depends	$(m.n^2) \times 4n^2$	depends

Table J-2. Calibration equation simulations, full-leakage correction, with reflection standards.

Ports n	Standards m	Unknowns $(2n)^2$	Arbitrary Variables	Dimensions A_E	Rank(A_E)
1	1	3	3	1 x 4	1
1	2	3	2	2 x 4	2
1	3	3	1	3 x 4	3
1	4	3	1	4 x 4	3
1	5	3	1	5 x 4	3
1	6	3	1	6 x 4	3
2	1	16	12	4 x 16	4
2	2	16	8	8 x 16	8
2	3	16	4	12 x 16	12
2	4	16	2	16 x 16	14
2	5	16	2	20 x 16	14
2	6	16	2	24 x 16	14
3	1	36	27	9 x 36	9
3	2	36	18	18 x 36	18
3	3	36	9	27 x 36	27
3	4	36	3	36 x 36	33
3	5	36	3	45 x 36	33
3	6	36	3	54 x 36	33
4	1	64	48	16 x 64	16
4	2	64	32	32 x 64	32
4	3	64	16	48 x 64	48
4	4	64	4	64 x 64	60
4	5	64	4	80 x 64	60
4	6	64	4	96 x 64	60
5	1	100	75	25 x 100	25
5	2	100	50	50 x 100	50

Table J-2. Calibration equation simulations, full-leakage correction, with reflection standards.

Ports n	Standards m	Unknowns $(2n)^2$	Arbitrary Variables	Dimensions A_E	Rank(A_E)
5	3	100	25	75 x 100	75
5	4	100	5	100 x 100	95
5	5	100	5	125 x 100	95
5	6	100	5	150 x 100	95
n	m	$4n^2$	depends	$(m \cdot n^2) \times 4n^2$	depends

From these two tables, it can be concluded that at least five n -port full standards will generate sufficient rank for an ordinary solution (for $n > 1$)¹. The "Arbitrary Variables" column clearly indicates when an ordinary solution is possible. Such a solution is only possible when there is only one arbitrary variable in the system of calibration equations.

Another important consideration of a calibration problem is the number and type of standards required to make A_E square. For the full-leakage model, this matrix is square when $4n^2 = m_F \cdot n^2$, where m_F is the number of full standards. Clearly, A_E is square with four standards. The rank associated with four standards is a maximum of $4n^2 - n$. Note that A_E is also square with four reflection standards, and the rank will also be a maximum of $4n^2 - n$. Also from Table J-1, it can be seen that at least five standards are required for an ordinary solution (where the rank of A_E is one less than the number of its columns). It is easily demonstrated that at least one of these standards must be a full standard with the appropriate number of non-zero transmission paths. This type of required full standard has been termed a complete standard.

1. For $n = 1$, the minimum number of standards is always three. All leakage models reduce to the same error model, and all standards reduce to on-port reflections.

The results for the half-leakage model are summarized in and Table J-3. For simplicity, only the results with full standards are shown. The results with reflection standards are similar to that of the full-leakage model in that reflection standards alone can never produce an ordinary solution. Only even port numbers are shown since this leakage model is only defined with an even number of ports.

Table J-3. Calibration equation simulations, half-leakage correction with full standards.

Ports n	Standards m	Unknowns $(2n)^2/2$	Arbitrary Variables	Dimensions A_E	Rank(A_E)
2	1	8	4	4 x 8	4
2	2	8	2	8 x 8	6
2	3	8	1	12 x 8	7
2	4	8	1	16 x 8	7
2	5	8	1	20 x 8	7
2	6	8	1	24 x 8	7
4	1	32	16	16 x 32	16
4	2	32	4	32 x 32	28
4	3	32	1	48 x 32	31
4	4	32	1	64 x 32	31
4	5	32	1	80 x 32	31
4	6	32	1	96 x 32	31
6	1	72	36	36 x 72	36
6	2	72		72 x 72	
6	3	72	1	108 x 72	71
6	4	72	1	144 x 72	71
6	5	72	1	180 x 72	71
6	6	72	1	216 x 72	71
n (even)	m	$2n^2$	depends	$(m.n^2) \times 2n^2$	depends

From this table, it can be concluded that at least three n -port full standards will generate sufficient rank for an ordinary solution (for $n > 1$) with the half-leakage error model. It is easily demonstrated that at least one of these standards must be a complete standard. For the half-leakage model, A_E is square when $2n^2 = m_F \cdot n^2 + m_R \cdot \left(\frac{n^2}{2}\right)$, where m_F is the number of full standards, and m_R is the number of reflection standards. Clearly, A_E is square when $4 = 2m_F + m_R$. The minimum number of standards that generates a square matrix is two, with $m_F = 2$ and $m_R = 0$. The rank associated with this set of standards is a maximum of $2n^2 - n$.

The results for the pair-leakage model are summarized in and Table J-4. Again, only the results with full standards are shown. The results with reflection standards are also similar to that of the full-leakage model in that reflection standards alone can never produce an ordinary solution. Only even port numbers are shown since this leakage model is only defined with an even number of ports.

Table J-4. Calibration equation simulations, pair-leakage correction with full standards.

Ports n	Standards m	Unknowns $8n$	Arbitrary Variables	Dimensions A_E	Rank(A_E)
2	1	16	4	4 x 16	4
2	2	16	2	8 x 16	8
2	3	16	1	12 x 16	12
2	4	16	1	16 x 16	14
2	5	16	1	20 x 16	15
2	6	16	1	24 x 16	15
4	1	32	16	16 x 32	16
4	2	32	4	32 x 32	28
4	3	32	1	48 x 32	31

Table J-4. (Continued) Calibration equation simulations, pair-leakage correction with full standards.

Ports n	Standards m	Unknowns $8n$	Arbitrary Variables	Dimensions A_E	Rank(A_E)
4	4	32	1	64 x 32	31
4	5	32	1	80 x 32	31
4	6	32	1	96 x 32	31
6	1	72		36 x 72	
6	2	72		72 x 72	
6	3	72		108 x 72	
6	4	72		144 x 72	
6	5	72		180 x 72	
6	6	72		216 x 72	
n (even)	m	$8n$	depends	$(m \cdot n^2) \times 8n$	depends

With the pair-leakage error model, it can be concluded that the required number of full n -port standards for an ordinary solution depends on the number of ports on the VNA. With two ports, at least five standards are required. With four ports, at least three standards are required. Again, it can be easily demonstrated that, for an ordinary solution, at least one of the applied standards must be a complete standard. Note that, by comparison with Table J-3, it can be seen that when $n = 4$, the half-leakage and pair-leakage models coincide.

For the pair-leakage model, A_E is square when $8n = m_F \cdot n^2 + m_R \cdot 2n$, where m_F is the number of full standards, and m_R is the number of reflection standards. Clearly, A_E is square when $8 = m_F \cdot n + 2m_R$. When $n = 4$, the minimum number of standards that generates a square matrix is also two, with $m_F = 2$ and $m_R = 0$. The rank associated with this set of standards is a maximum of 28.

The results for the no-leakage model are summarized in Table J-5. Again, only the results with full standards are shown. The results with reflection standards are also similar to that of the full-leakage model in that reflection standards alone can never produce an ordinary solution.

Table J-5. Calibration equation simulations, no-leakage correction with full standards.

Ports n	Standards m	Unknowns $4n$	Arbitrary Variables	Dimensions A_E	Rank(A_E)
1	1	3	3	1 x 4	1
1	2	3	2	2 x 4	2
1	3	3	1	3 x 4	3
1	4	3	1	4 x 4	3
2	1	8	4	4 x 8	4
2	2	8	2	8 x 8	6
2	3	8	1	12 x 8	7
2	4	8	1	16 x 8	7
3	1	12	4	9 x 12	8
3	2	12	1	18 x 12	11
3	3	12	1	27 x 12	11
3	4	12	1	36 x 12	11
4	1	16	4	16 x 16	12
4	2	16	1	32 x 16	15
4	3	16	1	48 x 16	15
4	4	16	1	64 x 16	15
5	1	20	1	25 x 20	19
5	2	20	1	50 x 20	19
5	3	20	1	75 x 20	19
5	4	20	1	100 x 20	19
n (even)	m	$4n$	depends	$(m \cdot n^2) \times 4n$	depends

Again with the no-leakage error model, the required number of full n -port standards for an ordinary solution depends on the number of ports on the VNA. With two ports, at least three standards are required. With four ports, at least two standards are required. With five ports, only one full five-port standard is required. Again, it can be easily demonstrated that, for an ordinary solution, at least one of the applied standards must be a complete standard.

For the pair-leakage model, A_E is square when $4n = m_F \cdot n^2 + m_R \cdot n$, where m_F is the number of full standards, and m_R is the number of reflection standards. Therefore, A_E is square when $4 = m_F \cdot n + m_R$. When $n = 4$, the minimum number of standards that generates a square matrix is one, with $m_F = 2$ and $m_R = 0$. The rank associated with this set of standards is a maximum of 12.

Table J-6. Number of equation generated by a single n -port standard.

Error Model Type	Number of Unknowns	Type of standard	
		Full	Reflect
Full-leakage	$4n^2$	n^2	n^2
Half-leakage (n even)	$2n^2$	n^2	$n^2/2$
Pair-leakage (n even)	$8n$	n^2	$2n$
No-leakage	$4n$	n^2	n

These finding on the rank of A_E have been summarized in Table J-6 and Table J-7. Table J-6 indicates the number of unknowns for each type of leakage model as a function of the number of port, n . Also shown are the number of equation provided by a single n -port standard, for both full and reflection standards. Table J-7 further shows the dimensions of A_E as a function of the number of ports, n , the number of full standards, m_F , and

the number of reflection standards, m_R . It also shows the minimum number of standards possible for an ordinary solution.

Table J-7. Calibration summary.

Error Model Type	Number of Unknowns	Dimensions A_E	Min. Stds for Ordinary Solution	Min. Stds for Ordinary Solution ($n=4$)
Full-leakage	$4n^2$	$n^2(m_F + m_R) \times 4n^2$	5	5
Half-leakage (n even)	$2n^2$	$(m_F n^2 + m_R n^2/2) \times 2n^2$	3	3
Pair-leakage (n even)	$8n$	$(m_F n^2 + 2m_R n) \times 8n$	depends on n	3
No-leakage	$4n$	$(m_F n^2 + m_R n) \times 4n$	depends on n	2

LIST OF REFERENCES

- [1] J. R. Carson and R. S. Hoyt, "Propagation of periodic waves over a system of parallel wires," *Bell Sys. Tech. Journal*, vol. 4, pp. 495-5454, July 1927.
- [2] B. M. Oliver, "Directional electromagnetic couplers," *Proc. IRE*, vol. 42, pp. 1686-1692, Nov. 1954.
- [3] S. B. Cohn and R. Levy, "History of microwave passive components with particular attention to directional couplers," *IEEE Trans. Microwave Theory Tech.*, vol. MTT-32, pp. 1046-1054, July 1984.
- [4] P. R. Gray and R. G. Meyer, *Analysis and Design of Analog Integrated Circuits*, 3rd. ed., Wiley, New York, 1993.
- [5] H. W. Ott, *Noise Reduction Techniques in Electronic Systems*, 2nd. ed., p. 61, John Wiley & Sons, New York, 1988.
- [6] S. B. Cohn, "Shielded coupled-strip transmission lines," *IRE Trans. Microwave Theory Tech.*, vol. MTT-3, pp. 29-38, Oct. 1955.
- [7] D. Park, "Planar Transmission Lines," *IRE Trans. Microwave Theory Tech.*, vol. MTT-3, pp. 8-12, April 1955
- [8] V. K. Tripathi, "Asymmetric coupled transmission lines in an inhomogeneous medium," *IEEE Trans. Microwave Theory Tech.*, vol. MTT-23, pp. 734-739, Sept. 1975.
- [9] K. D. Marx, "Propagation modes, equivalent circuits, and characteristic terminations for multiconductor transmission lines with inhomogeneous dielectrics," *IEEE Trans. Microwave Theory Tech.*, vol. MTT-21, pp. 450-457, Nov. 1973.
- [10] H. Amemiya, "Time-domain analysis of multiple parallel transmission lines," *RCA Rev.*, vol. 28, pp. 241-276, June 1967.

- [11] R. A. Speciale and V. K. Tripathi, "Wave-modes and parameter matrices of non-symmetrical coupled lines in a non-homogeneous medium," *Int. J. Electronics*, vol. 40, pp. 371-375, Apr. 1976.
- [12] G. I. Zysman and A. K. Johnson, "Coupled transmission line networks in an inhomogeneous dielectric medium," *IEEE Trans. Microwave Theory Tech.*, vol. MTT-17, pp. 753-759, Oct. 1969.
- [13] E. G. Vlostovskiy, "Theory of coupled transmission lines," *Telecommun. Radio Eng.*, vol. 21, pp. 87-93, Apr. 1967.
- [14] S. B. Cohn, "Characteristic impedances of broadside-coupled strip transmission lines," *IRE Trans. Microwave Theory Tech.*, vol. MTT-10, pp. 633-637, Nov. 1960.
- [15] R. A. Speciale, "Fundamental even- and odd-mode waves for nonsymmetrical coupled lines in non-homogeneous media," in *1974 IEEE MTT Int. Microwave Symp. Digest Tech. Papers*, June 1974, pp. 156-158.
- [16] C. Tsai and K. C. Gupta, "A generalized model for coupled lines and its applications to two-layer planar circuits," *IEEE Trans. Microwave Theory Tech.*, vol. MTT-40, pp. 2190-2199, Dec. 1992.
- [17] C. B. Sharpe, "An equivalence principle for nonuniform transmission line directional couplers," *IEEE Trans. Microwave Theory Tech.*, vol. MTT-15, pp. 398-405, July 1967.
- [18] E. M. T. Jones and J. T. Bolljahn, "Coupled-strip-transmission-line filters and directional couplers," *IRE Trans. Microwave Theory Tech.*, vol. MTT-4, pp. 75-81, Apr. 1956.
- [19] R. D. Middlebrook, *Differential Amplifiers*, Wiley, New York, 1963.
- [20] L. J. Giacoletto, *Differential Amplifiers*, Wiley, New York, 1970.
- [21] W. L. Gans and N. S. Nahman, "Shielded Balanced and Coaxial Transmission Lines- Parametric Measurements and Instrumentation Relevant to Signal Waveform Transmission in Digital Service," *NBS Technical Note 1042*, National Bureau of Standards, June 1981.

- [22] K. L. Su, *Fundamentals of Circuits, Electronics, and Signal Analysis*, Reprint ed., Waveland Press, Prospect Heights, IL, 1986.
- [23] G. Gonzalez, *Microwave Transistor Amplifiers*, Prentice-Hall, Englewood Cliffs, NJ, 1984.
- [24] K. Kurokawa, "Power waves and the scattering matrix," *IEEE Trans. Microwave Theory Tech.*, vol. MTT-13, pp. 194-202, March 1965.
- [25] T. T. Ha, *Solid-State Microwave Amplifier Design*, Reprint ed., Krieger, Malabar, FL, 1991.
- [26] D. E. Carlton, et. al., "Microwave wafer probing," *Microwave Journal*, vol. 29, pp. 121-129, Jan. 1985.
- [27] D. C. Smith, *High Frequency Measurements and Noise in Electronic Circuits*, Van Nostrand Reinhold, New York, 1993.
- [28] Toko America, Inc., *Coils and Filters: Balun Transformers*, pp. 74-75, Mt. Prospect, IL., 1992.
- [29] M. K. Krage and G. I. Haddad, "Characteristics of coupled microstrip transmission lines I: Coupled-mode formation of inhomogeneous dielectrics," *IEEE Trans. Microwave Theory Tech.*, vol. MTT-18, pp. 217-222, Nov. 1970.
- [30] D. E. Bockelman and W. R. Eisenstadt, "Combined differential and common mode scattering parameters: Theory and simulation," *IEEE Trans. Microwave Theory Tech.*, vol. MTT-43, pp. 1530-1539, July 1995.
- [31] F. R. Gantmacher, *The Theory of Matrices*, 2nd ed., Chelsea Pub. Co., New York, 1990.
- [32] Hewlett-Packard Company, *HP 85150B Microwave and RF Design Systems: User Documentation*, Santa Rosa, CA, 1992.
- [33] T. Kailath, *Linear Systems*, Prentice-Hall, Englewood Cliffs, NJ, 1980.
- [34] D. E. Bockelman and W. R. Eisenstadt, "Pure-mode network analyzer for on-wafer measurements of mixed-mode s-parameters of differential circuits,"

accepted for publication, *IEEE Trans. Microwave Theory Tech.*, anticipated publication, June 1997.

- [35] Merrimac Industries, *Product Data Pack: HJM-4R-6.5G 180° Power Divider/Combiner*, West Caldwell, NJ, June 1993.
- [36] M/A-Com, H-183-4 *180° Power Divider/Combiner: Product Literature*, Lowell, MA, 1996.
- [37] National Instruments Company, *LabVIEW: User Documentation*, Austin, TX, Aug. 1993.
- [38] Hewlett-Packard Company, *HP 85150B Microwave and RF Design Systems: Designer's Task Reference*, vol. 2, 3rd ed., Santa Rosa, CA, May 1994.
- [39] GGB Industries, *Product Literature: Dual Model 40A Probes*, Naples, FL, 1996.
- [40] Hewlett-Packard Company, *HP Momentum A.02: User's Guide*, 3rd ed., Santa Rosa, CA, April 1995.
- [41] B. Donecker, "Determining the measurement accuracy of the HP8510 microwave network analyzer," *Hewlett-Packard RF & Microwave Measurement Symp.*, pp. 4-71, Oct. 1984.
- [42] J. Fitzpatrick, "Error models for system measurements," *Microwave Journal*, vol. 21, pp. 63-66, May 1978.
- [43] Hewlett-Packard Company, *HP 8510C Network Analyzer: On Site Service Manual*, Santa Rosa, CA, Aug. 1991.
- [44] D. Rytting, "An analysis of vector measurement accuracy enhancement techniques," *Hewlett-Packard RF & Microwave Symp., Rec.*, Mar. 1982.
- [45] G. F. Engen and C. A. Hoer, "Thru-Reflect-Line: An improved technique for calibrating the dual six-port automatic network analyzer," *IEEE Trans. Microwave Theory Tech.*, vol. MTT-27, pp. 987-993, December 1979.
- [46] H.-J. Eul and B. Schiek, "Thru-match-reflect: one result of a rigorous theory for de-embedding and network analyzer calibration," *Proc. 18th European Microwave Conf.*, 1988.

- [47] J. V. Butler, D. K. Rytting, M. F. Iskander, R. D. Pollard, M. V. Bossche, "16-term model and calibration procedure for on-wafer network analysis measurements," *IEEE Trans. Microwave Theory Tech.*, vol. MTT-39, pp. 2211-2217, December 1991.
- [48] R. A. Speciale, "A generalization of the TSD network-analyzer calibration procedure, covering n-port scattering-parameter measurements, affected by leakage errors," *IEEE Trans. Microwave Theory Tech.*, vol. MTT-25, pp. 1100-1115, December 1977.
- [49] Hewlett-Packard Company, *Product Note 8510-8: Applying the HP8510 TRL Calibration for Non-Coaxial Measurements*, Santa Rosa, CA, Oct. 1987..
- [50] R. A. Speciale, "A complete and unambiguous solution to the super-TSD multiport-calibration problem," *IEEE Trans. Microwave Theory Tech. Symp. Digest*, pp. 251-252, 1983.
- [51] K. Brantervik, "A new four-port automatic network analyzer: Part II-theory," *IEEE Trans. Microwave Theory Tech.*, vol. MTT-33, pp. 569-575, July 1985.
- [52] A. Ferrero, U. Pisani, and K. J. Kerwin, "A new implementation of a multiport automatic network analyzer," *IEEE Trans. Microwave Theory Tech.*, vol. MTT-40, pp. 2078-2085, November 1992.
- [53] H. Heuermann and B. Schiek, "Results of network analyzer measurements with leakage errors corrected with the TMS-15-term procedure," *IEEE Trans. Microwave Theory Tech. Symp. Digest*, pp. 1361-1364, 1994.
- [54] S. Wolfram, *Mathematica*, 2nd ed., Reading, MA: Addison-Wesley Pub., 1991.
- [55] Lucas Weinschel Corp., *Product Literature: Power divider model 1580*, Gaithersburg, MA.
- [56] Hewlett-Packard Company, *HP 85052B 3.5mm Calibration Kit Product Manual*, Santa Rosa, CA, Mar. 1991.
- [57] J. C. Tippet and R. A. Speciale, "A rigorous technique for measuring the scattering matrix of a multiport device with a 2-port network analyzer," *IEEE Trans. Microwave Theory Tech.*, vol. MTT-30, pp. 661-666, May 1982.

- [58] Maury Microwave Corp., *Product Literature: Open Circuit Terminations, Precision 3.5mm Connectors*, Cucamonga, CA, Jan. 1991.
- [59] Maury Microwave Corp., *Product Literature: Precision Short Circuits, 3.5mm*, Cucamonga, CA, Sept. 1985.
- [60] W. H. Press, S. A. Teukolsky, W. T. Vetterling, B. P. Flannery, *Numerical Recipes in C*, 2nd ed., Cambridge, MA: Cambridge University Press, 1995.
- [61] R. A. Horn, *Topics in Matrix Analysis*, Cambridge, New York, Cambridge Univ. Press, 1991.
- [62] Hewlett-Packard Company, *HP 85057B 2.4mm Verification Kit Product Manual*, Santa Rosa, CA, Feb. 1991.
- [63] Hewlett-Packard Company, *HP 85056A 2.4mm Calibration Kit Product Manual*, Santa Rosa, CA, Nov. 1990.
- [64] I. Kasa, "A circle fitting procedure and its error analysis," *IEEE Trans. Instr. and Meas.*, vol. IM-25, pp. 8-14, March 1976.
- [65] R. Bellman, *Introduction to Matrix Analysis*, 2nd ed., New York: McGraw-Hill, 1970, pp. 235-6.
- [66] C. H. Ho, L. Fan, and K. Chang, "Ultra wide band slotline hybrid-ring couplers," in *IEEE MTT-S Int. Microwave Symp. Dig.*, 1992, pp. 1175-1178.
- [67] G. F. Mikucki and A. K. Agrawal, "A broad-band printed circuit hybrid-ring power divider," *IEEE Trans. Microwave Theory Tech.*, vol. MTT-37, pp. 112-117, Nov. 1989.
- [68] D. Kim and Y. Naito, "Broad-band design of improved hybrid-ring 3 dB directional coupler," *IEEE Trans. Microwave Theory Tech.*, vol. MTT-30, pp. 2040-2046, Nov. 1982.
- [69] C. Y. Pon, "Hybrid-ring directional couplers for arbitrary power division," *IRE Trans. Microwave Theory Tech.*, vol. MTT-9, pp. 529-535, Nov. 1961.
- [70] E. M. T. Jones, "Wide-band strip-line magic-T," *IRE Trans. Microwave Theory Tech.*, vol. MTT-8, pp. 160-168, Mar. 1960.

- [71] M. Muraguchi, T. Yukitake, and Y. Naito, "Optimum design of 3-dB branch-line couplers using microstrip lines," *IEEE Trans. Microwave Theory Tech.*, vol. MTT-31, pp. 674-678, Aug. 1983.
- [72] R. Levy and L. Lind, "Synthesis of symmetrical branch-guide directional couplers," *IEEE Trans. Microwave Theory Tech.*, vol. MTT-16, pp. 80-89, Feb. 1968.
- [73] L. Young, "Branch guide directional couplers," in *Proc. Nat. Electron. Conf.*, vol. 12, 1956, pp. 723-732.
- [74] D. Willems, and I. Bahl, "An MMIC-Compatible tightly coupled line structure using embedded microstrip," *IEEE Trans. Microwave Theory Tech.*, vol. MTT-41, pp. 2303-2310, Dec. 1993.
- [75] S. Arai, A. Kato, K. Minami, and T. Nishikawa, "A 900MHz 90 degrees hybrid for QPSK modulator," in *IEEE MTT-S Int. Microwave Symp. Dig.*, 1991, pp. 857-860.
- [76] C.H. Ho, L. Fan, and K. Chang, "Broad-band uniplanar hybrid-ring and branch-line couplers," *IEEE Trans. Microwave Theory Tech.*, vol. MTT-41, pp. 2116-2124, Dec. 1993.
- [77] T. Hirtoa, Y. Tarusawa, and H. Ogawa, "Uniplanar MMIC hybrids—A proposed new MMIC structure," *IEEE Trans. Microwave Theory Tech.*, vol. MTT-35, pp. 576-581, June 1987.
- [78] J. A. Navarro, Y. H. Shu, and K. Chang, "Broad-band electronically tunable planar active radiating elements and spatial power combiners using notch antennas," *IEEE Trans. Microwave Theory Tech.*, vol. MTT-40, pp. 323-328, Feb. 1992.
- [79] T. Tokumitsu, S. Hara, and M. Aikawa, "Very small ultra-wide-band MMIC magic-T and applications to combiners and dividers," *IEEE Trans. Microwave Theory Tech.*, vol. MTT-37, pp. 1985-1990, Dec. 1989.
- [80] H. Kamitsuna, and H. Ogawa, "Ultra-wideband MMIC active power splitters with arbitrary phase relationships," *IEEE Trans. Microwave Theory Tech.*, vol. MTT-41, pp. 1519-1523, Sept. 1993.

- [81] T. H. Chen, K. W. Chang, H. Wang, G. S. Dow, L. C. T. Liu, S. B. T. Bui, T. S. Lin, "Broadband monolithic passive baluns and monolithic double-balanced mixer," in *IEEE MTT-S Int. Microwave Symp. Dig.*, 1991, pp. 861-864.
- [82] F. L. M. van den Bogart, and R. Pyndiah, "A 10-14 GHz linear MMIC vector modulator with less than 0.1 dB and 0.8° amplitude and phase error," in *IEEE MTT-S Int. Microwave Symp. Dig.*, 1990, pp. 465-468.
- [83] Cascade Microtech, *Application Note: WPH-505/805 Waveguide-Input Wafer Probes*, Beaverton, OR, 1993.
- [84] D. E. Bockelman and W. R. Eisenstadt, "Combined differential and common mode analysis of power splitters and combiners," *IEEE Trans. Microwave Theory Tech.*, vol. MTT-43, pp. 2627-2632, Nov. 1995.
- [85] Z. A. Maricevic, T. K. Sarkar, Y. Hua, A. R. Djordjevic, "Time-domain measurements with the Hewlett-Packard network analyzer HP 8510 using the matrix pencil method," *IEEE Trans. Microwave Theory Tech.*, vol. MTT-39, pp. 538-547, March 1991.
- [86] Somlo, P. I., "The computation of coaxial line step capacitances," *IEEE Trans. Microwave Theory Tech.*, vol. MTT-15, pp. 48-53, Jan. 1967.
- [87] H. Hasegawa, M. Furukawa, H. Yanai, "Properties of microstrip line on Si-SiO₂ system," *IEEE Trans. Microwave Theory Tech.*, vol. MTT-19, pp. 869-881, Sept. 1971.
- [88] R. K. Wangsness, *Electromagnetic Fields*, 2nd. ed., John Wiley, New York, 1986.
- [89] R. E. Collin, *Foundations for Microwave Engineering*, John Wiley, New York, 1966.
- [90] D. C. Smith, "Balanced probe extends high-frequency measurements," *IEEE Circuits and Devices*, pp. 19-23, Nov. 1994.
- [91] Hewlett-Packard Company, *Product Note 8510-14: Using Multiple Test Sets with the HP8510B*, Santa Rosa, CA, Feb. 1989.
- [92] Hewlett-Packard Company, *HP 3488A Switch/Control Unit: Product Manual*, Santa Rosa, CA, Sept. 1987.

- [93] Hewlett-Packard Company, *HP8517A S-Parameter Test Set Manual*, Santa Rosa, CA, April 1991.
- [94] Hewlett-Packard Company, *HP8762/3/4 A, B, C Multiport Coaxial Switches: Technical Data*, Santa Rosa, CA, Feb. 1990.

BIOGRAPHICAL SKETCH

David E. Bockelman was born in Huntsville, Alabama, in 1967. He attended the Georgia Institute of Technology, where he earned a Bachelor of Electrical Engineering degree in 1989, and a Master of Science in Electrical Engineering degree in 1990. Since that time, he has been employed by Motorola Radio Product Group, where he has worked in the Applied Research Department. He began work on the doctorate degree in 1993, where he was sponsored by Motorola Radio Products Group Applied Research. He is currently a Staff Engineer, and has been awarded nine United States patents, and is a registered Professional Engineer in the State of Florida.

I certify that I have read this study and that in my opinion it conforms to acceptable standards of scholarly presentation and is fully adequate, in scope and quality, as a dissertation for the degree of Doctor of Philosophy.



William R. Eisenstadt, Chairman
Associate Professor of Electrical and
Computer Engineering

I certify that I have read this study and that in my opinion it conforms to acceptable standards of scholarly presentation and is fully adequate, in scope and quality, as a dissertation for the degree of Doctor of Philosophy.



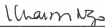
Gijs Bosman
Professor of Electrical and Com-
puter Engineering

I certify that I have read this study and that in my opinion it conforms to acceptable standards of scholarly presentation and is fully adequate, in scope and quality, as a dissertation for the degree of Doctor of Philosophy.



Robert M. Fox
Associate Professor of Electrical and
Computer Engineering

I certify that I have read this study and that in my opinion it conforms to acceptable standards of scholarly presentation and is fully adequate, in scope and quality, as a dissertation for the degree of Doctor of Philosophy.



Khai D. T. Ngo
Associate Professor of Electrical and
Computer Engineering

I certify that I have read this study and that in my opinion it conforms to acceptable standards of scholarly presentation and is fully adequate, in scope and quality, as a dissertation for the degree of Doctor of Philosophy.



Oscar D. Crisalle
Associate Professor of Chemical
Engineering

This dissertation was submitted to the Graduate Faculty of the College of Engineering and to the Graduate School and was accepted as partial fulfillment of the requirements for the degree of Doctor of Philosophy.

May 1997



Winfred M. Phillips
Dean, College of Engineering

Karen A. Holbrook
Dean, Graduate School

LD
1788
1977
1B66

